COMPUTATIONAL INSIGHTS INTO CATALYTIC HYDROGEN FORMATION: DRY REFORMING OF METHANE AND HYDROGEN EVOLUTION REACTION

Lea Gašparič

Doctoral Dissertation
Jožef Stefan International Postgraduate School
Ljubljana, Slovenia

Supervisor: Prof. Dr. Anton Kokalj, Jožef Stefan International Postgraduate School and Jožef Stefan Institute, Ljubljana, Slovenia

Evaluation Board:
Assoc. Prof. Dr. Nejc Hodnik, Chair, Jožef Stefan International Postgraduate School and National Institute of Chemistry, Ljubljana, Slovenia
Dr. Matic Poberžnik, Member, Jožef Stefan Institute, Ljubljana, Slovenia
Dr. Mira Todorova, Member, Institute for Sustainable Materials GmbH, Düsseldorf, Germany

MEDNARODNA PODIPLOMSKA ŠOLA JOŽEFA STEFANA
JOŽEF STEFAN INTERNATIONAL POSTGRADUATE SCHOOL



Lea Gašparič

COMPUTATIONAL INSIGHTS INTO CATALYTIC HYDROGEN FORMATION: DRY REFORMING OF METHANE AND HYDROGEN EVOLUTION REACTION

Doctoral Dissertation

MOLEKULSKO MODELIRANJE KATALITSKE TVORBE VODIKA: SUHA REFORMACIJA METANA IN REAKCIJA RAZVOJA VODIKA

Doktorska disertacija

Supervisor: Prof. Dr. Anton Kokalj

Ljubljana, Slovenia, October 2025

"Go back and really learn chemistry and physics and find problems. Find something that really interests you and that helps mankind, and then solve that problem."

— Karsten Reuter, panel discussion at ML4MD 2025, Espoo, Finland

Acknowledgments

This thesis is the result of the efforts of many people, and it would not have been possible without funding. I first wish to thank the Slovenian Research and Innovation Agency for supporting my doctoral studies.

I am especially grateful to my supervisor, Prof. Dr. Anton Kokalj, for his guidance and help, while allowing me the freedom to explore and learn from my mistakes. His mentorship has not only shaped this thesis but also influenced my development as a researcher.

I thank the members of the committee: Assoc. Prof. Dr. Nejc Hodnik, Dr. Matic Poberžnik, and Dr. Mira Todorova for their time and constructive feedback. I am also grateful to Assoc. Prof. Dr. Nejc Hodnik for collaboration on the topic of the hydrogen evolution reaction. Dr. Matic Poberžnik provided patient support and helpful guidance before and during my doctoral studies, acting as an informal mentor, for which I am sincerely thankful.

This thesis would not have been the same without the collaborations with research groups from the National Institute of Chemistry that helped shape its topic. I would especially like to thank Dr. Milutin Smiljanić for our collaboration on joint publications and for showing me how the work in the electrochemistry laboratory goes in practice. I also thank Dr. Albin Pintar for introducing me to the topic of dry reforming of methane.

I am grateful to Prof. Dr. Ingrid Milošev for welcoming me to her department when I was still an undergraduate student and for giving me the opportunity to learn and later pursue doctoral studies. My warm thanks go to my current and former colleagues at the Department of Physical and Organic Chemistry, Jožef Stefan Institute, for their support in both calm and stressful times. Thank you for your patience when my calculations kept the compute nodes busy, and for all the scientific and not-so-scientific discussions over coffee and lunch that made my days at the institute more enjoyable.

I am thankful for the opportunity to attend conferences and summer schools, where I met wonderful people who helped me maintain the motivation to pursue an academic career. I would also like to thank Dr. Nicolas Salles for hosting me on an Erasmus+ stay and for giving me the opportunity to explore the programming side of academic research.

My deepest thanks go to my friends for listening, for giving me space to relax and be myself. Many of them also chose academic careers, making it easier for us to share experiences and life lessons about working in academia. I am forever grateful to have met you and to have found a second home in Ljubljana.

Na koncu bi se rada zahvalila svoji družini in partnerju za njihovo ljubezen in stalno podporo. Hvala, ker ste bili moj pristan skozi leta študija, ker ste me spodbujali in poslušali, ko je bilo naporno, in z menoj praznovali majhne zmage. Brez vas bi bila ta pot bistveno težja in manj prijetna.

Abstract

The development of effective catalysts for sustainable hydrogen production is essential for the gradual transition to low-emission technologies. In this thesis, we focus on an *ab initio* investigation of experimentally relevant catalysts for dry reforming of methane and the hydrogen evolution reaction. Our aim is to explore structure–activity relationships and provide valuable insights for the design of highly efficient catalysts.

First, we investigate the process of dry reforming of methane ($CH_4 + CO_2 \longrightarrow 2\,CO + 2\,H_2$) on Ni-based catalysts. We examine the origin of the experimentally observed differences between undoped and Mn-doped CeO_2/Ni catalysts through vibrational analysis and reaction mechanism studies. Metallic Ni is found to be active for the reaction but prone to carbon deposition, whereas NiO is inactive but resistant to carbon poisoning. Our results suggest that the key difference between undoped and Mn-doped catalysts lies in the oxidation state of Ni: the Mn-doped catalyst contains partially oxidized Ni, which remains active while being more resistant to carbon deposition.

Next, we study the hydrogen evolution reaction on Pt- and Ru-based catalysts. For platinum, surface Pourbaix diagrams are constructed for both ideal surfaces and nanoparticle models, and kinetic analyses are performed on ideal surfaces. The results reveal higher reactivity for the nanoparticle models and a strong dependence of activation barriers on the coverage of chemisorbed H. For ruthenium, we compare the activity of hcp and fcc crystal phases by examining close-packed ideal surfaces and Wulff-constructed nanoparticles. Interestingly, the close-packed surfaces show the opposite activity trend to that observed in experiments for hcp- and fcc-structured nanoparticles, and the high activity of fcc Ru catalysts is attributed to the presence of less stable facets on the nanoparticles.

Finally, we investigate models of supported Pt and Ru nanoparticles to compare the conventional carbon support with the highly effective TiON support. The latter is found to influence the catalyst in two ways: (i) it strengthens the adhesion of metal nanoparticles to the support, enhancing durability and resistance to agglomeration, and (ii) it slightly weakens the binding of hydrogen atoms, thereby improving activity toward the hydrogen evolution reaction.

Povzetek

Razvoj učinkovitih katalizatorjev za trajnostno proizvodnjo vodika je bistven za postopni prehod k nizkoogljičnim tehnologijam. V tej disertaciji se osredotočamo na *ab initio* raziskave eksperimentalno relevantnih katalizatorjev za suho reformacijo metana in reakcijo razvoja vodika. Naš cilj je raziskati povezave med strukturo katalizatorjev in njihovo aktivnostjo ter ponuditi vpogled na atomskem nivoju za načrtovanje visoko učinkovitih katalizatorjev.

Najprej smo preučili proces suhega reformiranja metana ($CH_4 + CO_2 \longrightarrow 2\,CO + 2\,H_2$) na katalizatorjih iz niklja. S pomočjo vibracijske analize in študijo reakcijskega mehanizma smo raziskali izvor eksperimentalno opaženih razlik med nedopiranim CeO_2/Ni katalizatorjem in CeO_2/Ni, dopiranim z Mn. Ugotovili smo, da je kovinski Ni aktiven za reakcijo, vendar je nagnjen k nalaganju ogljika, medtem ko je NiO neaktiven, a odporen na vezavo ogljika. Naši rezultati nakazujejo, da je ključna razlika med nedopiranim in Mn dopiranim katalizatorjem v oksidacijskem stanju niklja: Mn-dopirani katalizator vsebuje delno oksidiran Ni, ki ostane aktiven, hkrati pa je bolj odporen proti nalaganju ogljika.

Nato smo raziskali reakcijo razvoja vodika na platinastih in rutenijevih katalizatorjih. Za platino smo izračunali površinske Pourbaixove diagrame za idealne površine in modele nanodelcev ter izvedli kinetično analizo na idealnih površinah. Rezultati so razkrili večjo reaktivnost nanodelcev in močno odvisnost aktivacijskih barier od pokritosti z adsorbiranimi atomi vodika. Pri ruteniju smo primerjali aktivnost hcp in fcc kristalnih faz z analizo najbolj stabilnih idealnih površin — Ru-hcp(001) in Ru-fcc(111) — in z Wulffovo konstrukcijo nanodelcev. Zanimivo je, da najbolj stabilne površine kažejo nasprotni trend aktivnosti od pričakovanega iz eksperimentnih opažanj za rutenijeve nanodelce. Nadaljnje analize so pokazale, da bi visoka aktivnost fcc-Ru katalizatorjev lahko bila posledica prisotnosti manj stabilnih površin na nanodelcih.

Nazadnje smo preučili modele Pt in Ru nanodelcev na različnih nosilcih, kjer nas je zanimala primerjava med običajnim ogljikovim nosilcem in učinkovitim TiON nosilcem. Za slednjega smo ugotovili, da kaže dva glavna vpliva na učinkovitost katalizatorja: (i) okrepi jakost vezave kovinskih nanodelcev na nosilec, kar izboljša obstojnost in odpornost proti aglomeraciji delcev, ter (ii) nekoliko oslabi vezavo vodikovega atoma, s čimer izboljša aktivnost za reakcijo razvoja vodika.

Contents

List of Figures **xv**

List of Tables **xvii**

Abbreviations **xix**

Symbols **xxi**

1 Introduction **1**
1.1 Hydrogen . . . 1
1.2 Dry Reforming of Methane . . . 2
1.3 Water Electrolysis and Hydrogen Evolution Reaction . . . 3

2 Aim of Work **5**

3 Technical Details **7**
3.1 Density-Functional Theory Calculations . . . 7
3.2 Energy Equations and Electronic Structure Analysis . . . 8
3.2.1 Reaction-mechanism analysis . . . 10
3.2.2 Gibbs energy . . . 12
3.3 Basic Computational Concepts in Electrocatalysis . . . 13
3.3.1 Electrolyte . . . 15
3.3.2 Electrode potential . . . 17
3.4 Analysis of Methane Dry Reforming . . . 18
3.4.1 Elementary steps of DRM . . . 19
3.5 Analysis of Hydrogen Evolution Reaction . . . 19
3.5.1 Elementary steps of HER . . . 22
3.5.2 Construction of surface Pourbaix diagrams . . . 23

4 Dry Reforming of Methane on Nickel-Based Catalysts **25**
4.1 Alloying Ni with Mn . . . 25
4.2 Vibrational Analysis . . . 26
4.3 Reaction Mechanisms . . . 29
4.3.1 Ni(111) surface . . . 29
4.3.2 NiO(100) surface . . . 31
4.4 Coadsorption Effects . . . 33

5 Hydrogen Evolution Reaction **39**
5.1 Platinum Catalysts . . . 39
5.1.1 Adsorption of H, OH, and O . . . 39
5.1.1.1 Adsorption patterns on the investigated nanoparticle . . . 42

5.1.1.2 Structural changes of the investigated nanoparticle upon adsorption . . . 45
5.1.2 Catalysts models under realistic conditions . . . 46
5.1.2.1 Effect of electrode potential and pH . . . 47
5.1.2.2 Pourbaix diagrams . . . 48
5.1.2.3 Contributions from solvation and vibrations for ideal surfaces 50
5.1.3 Kinetic analysis . . . 52
5.1.3.1 Tafel step on Pt(111) and Pt(100) . . . 54
5.2 Ruthenium Catalysts . . . 56
5.2.1 Comparison with platinum . . . 56
5.2.2 Uncommon fcc phase . . . 59
5.2.2.1 Binding of H and OH on Ru-hcp(001) and Ru-fcc(111) surfaces . . . 60
5.2.2.2 Activity of Ru-hcp(001) and Ru-fcc(111) . . . 63
5.2.2.3 Activation and reaction Gibbs energies . . . 66
5.2.2.4 Activity of low-index surfaces . . . 69
5.2.2.5 Wulff construction . . . 71
5.3 Models of Supported Nanoparticles . . . 74
5.3.1 Platinum . . . 75
5.3.2 Ruthenium . . . 79

6 Conclusions **85**

Appendix A Dry Reforming of Methane on Nickel-Based Catalysts **87**

Appendix B Platinum Catalysts for HER **93**

Appendix C Ruthenium Catalysts for HER **101**

Appendix D Structures of Supported Nanoparticles **105**

References **109**

Bibliography **121**

Biography **123**

List of Figures

Figure 3.1: Volcano plot concept . . . 9
Figure 3.2: Potential energy surface and minimum energy path . . . 11
Figure 3.3: Schematic representation of different potentials . . . 14
Figure 3.4: Implicit, explicit, and microsolvation models . . . 15
Figure 3.5: Models of an ice-like water bilayer . . . 16
Figure 3.6: Relevant structures for the analysis of DRM . . . 18
Figure 3.7: Investigated elementary steps of the DRM reaction . . . 20
Figure 3.8: Relevant structures for the analysis of HER . . . 21

Figure 4.1: Correlation of CO stretching frequency with C–O bond length and rigid adsorption energy . . . 28
Figure 4.2: Reaction and activation energies for DRM elementary steps on Ni(111) 30
Figure 4.3: Reaction energy profiles for reaction paths on Ni(111) . . . 31
Figure 4.4: Reaction and activation energies for DRM elementary steps on NiO(100) 32
Figure 4.5: Reaction energy profiles for reaction paths on NiO(100) . . . 33
Figure 4.6: Coadsorption effect on the NiO(100) surface . . . 35
Figure 4.7: Electron density difference for coadsorption structures . . . 37

Figure 5.1: Hydrogen surface adsorption energies on the considered Pt surface models 40
Figure 5.2: Average adsorption energies for H, OH, and O on ideal Pt surfaces . . . 41
Figure 5.3: Surface adsorption energies of OH and O on the investigated Pt surface models . . . 42
Figure 5.4: Average adsorption energy of H, OH, and O on the nanoparticle . . . 43
Figure 5.5: Gradual adsorption of H, OH, and O on the Pt_{55} nanoparticle . . . 43
Figure 5.6: Structural changes of the Pt_{55} nanoparticle upon adsorption . . . 46
Figure 5.7: Surface adsorption Gibbs energy as a function of electrode potential and pH . . . 48
Figure 5.8: Pourbaix diagrams constructed from the first approximation to Gibbs energy . . . 49
Figure 5.9: Pourbaix diagrams accounting for solvation and vibrational contributions 51
Figure 5.10: Reaction and activation energies for HER elementary steps . . . 53
Figure 5.11: Considered reaction pathway options for the Tafel step . . . 54
Figure 5.12: Reaction and activation energies of the Tafel step . . . 55
Figure 5.13: Surface adsorption energies of H, OH, and O on Ru-hcp(001) . . . 56
Figure 5.14: Pourbaix diagram for the Ru-hcp(001) surface . . . 57
Figure 5.15: Cohesion energy of Ru hcp and fcc nanoparticles . . . 58
Figure 5.16: Electron charge density difference for H* and OH* on Ru . . . 61
Figure 5.17: PDOS for H on fcc and top sites of Ru-hcp(001) and Ru-fcc(111) . . . 62
Figure 5.18: Possible dissociation pathways for water dissociation on close-packed Ru surfaces . . . 63
Figure 5.19: IS, TS, and FS for the dissociation of water on Ru closed-packed surfaces 65

Figure 5.20: Movement of the dissociating hydrogen atom during water dissociation 66
Figure 5.21: Reaction and activation Gibbs energies for water dissociation 68
Figure 5.22: Water dissociation energetics on low-index Ru surfaces 70
Figure 5.23: Wulff-constructed structures for Ru fcc and hcp crystal phases 71
Figure 5.24: Positions of Pt nanoparticles on TiON and graphene supports 75
Figure 5.25: Average H adsorption Gibbs energy on supported Pt nanoparticles . . . 76
Figure 5.26: Surface adsorption Gibbs energy versus electrode potential for supported Pt nanoparticles 77
Figure 5.27: Adhesion of Pt_{55} on TiON and graphene supports 78
Figure 5.28: Dependence of adhesion energy on hydrogen coverage for supported Pt_{55} 79
Figure 5.29: Positions of Ru nanoparticles on TiON and graphene supports 80
Figure 5.30: Electron density difference of $Ru_N^{\{6\}}$ pair on TiON and graphene supports 81
Figure 5.31: Chemisorption energy of a single H atom on supported hcp-$Ru_{54}^{\{6\}}$ particle 82
Figure 5.32: Supported hcp-$Ru_{54}^{\{6\}}$ nanoparticle with high H coverage 83

Figure A.1: Reaction pathways for the analyzed elementary steps on Ni(111) 87
Figure A.2: Reaction pathways for the analyzed elementary steps on NiO(100) . . . 90

Figure B.1: Snapshots of adsorption structures on Pt(111) 93
Figure B.2: Snapshots of adsorption structures on Pt(100) 94
Figure B.3: Snapshots of adsorption structures of H on Pt_{55} 94
Figure B.4: Snapshots of adsorption structures of O on Pt_{55} 95
Figure B.5: Snapshots of adsorption structures of OH on Pt_{55} 96
Figure B.6: HER reaction steps on Pt(111) with an ice-like water bilayer model. . . 97
Figure B.7: Reaction paths for the Tafel step on Pt(111) 98
Figure B.8: Reaction paths for the Tafel step on Pt(100) 99

Figure C.1: Reaction paths for water dissociation in the $(\sqrt{3} \times \sqrt{3})$R30° supercell . 101
Figure C.2: Reaction paths for water dissociation in the (3×3) supercell 102
Figure C.3: Adsorption geometries of H and OH on Ru surfaces 102
Figure C.4: Reaction paths for water dissociation on low-index surfaces 103

Figure D.1: Snapshots of H-covered structures of supported Pt_{55} 105
Figure D.2: Snapshots of H-covered structures of supported Pt_{38} 106
Figure D.3: Optimized structures of a single H atom on hcp-$Ru_{54}^{\{6\}}$/C 107
Figure D.4: Optimized structures of a single H atom on hcp-$Ru_{54}^{\{6\}}$/TiON 108

List of Tables

Table 4.1: C–O stretching frequencies of CH_xO species 26
Table 4.2: Energies, structural data and frequencies of CO adsorption on various surfaces of interest 27
Table 4.3: Coadsorption effect on Ni(111) and NiO(100) 34
Table 4.4: Coadsorption effect on NiO(100) for different supercell sizes 36

Table 5.1: Bader charges for adsorption on the Pt_{55} nanoparticle 44
Table 5.2: Surface energies and coordination numbers for low-index Ru surfaces . . 59
Table 5.3: Binding energies of H and OH on Ru slabs of different thickness 60
Table 5.4: Binding energies of H and OH on different sites of Ru 61
Table 5.5: Reaction and activation energies for water dissociation in the $(\sqrt{3} \times \sqrt{3})$R30° supercell 64
Table 5.6: Reaction and activation energies for water dissociation in the (3×3) supercell 64
Table 5.7: Gibbs energies for water dissociation in the $(\sqrt{3} \times \sqrt{3})$R30° supercell . . 67
Table 5.8: Gibbs energies for water dissociation in the (3×3) supercell 67
Table 5.9: Surface fractions of facets obtained from Wulff construction 72
Table 5.10: Effective barriers and surface fractions for Wulff-constructed particles . . 73
Table 5.11: Cohesion and adhesion energies of Ru nanoparticles on TiON and C supports 81

Abbreviations

DRM	...	dry reforming of methane
HER	...	hydrogen evolution reaction
SMR	...	steam–methane reforming
DFT	...	density functional theory
OER	...	oxygen evolution reaction
GGA	...	generalized gradient approximation
PBE	...	Perdew–Burke–Ernzerhof
IS	...	initial state
TS	...	transition state
FS	...	final state
PES	...	potential energy surface
MEP	...	minimum energy path
CI-NEB	...	climbing image nudged elastic band
ARTn	...	activation–relaxation technique nouveau
BEP	...	Brønsted–Evans–Polanyi
ZPE	...	zero point energy
SCCS	...	self-consistent continuum solvation
CHE	...	computational hydrogen electrode
SHE	...	standard hydrogen electrode
ML	...	monolayer
PBE+U	...	Perdew–Burke–Ernzerhof functional with Hubbard U correction
PAW	...	projector augmented wave
fcc	...	face-centered cubic
hcp	...	hexagonal close packed
CN	...	coordination number
PDOS	...	projected density of states
ILDOS	...	integrated local density of states
RHE	...	reversible hydrogen electrode

Symbols

Constants

k_B	=	$8.617333262 \times 10^{-5}$ eV/K	... Boltzmann constant
h	=	$4.135667696 \times 10^{-15}$ eV·s	... Planck constant
$\hbar$	=	$6.582119569 \times 10^{-16}$ eV·s	... reduced Planck constant
R	=	8.31451 J/mol·K	... universal ideal gas constant
F	=	9.648533×10^4 C/mol	... Faraday constant
π	=	3.14159265359	... the number pi
e_0	=	$1.60217663 \times 10^{-19}$ C	... elementary charge

Other symbols

N_i, n_i	... number of species i
∇^2	... Laplace operator
$\mathbf{r}$	... position
$v_\mathrm{ex}(\mathbf{r})$	... external potential
$v_\mathrm{H}(\mathbf{r})$	... Hartree potential
$v_\mathrm{xc}(\mathbf{r})$	... exchange–correlation potential
$\phi_i(\mathbf{r})$	... Kohn–Sham orbital i
ε_i	... eigenvalue of orbital $\phi_i(\mathbf{r})$
ρ	... electron density
E_el	... electronic energy
T_s	... kinetic energy
V_ex	... external energy
V_H	... hartree energy
E_ex	... exchange–correlation energy
E_i	... energy of species i
E_b	... binding energy
E_ads	... adsorption energy
$\overline{E}_\mathrm{ads}$	... average adsorption energy
γ	... surface adsorption energy
A	... area of the 2D supercell
Σ_surf	... surface energy per supercell
σ_surf	... surface energy per area
E_coh	... cohesion energy
E_adh	... adhesion energy
$\rho_i(\mathbf{r})$	... electron charge density of system i
$\Delta\rho(\mathbf{r})$	... electron charge density difference
$\Delta\rho(z)$	... planar integrated electron charge density difference along the z direction
ΔE	... reaction energy
E^act	... activation energy
k	... rate constant

C ... pre-exponetial factor
E_0 ... DFT energy
G ... Gibbs energy
T ... temperature
p ... pressure
V ... volume
S ... entropy
ν_i ... vibrational frequency
I ... moment of inertia
σ_{rot} ... rotational symmetry number
m ... mass
$\widetilde{\mu}$ ... electrochemical potential
μ_i ... chemical potential
$\mu_i^{\ominus}$ ... standard chemical potential
z_i ... charge of the species i
ϕ ... inner electrostatic potential
ψ ... outer electrostatic potential
χ ... surface potential
ΔG_{solv} ... solvation Gibbs energy
U ... electrode potential
a_i ... activity of species i
d_{ij} ... distance between i and j
E_{mix} ... mixing energy
E_{coads} ... coadsorption energy
$g(r)$ ... radial distribution function
r ... reaction rate
y_i ... number of active sites per area
x_i ... fraction of surface area

Chapter 1

Introduction

The main topic of this work revolves around the sustainable production of hydrogen, encompassing both the thermal catalysis of dry reforming of methane (DRM) and the electrochemical hydrogen evolution reaction (HER). The investigation of both reactions was inspired by collaboration with experimental groups, enabling the computational work to be aligned with experimentally relevant problems.

1.1 Hydrogen

Molecular hydrogen has a wide range of applications, as it can be used as a chemical precursor, a fuel, or an energy vector capable of storing and converting energy. At present, it is primarily used for the production of ammonia, methanol, and in the petrochemical industry [1]–[3]. Its role as a fuel and energy vector is also gaining a lot of attention due to its high gravimetric energy density [4], [5], the growing global demand for energy, and the necessity to reduce carbon emissions.

Conversion of hydrogen fuel into electricity is achieved using fuel cells, where hydrogen reacts with an oxidizing agent (usually oxygen) to produce electric current and water as the only byproduct. Although hydrogen consumption generates zero or very low emissions, the overall environmental sustainability is determined by the production pathway of molecular hydrogen. A common distinction between production routes is made using a color-based terminology. While many categories of hydrogen are reported in the literature [1], the three most common ones are gray, blue, and green hydrogen.

Gray hydrogen is produced by reforming methane, a naturally occurring hydrocarbon gas. The most established process is steam–methane reforming (SMR), in which methane reacts with water to produce synthesis gas (also known as syngas), a mixture of CO and H_2. In a subsequent water–gas shift reaction, CO reacts with water to form CO_2 and additional hydrogen. This route is currently the dominant industrial method of hydrogen production, but it generates large amounts of CO_2. Moreover, methane leakage during the process is a significant concern, as methane is a potent greenhouse gas with a stronger global warming effect than CO_2 [6]. An alternative reforming process is DRM, where methane reacts with CO_2 to yield synthesis gas. Because this reaction consumes CO_2 as a reactant, it is considered more attractive, though further research and catalyst development are required.

A related variant is blue hydrogen, often referred to as a cleaner form of gray hydrogen. The synthesis pathway is identical to gray hydrogen, but the generated CO_2 is captured rather than released into the atmosphere. Due to its relatively low overall cost [7], blue hydrogen is frequently considered a transitional option between gray and green hydrogen, which is a sustainable way to obtain hydrogen. Green hydrogen is based on water electrolysis powered by renewable electricity. In this process, water is split into hydrogen and

oxygen using electric energy.

In recent years, interest in hydrogen has increased considerably, and many experts regard it as a potential alternative to fossil fuels and a means of reducing greenhouse gas emissions. Others, however, caution that hydrogen production may not keep pace with demand and emphasize the need to also consider alternatives such as process electrification and battery technologies [8], [9]. In cases where such alternatives are not viable, hydrogen can still play an important role as an energy carrier. A critical aspect for the deployment of clean hydrogen technologies is the shift in production from conventional gray hydrogen to more sustainable blue and green pathways. The gradual transition toward lower-emission hydrogen production is also the central focus of this thesis. Specifically, dry reforming of methane was investigated as an attractive alternative to SMR, while the hydrogen evolution reaction was studied in the context of water electrolysis for green hydrogen production.

1.2 Dry Reforming of Methane

One part of this thesis is devoted to dry reforming of methane and was published as an article [10] in collaboration with an experimental group of Dr. Albin Pintar from the National Institute of Chemistry. This research is focused on Ni catalysts supported on doped and undoped CeO_2 and the discussion in this thesis is adapted from our article.

DRM is, as already noted, an attractive alternative to SMR because it converts two major greenhouse gases, CH_4 and CO_2, into synthesis gas — a mixture of H_2 and CO — also known as syngas. This syngas can be directly used as a fuel or further processed to obtain pure hydrogen. In addition to hydrogen production, DRM provides a route to transform CO_2 into a more viable form. The process is strongly endothermic and the overall reaction can be written as:

$$\mathrm{CH_4 + CO_2 \longrightarrow 2\,CO + 2\,H_2}, \quad \Delta H = 247\ \mathrm{kJ/mol\ at\ 25\ ^\circ C} \tag{1.1}$$

In addition to the high energy demand, deposition of atomic carbon on catalysts (i.e., coke formation) poses a significant challenge in DRM, particularly at lower temperatures [11]–[13]. While noble metals are effective catalysts with minimal coke formation, their high cost and scarcity limit large-scale application. Ni-based catalysts provide a more affordable alternative [13], [14], but they are highly susceptible to coke deposition [11]. Two common strategies to mitigate coke formation on Ni while enhancing its activity are alloying Ni with other metals [13], [15], [16] and tuning the metal–support interaction [13], [14], [17]. Among promising supports, CeO_2 (ceria) has received particular attention due to its high oxygen storage capacity and redox properties [18].

Ni, as a promising catalyst, has been studied extensively with DFT, and for the Ni(111) surface either the dissociation of the first H atom from CH_4 or the oxidation of CH or C has been identified as the rate-limiting step [19]–[22]. Several studies [21], [23] also emphasize the issue of strong CO adsorption, which accumulates on the surface and subsequently promotes coke formation.

In addition, more realistic catalysts in the form of supported metal nanoparticles have been investigated. CH_4 is reported to dissociatively adsorb on metallic particles [13], [24], [25], while CO_2 can adsorb on both the metal and the support, particularly in the vicinity of metal particles [13], [25]–[27]. Ceria is considered an effective support for Ni particles, as it exhibits strong metal–support interactions and significant charge transfer. At the interface, Ni atoms are oxidized to +1 or +2 oxidation states, while cerium ions are reduced [28], [29].

Ni nanoparticles are generally regarded as metallic under reaction conditions, although the potential roles of nickel carbide and nickel oxide in DRM have also been reported [30],

[31], with the latter showing greater resistance to coke formation [32]. Prior to testing, Ni catalysts are typically exposed to a reducing atmosphere, which converts NiO to metallic Ni [33]–[35]. However, the activated catalysts may retain a fraction of unreduced NiO, as the degree of reduction depends on the catalyst composition, as shown for NiO–Mg–ZrO_2 solid solutions [33], [36], [37].

Our research is primarily based on the experimental results of Sagar and Pintar [38], who investigated undoped and MnO_x-doped Ni/CeO_2 as potential catalysts for DRM. They reported that the MnO_x-doped catalyst (Ni/Mn_xCeO_2) exhibits enhanced resistance to coking and higher conversion rates of both methane and CO_2. The Ni/Mn_xCeO_2 catalyst also showed a higher concentration of oxygen vacancies and mobile oxygen species in the support. In addition, infrared spectra revealed the presence of a 2020 cm^{-1} peak on the Ni/CeO_2 catalyst, which is absent in Ni/Mn_xCeO_2. To account for these differences, the authors proposed two possible pathways: direct dissociation of methane and the reaction of methane with surface oxygen species.

1.3 Water Electrolysis and Hydrogen Evolution Reaction

The second part of this thesis focuses on the hydrogen evolution reaction (HER), the cathodic half-reaction of water electrolysis. It was carried out in collaboration with the experimental group of Dr. Nejc Hodnik from the National Institute of Chemistry, leading to three published articles [39]–[41], on which the discussion in this thesis is based.

Water electrolysis provides an emission-free route to hydrogen production, therefore both HER and the oxygen evolution reaction (OER), the anodic counterpart, have received significant scientific attention. In acidic media, HER can be written as:

$$H^+ + e^- \rightleftharpoons \frac{1}{2} H_2 \tag{1.2}$$

The most straightforward approach to evaluating catalytic activity for HER is to calculate the adsorption energy of hydrogen, since chemisorbed H atoms are reaction intermediates [42]. This adsorption energy is generally considered a reliable descriptor under acidic conditions. However, in alkaline media, HER kinetics have been observed to be two to three times slower than expected [43], [44], indicating that additional factors influence the reaction rate. Several explanations have been proposed [43]–[45], including the nature of the proton donor, the effect of co-adsorbed species, and solvent reorganization. Among these, the proton donor is considered an important factor. In acidic media, protons originate from H_3O^+-like species, whereas in alkaline media water molecules must act as the proton donor. Because water dissociation is kinetically slower than proton transfer from H_3O^+, it introduces a significant energy barrier to the hydrogen adsorption step [43], [45], [46], thereby contributing to the sluggish HER kinetics under alkaline conditions. Beyond H adsorption energy, the binding strength of OH has also been proposed as a relevant activity descriptor [47], and was later shown to correlate with the activation energy for hydrogen adsorption [48]. Another factor relevant in alkaline media is the difference in standard electrode potentials: while HER in acidic media has a standard potential of 0 V, in alkaline media it is -0.826 V. This leads to a higher negative charge density in alkaline and altered structure of interfacial water [44].

The conventional catalysts for HER are Pt-based, as Pt is among the most active materials for this reaction. Its high activity is attributed to a near-optimal hydrogen adsorption energy [42]. Since Pt binds hydrogen slightly too strongly, a modest weakening of the H–Pt interaction would, in theory, further enhance its catalytic activity by bringing it closer to the top of the volcano plot. Numerous mechanistic studies of HER on Pt already

exist [46], [49]–[51], investigating the prevailing mechanisms at ideal surfaces and the influence of electrode potential or pH. While these studies have deepened our understanding of Pt's exceptional catalytic performance under different conditions, a major limitation of Pt remains its high cost and scarcity [5], [52]. This challenge has motivated significant efforts to reduce platinum usage in catalysts. One strategy is the use of metal nanoparticles [5], [52], [53], which provide a high surface-to-volume ratio and exhibit excellent reactivity. Although DFT studies of nanoparticles are relatively scarce, some investigations have examined oxygen adsorption [54]–[56], showing that adsorbates bind strongly to edges.

An important factor influencing nanoparticle performance is the support material. Tuning the metal–support interaction represents a promising strategy for optimizing catalytic properties [5], [57]. In this context, a particularly attractive support material is $TiON_x$, synthesized and investigated by our collaborators at the National Institute of Chemistry. It can be combined with different metal nanoparticles to form effective catalysts for both HER and OER [40], [41], [58], [59].

Another strategy to reduce platinum usage in catalysts is to employ alternative materials, with ruthenium emerging as a particularly attractive option for alkaline media. Compared to platinum, Ru exhibits superior water-splitting performance under alkaline conditions [60], and a promising route to further enhance its catalytic activity is to control its crystal phase [60], [61]. While bulk Ru naturally crystallizes in the hexagonal close-packed (hcp) structure, Kusada et al. [62] successfully synthesized and characterized face-centered cubic (fcc) Ru nanoparticles, which showed higher activity toward CO oxidation for particles larger than 3 nm. Since then, this uncommon fcc phase has been reported in a variety of applications [63]–[67], including HER [68]–[71]. Although experimental evidence suggests that Ru-fcc catalysts outperform their Ru-hcp counterparts, the mechanistic origin of this difference remains insufficiently understood. Several DFT studies have address this question, but their conclusions are often contradictory. For instance, Li et al. [72] calculated hydrogen adsorption energies on various Ru surfaces and concluded that Ru-fcc(111) is less active, implying that the hcp phase may be more favorable for HER. In contrast, Chen et al. [69] examined a RuNi system interacting with a single water molecule and reported a lower activation barrier for water dissociation on the fcc phase. A highly influential study by Zheng et al. [68], which employed an ice-like water bilayer model, likewise found a lower activation barrier for water dissociation on Ru-fcc(111) compared to Ru-hcp(001). However, these results were obtained from thin slab models and did not include corrections for low-frequency vibrational modes — factors that appear to dominate the preference for the fcc phase in their calculations.

Chapter 2

Aim of Work

The purpose of this doctoral thesis is to gain insights into the structure–activity relationships of selected catalysts. Our aim is to analyze their activity toward HER and DRM and to identify the factors that govern their performance. By investigating experimental observations of novel catalysts, we seek to address key challenges and contribute to the development of advanced materials containing reduced amounts of expensive noble metals. Such advances would enable more accessible hydrogen production and, consequently, help reduce carbon dioxide emissions.

For DRM, the focus is on the observations of Sagar and Pintar [38]. The effects of doping the Ni/CeO_2 catalyst with MnO_x are examined to explore possible explanations for the observed activity enhancements. Vibrational analysis is employed to ascribe the 2020 cm^{-1} peak to the relevant DRM intermediate. Furthermore, reaction pathway analysis is performed on both Ni and NiO to investigate changes in the proposed mechanism and to assess the influence of oxidation on the activity of Ni-based catalysts.

For HER, the metals of interest are platinum and ruthenium. In the case of platinum, two catalyst models are investigated: nanoparticles and ideal surfaces. Pourbaix diagrams (pH–potential diagrams) are constructed to evaluate the reactivity of different surfaces and to identify the most relevant structures under experimental conditions. For ruthenium, a comparison of the activity of the fcc and hcp phases under alkaline conditions is carried out by analyzing water dissociation and the interactions of key intermediates with the metal surfaces. In addition, nanoparticles of both metals supported on carbon and $TiON_x$ are examined. Adhesion energies and hydrogen adsorption energies are calculated and compared for the two supports in order to evaluate support effects and to determine the factors that govern catalytic activity.

With the work presented in this thesis, we aim to investigate the following hypotheses:

1. Doping the Ni/CeO_2 catalyst with MnO_x alters the reaction mechanism, as proposed by Sagar et al. [38].

2. Models of ideal surfaces capture the same activity trends as nanoparticle models.

3. The fcc phase of Ru is more active toward HER than the thermodynamically stable hcp phase.

4. The TiON support forms stronger covalent bonds with metal nanoparticles but does not significantly affect the interaction between adsorbed H and the metal compared to a conventional carbon support.

Chapter 3

Technical Details

This chapter focuses on the theoretical concepts used in this thesis and the computational details that describe the setup for calculations. First, density functional theory is briefly discussed, followed by the energy equations and equations for electronic structure analysis, along with the corrections needed to calculate the Gibbs energy. Next, the basic computational concepts relevant to electrocatalytic reactions are briefly discussed. Finally, the computational details for the analysis of both DRM and HER are provided.

3.1 Density-Functional Theory Calculations

All catalytic systems considered in this thesis were studied using density functional theory (DFT), a computational quantum-mechanical modeling method. The theoretical foundation of quantum mechanics for chemistry is the time-independent Schrödinger equation within the Born–Oppenheimer approximation, that separates the motion of electrons and nuclei. By solving the Schrödinger equation, we obtain the wave function of the investigated system, which determines the energy. Analytical solutions for the time-independent Schrödinger equation can be obtained only for one-electron systems, while for many-body problems, approximate methods such as DFT must be used.

The central idea of the DFT approach is to simplify the description of a system. Instead of using a wave function (a $3N$ dimensional object, where N is the number of electrons) DFT uses an electron density that is only a 3 dimensional object. This dramatically reduces the computational load. The theory is based on two Hohenberg–Kohn theorems, which state that the total energy is a unique functional of the electron density and that the system in the ground state is determined by its electron density [73], [74]. While the formalism of DFT is, in principle, exact, it does not enable calculations in practice. Kohn and Sham developed a framework of applicable DFT with the help of an auxiliary system of non-interacting electrons that transforms the N-electron problem into a set of N one-electron equations. The resulting Kohn–Sham equations can be written as [75]:

$$\left[-\frac{1}{2}\nabla^2 + v_{\mathrm{ex}}(\mathbf{r}) + v_{\mathrm{H}}(\mathbf{r}) + v_{\mathrm{xc}}(\mathbf{r}) \right] \phi_i(\mathbf{r}) = \varepsilon_i \phi_i(\mathbf{r}) \tag{3.1}$$

Here, $-\frac{1}{2}\nabla^2$ is the kinetic term, while $v_{\mathrm{ex}}(\mathbf{r})$, $v_{\mathrm{H}}(\mathbf{r})$, and $v_{\mathrm{xc}}(\mathbf{r})$ are external, Hartree and exchange-correlation potentials, respectively. $\phi_i(\mathbf{r})$ is the Kohn–Sham orbital i and ε_i its eigenvalue. By self-consistently solving the above equations, we obtain orbitals and electron density, which are then used to calculate the electronic energy of the system:

$$E_{\mathrm{el}} = T_{\mathrm{s}}[\{\phi_i\}] + V_{\mathrm{ex}}[\rho] + V_{\mathrm{H}}[\rho] + E_{\mathrm{xc}} \tag{3.2}$$

which is a sum of kinetic (T_s), external (V_{ex}), Hartree (V_H) and exchange-correlation (E_{xc}) energy. In practical applications, DFT is not exact because the exchange–correlation term is not known and must be approximated. Many different approximations have been proposed, among which the generalized-gradient approximation (GGA) functionals are particularly popular due to their good balance between accuracy and computational efficiency.

For all the calculations within this thesis, we used the QUANTUM ESPRESSO software package [76], [77] with the Perdew–Burke–Ernzerhof (PBE) approximation to exchange-correlation energy [78]. PBE is a GGA functional that provides decent accuracy for a wide range of systems and is implemented in QUANTUM ESPRESSO. Periodic boundary conditions were applied and the electronic wave functions were expanded in a plane-wave basis set with pseudopotentials. More specific computational details for each system will be provided in the following sections.

3.2 Energy Equations and Electronic Structure Analysis

From DFT calculations, we obtain information about both the electronic structure and the total energy of the system. The electronic structure provides insight into the interactions between different components of the system, while the total energy is an indicator of its stability. Since the absolute value of the total energy depends on the chosen functional and computational parameters, only energy differences are physically meaningful, as they are comparable across different computational setups and more directly reflect realistic phenomena.

For our research, we are interested in the interaction between reaction intermediates and the catalyst surface, which can be quantified by the binding and adsorption energies. Throughout the thesis, the notation X* is used to denote an adsorbed X species, while * indicates an adsorption site. The binding energy is then defined as:

$$E_b = E_{X^*} - E_* - E_X \tag{3.3}$$

where E_{X^*} is the energy of a surface with an adsorbed X species, E_* is the energy of the bare surface model, and E_X is the energy of the isolated X species. Here, X can represent any species, which is not necessarily stable as a standalone entity. In contrast, adsorption energy is evaluated with respect to stable standalone species and the equation for it depends on the species involved in the adsorption reaction. For example, the adsorption energy of an arbitrary number of adsorbed hydrogen atoms can be calculated with respect to the hydrogen gas molecule as:

$$\begin{aligned} &\frac{n}{2}H_2 + {}^* \longrightarrow n\,H^* \\ &E_{ads}^H = E_{nH^*} - E_* - \frac{n}{2}E_{H_2} \end{aligned} \tag{3.4}$$

where n is the number of adsorbed hydrogen atoms, E_{nH^*} is the energy of the surface with adsorbed H atoms, E_* is the energy of the bare surface model and E_{H_2} is the energy of a hydrogen molecule. One can also calculate the average adsorption energy:

$$\overline{E}_{ads}^H = \frac{1}{n}\left(E_{nH^*} - E_* - \frac{n}{2}E_{H_2}\right) \tag{3.5}$$

To compare the stability of surfaces with different adsorbate coverages, the surface adsorption energy can be calculated as:

$$\gamma = \frac{E_{ads}}{A} \tag{3.6}$$

where E_{ads} is the total adsorption energy (for H* it is given with Eq. (3.4)) and A is the area of the 2D supercell. An analogous relation can also be used to obtain surface adsorption Gibbs energy from the total adsorption Gibbs energy. The structure with the lowest value of the surface adsorption Gibbs energy corresponds to the most stable state under the conditions for which the adsorption Gibbs energies are calculated.

According to the Sabatier principle, an ideal catalyst should bind adsorbates neither too strongly nor too weakly. A bond that is too strong prevents the products from desorbing from the surface, while a bond that is too weak fails to activate the reactants. This concept is often visualized using a volcano plot, which is schematically shown in Figure 3.1. The x-axis represents a measure of the adsorption energy, while the y-axis represents the reaction rate. A lower (more negative) adsorption energy indicates stronger binding, whereas a higher (less negative or more positive) adsorption energy corresponds to weaker binding.

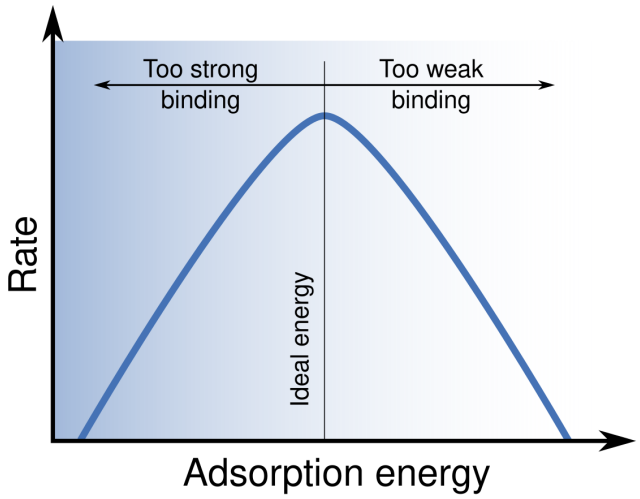


Figure 3.1: Schematic representation of a volcano plot. The top of the volcano corresponds to the ideal binding strength, where the reaction rate is maximized. On the left side, the binding is too strong, while on the right side, the binding is too weak. The reaction rate decreases on both sides away from the peak.

In addition to adsorption phenomena, the stability of the catalyst is also relevant. Metals can expose different facets, and their relative stability can be assessed by calculating the surface energies, which are obtained by fitting the equation:

$$E_{\text{slab}} = 2\Sigma_{\text{surf}} + nE_{\text{bulk}} \tag{3.7}$$

where E_{slab} is the energy of a slab with n atoms, Σ_{surf} is the surface energy per supercell, and E_{bulk} is the energy of a bulk atom. E_{slab} is calculated at different thicknesses and Σ_{surf} and E_{bulk} are determined as the intercept and slope from fitting Eq. 3.7. The factor of two in the expression arises from the presence of two surfaces in the slab. To obtain the surface energy per area, the Σ_{surf} must be divided by the area of the supercell:

$$\sigma_{\text{surf}} = \frac{\Sigma_{\text{surf}}}{A} \tag{3.8}$$

Based on the surface energies, the equilibrium shape of nanoparticles can be predicted using the Wulff construction. For a given volume, the most stable particle is the one that minimizes the total surface energy. The equilibrium shape is determined by the direction-dependent surface energies, where the directions reflect the symmetry of the crystal. For each crystalographic direction, a plane perpendicular to that direction is

drawn at a distance from the origin proportional to its surface energy. The inner envelope of these planes defines the Wulff construction and represents the equilibrium shape of the nanoparticle. In this work, the equilibrium shapes were generated using the Wulffpack Python library [79].

To study the stability of catalysts consisting of nanoparticles, we calculated cohesion energies according to equation:

$$E_{\text{coh}} = \frac{1}{n}(E_{\text{system}} - nE_{\text{atom}}) \tag{3.9}$$

where n is the number of metal atoms in the considered system, which could be either nanoparticle or bulk metal. E_{system} is the energy of the system (bulk primitive cell or nanoparticle) and E_{atom} is the energy of a metal atom in vacuum. Cohesion energy serves as a measure of stability and represents the energy change upon the formation of a bonded system from isolated entities. A lower cohesion energy indicates a more stable system.

In addition to nanoparticles in vacuum, we also considered supported nanoparticles, where adhesion energy was used as a measure of stability. It is similar to the binding energy, as it quantifies the interaction between the nanoparticle and the support:

$$E_{\text{adh}} = E_{\text{NP/support}} - E_{\text{NP}} - E_{\text{support}} \tag{3.10}$$

Here, $E_{\text{NP/support}}$ is the energy of the supported nanoparticle system, E_{NP} in the energy of an isolated nanoparticle, and E_{support} is the energy of the support. Adhesion energy reflects the strength of nanoparticle's binding to the support and can indicate the long-term stability of the system. A stronger binding between the nanoparticle and the support requires more energy for nanoparticle removal, resulting in a more stable system.

In addition to thermodynamic analysis, we are also interested in electron flow upon binding. This can be visualized by calculating electron charge density difference:

$$\Delta\rho(\mathbf{r}) = \rho_{\text{X}*}(\mathbf{r}) - \rho_{\text{X}}(\mathbf{r}) - \rho_{*}(\mathbf{r}) \tag{3.11}$$

where $\rho_{\text{X}*}(\mathbf{r})$ is the electron density of the surface with the bound species X (X can be either an intermediate species or a nanoparticle), $\rho_{\text{X}}(\mathbf{r})$ is the electron density of the unbound species X, and $\rho_{*}(\mathbf{r})$ is the electron density of the bare surface. In these calculations, the geometries of the unbound species X and the bare surface are kept the same as in the optimized X* system. The electron charge density difference allows us to spatially visualize the regions of electron deficit and surplus, showing the movement of electrons upon the binding of segment X. Additionally, we can calculate the planar integrated electron charge density difference along the z-direction:

$$\Delta\rho(z) = \int_A \Delta\rho(\mathbf{r})\mathrm{d}x\mathrm{d}y \tag{3.12}$$

where $\Delta\rho(\mathbf{r})$ is the electron charge density difference obtained with Eq. (3.11) and A is the area of the surface cell. This quantity allows us to extract a 1D plot from a 3D grid, making it easier to compare the differences in electron transfer between systems.

3.2.1 Reaction-mechanism analysis

To study catalytic activity, it is necessary to analyze the underlying reaction mechanism. The mechanism typically consists of a sequence of elementary steps, each involving an initial state (IS), a transition state (TS), and a final state (FS). Each of these states corresponds to a point on a multidimensional potential energy surface (PES), which represents the energy landscape of the system. The IS and FS are local minima on the PES, while the TS

is a first-order saddle point. The most energetically favorable pathway connecting these three states is the minimum energy path (MEP). Each point on the MEP is a minimum in all directions except along the reaction coordinate, and the highest point corresponds to the TS. A schematic representation of the PES and MEP is shown in Figure 3.2.

Computationally, the most accessible property when analyzing a reaction is the reaction energy (ΔE), a thermodynamic quantity that gives the energy difference between the FS and the IS:

$$\Delta E = E_{\mathrm{FS}} - E_{\mathrm{IS}} \tag{3.13}$$

A negative reaction energy indicates that the FS is energetically more stable than the IS. Such a reaction is classified as exothermic and involves the release of energy into the surroundings. If the reaction energy is positive, the reaction is endothermic, meaning the FS is higher in energy than the IS and energy is absorbed from the surroundings. The reaction energy reflects the relative energetic stability of the IS and FS, but it does not provide any information about the reaction rate. To evaluate the kinetics, one must identify the transition state and calculate the activation energy:

$$E^{\mathrm{act}} = E_{\mathrm{TS}} - E_{\mathrm{IS}} \tag{3.14}$$

The higher the activation energy, slower the reaction rate. The connection between the activation energy and the rate constant is described by the Arrhenius law:

$$k = C \exp(-\frac{E^{\mathrm{act}}}{k_{\mathrm{B}} T}) \tag{3.15}$$

where k is the rate constant, C the pre-exponential factor, k_{B} the Boltzmann constant, and T the temperature. The overall reaction rate is determined by the slowest elementary step, known as the rate-determining step. Effective catalysts can increase the reaction rate by providing alternative reaction mechanisms with lower activation energies.

The initial and final states of a reaction can be determined computationally using various geometry optimization techniques. The transition state, however, is a first-order saddle point on the PES and therefore cannot be located using conventional geometry optimization methods. It requires specialized techniques. In this thesis, transition states were identified using the climbing image nudged elastic band (CI-NEB) method [80], [81] and the activation-relaxation technique nouveau (ARTn), as implemented in QUANTUM ESPRESSO [82], [83]. The NEB method optimizes a sequence of intermediate images

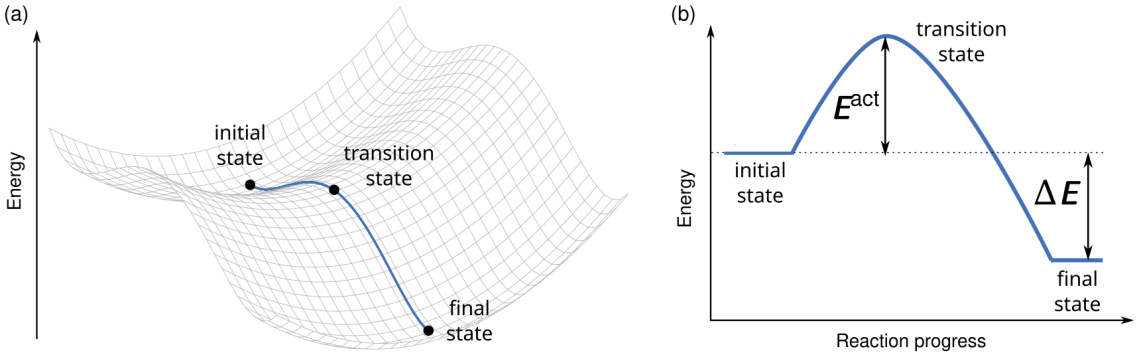


Figure 3.2: (a) 3D representation of the PES with the MEP shown as a blue line. (b) Schematic 2D representation of the MEP with labeled initial, transition, and final states, along with the activation (E^{act}) and reaction energies (ΔE).

along the reaction path, which are connected by spring forces. The introduction of an elastic band with spring interactions prevents the images from relaxing to the initial or final states. The climbing image (CI) extension of NEB enables accurate identification of the transition state by allowing one image to ascend along the reaction path to the highest energy point on the MEP, corresponding to the saddle point. While CI-NEB requires both initial and final states as input, the ARTn method requires only a single input structure and a small perturbation to initiate exploration of the PES. By randomly exploring the PES, it gradually identifies a negative eigenvalue in the Hessian matrix, which directs the search towards a transition state. This method can be used both to explore possible transitions from a given state and to perform targeted searches for specific transition states.

A simplified approach to evaluating activation energies is to employ the Brønsted–Evans–Polanyi (BEP) relation [84]. It assumes a linear relationship between the reaction energy and the activation energy. This relation is well established for the dissociation of diatomic molecules [84], [85], where the transition state is more final-state-like, and changes in the activation energy therefore follow changes in the reaction energy.

3.2.2 Gibbs energy

The total energy obtained from DFT calculations corresponds to electronic ground state in vacuum at 0 K. While trends at these conditions can offer valuable insights, calculating Gibbs energy at finite temperature and pressure is often necessary to link calculations with experimental observations. It can be calculated as:

$$G(T,p) = E_0 + E(T) - TS(T) + pV = E_0 + G_{\text{corr}}(T) \tag{3.16}$$

where E_0 is the total energy obtained from DFT calculations at 0 K in vacuum. $E(T)$ and $S(T)$ are the corrections to energy and entropy at finite temperature T. The pV term is negligible for solids, whereas for isolated molecules it is approximated using the ideal gas equation ($pV = k_{\text{B}}T$, where k_{B} is the Boltzmann constant). All the corrections can be expressed together as $G^{\text{corr}}(T)$ and can be calculated from translational, rotational and vibrational contributions. For periodic slab models of surfaces, only vibrational contributions are relevant, leading to thermal corrections in the form of $E(T) = E_{\text{vib}}(T)$ and $S(T) = S_{\text{vib}}(T)$. In contrast, for isolated molecules, vibrational, rotational and translational contributions must be considered. The total thermal corrections are then given by $E(T) = E_{\text{vib}}(T) + E_{\text{rot}}(T) + E_{\text{tr}}(T)$ and $S(T) = S_{\text{vib}}(T) + S_{\text{rot}}(T) + S_{\text{tr}}(T)$.

All vibrational frequencies in this thesis were calculated at the gamma q-point using density-functional perturbation theory, as implemented in `ph.x` code from Quantum ESPRESSO [86]. The equations for calculating Gibbs energies were taken from statistical mechanics [87] and were previously implemented in an in-house adaptation of the `dynmat.x` code from Quantum ESPRESSO [88], which was used for the calculations. For the vibrational contribution, the quantum mechanical harmonic oscillator approximation was employed and the corresponding expressions for the vibrational energy and entropy are given by:

$$E_{\text{vib}}(T) = \sum_i^N h\nu_i \left(\frac{1}{2} + \frac{1}{\exp(\frac{h\nu_i}{k_{\text{B}}T}) - 1} \right) \tag{3.17a}$$

$$S_{\text{vib}}(T) = k_{\text{B}} \sum_i^N \left(\frac{h\nu_i}{k_{\text{B}}T} \frac{1}{\exp(\frac{h\nu_i}{k_{\text{B}}T}) - 1} - \ln(1 - \exp(-\frac{h\nu_i}{k_{\text{B}}T})) \right) \tag{3.17b}$$

where h is the Planck constant, T is the temperature, ν_i are the vibrational frequencies, and N is the number of vibrational modes, which depends on the type of system under

investigation. Nonlinear molecules have $3n-6$ vibrational modes, linear molecules have $3n-5$, and periodic structures have $3n-3$, where n is the number of atoms in the considered supercell representing the structure of interest. When calculating vibrational contributions for transition states, only $N-1$ vibrational modes are considered, since the mode corresponding to the reaction coordinate is imaginary and therefore excluded from the analysis, as prescribed by the transition-state theory. In the equation for the energy contribution, the zero point energy ($E_{\mathrm{vib}}(0) = \mathrm{ZPE}$) is also included. To correct for the breakdown of the harmonic oscillator approximation at low frequencies, the Cramer–Truhlar correction was applied, where all vibrational modes below $1/2k_{\mathrm{B}}T$ (approximately 100 cm^{-1}) are raised to $1/2k_{\mathrm{B}}T$ [89].

Rotational degrees of freedom were treated with rigid rotor approximation. The contribution is calculated differently depending on whether the molecule is linear or nonlinear. Linear molecules have two rotational degrees of freedom and their contributions to energy and entropy are given by:

$$E_{\mathrm{rot}}^{\mathrm{lin}}(T) = k_{\mathrm{B}}T \tag{3.18a}$$

$$S_{\mathrm{rot}}^{\mathrm{lin}}(T) = k_{\mathrm{B}}\left(1 + \ln\frac{2Ik_{\mathrm{B}}T}{\hbar^2\sigma_{\mathrm{rot}}}\right) \tag{3.18b}$$

where $\hbar$ is the reduced Planck constant, I is the moment of inertia, and σ_{rot} is the rotational symmetry number. Nonlinear molecules have three rotational degrees of freedom and their thermodynamic contributions are:

$$E_{\mathrm{rot}}(T) = \frac{3}{2}k_{\mathrm{B}}T \tag{3.19a}$$

$$S_{\mathrm{rot}}(T) = k_{\mathrm{B}}\left(\frac{3}{2} + \ln\frac{\sqrt{8\pi(k_{\mathrm{B}}T)^3 I_{\mathrm{A}}I_{\mathrm{B}}I_{\mathrm{C}}}}{\hbar^3\sigma_{\mathrm{rot}}}\right) \tag{3.19b}$$

Finally, the translational contribution with three degrees of freedom is expressed as:

$$E_{\mathrm{tr}}(T) = \frac{3}{2}k_{\mathrm{B}}T \tag{3.20a}$$

$$S_{\mathrm{tr}}(T) = k_{\mathrm{B}}\left(\frac{5}{2} + \ln\left(\left(\frac{mk_{\mathrm{B}}T}{2\pi\hbar^2}\right)^{\frac{3}{2}}V\right)\right) \tag{3.20b}$$

where m is the mass of the molecule and V is the volume. Under the ideal gas approximation, the volume can be expressed as $V = k_{\mathrm{B}}T/p$.

3.3 Basic Computational Concepts in Electrocatalysis

Electrochemistry encompasses chemical reactions that involve the transfer of electrons — so-called redox reactions. These are oxidation (loss of electrons) and reduction (gain of electrons) reactions, which always occur simultaneously: one species is reduced and another is oxidized. One area of electrochemistry that has gained considerable attention is electrocatalysis, which deals with redox reactions occurring at an interface between an electrolyte and an electrode surface, which acts as a catalyst. In comparison to thermal heterogeneous catalysis, the computational modeling of electrocatalysis is more complex due to the additional influence of the electrolyte and the applied electrode potential.

To better understand the processes involved in electrocatalysis, we first briefly examine the definitions of different types of potentials. The most common potential defined for

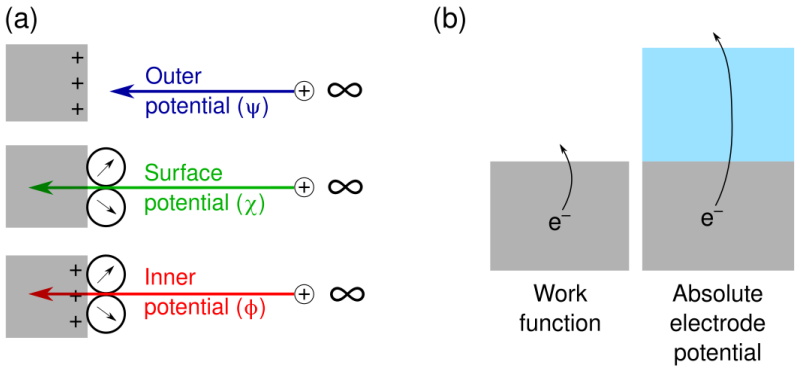


Figure 3.3: A schematic representation of different potentials relevant in electrochemistry: (a) electrostatic potentials, and (b) the similarity between the work function and the absolute electrode potential

charged species is the electrostatic potential, expressed in volts [V]. It is defined as the amount of work required to move a unit point charge from a reference location to a point of interest, normalized to a unit of charge. The reference point is often taken to be at infinity, where the potential is arbitrarily set to zero. In electrochemical systems, several specific electrostatic potentials are used to describe the environment near an electrode surface: the inner, outer, and surface potentials, which are schematically shown in Figure 3.3a. As summarized from the book by Bockris [90], the inner potential refers to the potential within the electrode, while the outer potential denotes the potential just outside the electrode surface, influenced by the system's charge. The surface potential is defined as the difference between the inner and outer potentials, arising from a dipole layer at the interface. Such a dipole layer appears even at the solid/vacuum interface, where electron spillover creates a dipole at the surface, giving rise to a nonzero surface potential.

A potential more commonly used in electrochemistry is the electrochemical potential, typically expressed in units of energy per mole [kJ/mol] or, in computational chemistry, as energy per particle [eV]. It represents the chemical potential of a charged species, explicitly including a contribution from the electrostatic potential:

$$\widetilde{\mu}_i = \left(\frac{\partial G}{\partial N_i}\right)_{p,T,N_j} = \mu_i + z_i e_0 \phi_i \tag{3.21}$$

This equation defines the electrochemical potential in the units of energy per species i. It can be divided into two contributions: the chemical potential (μ_i), which is a property of the uncharged species, and the $z_i e_0 \phi_i$ term, which accounts for the electrostatic contribution. Here, z_i is the charge of species i, e_0 is the elementary charge, and ϕ_i is the inner electrostatic potential felt by species i.

Related concepts are also the Fermi level and the work function. The Fermi level is a bulk property defined as the amount of work required to add one electron to the bulk of the system. The work function is the energy needed to move an electron from the bulk of the metal to a point just outside the surface. It depends on the surface structure — therefore, a metal has only one Fermi level but exhibits different work functions for various surface terminations.

Another important concept is the electrode potential. Trasatti [91] defined the absolute electrode potential as the potential difference associated with the process of removing an electron from the electrode in contact with an electrolyte and placing it at a point in vacuum just outside the electrolyte. This definition is conceptually similar to the work

function, which is the amount of work required to transfer an electron from the bulk of a metal to a point just outside its surface in vacuum, as schematically shown in Figure 3.3b. Since the absolute electrode potential is difficult to determine experimentally, the relative electrode potential is usually measured instead. It corresponds to the potential difference between the electrode of interest and a reference electrode. By convention, the reference electrode is the standard hydrogen electrode (SHE), whose electrode potential is arbitrarily set to 0 V.

3.3.1 Electrolyte

The first challenge in modeling electrocatalytic systems is the presence of the electrolyte, which gives rise to the electrode–electrolyte interface. Solvent molecules in the electrolyte can interact with both the surface and the adsorbed species, while ions contribute to the formation of the double layer at charged electrodes. The solvent can influence adsorption energetics through competitive adsorption or by strong interactions between adsorbates and solvent molecules, which may alter adsorption strengths. In general, three main approaches exist for modeling solvents within DFT: implicit, explicit, and microsolvation models [92]. These approaches are schematically illustrated in Figure 3.4.

Implicit solvent methods treat the solvent as a dielectric continuum and do not explicitly represent individual solvent molecules. These methods are computationally very efficient but cannot appropriately capture directional interactions (e.g., hydrogen bonding with solvent molecules) due to the absence of molecular-level details. Furthermore, implicit models have been shown to undersolvate metal surfaces and underestimate surface charge under applied potential [93]. This limits their applicability in modeling charge-transfer reactions. Various *ab initio* computational packages offer different implicit-solvent implementations. In our calculations, we employed the `Environ` plugin [94]–[96], which is compatible with the QUANTUM ESPRESSO suite. Within `Environ`, the solvent is represented as a dielectric continuum with its corresponding permittivity. The solvation Gibbs energy within this model is calculated as:

$$\Delta G_{\text{solv}} = E_{\text{solv}} - E_0 \tag{3.22}$$

where E_{solv} is the energy of the system obtained from calculations with solvent, and E_0 is the energy of the same system in vacuum. The `Environ` module includes various types of continuum solvation models, which differ in the definition of the solute cavity. For our calculations, we employed the self-consistent continuum solvation (SCCS) model developed

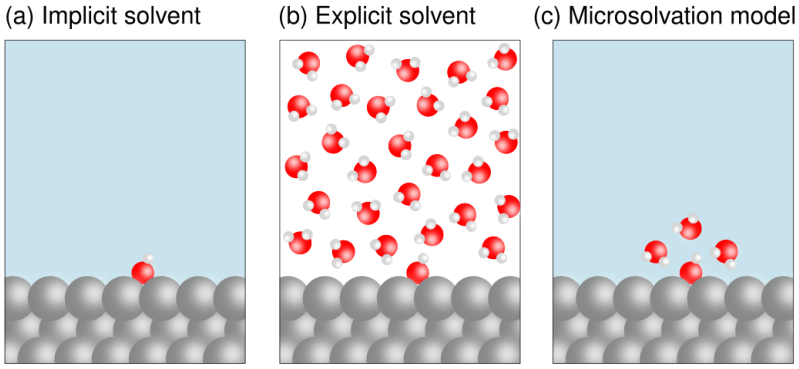


Figure 3.4: Three approaches for modeling solvents within DFT: the implicit, explicit, and microsolvation models.

by Andreussi et al. [95], in which the cavity is defined self-consistently based on the electron density of the solute species.

In comparison to implicit solvent methods, the explicit solvent and microsolvation models treat solvent molecules explicitly. In the explicit solvent model, the entire solvent environment is represented on a molecular level. In contrast, the microsolvation model combines an implicit continuum with a few explicit solvent molecules placed around a region of interest — typically the active site or the adsorption site. Both approaches offer a more realistic representation of the local environment, particularly when directional interactions are present. The main drawbacks of these models are high computational cost of the calculations and the limited sampling of solvent configurations when used with geometry optimization algorithms. As a result, the estimation of Gibbs energies may be biased toward the most stable configurations, potentially leading to an inaccurate representation of the system's thermodynamic properties. To overcome this limitation, such models are often employed in *ab initio* molecular dynamics, which allows for a broader sampling of the configurational space and enables modeling of the liquid character of solvents.

For electrocatalysis, the relevant interface is that between the electrode and a aqueous based electrolyte. The most commonly used model that includes explicit water molecules is the ice-like water bilayer structure, originally proposed by Ogasawara *et al.* for Pt(111) surfaces [97]. This model represents water in a "frozen" state, where only a single, highly stable configuration of water molecules is considered. The structure of the water bilayer includes two distinct groups of water molecules arranged in a hexagonal pattern above the surface. Half of the water molecules lie parallel to the surface, each donating two hydrogen bonds to the neighboring water molecules. The other half are oriented with one O–H bond perpendicular to the surface plane with the hydrogen atom pointing either toward or away from the surface. These molecules donate one hydrogen bond and act as acceptors of two, forming a structured hydrogen-bond network. The structure of the ice-like water bilayer is shown in Figure 3.5. Since this model includes explicit water molecules, it exhibits similar drawbacks to those already discussed for explicit solvation models. It has been demonstrated that different orientations of water molecules can significantly affect the calculated work function [98]–[100], even for structures with similar stability [100]. A difference of more than 2 eV has been observed in the work functions of H-up and H-down water-bilayer structures [99], [101]. Despite its limitations, the ice-like bilayer model remains highly valuable, especially in cases where water molecules play a direct role in the studied reactions.

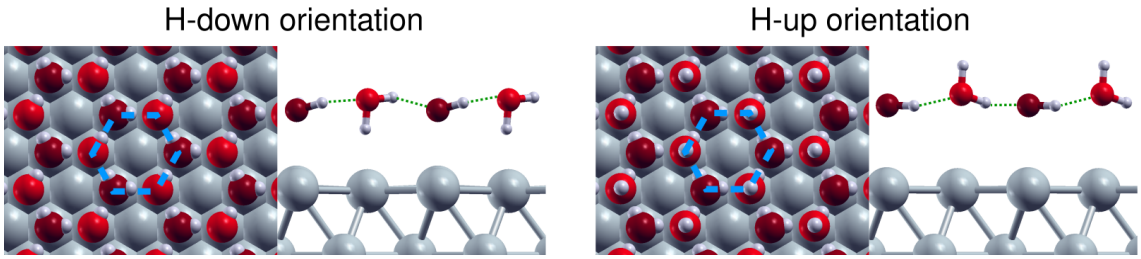


Figure 3.5: H-down (left) and H-up (right) models of the ice-like water bilayer. Oxygen atoms in water molecules are colored differently for clarity: water molecules with O–H bonds parallel to the surface are shown in dark red, while those with an O–H bond perpendicular to the surface are shown in light red.

3.3.2 Electrode potential

In electrocatalytic systems, the electrode potential serves as the driving force of a reaction, and changes in the potential directly influence the reaction rate. Experimentally, control of the electrode potential is crucial for many setups and can be achieved using a potentiostat. In DFT, however, incorporating the effect of electrode potential into the treatment of a system is challenging. In the conventional DFT approach, the number of electrons is kept constant, and the potential adjusts accordingly. The first widely adopted method that introduced the effect of electrode potential and enabled the treatment of electrocatalytic reactions within DFT is the computational hydrogen electrode (CHE) model, formulated by Nørskov et al. in 2004 [102]. In this method, all calculations are performed on uncharged systems using standard DFT, and the effect of the electrode potential is introduced as an *a posteriori* correction. The foundation of the CHE is the reaction for the standard hydrogen electrode (SHE; $H^+ + e^- \rightleftharpoons \frac{1}{2} H_2$). The electrode potential at which the reaction $H^+ + e^- \rightleftharpoons \frac{1}{2} H_2$ is at equilibrium under standard conditions ($p = 1$ atm, pH = 0, and $T = 298$ K) is called the standard electrode potential (or the potential of the SHE). This potential is used as the reference on the electrochemical scale and is therefore assigned a value of zero volts. Because the reaction Gibbs energy is zero at equilibrium, the following relation holds:

$$\widetilde{\mu}^{\ominus}_{H^+} + \widetilde{\mu}^{\ominus}_{e^-} = \frac{1}{2}\mu^{\ominus}_{H_2} \tag{3.23}$$

The equation expresses the Gibbs energies of the charged species H^+ and e^- in terms of the Gibbs energy of H_2. Since the treatment of charged species is problematic within periodic DFT, this approach immensely simplifies the analysis of electrochemical reactions. Moreover, the effects of pH and electrode potential can be added to the equation. The pH contribution arises from the activity of H^+ ions in the solution, while the effect of an applied electrode potential is introduced through an additional $-e_0U$ term associated with the electron, where U is the potential versus SHE. This results in the following expression:

$$\widetilde{\mu}_{H^+} + \widetilde{\mu}_{e^-} = \frac{1}{2}\mu^{\ominus}_{H_2} + kT\ln(a_{H^+}) - e_0U \tag{3.24}$$

The CHE method allows the calculation of reaction energies for electrochemical reactions and associates the Gibbs energy of an electron–proton pair with that of gas-phase hydrogen. To observe the dependence of activation energies on the electrode potential, different approaches must be used. The most straightforward one is to calculate activation barriers for the investigated reaction at different numbers of electron–proton pairs in the calculation [98], [101], [103]. The ice-like water bilayer can be utilized as a water model and surplus hydrogens are added to the water molecules to obtain $(H(H_2O)_n)^+$ complexes. The surplus electrons are located at the metal surface [101]. One notable problem with varying the number of proton–electron pairs is the finite size effect [101], [103], which can significantly impact the results, especially for small supercells. Adding one hydrogen atom to a cell with a few surface metal atoms results in an unrealistically large value of electrode potential. Another issue arises for the calculations of charge transfer reaction steps, where the potential difference between initial and final states can be substantial.

The methods described thus far employ classical DFT calculations with a constant number of particles. Recently, schemes enabling DFT calculations at constant potential have been developed, where the number of electrons is allowed to vary [104], [105]. In these methods, an appropriate counter-charge technique must be employed to allow a continuous change in the system's charge. With the development of constant potential DFT methods, a combination with the CHE model was proposed — the decoupled computational electrode

[49]. This method decouples proton–electron transfer steps and allows for a non-integer number of transferred electrons. It can be used for the calculation of both reaction and activation energies, providing a more accurate description of reaction mechanisms as a function of the electrode potential.

3.4 Analysis of Methane Dry Reforming

To analyze the effect of doping the CeO_2/Ni catalyst with MnO_x and to explain the differences between the doped and undoped catalysts observed by Sagar *et al.* [38], we performed a DFT study of simplified catalyst models. We considered models of Ni(111), Ni(110), Ni(100), NiO(100), $NiMn_x$(100), and CeO_2(111), which are shown in Figure 3.6. Ferromagnetic Ni was used as a model of fully metallic Ni, while antiferromagnetic NiO represented a fully oxidized Ni catalyst. These two models can be seen as limiting cases for different oxidation states of Ni in the catalysts. In addition, Ni(100) with chemisorbed O atoms up to 1 monolayer (ML) coverage was used as a simplified model of partially oxidized Ni particles. Doping CeO_2/Ni with Mn can also result in the formation of a Ni–Mn alloy, which was investigated using the $NiMn_x$(100) model, where 25% of surface Ni atoms were replaced with Mn atoms. For the calculations, plane-wave basis set and ultrasoft pseudopotentials [106], [107] were used to describe the Kohn–Sham orbitals. For Ni and NiO systems, cutoffs of 30 Ry and 300 Ry were used for the wave function and

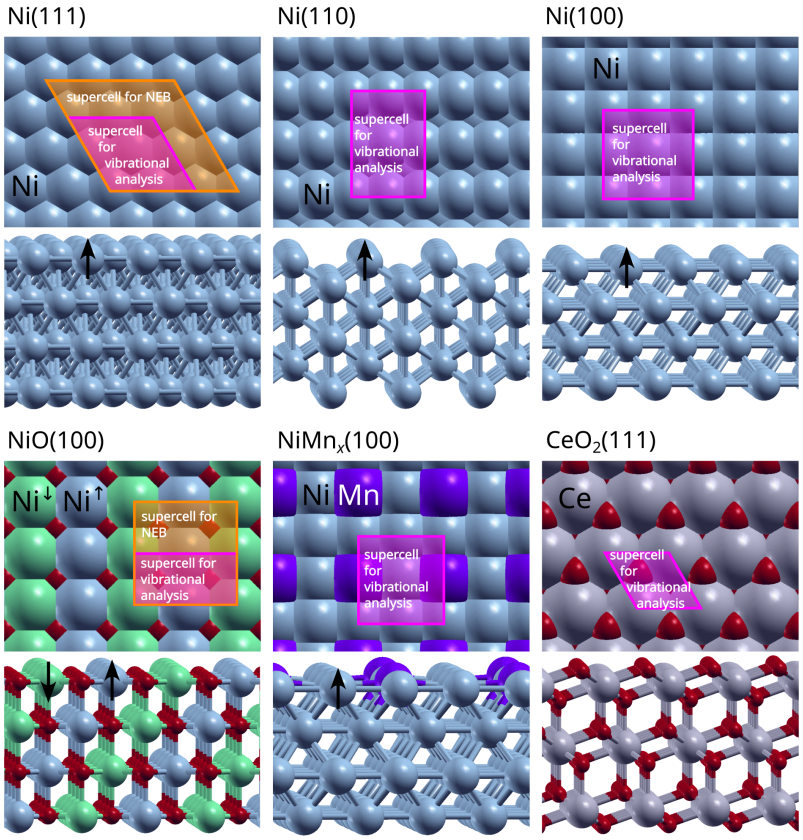


Figure 3.6: Relevant structures for the analysis of DRM on Ni-based catalysts. Arrows represent the spin of nickel atoms; metallic Ni is ferromagnetic and NiO is antiferromagnetic. Spin-up nickel atoms are colored blue and spin-down green. Supercells used for calculating vibrations and reaction paths are also denoted on the pictures.

electron density, respectively, whereas for $NiMn_x(100)$ and $CeO_2(111)$ higher cutoffs of 50 Ry for the wave function and 500 Ry for the electron density were employed. NiO and CeO_2 were described using the PBE+U scheme [108], [109], with U parameters of 4.6 eV for Ni ions and 4.7 eV for Ce ions, as computed self-consistently with the `hp.x` code [110].

The Ni(111), Ni(100), $NiMn_x(100)$, and NiO(100) slabs consisted of four atomic layers, while the Ni(110) slab was composed of six layers to achieve a comparable slab thickness across all Ni surfaces. A vacuum region of approximately 12 Å was introduced along the surface normal to separate periodic images. Adsorbates were placed on the top side of the slab, and the atoms in the bottommost layer were constrained to their bulk positions, except for Ni(110), where the two bottommost layers were fixed. All other atoms were fully relaxed. The in-plane lattice parameters were set according to the calculated equilibrium bulk lattice constants: 3.52 Å for Ni and 4.23 Å for NiO. For Brillouin-zone integrations, Methfessel–Paxton smearing [111] was employed, with a width of 30 mRy for Ni and 1 mRy for NiO. The $CeO_2(111)$ surface was modeled using a slab consisting of three O–Ce–O trilayers, with the bottom trilayer constrained to bulk positions. The in-plane lattice parameter was set to the calculated bulk value of 5.51 Å. Marzari–Vanderbilt smearing [112] with a width of 20 mRy was applied to facilitate convergence.

Vibrational frequencies were calculated for relevant adsorbed and isolated CH_xO fragments ($x = 0, 1, 2$). The vibrational properties of isolated molecules were computed in a cubic box of 15 Å side length using only the Γ q-point. For the adsorbed fragments, only the adsorbed molecule and the two uppermost layers of Ni(111), Ni(110), Ni(100), $NiMn_x(100)$, and $CeO_2(111)$ were perturbed, while for NiO(100), only the topmost layer was perturbed. For vibrational calculations, Ni(111)–(2×2), Ni(100)–(2×2), $NiMn_x(100)$–(2×2), Ni(110)–(2×2), NiO(100)–(1×2), and $CeO_2(111)$–(1×1) supercells were employed, with corresponding uniformly shifted k-point grids of $6\times6\times1$, $6\times6\times1$, $6\times6\times1$, $6\times4\times1$, $6\times3\times1$, and $3\times3\times1$, respectively. In addition, elementary reaction steps in the DRM mechanism were modeled on Ni(111) and NiO(100) using the CI-NEB method [80], [81]. For these calculations, larger supercells were utilized, specifically Ni(111)–(3×3) and NiO(100)–(2×2), with $4\times4\times1$ and $3\times3\times1$ uniformly shifted k-point grids, respectively.

3.4.1 Elementary steps of DRM

The mechanism of dry reforming of methane (DRM) consists of many elementary steps and can follow different pathways depending on the catalyst. We investigated the elementary steps shown in Figure 3.7. For methane dissociation, two possibilities were considered: direct decomposition to elemental carbon and a reaction pathway proceeding through CH_xO fragments. The carbon dioxide molecule initially physisorbs on the surface with a linear geometry and, in this form, exhibits low reactivity. To activate the molecule, covalent bonds must be formed with the surface, resulting in a bending of the molecular geometry. From this activated state, three different pathways to form CO were considered: direct dissociation, reaction through an HCOO intermediate, and reaction through a COOH intermediate. Additionally, the reactions leading to the formation of hydrogen and water molecule were considered, with the latter being an undesired side reaction in DRM.

3.5 Analysis of Hydrogen Evolution Reaction

HER was analyzed on models of ideal surfaces, supported nanoparticles, and isolated nanoparticles of platinum and ruthenium. Electron orbitals were described using a plane-wave basis set and projector augmented-wave (PAW) pseudopotentials [113] taken from the PSlibrary [114], [115]. Plane wave cutoff energies were set to 50 Ry for the wave functions

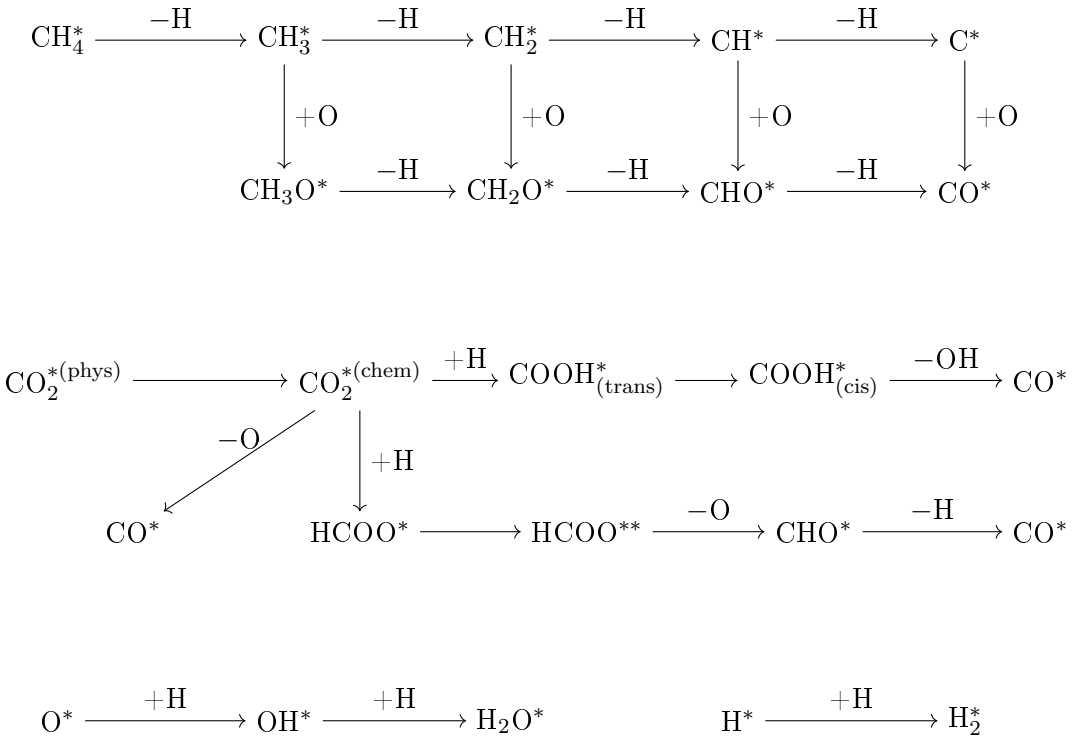


Figure 3.7: Investigated elementary steps of the DRM reaction. The first part depicts the considered steps for the decomposition of a methane molecule. The second part shows three different pathways for the conversion of CO_2 to CO. Finally, reactions leading to the formation of water and hydrogen are presented.

and 575 Ry for the electron density. Methfessel–Paxton smearing with a width of 0.02 Ry was employed to facilitate convergence [116]. For both metals, the bulk unit cells were first relaxed. Platinum crystallizes in a face-centered cubic (fcc) phase, with a calculated lattice constant of $a = 3.98$ Å. For ruthenium, both the thermodynamically stable hexagonal close-packed (hcp) phase (calculated $a = 2.72$ Å, $c = 4.29$ Å) and the metastable fcc phase (calculated $a = 3.81$ Å) were investigated. All relevant models of ideal surfaces are shown in Figure 3.8a. The thickness of the ideal surface models varied between 3 and 8 atomic layers for Ru, while for Pt, 4 layers were used. The bottom layer of atoms was fixed to bulk positions in all cases, and at least 15 Å of vacuum was added between the slabs, along with a dipole correction [117]. To model different coverages, various supercell sizes were employed, and Brillouin-zone integrations were performed on shifted k-point grids corresponding to the $12 \times 12 \times 1$ grid for the fcc(111)–(1×1) and hcp(001)–(1×1) surface cells. The D3 dispersion correction by Grimme [118] was applied in the kinetic analysis of HER on Pt to capture the interactions of water and hydrogen molecules with the surface. To compare the activity of the hcp and fcc Ru crystal phases, the Grimme-D3 correction including only two-body terms was used, enabling additional vibrational calculations with the `ph.x` module of Quantum ESPRESSO. Reaction pathways were determined using the NEB method [80], [81], and for the analysis of water dissociation on Ru, transition states were subsequently refined with the ARTn plugin [82], [83] to relax all atoms and obtain more accurate geometries prior to vibrational analysis.

Nanoparticles were treated either as isolated or as supported on TiON and carbon. Isolated nanoparticles were surrounded by 15 Å of vacuum, and the Makov–Payne correction to the total energy was applied [119]. For Brillouin-zone integration, only the Γ q-point

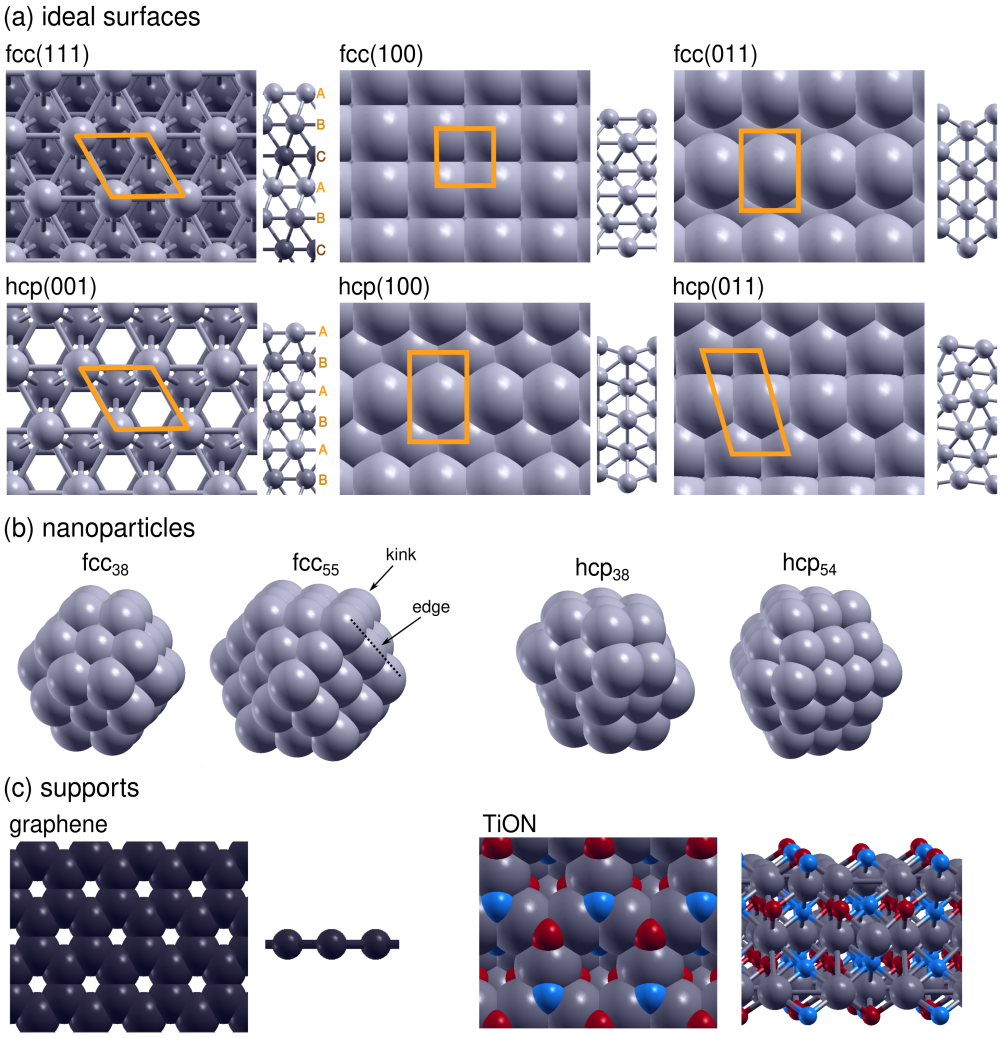


Figure 3.8: Relevant structures for the analysis of HER. (a) Top and side views of fcc and hcp ideal surfaces with the (1×1) cells indicated. (b) Models of nanoparticles, where the number in each name indicates the number of atoms in the nanoparticle. For the fcc_{55} particle, the locations of edge and kink sites are also labeled. (c) Top and side views of the structures used as supports for the nanoparticles.

was used. Different shapes and sizes of fcc and hcp nanoparticles were constructed. The two most utilized fcc nanoparticles in this thesis have the shape of truncated octahedra and consist of 38 and 55 atoms, with 32 and 42 surface atoms, respectively. They were analyzed both as standalone and as supported. We also investigated two hcp nanoparticles consisting of 38 and 54 atoms, having 30 and 42 surface atoms, respectively. The structures of these four nanoparticles are shown in Figure 3.8b. The general labeling convention for all nanoparticles used throughout this thesis is phase-M_n, where "phase" denotes either fcc or hcp, n is the number of atoms in the nanoparticle, and M is the metal. For platinum nanoparticles, the phase label is omitted because only the fcc phase was investigated.

Calculations of supported nanoparticles were performed on two different supports: TiON and graphene (used as a model for carbon support). The TiON structure was taken from previous calculations by Kokalj [58] and was modeled using a $Ti_{1.5}ON(111)$ slab consisting of three Ti layers, terminated on both sides by an O/N layer containing only 50% of O and N ions. Calculations involving the TiON support employed the

PBE+U method [108], [120], with the U parameter for Ti ions set to 4.0 eV, as self-consistently determined by Kokalj [58]. The carbon support was modeled using a single layer of graphene, which has a hexagonal unit cell with computationally optimized lattice parameters of $a = b = 2.467$ Å. Both support structures are shown in Figure 3.8c. TiON was modeled with a (3×3) supercell and graphene with a (7×7) supercell to accommodate the nanoparticles. Both supercells are hexagonal and have similar lateral dimensions: 17.27 Å for graphene and 17.70 Å for the TiON model. In all cases, the (111) facet of fcc nanoparticles was oriented toward the support, consistent with experimental observations [40]. To achieve a comparable structure, the (001) facet of hcp nanoparticles was similarly oriented toward the support. In calculations involving supported nanoparticles, D3 dispersion correction by Grimme [118] was employed to account for dispersion interactions, which are particularly relevant for the adhesion of metal nanoparticles on the graphene layer.

3.5.1 Elementary steps of HER

HER proceeds via a well-established mechanism involving three elementary steps: the Volmer, Tafel, and Heyrovsky steps. Under acidic conditions, these steps can be written as:

$$\text{Volmer} : \mathrm{H^+ + e^- + {}^* \longrightarrow H^*} \tag{3.25a}$$

$$\text{Tafel} : \mathrm{H^* \longrightarrow \frac{1}{2}H_2 + {}^*} \tag{3.25b}$$

$$\text{Heyrovsky} : \mathrm{H^* + H^+ + e^- \longrightarrow H_2 + {}^*} \tag{3.25c}$$

and the overall reaction is:

$$\mathrm{H^+ + e^- \rightleftharpoons \frac{1}{2}\,H_2} \tag{3.26}$$

The first step, known as the Volmer step, involves the electrochemical adsorption of a hydrogen atom from a hydrated proton. Following adsorption, the Tafel step, the Heyrovsky step, or both may occur. The Tafel step is a chemical process that does not involve electron transfer: two adsorbed hydrogen atoms combine to form a hydrogen molecule. In contrast, the Heyrovsky step is an electrochemical process, in which a hydrated proton and an electron from the catalyst combine with an adsorbed hydrogen atom to produce a hydrogen molecule. Depending on the relative rates of the Tafel and Heyrovsky steps, the HER may proceed via either the Volmer–Tafel or Volmer–Heyrovsky pathway, whichever is kinetically favored. If the activation barriers for both steps are comparable, both pathways are relevant.

In alkaline conditions, the steps are different because the source of hydrogen changes. Since there is no surplus of hydrated protons, a water molecule acts as the hydrogen source:

$$\text{Volmer} : \mathrm{H_2O + e^- + {}^* \longrightarrow H^* + OH^-} \tag{3.27a}$$

$$\text{Tafel} : \mathrm{H^* \longrightarrow \frac{1}{2}\,H_2 + {}^*} \tag{3.27b}$$

$$\text{Heyrovsky} : \mathrm{H^* + H_2O + e^- \longrightarrow H_2 + OH^- + {}^*} \tag{3.27c}$$

The overall reaction can be written as:

$$\mathrm{H_2O + e^- \rightleftharpoons \frac{1}{2}\,H_2 + OH^-} \tag{3.28}$$

By accounting for the self-ionization of water, $H_2O \rightleftharpoons H^+ + OH^-$, the thermodynamic treatment of the HER mechanism in acidic and alkaline conditions becomes analogous. The thermodynamical difference between the two mechanisms lies in the activity of the H^+ and OH^- species. In acidic conditions, the standard electrode potential of the HER (Eq. (3.26)) is defined as 0 V under standard conditions, where $a(H^+) = 1$. In alkaline conditions, the HER is described by Eq. (3.28) and its standard electrode potential is -0.826 V because, for this reaction, the standard state corresponds to $a(OH^-) = 1$. The more pronounced difference, however, arises from the reaction kinetics. Under acidic conditions, H_3O^+-like species readily donate protons, whereas in alkaline media the protons originate from water, which dissociates more slowly. Consequently, when investigating alkaline HER, we also considered the kinetic barriers associated with water dissociation.

3.5.2 Construction of surface Pourbaix diagrams

To determine the relevant adsorbed species and their coverage on different surfaces, we constructed surface Pourbaix diagrams. These diagrams indicate the thermodynamically stable surface structures as a function of pH and electrode potential. In our analysis, we considered only the species obtained from water dissociation (H*, OH*, O*):

$$H^+ + e^- + * \longrightarrow H^* \tag{3.29a}$$
$$H_2O + * \longrightarrow OH^* + H^+ + e^- \tag{3.29b}$$
$$H_2O + * \longrightarrow O^* + 2\,H^+ + 2\,e^- \tag{3.29c}$$

In the equations above, each reaction is written as an electrochemical adsorption step involving a single species. Combining these reactions allows for different coverage combinations, resulting in a general adsorption equation:

$$(b\ +\ c)\,H_2O + * \longrightarrow a\,H^* + b\,OH^* + c\,O^* + (b\ +\ 2\,c\ -\ a)\,(H^+ + e^-) \tag{3.30}$$

where a, b and c are the number of adsorbed H*, OH* and O* species, respectively.

The adsorption energy for various adsorbate coverages can be defined relative to water and hydrogen molecules as:

$$\Delta E = E_{H^*/OH^*/O^*} + \frac{1}{2}(b + 2c - a)E_{H_2} - (b + c)E_{H_2O} - E_* \tag{3.31}$$

where the energy of the adsorbed state (aH^* + bOH^* + cO^*) is written as $E_{H^*/OH^*/O^*}$ for brevity. Since electrochemical reactions occur at finite temperature and pressure in aqueous electrolytes, a more relevant quantity to analyze is the adsorption reaction Gibbs energy:

$$\Delta G = \mu_{H^*/OH^*/O^*} + (b + 2c - a)(\mu_{H^+} + \mu_{e^-}) - (b + c)\mu_{H_2O} - \mu_* \tag{3.32}$$

To include the effects of pH and electrode potential to the adsorption Gibbs energy, we use the expression for $\mu_{H^+} + \mu_{e^-}$ from the computational hydrogen electrode (CHE) approach, as given in Eq. (3.24). In this approximation, it is assumed that the electrode potential and pH do not affect the chemical potential of neutral species. The adsorption Gibbs energy can then be calculated as:

$$\Delta G = \Delta G^\ominus - (b + 2c - a)(kT\ln(10)\mathrm{pH} + eU) \tag{3.33}$$

where the standard adsorption Gibbs energy is given by:

$$\Delta G^{\ominus} = \mu_{\mathrm{H^*/OH^*/O^*}} + \frac{1}{2}(b + 2c - a)\mu^{\ominus}_{\mathrm{H_2}} - (b + c)\mu^{\ominus}_{\mathrm{H_2O}} - \mu_* \tag{3.34}$$

The chemical potentials of hydrogen gas and water are calculated under standard conditions, 25 °C and 1 atm pressure. At these conditions, water is in the liquid state and its chemical potential can be determined by calculating the chemical potential of water vapor in equilibrium with liquid water. The vapor pressure of water at 25 °C is 0.0313 atm, meaning that water vapor at this pressure has the same chemical potential as the corresponding liquid phase.

The Eq. (3.33) allows us to assess the Gibbs energy dependence of a given surface structure with respect to pH and electrode potential. The structure with the lowest adsorption Gibbs energy is thermodynamically the most stable under the given conditions. The boundaries between two arbitrary states can be determined by equating their adsorption Gibbs energies ($\Delta G_1 = \Delta G_2$), as defined by Eq. (3.33). One obtains the following equation for the boundary lines in the Pourbaix diagram:

$$eU = \left(\Delta G_1^{\ominus} - \Delta G_2^{\ominus}\right)\frac{1}{\Delta N} - kT\ln(10)\mathrm{pH} \tag{3.35a}$$

$$\Delta N = (b_1 + 2c_1 - a_1) - (b_2 + 2c_2 - a_2) \tag{3.35b}$$

From this equation, we observe that the slope of the lines in the Pourbaix diagram for structures covered with H*, OH*, and O* is independent of the actual coverage of the adsorbed species in the two corresponding structures. This is because the same number of H^+ and e^- species is transferred in all adsorption reactions, resulting in the cancellation of any coverage dependence. Consequently, the slope of all lines is the same and given by $-kT\ln(10)$. In contrast, the starting value is structure-dependent and differs for each line, depending on the specific pair of surface structures involved.

Calculations on ideal periodic surfaces were performed using various supercell sizes to achieve different coverages of adsorbed species. Due to the varying surface areas of the employed supercells, we compared the surface adsorption Gibbs energy (obtained from the total adsorption Gibbs energy with Eq. (3.6)). Similarly to the adsorption Gibbs energy, the boundaries between different surface structures in the Pourbaix diagram can be determined by equating their surface adsorption Gibbs energies ($\gamma_1 = \gamma_2$), resulting in:

$$eU = \left(\frac{\Delta G_1^{\ominus}}{A_1} - \frac{\Delta G_2^{\ominus}}{A_2}\right)\frac{1}{\Delta N} - kT\ln(10)\mathrm{pH} \tag{3.36a}$$

$$\Delta N = \frac{b_1 + 2c_1 - a_1}{A_1} - \frac{b_2 + 2c_2 - a_2}{A_2} \tag{3.36b}$$

Chapter 4

Dry Reforming of Methane on Nickel-Based Catalysts

The study of DRM reaction on CeO_2/Ni based catalysts is already published in Applied Surface Science [10] under Creative Commons license and the content of this section is adapted from the article.

This chapter focuses on explaining the differences between the undoped and Mn-doped CeO_2/Ni catalysts for dry reforming of methane. Sagar and Pintar [38] reported that Mn-doped CeO_2/Ni is more active and exhibits lower carbon poisoning compared to the undoped CeO_2/Ni catalyst. Additionally, an IR peak at 2020 cm^{-1} was observed on the undoped catalyst but not on the Mn-doped one. In order to explain these observations, we first investigated the formation of Ni–Mn alloys to assess the possibility of doping the metallic Ni component of the catalyst with Mn. Next, the analysis of vibrational frequencies was performed to identify which species corresponds to the experimentally observed 2020 cm^{-1} peak for the CeO_2/Ni catalyst. Finally, the reaction mechanism for dry reforming of methane on Ni(111) and NiO(100) was analyzed to determine the feasibility of DRM on both surfaces. Additionally, the coadsorption of different species present in the initial or final states of elementary reactions is discussed in more detail.

4.1 Alloying Ni with Mn

Here, we address the possibility that Mn from the Mn_xCeO_2 support could alloy with Ni particles. The calculated mixing energy[1] for the bulk $NiMn_x$ alloy, where 25% of Ni atoms are replaced with Mn atoms, is -0.77 eV/Mn-atom. This indicates that the $NiMn_x$ alloy is thermodynamically stable. Moreover, the configurational entropy would further favor alloy formation. As a first approximation, for a binary alloy, the configurational entropy can be estimated by the ideal entropy of mixing, $S_{\mathrm{mix}} = -k_{\mathrm{B}}[x \ln x + (1-x)\ln(1-x)]$, where x is the atomic fraction of one of the two metals. Even for more complicated cases, it can be argued that alloying generally increases the number of accessible microstates, such that

[1] The mixing energy was calculated as:

$$E_{\mathrm{mix}} = \frac{1}{m}(E_{\mathrm{NiMn}_x} - nE_{\mathrm{Ni}} - mE_{\mathrm{Mn}}),$$

where E_{NiMn_x} is the energy of the $NiMn_x$ bulk alloy supercell consisting of n Ni and m Mn atoms. E_{Ni} and E_{Mn} are the energies of Ni and Mn atoms in their respective bulk crystals. The calculated mixing energy is normalized per Mn atom. The fcc lattice of Ni was used as the starting structure of the $NiMn_x$ alloy, which was further relaxed with variable cell optimization. For bulk Mn, a plain bcc lattice was used for simplicity, although α-Mn has a unique bcc lattice with 58 atoms in the unit cell [121].

the configurational entropy provides an additional stabilizing contribution, particularly at elevated temperatures. Mn atoms show a slight tendency toward surface segregation; specifically, the $NiMn_x(100)$–(2×2) structure with a Mn atom in the surface layer, shown in Figure 3.6, is by 0.04 eV/supercell more stable than the analogous structure with the Mn atom in the bulk layer, as estimated using a seven-layer thick slab.

Although the thermodynamic stability of the $NiMn_x$ alloy does not prove that Ni particles supported on Mn_xCeO_2 are doped with Mn, it suggests that Mn could be present not only in the CeO_2 support but also in the metallic part of the catalyst. Therefore, Mn-doped surfaces will be included in the vibrational analysis but excluded from the reaction path calculations due to their increased complexity.

4.2 Vibrational Analysis

Sagar et al. [38] attributed the 2020 cm^{-1} peak observed on the CeO_2/Ni catalyst to the CH_xO species. To determine the origin of that peak, we performed vibrational analysis for CO, CHO, and CH_2O species adsorbed on Ni(111). Isolated species and CO adsorbed on other Ni surfaces were also considered for comparison. The calculated and experimental C–O stretching frequencies are reported in Table 4.1. As observed from the table, the DFT calculated frequencies are systematically lower than the experimental ones, with the highest difference between them being approximately 70 cm^{-1}. Even when this discrepancy is taken into account, the only calculated frequency sufficiently close to 2020 cm^{-1} is that of CO adsorbed on a top site of Ni surfaces; all three surface terminations give similar values of about 2000 cm^{-1}. This agrees well with the experimentally determined value of 2017 cm^{-1} for CO on CeO_2/Ni [126]. The calculated frequency of isolated CO is too high (2107 cm^{-1}) and that of adsorbed CHO (1292 cm^{-1}) and CH_2O (1091 cm^{-1}) on Ni(111) are significantly lower.

Campuzano et al. [123] showed that CO adsorbs preferentially at three-fold hollow sites on Ni(111) at low coverages. As the coverage increases, bridge sites are occupied, and at even higher coverages, CO binds to top sites. DFT calculations agree with this trend: CO adsorbs most strongly at the hcp site (−1.83 eV), followed by the fcc (−1.80 eV) and bridge (−1.71 eV) sites, and finally at the top site (−1.49 eV). The calculated stability difference between the thermodynamically favored hcp site and the inferior top site associated with the observed IR peak is substantial. However, this difference is likely overestimated because it is well-known that DFT favors CO adsorbed to hollow rather than top sites [127]–[129]. Furthermore, real catalysts consist of Ni nanoparticles that have a significant fraction of kink and edge sites, which increases the number of available top sites compared to the hollow ones.

Table 4.1: Calculated C–O stretching frequencies (in cm^{-1}) for CH_xO species ($x = 0, 1, 2$) either isolated or adsorbed on different surface terminations of Ni. Available experimental values are written in parentheses. $CO_{(top)}$ and $CO_{(hollow)}$ stand for CO adsorbed on a top and hollow (hcp for Ni(111)) site, respectively.

	$CO_{(top)}$	$CO_{(hollow)}$	CHO	CH_2O
isolated	2107 (2169)[a]	2107 (2169)[a]	1838	1740 (1746)[a]
Ni(111)	2005 (2045)[b]	1773 (1817)[b]	1292	1091
Ni(100)	1997 (2024)[c]	1641 (1710)[c]		
Ni(110)	1986 (1984)[d]			

[a] Ref. [122],[b] Ref. [123], [c] Ref. [124], [d] Ref. [125]

Table 4.2: Calculated properties of CO adsorbed on the relevant surface model. All calculations were performed using the (2×2) supercells. Labels used in the table have the following meaning: E_{ads} – adsorption energy, $E_{\text{ads}}^{\text{rigid}}$ – rigid adsorption energy, $d_{\text{M-C}}$ – distance between the carbon atom of CO and the metal atom(s) to which the CO binds, $d_{\text{C-O}}$ – intramolecular CO bond distance, ν_{CO} – CO stretching frequency.

Surface	adsorption site	E_{ads} (eV)	$E_{\text{ads}}^{\text{rigid}}$ (eV)	$d_{\text{M-C}}$ (Å)	$d_{\text{C-O}}$ (Å)	ν_{CO} (cm^{-1})
Ni(111)	hcp hollow	−1.83	−1.97	1.949	1.188	1773
Ni(100)	hollow	−1.85	−2.10	2.046	1.207	1641
Ni(100) + O($\frac{1}{4}$ ML)	hollow	−1.65	−1.91	2.031	1.205	1657
Ni(111)	top	−1.49	−1.54	1.742	1.159	2005
Ni(110)	top	−1.62	−1.67	1.754	1.159	1986
Ni(100)	top	−1.60	−1.67	1.749	1.159	1997
NiMn_x(100)	top_{Ni}	−1.59	−1.65	1.744	1.161	1984
NiMn_x(100)	top_{Mn}	−1.08	−1.12	1.889	1.158	1958
Ni(100) + O($\frac{1}{2}$ ML)	top	−0.20[a]	−1.12	1.799	1.151	2049
NiMn_x(100) + O($\frac{1}{2}$ ML)	top_{Mn}	−0.05	−0.18	2.181	1.142	2071
Ni(100) + O($\frac{3}{4}$ ML)	top	−1.19	−1.48	1.784	1.151	2057
NiO(100)	top_{Ni}	−0.47	−0.56	1.944	1.143	2086
CeO_2(111)	top_{Ce}	−0.18	−0.19	2.877	1.139	2100

[a]The reason for the abnormally small magnitude of E_{ads} is a pronounced outward relaxation of the Ni atom to which CO binds, which costs about 0.9 eV. Note that for this particular case, the difference between E_{ads} and $E_{\text{ads}}^{\text{rigid}}$ is considerably higher than for the other cases.

Our results suggest that the 2020 cm^{-1} peak arises from CO adsorbed on a top site of metallic Ni particles, with different Ni surface terminations displaying similar vibrational frequencies. Because CO is a product of the DRM reaction, it must be present on both CeO_2/Ni and Mn_xCeO_2/Ni catalysts. However, as both catalysts contain Ni particles, the absence of the 2020 cm^{-1} peak on one of them suggests a change in the chemical nature of Ni particles, which influences their interaction with CO. Sagar and Pintar [38] reported that the Mn_xCeO_2/Ni catalyst has a higher content of mobile oxygen in the support structure compared to the CeO_2/Ni catalyst. This could result in more oxidized Ni particles when supported on Mn_xCeO_2. Additionally, as discussed above, Mn ions present in the support could also alloy with Ni nanoparticles, changing their chemical characteristics. To investigate these possibilities, we calculated the stretching frequencies of CO adsorbed on both oxidized and Mn-doped Ni surfaces, which are given in Table 4.2. Some other relevant characteristics of CO binding are also presented: the adsoprtion energy calculated as the binding energy of CO molecule according to Eq. (3.3), rigid adsorption energy,[2] and some characteristic bond distances. O/Ni(100) and NiO(100) were used as simple models of partially and fully oxidized Ni surfaces, respectively, while NiMn_x(100) and O/NiMn_x(100) served as simple models of Mn-doped Ni surfaces. For comparison, the calculated CO stretching frequency on CeO_2(111) was also calculated.

First, we examine the C–O stretching frequencies on increasingly oxidized Ni(100) surfaces. At 0.25 ML coverage of O on the surface, CO preferentially adsorbs at a four-

[2]The rigid adsorption energy was calculated as:

$$E_{\text{ads}}^{\text{rigid}} = E_{\text{CO/slab}} - E_{\text{CO}}^{\text{rigid}} - E_{\text{slab}}^{\text{rigid}}$$

where $E_{\text{CO/slab}}$ is the energy of the relaxed CO/slab system, whereas $E_{\text{CO}}^{\text{rigid}}$ and $E_{\text{slab}}^{\text{rigid}}$ are the energies of CO and slab with the same geometry as in the CO/slab system, respectively.

fold hollow site, resulting in a characteristically low frequency. At higher O coverage, CO adsorbs on a top site, with more than 50 cm^{-1} higher frequencies compared to the calculated value for top position on bare Ni(100). On fully oxidized NiO(100), the CO stretching frequency is about 90 cm^{-1} higher than on metallic Ni, which can be attributed to weaker CO adsorption on the oxide surface. As previously observed, the frequencies calculated with DFT are systematically lower than the experimental values. Therefore, even at 0.5 ML O coverage, the calculated CO frequency (2049 cm^{-1}) is too high to match the experimentally observed 2020 cm^{-1} peak. These results indicate that partial oxidation of Ni particles on the Mn_xCeO_2 support would explain the absence of 2020 cm^{-1} peak in experimental spectra.

Next, we focus on CO adsorption on Mn-doped surfaces. On the $NiMn_x(100)$ surface alloy, CO binds to a Ni atom by about 0.5 eV stronger than to a Mn atom. The corresponding CO stretching frequencies are 1984 and 1958 cm^{-1} for CO adsorbed on top of Ni and Mn atoms, respectively. Since Sagar et al. [38] did not report any IR peaks in the 1960–2100 cm^{-1} range for the Mn_xCeO_2/Ni catalyst, we can argue that the presence of a $NiMn_x$ alloy alone cannot explain the observed differences in the IR spectra. In contrast, on a partially oxidized $NiMn_x(100)$ surface, modeled as $NiMn_x(100)$ covered with 1/2 ML of O, the calculated CO stretching frequency is 2071 cm^{-1}, which is similar to the frequency on NiO(100) surface. This suggests that any oxidized Ni surface, either doped or undoped, would explain the absence of the 2020 cm^{-1} peak. Furthermore, the $NiMn_x(100)$ surface shows stronger chemisorption of oxygen atom compared to Ni(100). Binding energies calculated according to Eq. (3.3) are −5.3 eV for pristine Ni and −5.6 eV for the NiMn alloy. These results indicate that Ni particles doped with Mn may have a higher affinity toward oxidation, supporting the hypothesis that the absence of the 2020 cm^{-1} peak in the Mn_xCeO_2/Ni catalyst is due to the higher oxidation of Ni particles relative to those on CeO_2.

In comparison, CO adsorbed on $CeO_2(111)$ exhibits a frequency of 2100 cm^{-1}, which is similar to other reported oxide surfaces. Therefore, we suggest that the 2100 cm^{-1} peak, observed by Sagar et al. [38], corresponds to CO adsorbed on oxide surfaces, which do not

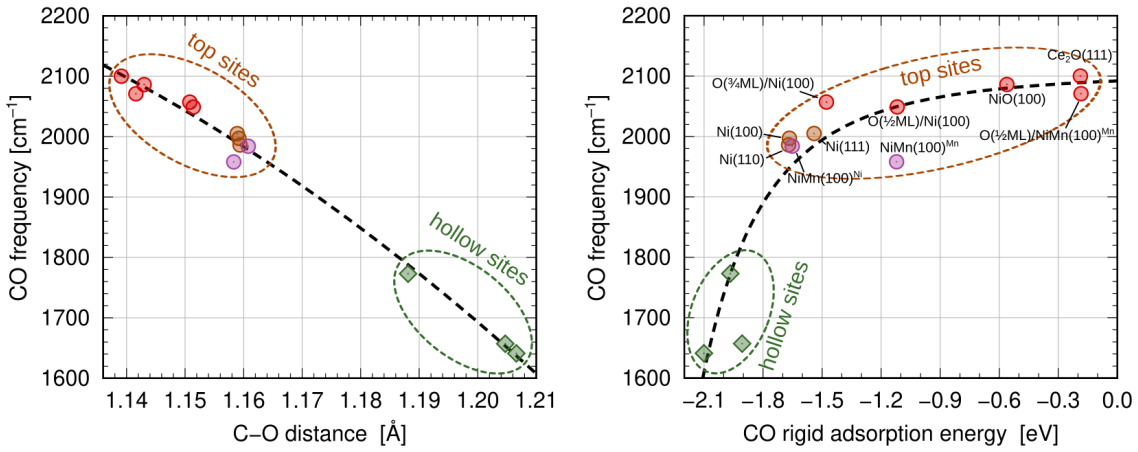


Figure 4.1: Correlation of the CO stretching frequency with the C–O bond length and the rigid adsorption energy. Data points corresponding to CO adsorbed at top sites are circled with brown and are color-coded based on the adsorbent structure: pristine Ni surfaces are shown in brown, $NiMn_x$ in purple, and all oxidized surfaces in red. The points corresponding to CO adsorption at hollow sites are green. Curves are drawn to guide the eye.

weaken the C–O bond as much as metallic Ni. The correlation between CO stretching frequencies and relevant characteristics of CO adsorption is shown in Figure 4.1. A general trend is observed: stronger adsorption energies and longer C–O bond lengths correspond to lower CO stretching frequencies. Hollow sites exhibit the lowest vibrational frequencies, the strongest CO rigid adsorption energies, and the greatest CO bond elongation. Among top-site configurations, pristine Ni and Mn-doped Ni surfaces show similar C–O bond lengths and rigid adsorption energies, with CO adsorbed on Mn atom being an outlier. Oxidized and partially oxidized surfaces display a broader range of rigid adsorption energies, but they all fall within a flatter region of the plot, where frequencies gradually approach that of an isolated CO molecule. This results in similar vibrational frequencies of all oxide surfaces. In contrast, the correlation between the C–O bond length and the stretching frequency is more linear and gives a clearer distinction between metallic and oxidized surfaces than the correlation based on rigid adsorption energy.

4.3 Reaction Mechanisms

To evaluate the hypothesis that emerged from the vibrational analysis, which ascribes the absence of the 2020 cm^{-1} peak to oxidized Ni particles, the DRM reaction mechanism was explored on Ni(111) and NiO(100) surfaces. The reaction steps considered in the analysis are illustrated in Figure 3.7. For methane dissociation, two reaction pathways were examined: direct dissociation via successive C–H bond cleavages and indirect reaction proceeding through CH_xO intermediates. For the CO_2 dissociation, three reaction pathways were explored: direct dissociation into CO and O, as well as two indirect paths through the formation of either carboxylic (COOH) or formate (HCOO) intermediates.

The structures of the initial and final states corresponding to relevant stable structures were used in the NEB calculations. It should be noted that the energies of adsorbed species depend on surface coverage and the presence of other coadsorbed species [130], an aspect that will be addressed in the following sections. For this reason, the presented reaction and activation energies are intended for comparison between the two catalysts and should be taken qualitatively only.

4.3.1 Ni(111) surface

All tested elementary reaction steps for CH_4 and CO_2 decomposition on Ni(111), along with their corresponding reaction and activation energies, are shown in Figure 4.2, and are presented in more detail in Figure A.1 in the Appendix. The reaction pathways that include the elementary steps with the lowest activation barriers are highlighted in green and their reaction energy profiles are shown in Figure 4.3.

The first abstraction of an H atom from methane exhibits a relatively high activation barrier of 0.99 eV, while the two subsequent steps leading to the formation of the CH* fragment have lower barriers. The final abstraction step (CH* $\rightarrow$ C* + H*), displays the highest H-abstraction activation energy of 1.31 eV. The activation energy for the oxidation of C* to CO* is very high (2.11 eV), which is consistent with the well-known observation that adsorbed carbon acts as a poison for the catalyst. Hence, the formation of CO preferentially follows the path through the CHO* fragment: CH* + O* $\rightarrow$ CHO* $\rightarrow$ CO* + H*. Although the activation barrier for the CH* + O* $\rightarrow$ CHO* step (1.15 eV) is lower than the one for CH* $\rightarrow$ C* + H* (1.31 eV), the small difference suggests that C* could still form as a byproduct of the reaction and eventually poison the surface. Another potential path to CO* involves the oxidation of CH_2*, which has a slightly lower activation energy (1.05 eV) than the CH* + O* reaction. However, since the barrier for the H abstraction

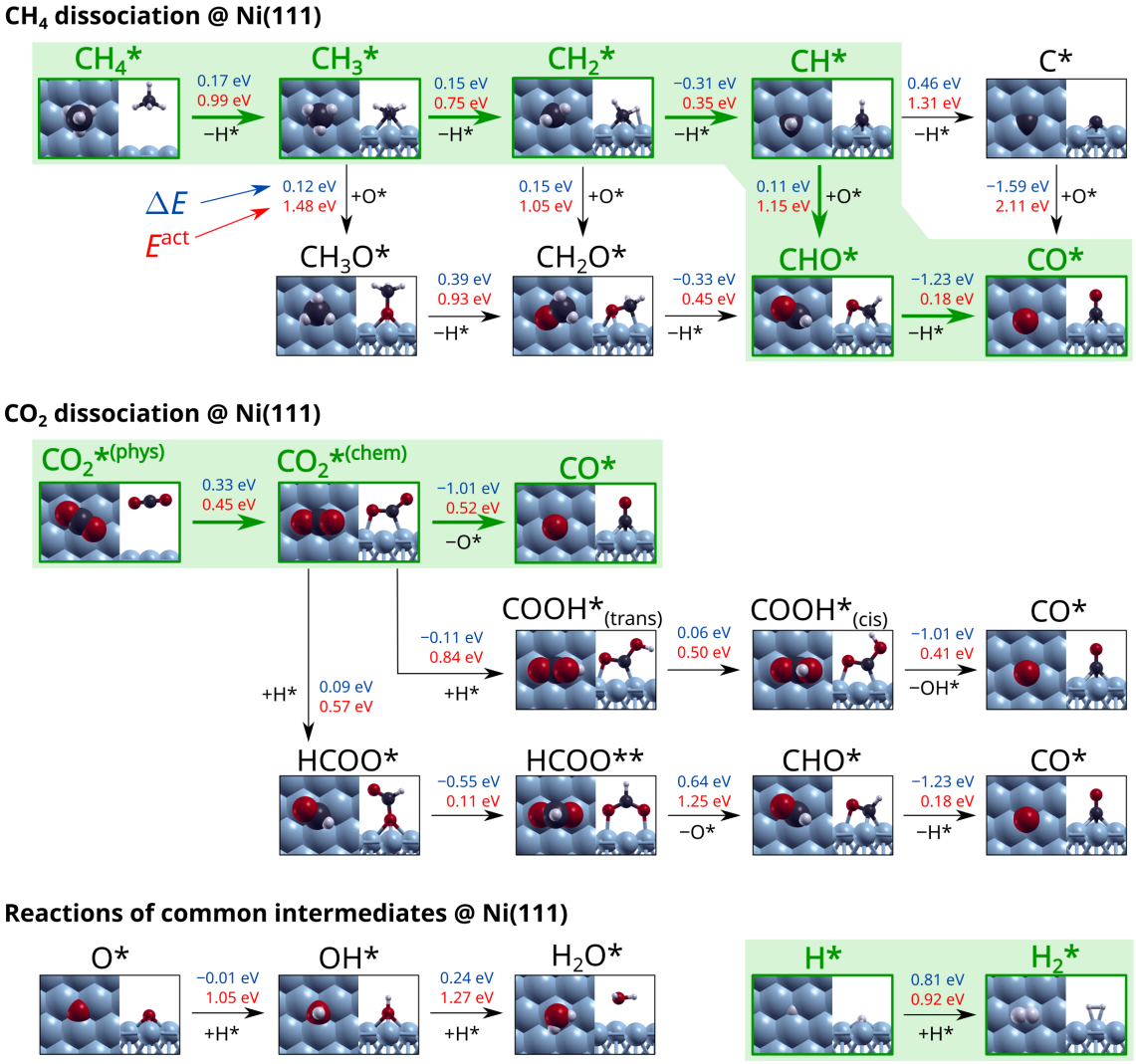


Figure 4.2: Snapshots and calculated reaction (ΔE, blue) and activation (E^{act}, red) energies for the considered elementary steps on Ni(111). The reaction paths involving the elementary steps with the lowest activation barriers are highlighted in green for each reaction.

of CH_2* to CH* is considerably lower (0.35 eV), the path through CH_2O* is less likely. These results suggest that CO* formation from methane primarily proceeds via sequential H abstraction to CH*, which then oxidizes to CHO* and finally converts to CO*.

The second group of reactions pertains to CO_2 decomposition. The CO_2 molecule can adsorb in two modes: a weakly bound physisorbed state ($E_{\mathrm{ads}} = -0.03$ eV) and an activated, V-shaped chemisorbed configuration with an endothermic adsorption energy ($E_{\mathrm{ads}} = +0.36$ eV). The V-shaped structure is metastable, as it corresponds to a shallow local minimum on the potential-energy surface, but is a necessary intermediate for the reaction to proceed. According to our calculations, once CO_2 is chemisorbed, direct dissociation into CO* and O* is the most favorable pathway. This route exhibits a lower activation energy (0.52 eV) than alternative paths involving the formation of HCOO* (0.57 eV) or COOH* (0.84 eV) intermediates. The oxygen atoms formed in the CO_2 dissociation are used in reactions with CH_2* and CH* fragments, facilitating the dissociation of methane molecule to CO*.

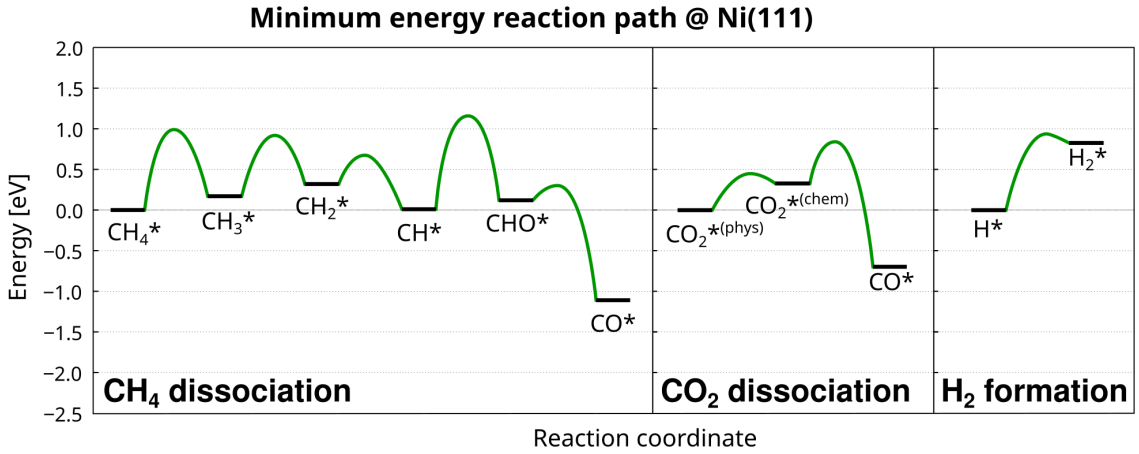


Figure 4.3: Reaction energy profiles for the pathways with the lowest activation energies on Ni(111). The displayed elementary steps correspond to those highlighted in green in Figure 4.2.

The activation barriers for reactions involving H* and O* intermediates were also calculated. The associative formation of hydrogen, $2H^* \rightarrow H_2^*$, has an activation barrier of 0.92 eV. For water formation, the calculated activation energies are 1.05 eV for the $O^* + H^* \rightarrow OH^*$ step and 1.27 eV for the subsequent $H^* + OH^* \rightarrow H_2O^*$ step. These results indicate faster formation of H_2 compared to H_2O on metallic Ni surfaces.

Because most of the considered reaction steps involve either H* or O*, we also calculated their diffusion barriers. They were estimated as the energy difference between the less stable bridge site and the most stable fcc site, consistent with the expected diffusion pathway of H* and O* on Ni(111): fcc→bridge→hcp→bridge→fcc. The results reveal that H* is considerably more mobile than O*, with calculated diffusion barriers of 0.1 and 0.5 eV, respectively. Both barriers are sufficiently low to allow efficient surface diffusion at reaction temperatures.

The DFT results presented above suggest that metallic Ni is a viable DRM catalyst because it can dissociate both CH_4 and CO_2 molecules into CO and H_2. Considering the most probable reaction pathways on Ni(111) — colored green in Figure 4.2 — the elementary reaction steps with the highest activation energies are the first H-abstraction from methane, the reaction of CH* with O*, and the formation of H_2. One problem associated with the Ni(111) surface is that the activation barrier for C* formation is not considerably higher than the barriers for the competing reactions leading to the DRM products. Moreover, the subsequent oxidation of C* to CO* exhibits a huge activation barrier. Therefore, C* may accumulate on the surface and eventually poison the catalyst, making it inactive.

4.3.2 NiO(100) surface

The considered reaction paths on NiO(100) are shown in Figure 4.4 and are presented in more detail in Figure A.2 in the Appendix. The corresponding energy profiles for reaction pathways with the lowest activation barriers are shown in Figure 4.5. The investigated reaction steps are analogous to those examined above on Ni(111). The first H abstraction from the methane molecule on NiO(100) exhibits a higher activation energy (1.37 eV) compared to Ni(111) (0.99 eV). The subsequent $CH_3^* \rightarrow CH_2^* + H^*$ step displays remarkably high activation energy of 2.27 eV, making the direct H abstraction path unfavorable. Therefore, the reaction proceeds through the CH_xO intermediates. All $CH_x^* + O^*$ re-

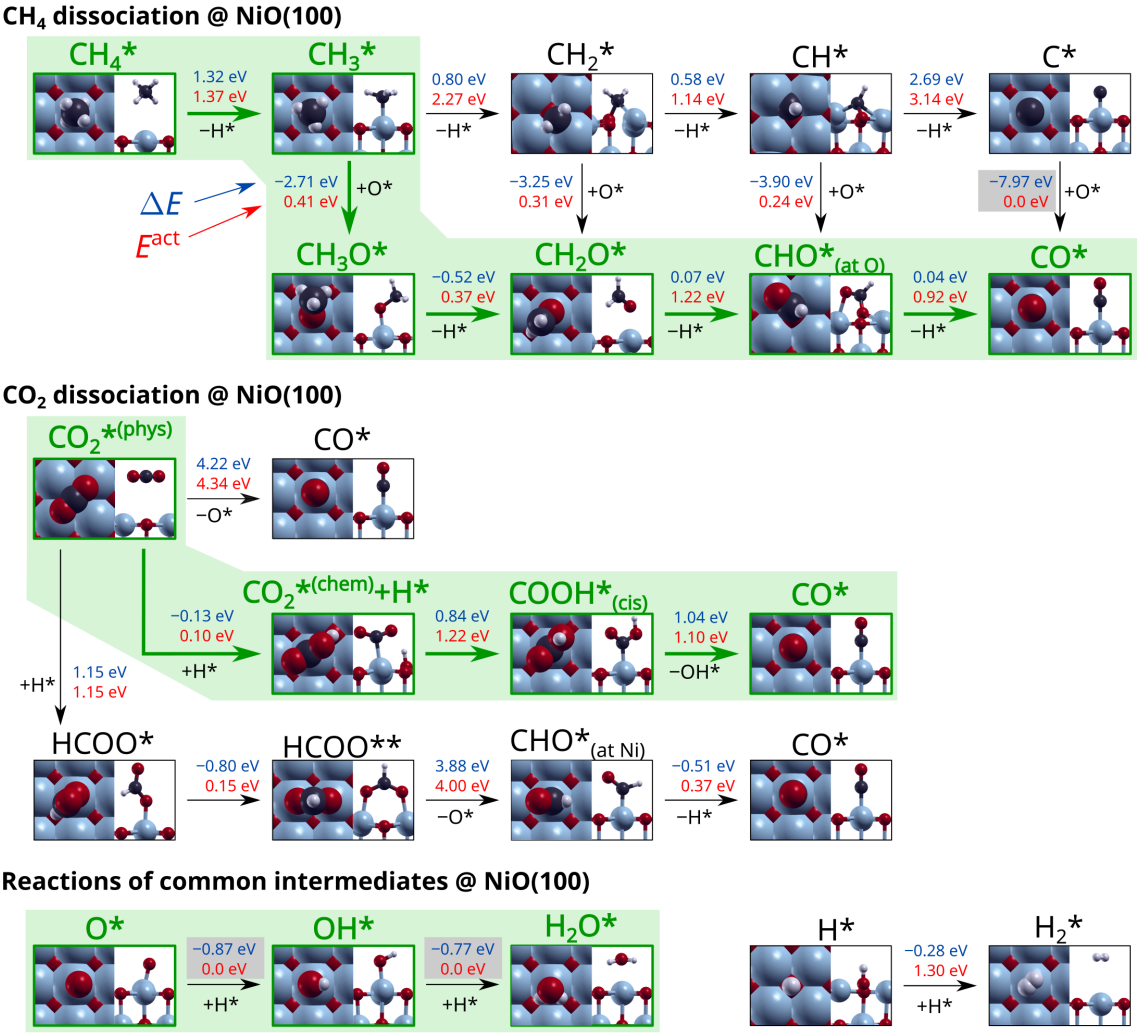


Figure 4.4: Similar to Figure 4.2, but for reactions on NiO(100). The reaction pathways involving the elementary steps with the lowest activation barriers are highlighted in green. Gray-shaded ΔE values were calculated with constrained relaxations of co-adsorbed reactants because full relaxation resulted in the product; those reactions are barrierless ($E^{\text{act}} = 0$ eV).

actions are highly exothermic and display rather small activation energies. The following H abstraction steps of CH_xO^* intermediates all exhibit lower activation barriers than the initial H abstraction from methane. The formation of carbon on NiO(100) is unfavorable due to the exceedingly high activation barrier of the CH* → C* + H* reaction (3.14 eV). Moreover, the oxidation of C* to CO* is highly exothermic and barrierless, making carbon accumulation and gradual surface poisoning highly unlikely on NiO(100).

As for reactions involving CO_2, direct dissociation of CO_2* to CO* + O* on NiO(100) can be excluded due to its extremely high activation energy and highly endothermic reaction energy ($\Delta E > 4$ eV). Instead, the reaction proceeds via a V-shaped chemisorbed CO_2* that is stabilized by the nearby H*. This intermediate first converts to a cis-carboxylic COOH* species ($E^{\text{act}} = 1.22$ eV) and then decomposes to CO* + OH* ($E^{\text{act}} = 1.10$ eV). The formed OH* fragment can then react barierlessly with a nearby H* to form an H_2O molecule. It should be noted that the formation of the formate (HCOO*) intermediate displays a slightly lower activation barrier (1.15 eV) than the formation of the carboxylic

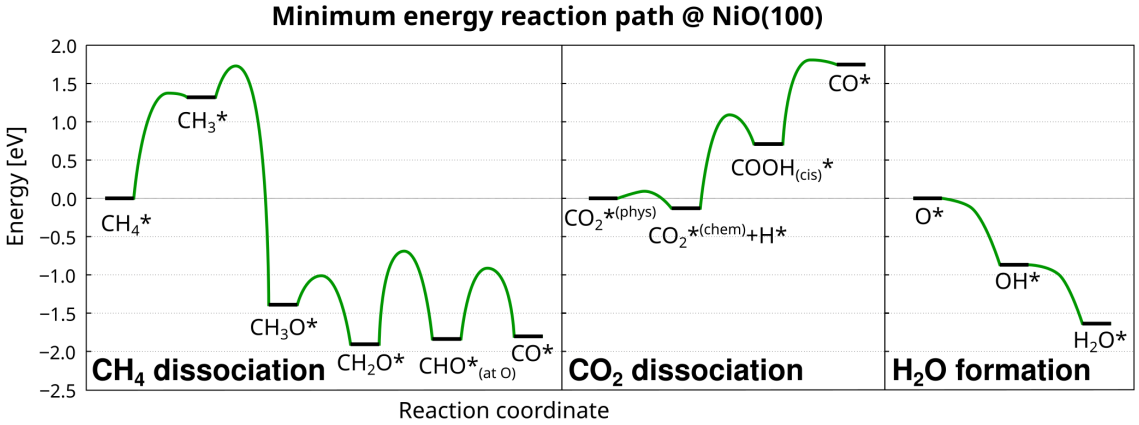


Figure 4.5: Reaction energy profiles for reaction pathways with the lowest energy barriers on NiO(100). The displayed elementary steps correspond to those highlighted in green in Figure 4.4.

COOH* species (1.22 eV). However, the formate pathway is a dead end, as the decomposition of HCOO* to CHO* exhibits an extremely high activation barrier ($E^{\mathrm{act}} = 4.0$ eV), preventing subsequent CO* formation.

It is a notable observation that O* species cannot form on NiO(100) because both CO_2* and CO* dissociations are extremely endothermic (Figure 4.4). Furthermore, even if O* would form on NiO(100), it would react barrierlessly with nearby H* atoms, exothermally forming water molecules. As mentioned above, CH_4 dissociation goes through CH_xO intermediates and requires excess oxygen atoms on the surface. Since their formation is unlikely, CH_4 dissociation on NiO(100) is questionable, unless O* forms on reduced Ni patches or originates from the ceria support.

The associative formation of hydrogen, $2H^* \rightarrow H_2^*$, is exothermic ($\Delta E = -0.28$ eV), but displays a relatively high activation energy of 1.30 eV, which is higher than on Ni(111) (0.92 eV). Additionally, diffusion barriers for H* and O* on NiO(100), calculated with CI-NEB are 0.9 eV and 0.5 eV, respectively. The barrier for hydrogen diffusion is considerably higher than on Ni(111), while that for O* is comparable. As a result, on NiO(100), O* is more mobile than H* and thus more likely to react with surface intermediates. This makes H_2 formation even less favorable compared to H_2O formation.

The presented results show that NiO alone is not an effective catalyst for the DRM reaction. Methane decomposition either requires an excess of surface O* species — which are unlikely to form on NiO — or proceeds through an O-free pathway that involves excessively high activation energies for some elementary steps. On the other hand, carbon formation is not expected on NiO, which is a plus. This observations suggests that partially oxidized Ni may be a better catalyst than both metallic Ni and fully oxidized NiO. By simple extrapolation, partially oxidized Ni should exhibit a lower affinity to carbon accumulation than metallic Ni, while maintaining higher DRM activity than NiO. The viability of the DRM reaction on partially oxidized Ni nanoparticles could be further enhanced when supported on oxides capable of supplying O* species, such as CeO_2 and Mn_xCeO_2.

4.4 Coadsorption Effects

As previously mentioned, the reaction and activation energies presented in Figures 4.2–4.5 are to be taken qualitatively because they were calculated with the selected structures without accounting for surface coverage and coadsorption effects. To gain some insight into

these factors, we performed a simple estimation of how H* and O* species influence the thermodynamic stability of relevant DRM reaction intermediates. The coadsorption effect (ΔE_{coads}) on the adsorption energy was estimated by considering the coadsorbed X* + Y* configuration in a given supercell compared to the standalone X* and Y* configurations in the same supercell, where X* are the relevant intermediates and Y* is either H* or O*:

$$\Delta E_{\text{coads}} = E_{(\text{X+Y})*} + E_* - (E_{\text{X}*} + E_{\text{Y}*}), \tag{4.1}$$

Here, $E_{(\text{X+Y})*}$ is the energy of the coadsorbed (X+Y)* configuration, E_* is the energy of the clean surface, and $E_{\text{X}*}$ and $E_{\text{Y}*}$ are the energies of the standalone adsorbed X* and Y* configurations, respectively. All energies are calculated with the same supercell. The energies obtained with this equation for Ni(111) and NiO(100) surfaces are presented in Table 4.3.

According to the Ni(111) results, H* has only a marginal influence on the adsorption energies of coadsorbed species, with ΔE_{coads} magnitudes below 0.1 eV. In contrast, the effect of O* is somewhat more pronounced, though still relatively small, with $\Delta E_{\text{coads}} \leq 0.25$ eV. All ΔE_{coads} values are positive, indicating that both H* and O* tend to slightly destabilize the coadsorbed species. Given the small energy differences, the previously discussed DRM mechanism on Ni(111) remains valid, and the reported reaction and activation energies are reliable.

In contrast to Ni(111), the coadsorption effects on NiO(100) are significantly more pronounced, with all considered coadsorbed structures stabilized relative to their singly adsorbed counterparts. Snapshots of the coadsorbed structures on NiO(100) are shown in Figure 4.6, with H* adsorbed on surface oxygen atoms and O* preferentially bound to Ni sites. H* stabilizes the coadsorbed species by approximately 0.5 to 1.1 eV. For the H* + O* and H* + OH* pairs, the stabilization is even stronger (1.7 and 1.9 eV, respectively); however, in these cases the coadsorbed structures at neighboring sites are not stable and spontaneously relax to OH* and H_2O*, respectively. In contrast, O* exhibits either a

Table 4.3: The coadsorption effect on Ni(111) and NiO(100) surfaces calculated with Eq. (4.1). All the considered structures were modeled with the Ni(111)–(3×3) or NiO(100)–(2 × 2) supercell and correspond to IS or FS from NEB calculations.

ΔE_{coads} (eV)				
	Ni(111)		NiO(100)	
X*	Y* = H*	Y* = O*	Y* = H*	Y* = O*
CH_3*	0.06	0.04	−0.72	−0.01
CH_2*	0.02	0.19	−0.81	−1.15
CH*	0.00	0.22	−0.99	−1.43
C*	0.01	0.18	−1.09	−0.44[a]
CH_2O*	0.09	/	−0.45	/
CHO*	0.00	0.06	−0.50	−0.04[b]
CO*	0.05	0.04	−0.66	−0.08
H*	0.00	0.10	−0.58	−1.66[a]
O*	0.10	/	−1.66[a]	/
OH*	0.09	/	−1.87[a]	/

[a] The coadsorbed structure is taken from the constrained calculation because the full relaxation of X* + Y* resulted in the XY* formation.

[b] The coadsorption effect was calculated with respect to a local minimum of standalone CHO* adsorbed on a Ni site.

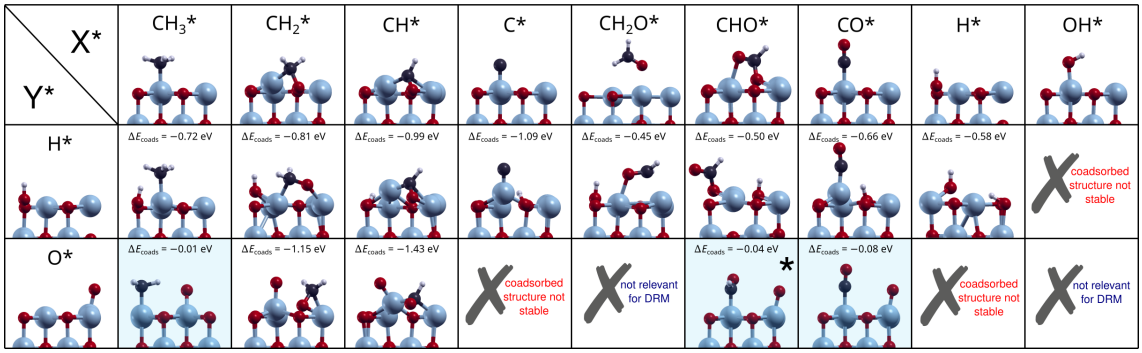


Figure 4.6: The top row shows the snapshots of standalone X* adsorbates on NiO(100), while the leftmost column shows the standalone H* and O* structures. The other snapshots display coadsorbed X* + Y* structures, with the associated ΔE_{coads} values written above them. The coadsorption structures with both X* and Y* adsorbed to Ni ions are highlighted with a blue background. A cross indicates that the coadsorbed state is either unstable or irrelevant for the DRM reaction.
* The coadsorption effect for the CHO* + O* structure was calculated relative to standalone CHO* bonded to a Ni site, in order to isolate the coadsorption effect from the substantial energy difference between CHO* adsorbtion on Ni versus O sites.

marginal effect ($|\Delta E_{\text{coads}}| < 0.1$ eV) or a substantial one ($|\Delta E_{\text{coads}}| \gtrsim 1.2$ eV), depending on the adsorption geometry. A marginal coadsorption effect is observed when both fragments are bonded to Ni atoms (structures highlighted in blue in Figure 4.6), which is possible only when O* is the coadsorbed species. In contrast, when at least one fragment binds to a surface O atom — as is the case for all H*-coadsorbed structures — the coadsorption effect is strong. These results suggest that, for the majority of coadsorbed structures on NiO(100), the calculated reaction and activation energies are highly susceptible to surface coverage and the distance between the reacting coadsorbates.

We further analysed the coadsorption effect on NiO(100) by examining two possible contributing factors: coverage and closeness. The coverage effect captures the influence of overall surface coverage on the coadsorption energy, while the closeness effect accounts for the changes in coadsorption energy arising from the spatial proximity of the two adsorbates. To evaluate these contributions, we performed ΔE_{coads} calculations with three NiO(100) supercells of increasing size: (2×2), (4×2), and (4×4) for three coadsorption pairs: H* + CH_3*, H* + CH_2*, and O* + CH_2*. For the larger supercells, each X* and Y* pair was modeled in two configurations: one with the coadsorbates placed close to each other, as in the NEB calculations (denoted as “close”) and one with the adsorbates positioned farther apart (denoted as "far"). The results of these calculations are shown in Table 4.4. For the H* + CH_3* and O* + CH_2* coadsorption pairs, the results reveal that the coadsorption effect persists with decreasing coverage. In the large (4×4) supercell, the effect remains significant, particularly if the coadsorbates are located close to each other. This suggest that the close proximity between the coadsorbates has a greater impact on ΔE_{coads} than the coverage, but there is also an additional long-range effect that persists even if the adsorbates are further apart. In contrast, for the H* + CH_2* pair, the coadsorption effect diminishes much faster with decreasing coverage in both close and far configurations, indicating that surface coverage plays an important role in this case. At higher coverage, also the closeness effect is important, because the close configuration display stronger coadsorption effect compared to the far configuration.

An analysis of the electron density difference was carried out for the same coadsorption

Table 4.4: The coadsorption effect on NiO(100) as a function of supercell size and the spatial proximity between the two coadsorbates. The $\Delta E_{\text{coads}}^{\text{close}}$ values correspond to configurations with coadsorbates close to each other, whereas the $\Delta E_{\text{coads}}^{\text{far}}$ values refer to configurations with coadsorbates far apart.

coadsorbates	supercell	$\Delta E_{\text{coads}}^{\text{close}}$ (eV)	$\Delta E_{\text{coads}}^{\text{far}}$ (eV)
CH_3* + H*	(2×2)	−0.72	/
	(4×2)	−0.76	−0.48
	(4×4)	−0.63	−0.34
CH_2* + H*	(2×2)	−0.81	/
	(4×2)	−0.54	−0.17
	(4×4)	−0.02	0.04
CH_2* + O*	(2×2)	−1.15	/
	(4×2)	−1.13	−0.81
	(4×4)	−1.09	−0.71

pairs as discussed above (H* + CH_3*, H* + CH_2*, and O* + CH_2*) in order to better understand the differences in coadsorption behavior. The electron density difference was calculated analogously to Eq. (3.11); however, since two adsorbates are present, one was treated as "preadsorbed" and was included as part of the surface system. Therefore, the equation for the electron density difference can be written as:

$$\Delta\rho(\mathbf{r}) = \rho_{(\text{A+B})*}(\mathbf{r}) - \rho_{\text{A}*}(\mathbf{r}) - \rho_B(\mathbf{r}) \tag{4.2}$$

Here, A* is treated as the "preadsorbed" species, and the effect of subsequently adsorbing B in its vicinity is analyzed. We calculated $\Delta\rho(\mathbf{r})$ for the coadsorption pairs listed in Table 4.4 using the (2×2) cells, as well as for the far-(4×4) CH_3* + H* structure for comparison. The results, shown in Figure 4.7, reveal that in some cases, the adsorption of one fragment influences the binding of the already "preadsorbed" species. For the CH_3* + H* pair, adsorption of H* modifies the electron density of Ni–CH_3 adsorption bond, while the reverse effect is not observed — meaning that binding of H* is not greatly affected by the presence of CH_3. We observe similar pattern for the CH_2* + O* pair, where the electron density of O* is perturbed by CH_2 adsorption and not vice versa. In both cases, the adsorbate that influences the other fragment is either partially or fully adsorbed on a surface O atom (H* or CH_2*), while the affected species (CH_3* or O*) is bonded to a Ni site. Even for the far-(4×4) CH_3* + H* configuration, we can still observe an influence of H* on the CH_3* bonding. This highlights the presence of a non-negligible long-range interaction, which is consistent with trends observed in the coadsorption energies. In contrast, for the CH_2* + H* pair, both species are at least partially adsorbed on surface O atoms, and their binding appears electronically independent. This pair also exhibits significant dependence of coadsorption energy on the coverage as seen in Table 4.4, suggesting that the observed coadsorption effect arises primarily from structural changes at higher coverage rather than electronic interactions.

These three coadsorption cases reveal that the ΔE_{coads} effect on NiO(100) can be broadly grouped into structural and electronic origin. The structural coadsorption effect arises from significant geometric distortions upon binding and is generally short-ranged.

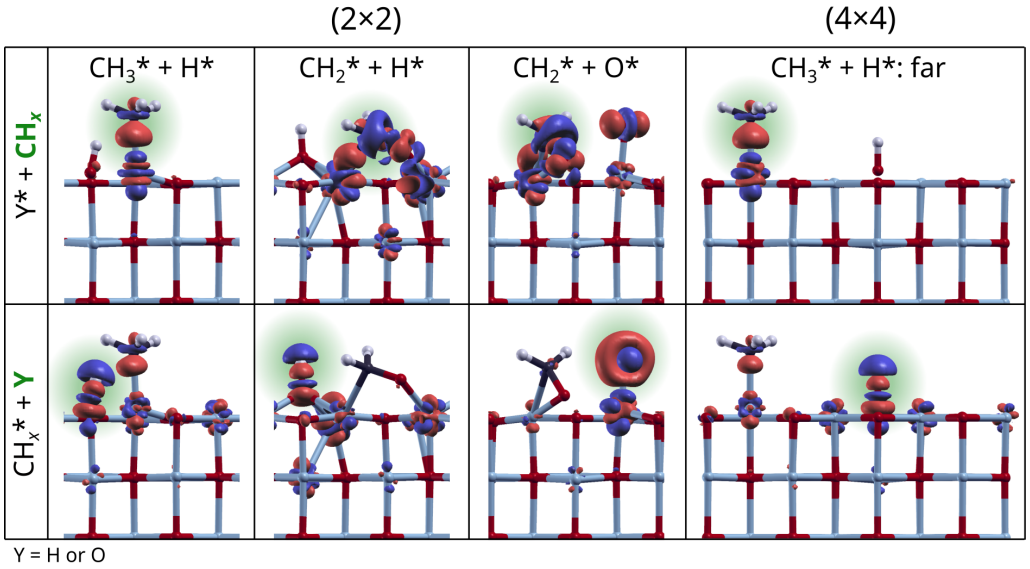


Figure 4.7: Electron density difference plots for selected coadsorption structures, calculated according to Eq. (4.2). The isosurfaces correspond to electron density ± 0.01 e/a_0^3. The adsorbate written in black represents the preadsorbed species (denoted A* in Eq. (4.2)), while the species written with with green and denoted with green background corresponds to the fragment of interest (denoted B in Eq. (4.2)).

As the surface coverage decreases or the distance between coadsorbates increases, the effect diminishes rapidly. In contrast, the electronic coadsorption effect is long-ranged and shows little sensitivity to coverage. In this case, the adsorption of one species perturbs the electron distribution and thereby affects the binding of other species. While this effect is more pronounced when the coadsorbates are in close proximity, it remains present even at larger distances.

When the coadsorption effect is based on electronic origin, the calculated E^{act} values of Figure 4.4 should be rather insensitive to coverage and thus reliable. On the other hand, when the coadsorption effect is of structural origin, the corresponding E^{act} values are more dependent on surface coverage and are therefore less reliable. In such cases, the coverage dependence of E^{act} can be estimated with the Brønsted–Evans–Polanyi (BEP) relation [84]. For dissociation reactions (XY* $\rightarrow$ X* + Y*), the two emerging species are adsorbed close to each other after the bond cleavage. Stabilizing the X* + Y* structure proportionally lowers E^{act}, particularly if TS is FS-like. In contrast, for association reactions (X* + Y* $\rightarrow$ XY*), the two involved species must come into close contact to react. In such cases, stabilization of the X* + Y* initial state affects E^{act} to a lesser extent, especially when the TS is IS-like. These considerations imply that, for dissociation reactions, the E^{act} values reported in Figure 4.4 should be considered as lower-bounds, since they were calculated with relatively small supercells. In contrast, for association reactions, the reported activation energies are more reliable.

Chapter 5

Hydrogen Evolution Reaction

This chapter is divided into three parts. The first part focuses on Pt catalysts, primarily through thermodynamic analysis, with some discussion of kinetics. The second part addresses Ru catalysts and compares the activity of the fcc and hcp crystal phases. Finally, the third part analyzes models of supported Pt and Ru nanoparticles, with particular emphasis on adhesion and H adsorption.

5.1 Platinum Catalysts

As a highly active catalyst for HER in acidic media, platinum (Pt) serves as an ideal benchmark metal for analyzing and comparing activity trends. It exhibits high resistance to corrosion and is in metallic state under typical HER experimental conditions. This section addresses both the thermodynamic properties of ideal Pt surfaces and nanoparticles as well as the kinetic behavior of ideal surfaces. First, the adsorption of water-dissociation products (H*, O*, and OH*) is examined, and the corresponding Pourbaix diagrams are presented to illustrate the stability regions. Second, the kinetics of the HER, especially the Tafel step, on ideal Pt(111) and Pt(100) surfaces is analyzed.

5.1.1 Adsorption of H, OH, and O

To compare models of ideal surfaces and nanoparticles and to identify the surface structures relevant under HER conditions, we calculated the adsorption energies of H, OH, and O on Pt(111) and Pt(100) ideal surfaces, as well as on the Pt_{55} nanoparticle, at varying coverages. All considered surface models are presented in Figure 3.8 in Section 3.5. The Pt_{55} nanoparticle was selected because of its cuboctahedral geometry, which exposes Pt(111) and Pt(100) facets. In addition, its moderate size makes the DFT analysis computationally feasible. The structural patterns of adsorption on the nanoparticle will be discussed in more details in the following section.

Testing of different adsorption configurations at various coverages was carried out, and the most stable identified structures were used for the subsequent analysis. On the ideal surfaces, different surface coverages were obtained by employing supercells of varying size. To enable a consistent comparison of adsorption stability, we calculated the surface adsorption energy (see Eq. (3.6)). It is determined as the adsorption energy, calculated according to Eq. (3.31), normalized by the supercell surface area. For the analysis of the nanoparticle, the same simulation cell was used for all the calculations. However, to ensure comparability with the results for ideal surfaces, we also calculated the surface adsorption energy by normalizing the total adsorption energy with the surface area of the

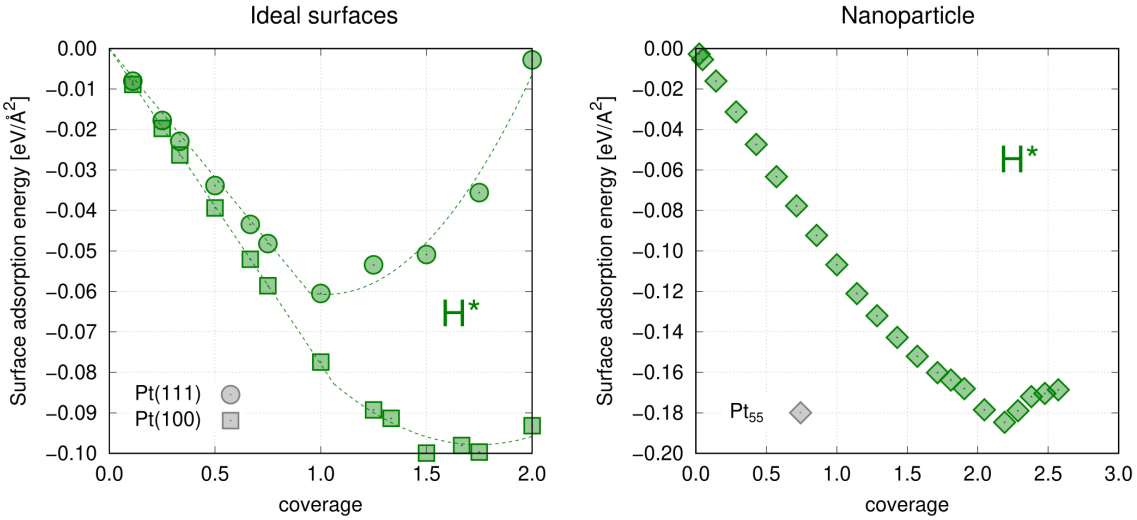


Figure 5.1: Surface adsorption energy of hydrogen as a function of coverage for (left) the Pt(111) and Pt(100) surfaces and (right) the Pt_{55} nanoparticle. Circles denote the Pt(111) surface, squares the Pt(100) surface, and diamond markers the nanoparticle. The dotted lines represent fits to the calculated points: a linear function was applied for coverages up to 1 ML, and a quadratic function for coverages above 1 ML. The intersection of these functions is taken as the breakpoint, ensuring a continuous function.

nanoparticle.[1] The coverage on the Pt_{55} nanoparticle was defined relative to the number of surface Pt atoms, which amounts to 42.

The results for the surface adsorption energies of H are shown in Figure 5.1 and the corresponding structures are given in Figures B.1–B.3 in the Appendix. For the ideal surfaces, coverages up to 2.0 ML (monolayer — corresponding to one adsorbate per one surface atom) were considered, while for the nanoparticle the maximum considered coverage was 2.57 ML. For all surface models, the calculated surface adsorption energies of hydrogen are negative, indicating that, at pH = 0 and zero overpotential vs. SHE, Pt favors H-covered surfaces over bare ones. Among the investigated ideal surfaces, Pt(111) binds H* more weakly than Pt(100). The most stable coverage on Pt(111) is 1.0 ML, with H* adsorbed at fcc sites. Beyond this coverage, H* begins to occupy top sites. Interestingly, at 1.5 and 1.75 ML, some H* migrate from fcc to top sites, so the lowest-energy structures are not those with a complete monolayer of fcc H atoms (see Figure B.1 in the Appendix). On Pt(100), H* adsorbs at bridge sites across all investigated coverages, with the most stable configuration found at approximately 1.5 ML.

It is noteworthy that, up to a coverage of 1.0 ML, both ideal surfaces exhibit a linear trend of surface adsorption energies with respect to coverage. Beyond this point, however, the data follow a quadratic dependence. An ideal linear dependence of surface adsorption energies with respect to coverage indicates that the adsorption energy per adsorbate remains constant. This can be seen roughly from Figure 5.2, which shows the average adsorption energies (adsorption energy divided by the number of adsorbates) for the ideal surfaces. That kind of dependence implies that attractive and repulsive adsorbate–adsorbate interactions are not present or effectively cancel each other. A surface exhibiting an ideal

[1] The nanoparticle surface area was obtained from the optimized structure of the bare Pt_{55} cluster in vacuum by calculating the areas of the (111) and (100) facets. The (100) facet has the shape of a square, while the (111) facet has the shape of a triangle, with their corners defined by the positions of the kink atoms.

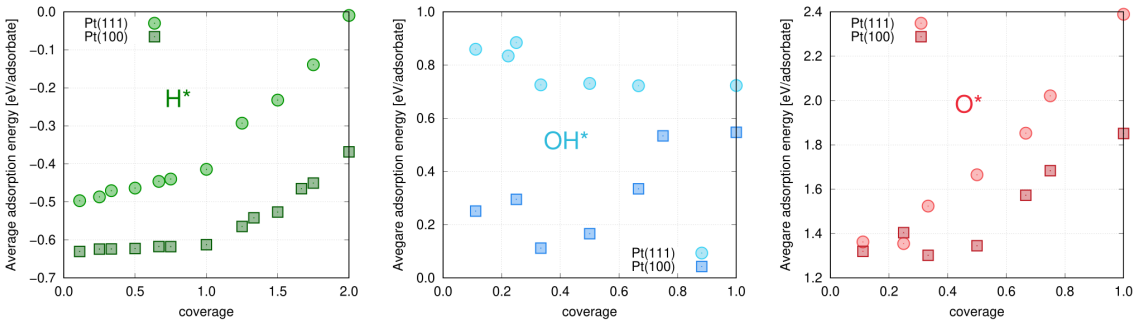


Figure 5.2: Average adsorption energies for H*,OH* and O* on Pt(111) and Pt(100). Data points corresponding to Pt(111) are shown as circles in a lighter color, whereas those for Pt(100) are represented by squares in a darker color.

linear dependence of surface adsorption energy between 0 and 1 ML will be stable either in the bare state or at full monolayer coverage, depending on the chemical potential of H. In contrast, a quadratic dependence of the surface adsorption energy, with the parabola opening upwards, implies that the the magnitude of the adsorption energy per particle decreases with coverage, as seen from Figure 5.2 for the H* coverages between 1.0 and 2.0 ML. This behavior reflects the presence of repulsive interactions between adsorbates, which gradually destabilize adsorption.

The results for the surface adsorption energy on the nanoparticle indicate stronger binding of H atoms and higher surface coverage compared to the ideal surfaces. The coverage at the energy minimum exceeds 2 ML, with the corresponding surface adsorption energy of approximately -0.19 eV/Å^2. The higher coverage and stronger binding can be attributed to the presence of kink and edge sites, which have lower coordination numbers and are thus capable of adsorbing a larger number of atoms compared to the more highly coordinated terrace sites. At lower coverages, the nanoparticle exhibits an almost linear dependence of the surface adsorption energy on coverage, whereas at higher coverages the trend becomes more piecewise, reflecting the sequential occupation of different adsorption sites.

For O and OH adsorption, the calculated surface adsorption energies are shown in Figure 5.3, with the corresponding structures provided in Figures B.1, B.2, B.4, and B.5 in the Appendix. Across all investigated surface models, OH* exhibits lower adsorption energies than O*. On the ideal surfaces, both adsorbates display positive adsorption energies over the entire coverage range, indicating that a Pt surface with O* or OH* is less stable than the bare surface. Similar as for the H adsorption, the Pt(100) surface binds both O* and OH* more strongly than the Pt(111) surface. The most stable binding site for O* is the fcc site on Pt(111) and the bridge site on Pt(100). For OH adsorption, the site preference is governed by hydrogen-bonding interactions. On Pt(111), OH* occupies bridge sites at low coverage, but at higher coverage the preferred site shifts to the top position, where hydrogen bonds can form more freely. On Pt(100), the bridge site remains the most favorable regardless of coverage, as hydrogen bonding is possible there. On Figure 5.2, one can notice a drop in the average adsorption energy at a coverage of around 0.33 ML, where H-bonds start to form between OH* groups.

For O adsorption on both ideal surfaces, a parabolic dependence of surface adsorption energy on coverage is observed, indicating that successive adsorption of O atoms becomes progressively less favorable due to repulsive interactions between adsorbates. In contrast, OH adsorption shows different trends on the two surfaces. On Pt(111), the adsorption energy increases almost linearly with coverage, suggesting that the surface will tend to be

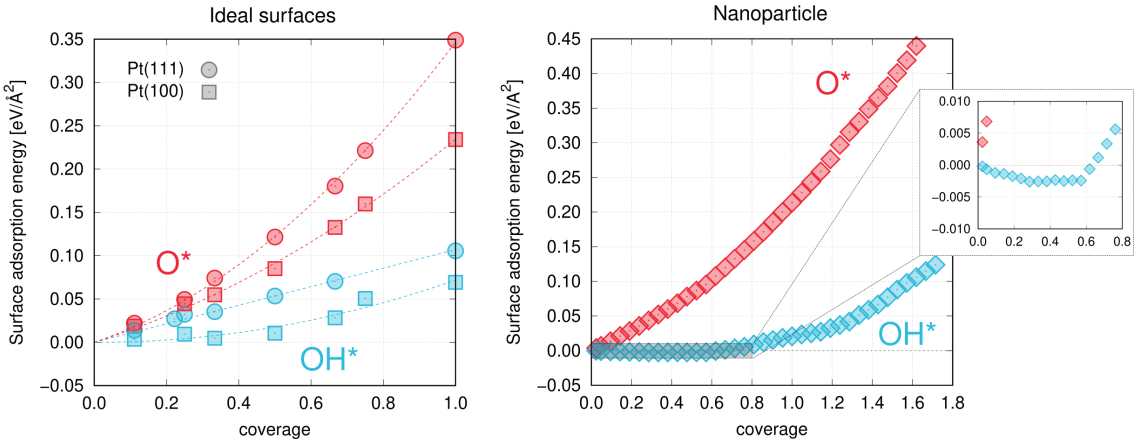


Figure 5.3: Similar to Figure 5.1, but for OH and O adsorption. Red points correspond to O*, and blue points to OH*. A close-up of the graph is shown for the highlighted area.

either bare or fully covered with 1 ML of OH* at sufficiently high electrode potentials and pH values. On Pt(100), however, the trend is more quadratic, indicating a gradual increase in OH* coverage with increasing electrode potential and pH.

On the nanoparticle surface, OH adsorption yields negative energies up to 0.6 ML coverage, indicating that its adsorption is energetically favored over the bare nanoparticle. This demonstrates that the nanoparticle is more reactive than the ideal surfaces, binding adsorbates more strongly and reaching higher coverages. The surface adsorption energy curve again shows piecewise linear and quadratic regimes, depending on the adsorption patterns at specific coverages.

5.1.1.1 Adsorption patterns on the investigated nanoparticle

The adsorption of H, O, and OH on the Pt_{55} nanoparticle was further analyzed in terms of the average adsorption energy and the sequence in which adsorption sites became occupied with increasing adsorbate coverage. The same adsorption structures as above were considered, where the number of adsorbed H atoms was increased in increments of six or eight atoms until a maximum coverage of 108 H*, corresponding to approximately 2.57 ML. For O* and OH*, structures were sampled by adding two adsorbates at a time, up to maximum coverages of 68 O* (1.62 ML) and 72 OH* (1.71 ML). The adsorption energy per adsorbate, i.e., the average adsorption energy, was calculated as the total adsorption energy (given by Eq. (3.31)) divided by the number of adsorbates (given in Eq. (3.5) for H* adsorption). The resulting graphs of average adsorption energy for all three adsorbates are presented in Figure 5.4, and the corresponding structural representations are summarized in Figure 5.5. The snashots of all relaxed structures are shown in the Figures B.3–B.5 in the Appendix. In all cases, the energy curves display similar qualitative behavior: at low coverage, the average adsorption energy increases only gradually, indicating weak repulsive interactions between adsorbates. At higher coverages, a more pronounced increase is observed, as adsorbates become crowded and stronger repulsive forces arise due to their proximity. It can also be observed that the average adsorption energy of H* remains negative throughout the entire investigated coverage range, whereas that of OH* is negative only at low coverage, and that of O* is positive across all coverages.

At the lowest coverage, an U-shaped trend is observed in the average adsorption energy curves for O* and OH*, but not for H*. This indicates that the binding of two adsorbates is more stable than that of a single one. A single OH* adsorbs on a low-coordinated kink

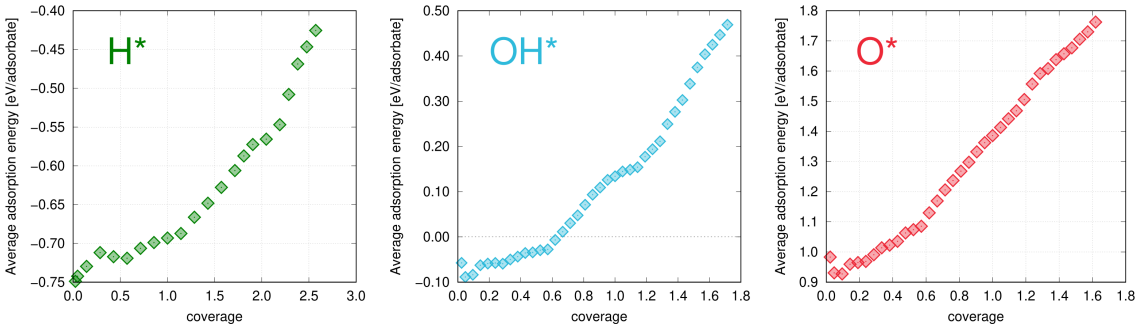


Figure 5.4: Graphs of average adsorption energy of H* (green), OH* (blue) and O* (red) on the Pt_{55} nanoparticle.

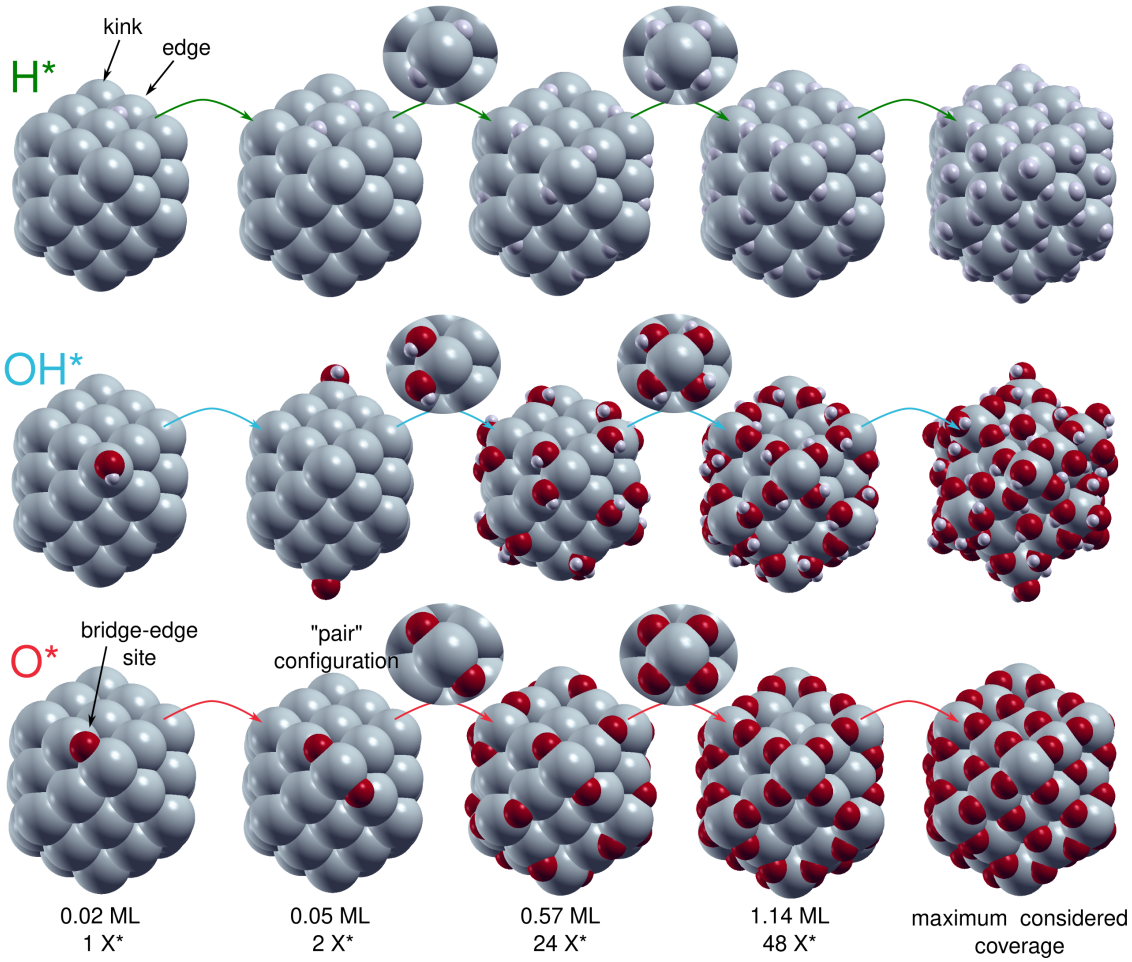


Figure 5.5: Adsorption structures of H, OH and O on Pt_{55} nanoparticle at different coverages. Bellow the structures, the coverage of adsorbates is written in units of monolayer and the number of adsorbates per particle.

Pt atom (see Figure 5.5) with an adsorption energy of −0.06 eV/atom. The second OH* prefers the opposite kink atom, giving an average adsorption energy of −0.09 eV/atom, while adsorption on other kink atoms is less stable (−0.05 eV/atom). After six OH* adsorbates, the most favorable sites shift from kink atoms to edge sites adjacent to them.

The first O* atom adsorbs on a bridge site between a kink and an edge atom (called

Table 5.1: Bader charges for the bare particle, single adsorption, and the "pair" adsorption configuration on the Pt_{55} nanoparticle.

Pt_{55} structure	adsorbate	Pt(kink)
bare	/	−0.11
1H*	−0.11	−0.02
2H* – "pair"	−0.14	+0.07
1O*	−0.77	+0.29
2O* – "pair"	−0.80	+0.70

bridge-edge site) with an adsorption energy of 0.98 eV. The second O* prefers the bridge site on the opposite side of the kink atom, resulting in an almost linear O–Pt(kink)–O configuration (called "pair" adsorption) with an average adsorption energy of 0.93 eV/atom. In contrast, adsorption of an O atom on an equivalent but distant site yields a higher average adsorption energy of 1.00 eV/atom. This shows that stabilization arises primarily from the paired adsorption configuration.

A similar trend is observed for H adsorption: one H atom at a bridge-edge position has an adsorption energy of −0.64 eV/atom, while a "pair" gives an average adsorption energy of −0.71 eV/atom. However, for hydrogen, the bridge site at the center of the (100) facet is energetically more stable, and only for more than 12 H* does the pair configuration become more favorable than the more stable adsorption site. This explains why the U-shaped pattern is not observed for H adsorption.

To gain further insight into the stabilization of the "pair" adsorption structure, Bader charge analysis was performed and the results are summarized in Table 5.1. The data show that both H* and O* are negatively charged, with the H charge of about −0.1 and the O charge of approximately −0.8. In contrast, the kink Pt atom to which the adsorbate binds becomes increasingly positively charged. Upon adsorption of each H atom, the charge of the kink Pt atom increases by approximately +0.1, whereas adsorption of each O atom increases the charge of Pt by about +0.4. This demonstrates that the more electronegative O atom has a stronger effect on the charge distribution of the surface Pt atoms compared to H. If we consider only the purely electrostatic contribution of the "pair" configuration with Coulomb interaction,[2] we obtain stabilization energies of −0.06 and −1.3 eV per adsorbed atom for H* and O*, respectively. For H*, the estimated stabilization is close to the difference observed from the calculated average adsorption energies, whereas for oxygen it is considerably lower. In the case of O adsorption, significant Pauli repulsion is present and counterbalances the strong electrostatic attraction. For H adsorption, the repulsive contribution is less pronounced, and therefore the estimated stabilization energy provides a more realistic assessment. For OH adsorption, no clear origin of stabilization could be identified. Both the charge density difference and the Bader charge analysis yield similar results for single and paired OH adsorption.

[2]The electrostatic interaction energy was calculated using the Coulomb expression, which in atomic units is given by:

$$E_{i,j} = \frac{q_i q_j}{r_{ij}} \tag{5.1}$$

where q_i and q_j are the charges and r_{ij} is the distance between i and j charges. The electrostatic contribution to the stabilization of the "pair" configuration was obtained as:

$$\Delta E^{\text{"pair"}} = \left(2E_{\text{X,Pt}} + E_{\text{X,X}}\right)^{\text{"pair"}} - \left(2E_{\text{X,Pt}}\right)^{1\text{X}^*} \tag{5.2}$$

where X is either H or O. The first part is calculated from the "pair" configuration and the second part from a single-adsorbate calculation.

With increasing coverage, the first noticeable change in the slope of the average adsorption energy appears at 24 adsorbates, corresponding to approximately 0.6 ML. At this coverage, all adsorbates occupy bridge-edge positions, with one adsorbate per edge and two adsorbates bound to each kink atom. O* and H* atoms adopt the "pair" configuration, whereas OH* groups adsorb in pairs with a hydrogen-bond-like arrangement (see Figure 5.5). Our results agree with the observations that the bridge-edge sites strongly bind O atoms [54]–[56]. Because of this strong binding, they are considered inactive toward the oxygen reduction reaction [55].

Upon increasing the coverage beyond 24 adsorbates, two species adsorb on the same edge, introducing repulsive interactions, particularly for the OH and O adsorbates, as seen from the increase in the average adsorption energy. O and H atoms tend to adsorb in configuration of 4 adsorbates around one kink atom (or two "pair" configurations) which is more stable than having three atoms around one kink. For O adsorption, it was also observed that at certain coverages, two O atoms prefer bridge positions on the (100) facet rather than at bridge-edge sites. OH groups adsorb progressively, eventually leading to three OH groups around a single kink atom, and subsequently four.

The next distinct change in the average adsorption energy occurs at 48 adsorbates, corresponding to a coverage of roughly 1.2 ML, where all bridge-edge positions are occupied and each kink atom is surrounded by four adsorbates. Beyond this coverage, O atoms increasingly occupy bridge sites on the (100) facets, while OH groups bind to the central top positions of these facets. Additional OH and O species are subsequently adsorbed on the (111) facets and at kink sites. With OH* adsorption at a (111) hollow site, a spontaneous formation of water molecule was observed in some cases, indicating that the super high coverages are not realistically achievable.

For H adsorption, a wider coverage range was investigated, as the small size of the H atom allows for higher coverages compared to O and OH. Between 1.2 ML and 1.9 ML, no pronounced change is observed in the trend of the average adsorption energy. Within this range, H* occupies half of the bridge sites at the center of the (100) facets, the kink sites, and the hollow sites on the (111) facets. Beyond this point, the remaining bridge sites on the (100) facets become progressively occupied, followed by a sharp increase in the average adsorption energy. This increase arises when all bridge sites on the (100) facets are occupied and additional H atoms adsorb on the bridge positions of the (111) facets, accompanied by the displacement of H atoms from hollow to bridge sites to accommodate the new adsorbates.

5.1.1.2 Structural changes of the investigated nanoparticle upon adsorption

Upon increasing the number of adsorbed atoms, the structure of the nanoparticle is also affected. To visualize this effect, we calculated the radial distribution function of Pt atoms around the central Pt atom for the bare nanoparticle and the nanoparticles at the maximum considered coverage of each adsorbate.[3] The results are shown in Figure 5.6, which reveals that adsorption of OH* induces the strongest deformation of the nanoparticle, as

[3]The radial distribution function was calculated as the ratio of the local number density of Pt atoms in the nanoparticle (ρ_{local}) to the average number density in bulk Pt (ρ_{Pt}) according to:

$$g(r) = \frac{\rho_{\text{local}}}{\rho_{\text{Pt}}} = \frac{1}{\rho_{\text{Pt}}} \frac{N}{\frac{4}{3}\pi(r_{\text{max}}^3 - r_{\text{min}}^3)} \tag{5.3}$$

where N is the number of atoms within the distance interval $[r_{\text{min}}, r_{\text{max}}]$ from the origin, and the denominator corresponds to the volume of the spherical shell defined by r_{min} and r_{max}. The bulk number density was obtained from the calculated bulk lattice parameter and the radial distribution function was evaluated in increments of 0.1 Å.

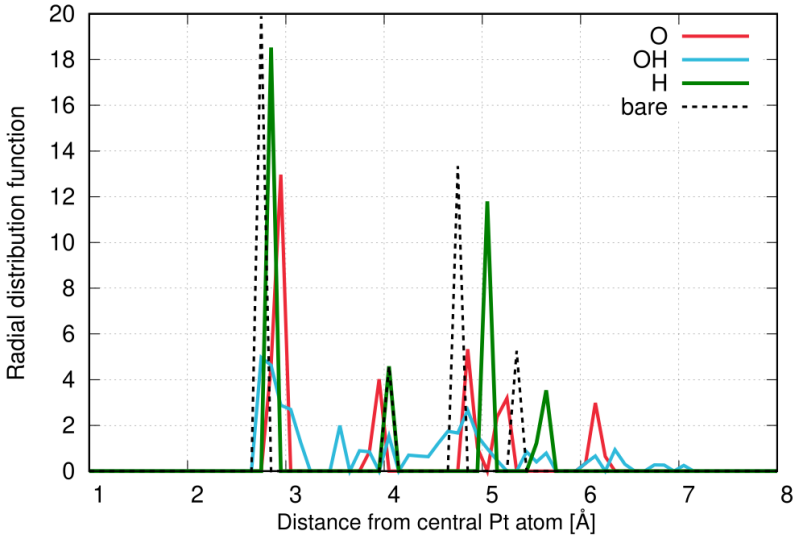


Figure 5.6: Radial distribution function of Pt atoms around the central Pt atom. For each adsorbate, the data correspond to the structure with the highest investigated coverage, while the clean nanoparticle is shown as a reference. The H-covered nanoparticle is represented in green, OH in blue, and O in red.

all peaks broaden and the distinct layering characteristic of the bare particle is lost. In comparison, the H- and O-covered nanoparticles retain a more ordered structure, with only small displacements of Pt atoms around the particle center, while the outermost atoms exhibit larger deviations. In particular, the kink atom in the O-covered structure is displaced by approximately 0.8 Å, leading to an overall increase of about 1.5 Å in the particle diameter. The significant displacement of kink atoms suggests that these atoms may serve as the initial sites for oxidation of the nanoparticle. For H adsorption, the displacement of kink atoms is smaller, amounting to only about 0.3 Å.

During relaxation of the O- and OH-covered structures at various coverages, a tendency toward deformation was observed, particularly at high OH* coverages, where the nanoparticles exhibited pronounced structural distortions. Deformation of nanoparticles was also reported by Verga et al. [54], who noted a tendency of oxygen atoms to move toward subsurface sites as the coverage increases. In our case, this effect was not observed during geometry optimization and was also not explicitly investigated.

5.1.2 Catalysts models under realistic conditions

The previous section focused on the analysis of DFT energies, whereas we now turn to surface structures under realistic electrocatalytic conditions. For this purpose, the Gibbs energy is more relevant than the energy directly obtained from DFT calculations. In a first approximation, we can assume that the vibrational contributions of reactants and products approximately cancel out, and we account only for the rotational and translational degrees of freedom of the gas-phase species (H_2 and H_2O, since the Gibbs energy of water is calculated as that of water vapor at 25 °C):

$$\begin{aligned} \mu_i^{\text{gas}} &= E_0 + G_{\text{rot}}(T) + G_{\text{tr}}(T) + pV \\ \mu_i^{\text{solid}} &= E_0 \end{aligned} \tag{5.4}$$

Here, E_0 is the DFT energy, and $G_{\text{rot}}(T)$ and $G_{\text{tr}}(T)$ are the contributions from the rotational and translational degrees of freedom, respectively. We will refer to this as the

first approximation.

In electrochemical systems, the catalyst surface is exposed to an aqueous environment, and this contribution can become significant, especially for polar adsorbates or when hydrogen bonding with the solvent occurs. Therefore, the expression for the Gibbs energy of the solid phase is modified to include the solvation term:

$$\begin{aligned} \mu_i^{\text{gas}} &= E_0 + G_{\text{rot}}(T) + G_{\text{tr}}(T) + pV \\ \mu_i^{\text{solid}} &= E_0 + \Delta G_{\text{solv}} \end{aligned} \tag{5.5}$$

This approximation will be referred to as the approximation with solvation. Since the reference H_2 and H_2O molecules are in the gas phase, solvation effects are not applicable to them.

A complete treatment of the Gibbs energy would also include vibrational contributions for both gas-phase and solid species. In that case, the expressions for the Gibbs energy, as introduced in Section 3.2.2, have the form:

$$\begin{aligned} \mu_i^{\text{gas}} &= E_0 + G_{\text{vib}}(T) + G_{\text{rot}}(T) + G_{\text{tr}}(T) + pV \\ \mu_i^{\text{solid}} &= E_0 + G_{\text{vib}}(T) + \Delta G_{\text{solv}} \end{aligned} \tag{5.6}$$

These equations were applied only to ideal surfaces, as the calculation of vibrational contributions for nanoparticles is computationally expensive.

5.1.2.1 Effect of electrode potential and pH

The effect of pH and electrode potential on the surface adsorption Gibbs energy at room temperature (25 °C) was analyzed within the CHE approximation (see Eq. (3.24)) for all three adsorbates. The results for selected adsorbate coverages on the Pt(111) surface with standard Gibbs energies calculated according to Eq. (5.6) are shown in Figure 5.7 for three different pH values. Each line in the graph corresponds to a different surface coverage, which determines the slope — higher coverages lead to steeper slopes. Within the CHE approximation, the effect of pH and electrode potential is added *a posteriori* and is therefore independent on the surface model, apart from the surface area.

For adsorption structures containing H atoms, the slope is positive irrespective of the coverage, indicating that increasing the electrode potential destabilizes H*. This behavior is expected, since the electro-adsorption of H* from H^+ requires an electron from the electrode (see Eq. (3.29a)). As the electrode potential increases, electrons become less available for H adsorption, making the adsorption process more difficult. In contrast, O* and OH* exhibit negative slopes, implying that their adsorption becomes more exothermic at positive potentials. Both O and OH species originate from water dissociation and donate electrons to the surface upon formation (see Eqs. (3.29b) and (3.29c)). The slope for O* is steeper than that for OH* at the same coverage, as O* formation involves a transfer of two electrons, whereas OH* formation involves only one. From these results, a general trend can be observed: at high electrode potentials the surface becomes predominantly covered with OH* or O* fragments, while at lower potentials H* is present on the surface.

Within the CHE approximation, a change in pH affects only the intercept of the adsorption energy lines, while the slope remains unchanged. As a result, the graphs shift to the left with increasing pH, indicating that, at a given potential, the OH- and O-covered surfaces become more stable compared to the H-covered ones. At lower pH, the concentration of H^+ ions in the solution is higher, making the adsorption of H* more exothermic at a given electrode potential.

The presented dependence of surface adsorption energy on electrode potential and pH represents an idealized picture. Within the CHE approach, electron and proton transfer

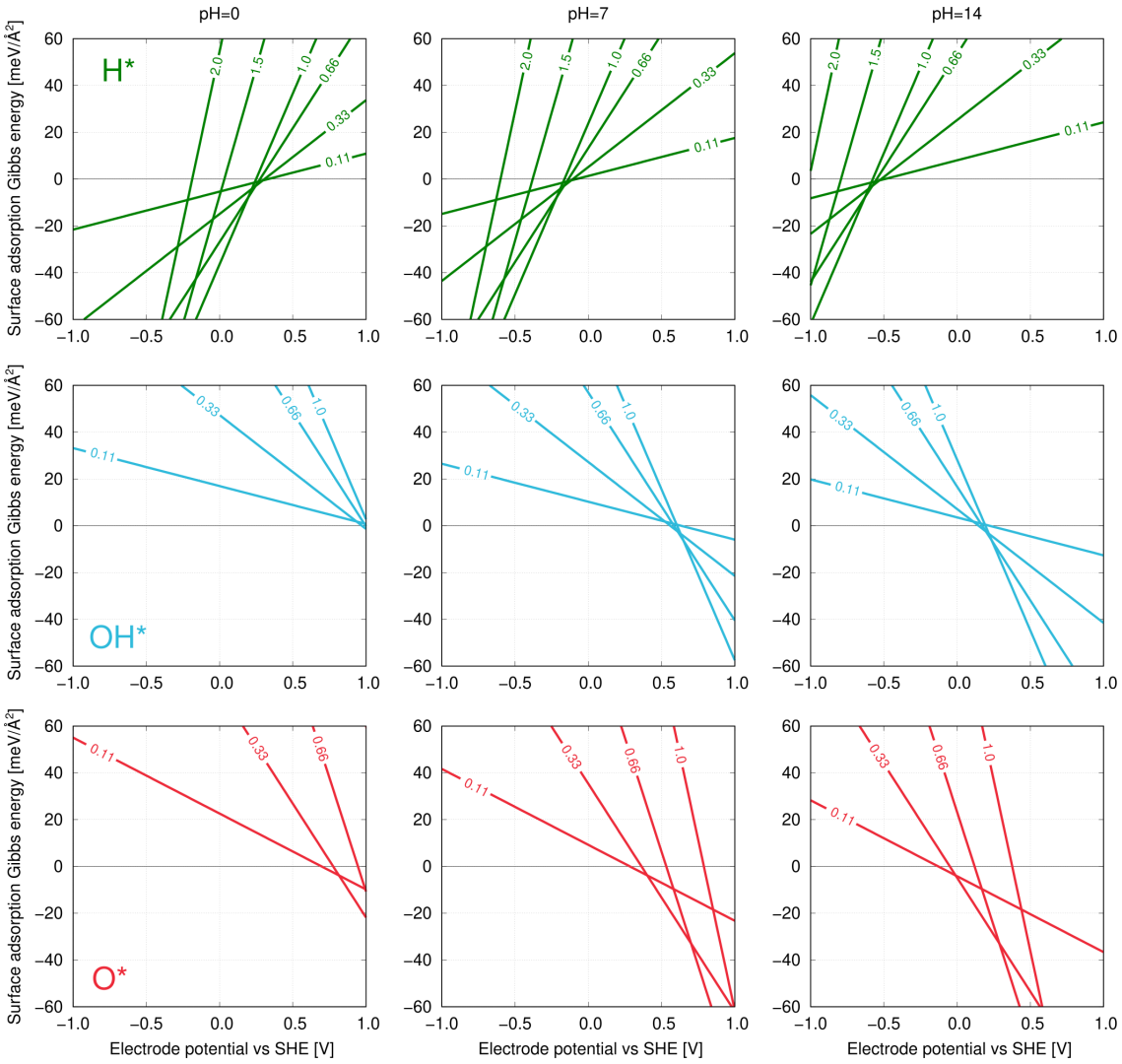


Figure 5.7: Surface adsorption Gibbs energy on Pt(111) as a function of electrode potential versus SHE at different pH values, calculated using the CHE approximation. Green lines correspond to H-covered surfaces, blue lines to OH-covered surfaces, and red lines to O-covered surfaces. Each line represents a different coverage as indicated in the graphs. For clarity, not all investigated coverages are displayed.

are assumed to be coupled, and the adsorbed state is treated as independent of electrode potential and pH. While this approximation is highly useful for comparing different catalyst models under given conditions, a deeper understanding of the electrode-potential dependence requires more advanced methods that explicitly account for it.

5.1.2.2 Pourbaix diagrams

To allow a direct comparison of surface structures under different conditions for the investigated models, Pourbaix diagrams were constructed. These were obtained within the CHE approximation, following the procedure outlined in Section 3.5.2. As a first approximation for calculating the standard Gibbs energy of adsorption, we added only rotational and translational contributions — see Eq. (5.4). For the analysis, the dissolution of Pt was not considered, as it occurs outside the potential range shown in the diagrams. Likewise,

the formation of platinum oxides was excluded, since only adsorption phenomena were addressed. In addition to "pure" adsorption structures, we also sampled mixed adsorption pairs (OH*+H*, O*+H*, O*+OH*) on the ideal surfaces. However, due to the large number of possible configurations, mixed states were not considered for the Pt_{55} particle

The resulting diagrams are shown in Figure 5.8. All surface models exhibit a general trend: at lower pH and lower potentials, the surface is predominantly covered with H*, whereas at higher pH and potentials it becomes covered with OH* or O*. For the ideal surfaces, among the considered adsorbate pairs, only the O*+OH* combination appears in the Pourbaix diagrams, while both combinations involving H* are absent. For the Pt(111) surface, increasing the potential and pH leads to a gradual decrease in H* coverage, followed by a wide region where the surface is bare. At higher potentials and pH, O-covered structures become more stable, with their coverage gradually increasing. The Pourbaix diagram for Pt(111) shows no region where OH* is thermodynamically the most stable. In contrast, Pt(100) exhibits only a narrow region in which the bare surface is most stable

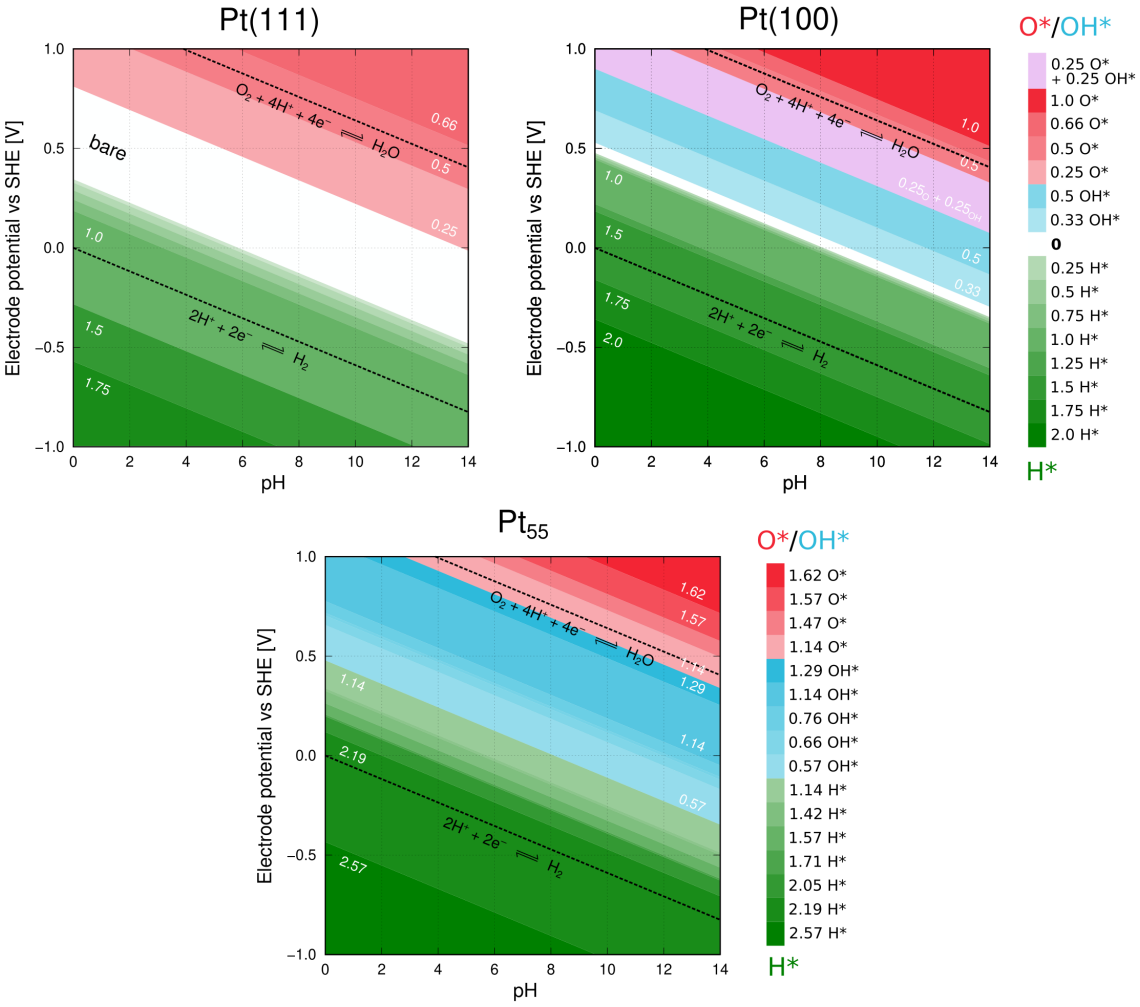


Figure 5.8: Pourbaix diagrams for Pt(111), Pt(100), and Pt_{55} surface models constructed from the first approximation to Gibbs energies (see Eq. (5.4)). Green denotes H-covered surfaces, blue corresponds to OH, and red to O. Mixed O+OH coverages are shown in purple. Black dotted lines indicate the water reduction and oxidation lines. The legend is provided on the right, and the most abundant structures have their coverages written directly in the graphs.

and as the potential and pH rise beyond the bare region, OH* adsorption occurs first. Further increases lead to a mixed OH*/O* state, and eventually, at the highest values, the surface becomes fully covered by O*. The conditions relevant for HER lie around the hydrogen line, where the Pt(111) surface is covered with 1 ML H*, whereas the Pt(100) surface exhibits higher coverage, reaching about 1.5 ML of H*. Overall, consistent with the surface adsorption energy results (see Figures 5.1 and 5.3), the Pt(100) surface is more reactive and exhibits higher coverages of the investigated adsorbates.

For the nanoparticle, a similar trend is observed, but the adsorbate coverages are overall higher. The maximum H* coverage considered is 2.57 ML, which is also the highest observed value in the Pourbaix diagram. Increasing the coverage further would likely lead to spontaneous H_2 formation, as hydrogen molecule was occasionally formed even at lower coverages during geometry optimization. The structure most relevant under HER conditions corresponds to the 2.19 ML H-covered particle, where all bridge-edge sites, all bridge sites on (100) facets, kink atoms, and hollow sites on (111) facets are occupied. The lowest H* coverage appearing in the Pourbaix diagram is 1.14 ML. In contrast to the bare surfaces, the nanoparticle model does not exhibit any region where the bare surface is the most stable. Instead, the surface structure transitions directly from an H-covered to an OH-covered state. Initially, half of the bridge-edge sites are occupied with OH* (0.57 ML coverage), followed by a rapid increase to 1.14 ML, where all bridge-edge sites are filled. A further increase in potential results in the adsorption of several additional OH groups, after which the surface transitions to an O-covered state with all bridge-edge sites occupied. Increasing the pH and electrode potential even further leads to an O* coverage of 1.62 ML, which represents the highest value considered in this study. Mixed OH*/O* phases were not included in the analysis, although, based on the Pourbaix diagrams of the ideal surfaces, such mixed states would likely be present at higher pH and electrode potentials.

From this analysis, it can be concluded that at low potentials and pH the Pt surfaces are predominantly covered with H*. With increasing pH and potential, OH* becomes stable on some surfaces, while at sufficiently high pH and potentials all surfaces are eventually covered with O*. For the nanoparticle model, higher adsorbate coverages are observed, making the analysis of low-covered particle less relevant for representing realistic conditions. The bridge-edge sites are fully occupied in most cases, except at OH* coverages below 1 ML, where partial occupation of these sites is observed. This indicates that these sites are mostly occupied under realistic conditions and are therefore likely less active for catalytic reactions, as noted by Jinnouchi et al. for the OER [55].

5.1.2.3 Contributions from solvation and vibrations for ideal surfaces

In addition to the first approximation to evaluate the standard Gibbs energy as presented above, we also included corrections arising from water solvation (the approximation with solvation given with Eq. (5.5)), as well as contributions from vibrational degrees of freedom to both energy and entropy (the complete treatment of the Gibbs energy according to Eq. (5.6)). The solvation contribution was evaluated according to Eq. (3.22) with implicit solvent model, while the Gibbs energy corrections for vibrations were calculated following the equations presented in Section 3.2.2. These corrections were applied only to the energetically most stable structures at a given coverage, under the assumption that the relative order of stability would not change — or, if it does, the resulting Gibbs energies of the competing structures remain similar.

The resulting Pourbaix diagrams are shown in Figure 5.9. When comparing the diagrams obtained from the approximation with solvation (first row) to the corresponding diagrams obtained from the first approximation (see Figure 5.8), only minor differences

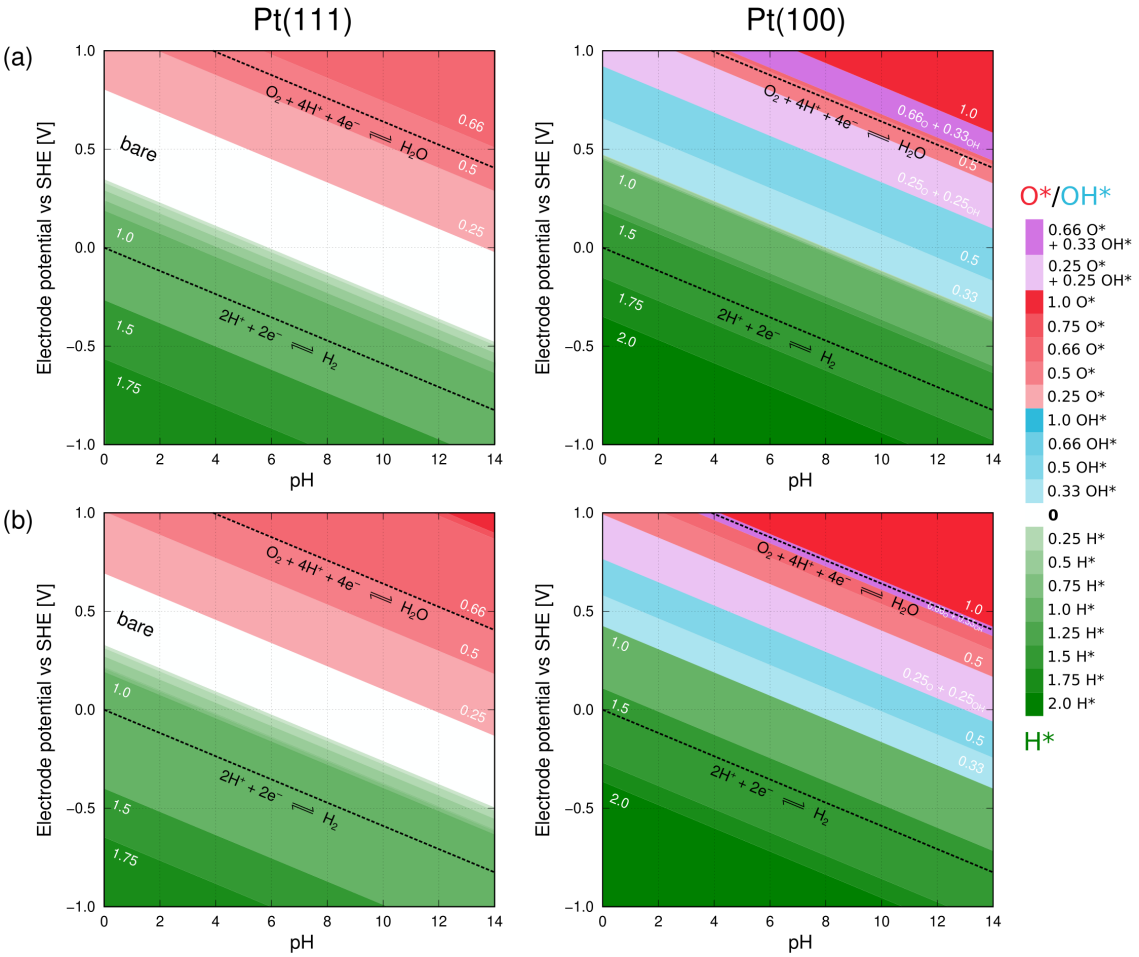


Figure 5.9: Pourbaix diagrams on the Pt(111) and Pt(100) ideal surfaces calculated with (a) the approximation of the Gibbs energy with solvation (see Eq. (5.5)), and (b) the complete treatment of the Gibbs energy (see Eq. (5.6)).

are observed. The solvation contribution for OH* averages around −0.13 eV/OH for standalone OH* and increases to −0.04 eV/OH when OH* groups form H-bonded network at higher coverages. For O*, the solvation contribution is approximately −0.01 eV/atom on Pt(111) and −0.03 eV/atom on Pt(100). For H*, the contributions are close to zero (about −0.005 eV/atom). Thus, the only relevant difference is the stabilization of certain OH* structures, leading to their slightly higher presence in the Pourbaix diagrams with solvation included. For the Pt(100) surface, this causes a direct transition from the H-covered surface to the OH-covered one, without an intermediate region of bare surface, which was present in the diagrams based on the first approximation to Gibbs energies.

It should be noted, however, that the stabilization of OH* is likely underestimated in these calculations, since the implicit solvent model cannot properly capture hydrogen bonding with the surrounding water molecules. At low coverages, OH* can form H-bonds with solvent molecules, which would increase its stability beyond the implicit-solvent prediction, while at high coverages H-bonding between OH* adsorbates reduces the relative impact of solvation. Consequently, the occurrence of low-coverage OH* structures in the O*/OH* region of the Pourbaix diagram is likely higher than currently predicted. For comparison, Rossmeisl et al. estimated the solvation stabilization of OH* to be around −0.3 eV using an explicit ice-like water bilayer model [131].

Further, the Pourbaix diagrams constructed based on the complete treatment of the Gibbs energies (Figure 5.9b) are similar to those obtained using the approximate Gibbs energy. A slightly increased stability of O-covered structures compared to OH* is observed, resulting in a narrower region of OH* adsorption. The overall $\Delta G^{\mathrm{corr}}(T)$ correction for the adsorption process amounts to approximately 0.3 eV for OH*, 0.2 eV for H*, and only 0.02 eV for O*. These values are consistent with those reported in the tables by Nørskov and Rossmeisl [42], [102]. The similarity between the Pourbaix diagrams constructed using different approaches to calculate the Gibbs energy indicates that even the first approximation, which includes only the rotational and translational contributions of gas-phase species, already provides reliable results.

According to experimental observations, surface oxidation of Pt begins with the adsorption of OH* at potentials of around 0.75 V in acidic media [132]. Our results for Pt(111) do not predict any region where the OH-covered surface is the most stable, whereas the OH-covered region predicted for Pt(100) corresponds well to the experimental observations. This highlights the importance of employing more realistic water models that can account for hydrogen bonding between OH* and the surrounding water environment. The significance of the water solvent was also emphasized by Wakisaka et al. [133], who reported that the concentrations of OH* groups and adsorbed water molecules in the first solvation layer are approximately equal, corresponding to the coverage expected for an ice-like water bilayer. For low-index surfaces, it has been reported that on Pt(100) the electrode potential at which OH* adsorption occurs overlaps with the hydrogen adsorption/desorption region [133], [134]. This observation aligns with our Pourbaix diagrams, which show a direct transition from H- to OH-covered surfaces without an intervening bare-surface region.

5.1.3 Kinetic analysis

All three elementary steps of the HER (Volmer, Tafel, and Heyrovsky — see Eqs. (3.25a)–(3.25c)) were investigated on Pt(111) using NEB calculations at different H* coverages. An ice-like water bilayer model was employed to represent the aqueous environment and to provide protons for the Volmer and Heyrovsky steps. The Tafel step was modeled using the conventional H-down water bilayer, while the Volmer and Heyrovsky steps were modeled with the ice-like bilayer containing an additional proton, simulating an $(H_2O)_nH^+$ species that acts as a proton donor under acidic conditions. The ice-like water bilayer model represents a simplified interfacial structure and cannot capture the liquid character of water. Moreover, the absence of water molecules above the bilayer affects the orientation and hydrogen-bonding environment of water molecules in the model. Given these limitations of the ice-like bilayer model, as well as the use of calculations performed at a constant number of electrons, the presented results should be interpreted as providing only a qualitative, approximate description of the HER mechanism.

The reaction and activation energies obtained for low and high H* coverages are shown in Figure 5.10, while details of all reaction pathways are provided in the Figure B.6 in the Appendix. For the Volmer step, the low-coverage case corresponds to adsorption on a bare surface, where a single H atom adsorbs on an fcc site. In the high-coverage case, a complete monolayer of H* is pre-adsorbed on the fcc sites, and the additional H atom adsorbs on a top site. For the Tafel step, at low coverage, two H atoms adsorbed on neighboring fcc sites recombine, whereas, at high coverage, a top-site H atom reacts with an adjacent fcc H atom. For the Heyrovsky step, one fewer H atom is present on the surface, since, in contrast to the Tafel step, one H is supplied from the water phase.

A clear dependence of the reaction and activation energies on coverage is evident from the graphs. The Volmer step becomes increasingly endothermic and slower with higher H* coverage, since adsorption becomes more difficult as the surface becomes saturated. In

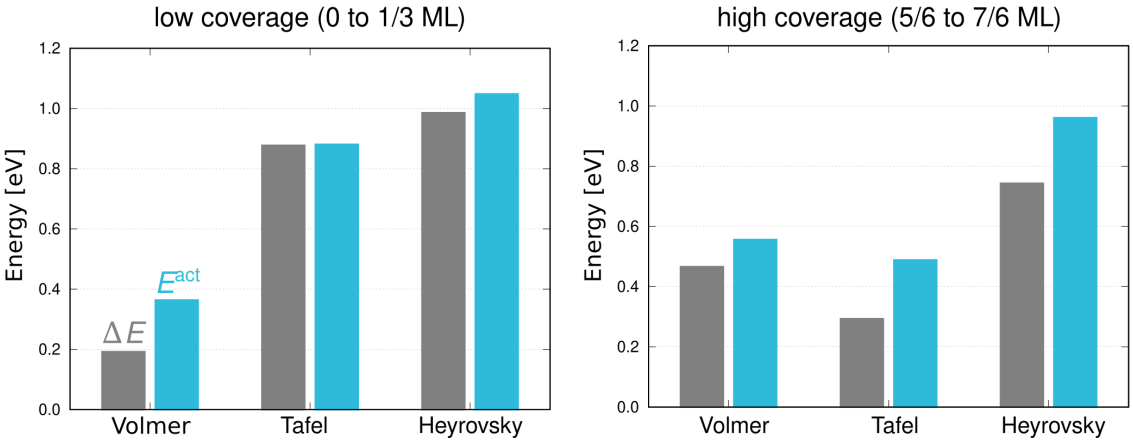


Figure 5.10: Reaction energies (gray) and activation energies (blue) for the elementary steps of the HER. Low coverage corresponds to the minimal coverage required for the reaction within the considered supercell, while high coverage refers to approximately 1 ML.

contrast, both the Tafel and Heyrovsky steps become more exothermic and exhibit lower activation barriers at higher coverage. For the Tafel step, the reacting hydrogen atoms change from an fcc–fcc pair at low coverage to an fcc–top pair at high coverage. It is noteworthy that at low coverage the barriers for the Tafel and Heyrovsky steps are largely determined by the endothermic energy of the reactions, whereas at higher coverage, a noticeable difference emerges between the reaction energy and the activation barrier. From these trends, it follows that at low coverage H_2 formation is the rate-determining step, while at higher coverage, which is expected from the Pourbaix diagrams under conditions relevant to HER, the Volmer step becomes slower and has an activation barrier comparable to that of the Tafel step.

Lindgren et al. [49] performed a kinetic study of HER on Pt using constant-potential calculations. They observed a strong dependence of the Volmer and Heyrovsky steps on the applied potential, whereas the Tafel step showed little variation. This is consistent with the equations of each elementary step (see Eqs. (3.25a)–(3.25c)), where the Volmer and Heyrovsky steps involve electron transfer, while the Tafel step does not. As the electrode potential decreases, both the Volmer and Heyrovsky steps become faster; however, in the potential region relevant for HER, the Volmer–Tafel pathway was predicted to be predominant. They further reported that coverages above 1 ML are required for the reaction to proceed, since H* atoms adsorbed in hollow sites are too strongly bound to the surface to participate in the reaction. In contrast, Tang et al. from the Nørskov group [51], employed the charge extrapolation method [135] and concluded that the Volmer–Heyrovsky pathway dominates. They also found that H* coverage saturates at 1 ML, with additional H atoms beyond this coverage being unlikely to have a significant effect on the catalytic activity.

Our results indicate that the Tafel step exhibits a lower barrier than the Heyrovsky step. However, no explicit effect of electrode potential was included in our study, which is expected to predominantly influence the Heyrovsky step, while having little impact on the Tafel step [49], [51]. The treatment of electrochemical processes within the conventional constant-electron DFT framework and periodic boundary conditions suffers from a well-known finite-size effect: the introduction of a proton–electron pair substantially alters the electrode potential. This leads to two major complications: (i) the calculated reaction and activation energies depend on the supercell size, and (ii) the electrode potential is inconsistent between the initial, transition, and final states within the same supercell. For

the low-concentration case of the Volmer step, we calculated a difference in work function of approximately 1.5 eV between the initial and transition states.

Due to these limitations, a direct comparison between the electrochemical Heyrovsky step and the chemical Tafel step is not straightforward based on our results. We therefore focused more attention on the chemical Tafel step, which is largely independent of the electrode potential.

5.1.3.1 Tafel step on Pt(111) and Pt(100)

We analyzed the dependence of the reaction and activation energies of the Tafel step on H* coverage for both Pt(111) and Pt(100) surfaces in vacuum. Calculations were performed in a (2×2) supercell with initial-state coverages ranging from 0.5 to 2.0 ML. The initial state (IS) corresponds to the most stable structure identified at a given coverage, while the final state (FS) was chosen as the most chemically sensible configuration, though not necessarily the lowest in energy. On the Pt(111) surface, three different reaction pathways for H_2 formation were considered, depending on the positions of the reacting H atoms: fcc–fcc, fcc–top, and top–top. On Pt(100), where H* preferentially adsorbs on bridge sites, two possible pathways were examined according to the relative orientation of the reacting H atoms: the 90° and 180° configurations. All these options are illustrated schematically in Figure 5.11.

The reaction and activation barriers as a function of coverage are shown in Figure 5.12a and the reaction paths are given in Figures B.7 and B.8 in the Appendix. Both energies decrease with increasing coverage. Across the entire coverage range, Pt(111) consistently exhibits lower activation and reaction energies compared to Pt(100). Among the three possible pathways on Pt(111), the fcc–fcc combination displays the highest barrier and was therefore examined only up to 1 ML coverage. Its activation energy shows little dependence on coverage and is between 0.9 and 1.0 eV. At higher coverages, the top–fcc and top–top mechanisms become the viable pathways. The reaction energies are identical in both cases, since the same final state is involved. In terms of activation energies, the fcc–top pathway exhibits lower values, which decrease with increasing coverage. In contrast, for the top–top mechanism, the activation energies do not show a consistent trend with the coverage. Therefore, the fcc–top pathway is expected to play a more dominant role at higher concentrations.

On the Pt(100) surface, only the 180° pathway was analyzed for coverages up to 1 ML, due to the structure of the initial state. Similar to Pt(111), the activation energy below 1 ML shows little dependence on coverage and is largely determined by the reaction energy, which is significantly endothermic. At higher coverages, both the 90° and 180° pathways become viable, with the 90° option generally yielding lower activation barriers. The 180° pathway shows some variation in activation energies as the coverage increases, but the val-

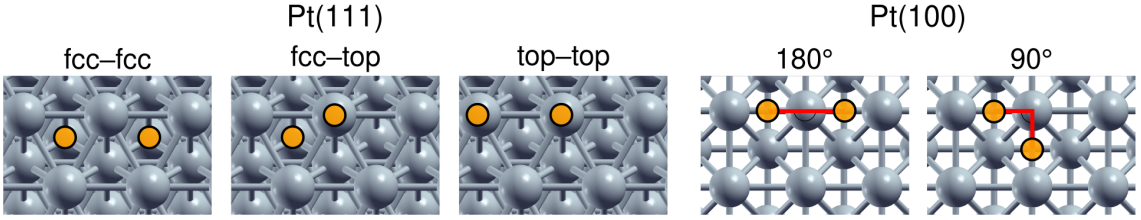


Figure 5.11: Positions of reacting H* atoms for the considered reaction pathway options for the Tafel step on Pt(111) (left) and Pt(100) (right). Hydrogen atoms are shown as orange circles.

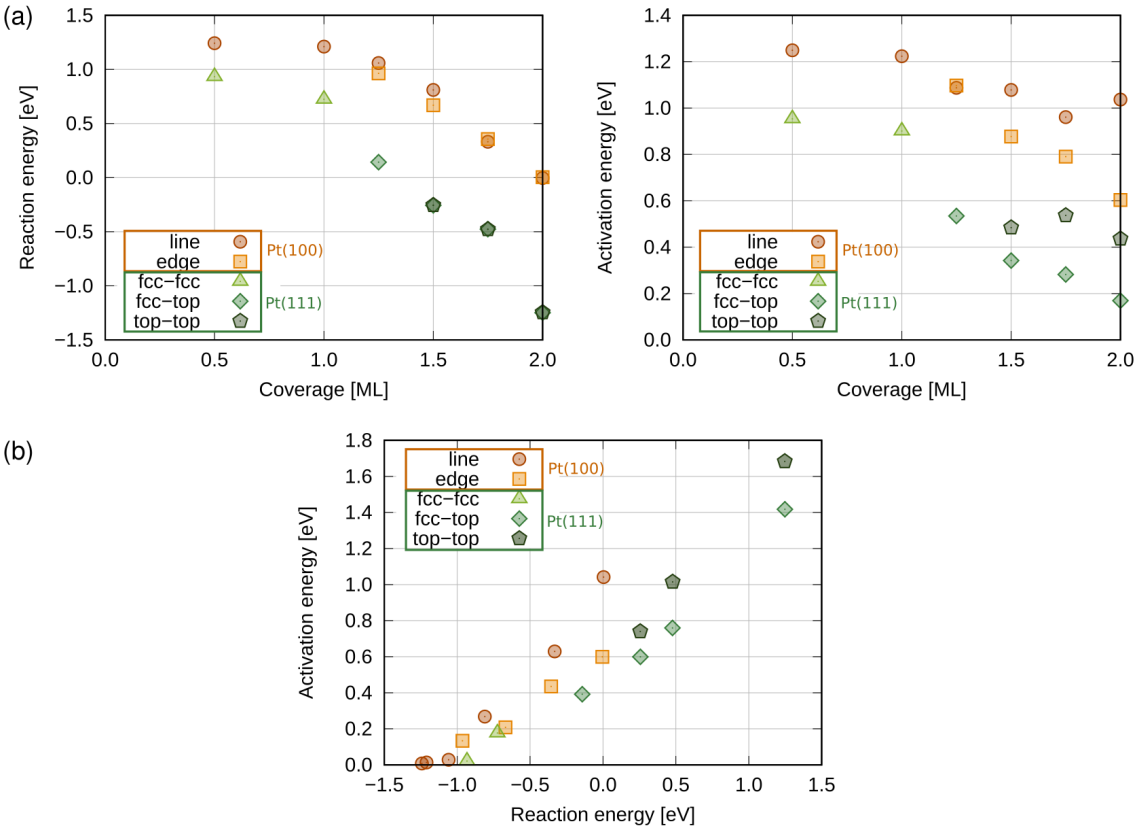


Figure 5.12: (a) Reaction and activation energies of the Tafel step as a function of coverage. (b) Activation energy as a function of reaction energy for hydrogen chemisorption on Pt surfaces (reverse of the Tafel step). The orange-like color corresponds to Pt(100), and the green color to Pt(111).

ues remain around 1 eV. In contrast, the 90° pathway exhibits a more apparent dependence on coverage, with activation energies steadily decreasing as coverage increases. Reaction energies are similar across coverages up to 1 ML, but decrease beyond this point. Due to differences in the final states of the two pathways, their reaction energies are not the same.

The expected H* coverage under HER-relevant conditions is 1 ML for Pt(111) and around 1.5 ML for Pt(100). On Pt(111), this corresponds to a Tafel barrier of about 0.9 eV via the fcc–fcc mechanism. If additional H atoms adsorb beyond 1 ML, the top–fcc pathway becomes accessible, which exhibits a significantly lower barrier. The top–top mechanism, however, appears unlikely, as it requires two additional H* atoms on top of the 1 ML coverage and displays a higher barrier than the fcc–top pathway. On Pt(100) covered with 1.5 ML of H*, the Tafel barrier is also around 0.9 eV and does not change significantly with the addition of H* atoms. This suggests that the Heyrovsky step could be relevant on Pt(100) due to the relatively high barrier of the Tafel pathway. In contrast, on Pt(111), the top–fcc mechanism could facilitate H_2 formation, though the additional H* on top positions are not thermodynamically favored under HER conditions. These findings are consistent with the conclusions of Lindgren et al. [49], who reported that coverages above 1 ML are required for HER to proceed.

For dissociative chemisorption reactions, a linear relationship between activation and reaction energies is often observed [85], known as the Brønsted–Evans–Polanyi (BEP) relation. Since hydrogen chemisorption is the reverse of the Tafel step, the corresponding reaction and activation energies for the dissociation reaction obtained from Tafel analysis

are shown in Figure 5.12b. A linear-like trend is observed, suggesting that the analysis of the activation energy for the Tafel step on both Pt(111) and Pt(100) surfaces can be simplified using the BEP relation, provided that the slope and intercept are properly determined.

5.2 Ruthenium Catalysts

Parts of this section, focusing on the comparison of close-packed surfaces of fcc and hcp ruthenium, are based on our article published in the Journal of Catalysis [39].

Ruthenium is considered to be a promising catalyst material for HER in alkaline conditions. To better understand its catalytic behavior, we first evaluate ruthenium's performance relative to platinum catalysts. We then focus on the effect of crystal phase on its activity, comparing the thermodynamically stable hcp phase and the uncommon fcc phase, which has been observed in catalysts with ruthenium nanoparticles [62], [68]–[71]. Experimental studies have shown that for HER, catalysts containing the fcc-structured nanoparticles exhibit higher activity compared to those with only the hcp ones [68]–[71].

5.2.1 Comparison with platinum

Similarly to Pt, we investigated the adsorption of H, OH, and O on the close-packed Ru-hcp(001) surface at different coverages. The resulting surface adsorption energy plots, calculated according to Eq. (3.6) and Eq. (3.31), together with the fitted lines obtained for Pt(111), which is structurally very similar, are presented in Figure 5.13. The adsorption of H* is stronger on Ru than on Pt, and a linear trend of surface adsorption Gibbs energies is observed up to a coverage of 1 ML. This suggests that the surface is either bare or fully covered with 1 ML of hydrogen, which preferentially occupies the fcc sites. At higher coverages, additional H atoms adsorb on top sites, giving rise to a concave quadratic trend, i.e., a parabola that opens downwards. As a result, the transition between 1 ML and 2 ML coverage is discrete and does not involve any intermediate coverage.

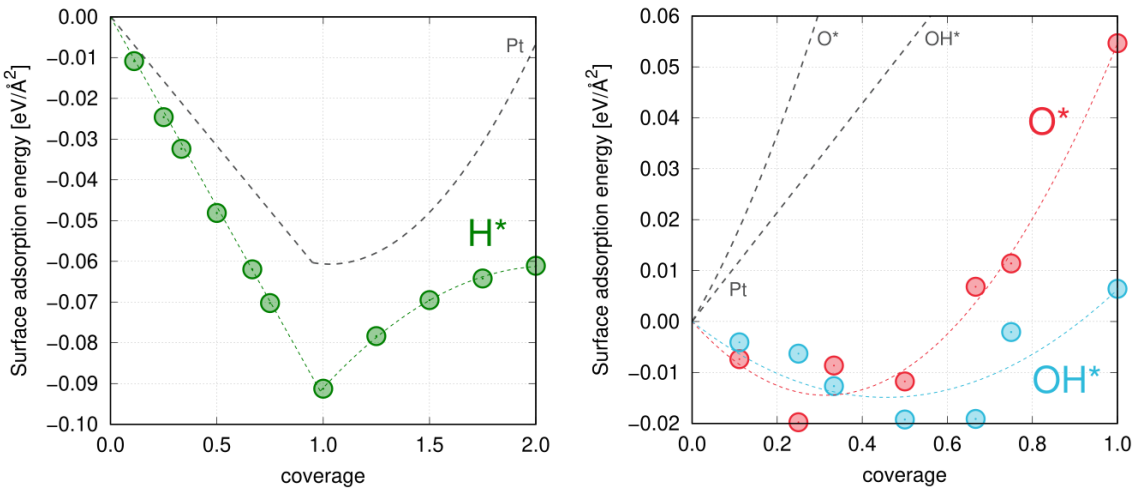


Figure 5.13: Surface adsorption energies of H*, OH*, and O* on Ru-hcp(001). Green lines correspond to H* adsorption, blue to OH*, and red to O*. For comparison, the fitted adsorption energies on Pt(111) are shown in gray.

Similar as for H*, the adsorption of O and OH is also more favorable on Ru-hcp(001) compared to the structurally similar Pt(111) surface. On Ru-hcp(001), the adsorption energies at lower coverage are even negative, indicating that surfaces covered with either OH* or O* are more stable than the bare surface. Oxygen atoms preferentially adsorb on hcp sites, whereas OH groups initially occupy fcc sites. At higher coverages, when H-bonded networks form, OH* also adsorbs on bridge or top sites. The surface adsorption energy trends loosely follow quadratic profiles, with a minimum at approximately 0.5 ML for OH* and 0.2 ML for O*.

From the obtained adsorption states, we constructed the surface Pourbaix diagram for Ru-hcp(001), shown in Figure 5.14a. We used the approximation accounting only for rotational and translational degrees of freedom (see Eq. (5.4)), and the diagram was constructed analogously to that of Pt, following the procedure outlined in Section 3.5.2. In contrast to Pt, mixed adsorbate phases were not considered, and only pure H*, OH*, or O* states were included in the analysis. The diagram shows that under HER-relevant conditions, Ru-hcp(001) is covered with 1 ML of H*, and at low enough pH and potentials the coverage changes to 2 ML, consistent with the surface adsorption energy graphs. At high pH and electrode potentials, only O-covered surfaces appear, indicating that Ru preferentially adsorbs O* rather than OH*. The surface is rapidly saturated with 1 ML of O*, reflecting its tendency toward oxidation. Compared to the Pourbaix diagram for Pt(111) (Figure 5.8), Ru exhibits higher coverages of both H* and O*, and a shift of the potential for O* adsorption to lower values. This highlights that Ru is more reactive than Pt, favors O* over OH*, and is more prone to oxidation.

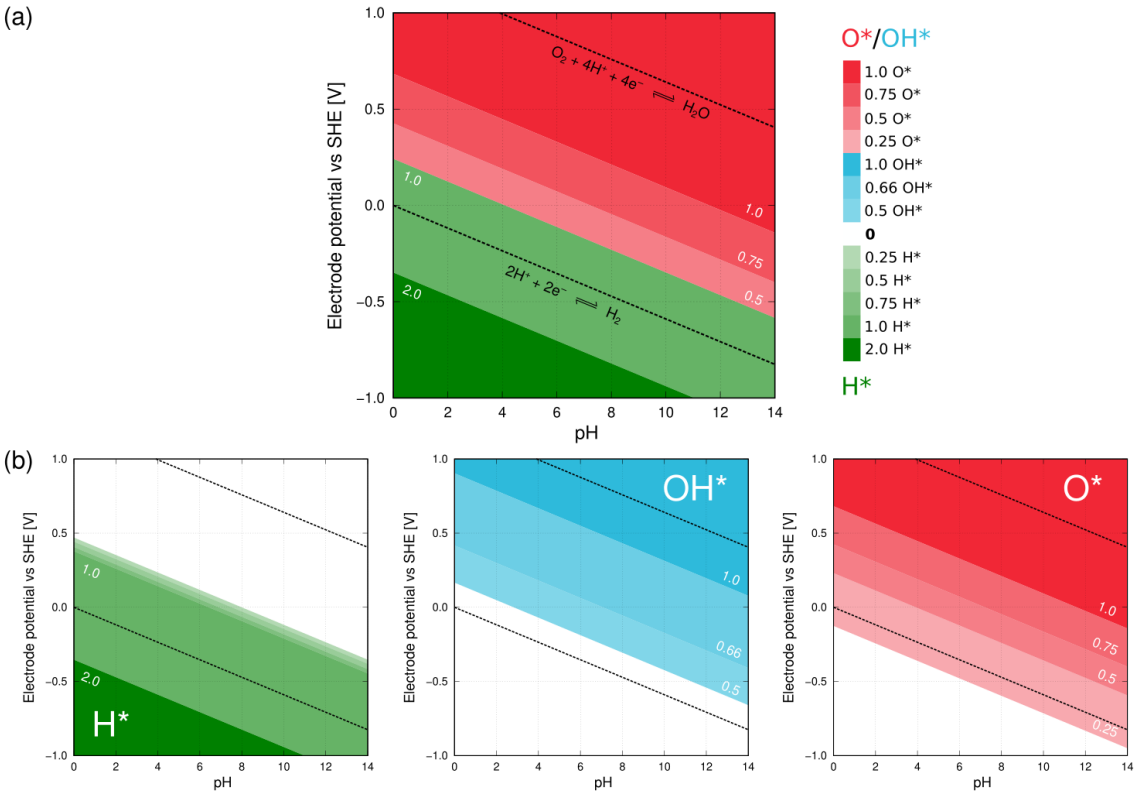


Figure 5.14: (a) The complete Pourbaix diagram for the Ru-hcp(001) surface and (b) the Pourbaix diagrams for each individual species. Green, blue, and red denote H*, OH*, and O*, respectively.

Additionally, we constructed Pourbaix diagrams for each individual investigated species (H*, OH*, and O*) as shown in Figure 5.14b. These diagrams allow us to identify the potential–pH regions in which each species is thermodynamically stable relative to the bare surface, assuming no competing adsorption from other species arising from water dissociation. For H*, the partial Pourbaix diagram additionally reveals a sharp transition between 1.0 ML coverage and the bare surface, as expected from surface adsorption energies. This transition is not visible in the complete Pourbaix diagram due to the competing adsorption of O*. Similarly, the partial Pourbaix diagram for O* also shows an intermediate low-coverage region before the bare surface becomes more stable. In contrast, OH* does not appear in the complete Pourbaix diagram, but occupies a region similar to that found in the partial Pourbaix diagram for O*.

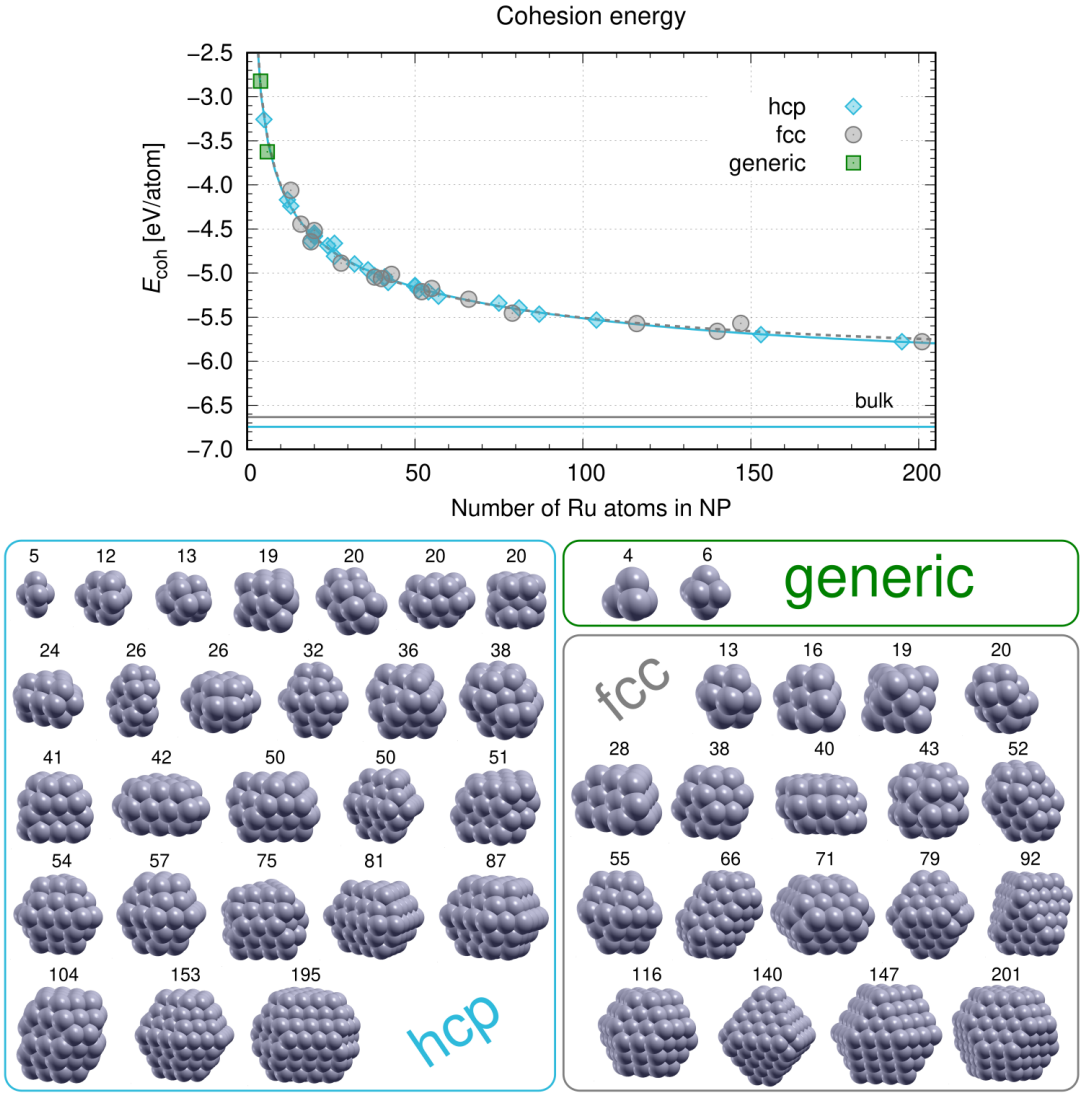


Figure 5.15: Cohesion energy of Ru hcp and fcc nanoparticles as a function of the number of atoms. Blue and gray correspond to the hcp and fcc phases, respectively, while green represents generic nanoparticles consistent with both crystal structures. Separate fitted curves are shown for the hcp and fcc data points. The cohesion energies of the bulk phases are shown as two straight lines. Below the graph, snapshots of the constructed nanoparticles are shown, along with the number of Ru atoms in each.

5.2.2 Uncommon fcc phase

As Ru-fcc phase was observed in catalysts relevant for HER [68]–[71], we compared the Ru-hcp and Ru-fcc phases in terms of thermodynamics and kinetic parameters. First, to determine the thermodynamic stability of both crystal phases, cohesion energies (Eq. (3.9)) for bulk structures and nanoparticles[4] were calculated. For bulk, values of -6.74 and -6.63 eV/atom were obtained for Ru-hcp and Ru-fcc, respectively. This signifies that the hcp bulk phase is by 0.11 eV/atom more stable compared to the fcc crystal phase. For nanoparticles, the results and the analyzed structures are presented in Figure 5.15. In contrast to the bulk structure, no significant difference in thermodynamic stability between the two phases was observed. The fitted curves for the Ru-hcp and Ru-fcc particles are almost superimposed across the investigated size range, with small differences observed only for the largest particles. This results suggest that both hcp and fcc crystal structures are thermodynamically feasible for small Ru nanoparticles with diameters of up to $\sim$2 nm (corresponding to the largest nanoparticles considered in this study), and potentially even larger, though this was not examined here.

Table 5.2: Surface energies and coordination numbers (CN) for the low index surfaces of Ru-hcp and Ru-fcc. All coordination numbers lower than 12 are given: the first number refers to the upper-most layer of atoms and if the second number is stated it refers to the second layer. For comparison, surface energies obtained by Zhao et al. [64] and Li et al. [63] are also given.

surface	CN	σ_{surf} (meV/Å^2)		
		our data	Zhao et al. [64]	Li et al.[63]
Ru-hcp(001)	9	164	164	160
Ru-hcp(100)	8, 10	184	181	181
Ru-hcp(011)	8, 9	184	180	177
Ru-fcc(111)	9	149	150	145
Ru-fcc(100)	8	189	176	184
Ru-fcc(011)	7, 11	176	162	171

To make the analysis of the activity of Ru-fcc and Ru-hcp phases feasible, we concentrated on the calculations with low-index ideal surfaces (Ru-hcp(001), Ru-hcp(100), Ru-hcp(011) and Ru-fcc(111), Ru-fcc(100), Ru-fcc(011)), which are shown in Figure 3.8 in Section 3.5. We calculated their surface energies by fitting Eq. (3.7) with slabs of thicknesses ranging from 20 Å to 40 Å. The results are presented in Table 5.2, alongside the characteristic coordination numbers of surface atoms and reference surface energies reported in the literature [63], [64]. From these results, we can observe that the close-packed surfaces — Ru-hcp(001) and Ru-fcc(111) — are thermodynamically the most stable. For the Ru-hcp phase, the (100) and (011) terminations exhibit similar stability, whereas for the fcc phase, the (100) termination is the least stable. The observation that the Ru-fcc(100) surface has a larger surface energy than the more open Ru-fcc(110) surface may seem surprising. This can be attributed to the larger surface area of the primitive cell of Ru-fcc(110) compared to that of Ru-fcc(100). When compared with the literature, the calculated surface energies for the hcp crystal phase are consistent with both previously reported studies. For the fcc phase, our results align well with those of Li et al., but

[4]Spin-polarized calculations were performed for nanoparticles containing less than 30 Ru atoms. For larger nanoparticles, the effect of magnetization on energy was negligible (less than 1 meV/atom) and therefore not considered.

differ from the values reported by Zhao et al., who reported relatively high stability of the Ru-fcc(100) and Ru-fcc(011) surfaces. This may be a consequence of the use of RPBE functional in their study.

5.2.2.1 Binding of H and OH on Ru-hcp(001) and Ru-fcc(111) surfaces

Ru-hcp(001) and Ru-fcc(111) represent the most stable low-index surfaces of their corresponding crystal phases and are structurally very similar. They both exhibit the same structure of layers, but differ in their stacking sequence. This structural resemblance and their thermodynamic stability, makes them well-suited for a direct comparison of the hcp and fcc phases of ruthenium. To investigate their catalytic activity towards HER, we first investigated adsorption behavior of H and OH fragments. Calculations were performed across multiple slab thicknesses to ensure convergence and to enable comparison with values reported in the literature.

A convergence test of adsorption energies with respect to slab thickness was performed for top and fcc sites within the $(\sqrt{3} \times \sqrt{3})$R30° supercell, and the corresponding values are reported in Table 5.3. The results indicate that binding energies obtained for 3- and 4-layer slabs are generally not converged. Therefore, it is advisable to use slabs consisting of at least 5 or 6 atomic layers to obtain reliable results. To examine the spatial extent of charge redistribution upon adsorption, planar integrated electron charge density difference plots were calculated for the fcc site and are shown in Figure 5.16. They show that charge redistribution effects are still clearly visible at the third atomic layer and progressively vanish deeper into the slab.

Results of the binding energies on different sites for $(\sqrt{3}\times\sqrt{3})$R30° and (3×3) supercells at a slab thickness of six atomic layers are reported in Table 5.4. For the H binding energies, we observe that the values obtained for the two supercell sizes are very similar. The most stable adsorption site for H* on both surfaces is the fcc site, which yields identical binding energies for Ru-hcp(001) and Ru-fcc(111) slabs with a thickness of 6 layers. For other slab thicknesses (Table 5.3), Ru-hcp(001) generally binds H slightly more strongly. The second most stable site is the hcp site, where the Ru-fcc(111) surface binds H slightly more strongly than Ru-hcp(001). Adsorption of H on the bridge site is not stable on either surface, therefore, the reported energies were obtained from constrained calculations and are nearly identical for both crystal phases. The least stable configuration for H adsorption is the top site, which exhibits a more pronounced difference between the two surfaces: Ru-hcp(001) binds H* approximately 0.1 eV more strongly than Ru-fcc(111). Previous studies of H adsorption energies also identify the fcc site as the most stable adsorption site on both

Table 5.3: Convergence of binding energies of H* and OH* at fcc and top sites on Ru-hcp(001) and Ru-fcc(111) with respect to slab thickness.

	E_b(H @ fcc) (eV)		E_b(H @ top) (eV)		E_b(OH @ fcc) (eV)		E_b(OH @ top) (eV)	
layers	hcp(001)	fcc(111)	hcp(001)	fcc(111)	hcp(001)	fcc(111)	hcp(001)	fcc(111)
3	−2.89	−2.94	−2.52	−2.35	−3.38	−3.20	−3.10[a]	−2.87[a]
4	−2.97	−2.97	−2.52	−2.48	−3.47	−3.50	−3.10[a]	−3.11[a]
5	−2.96	−2.94	−2.53	−2.40	−3.47	−3.41	−3.11[a]	−3.02[a]
6	−2.95	−2.95	−2.53	−2.42	−3.41	−3.41	−3.12[a]	−3.03[a]
7	−2.96	−2.93	−2.52	−2.42	−3.43	−3.42	−3.12[a]	−3.04[a]
8	−2.96	−2.95	−2.53	−2.40	−3.44	−3.40	−3.12[a]	−3.01[a]

[a]Obtained by laterally constraining the bottommost adsorbate atom.

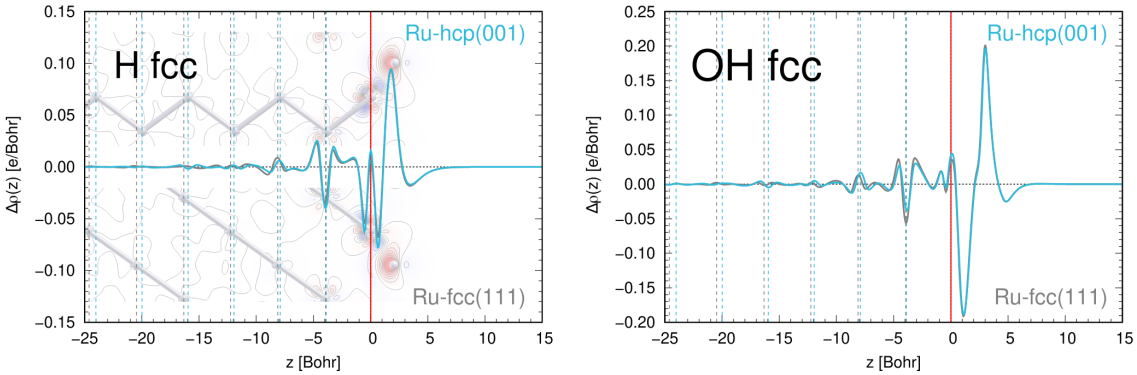


Figure 5.16: Planar integrated electron charge density difference in the surface normal direction for H and OH adsorbed on the fcc site on Ru-hcp(001) and Ru-fcc(111) calculated for 8-layer thick slabs. Ru-hcp(001) is represented with the blue colored curve and Ru-fcc(111) with the gray one. Vertical dotted lines represent Ru layers and the red line is the surface Ru layer on both models

Table 5.4: Binding energies of H and OH at different sites on Ru-hcp(001) and Ru-fcc(111). Results were obtained using six-layer slabs and the $(\sqrt{3}\times\sqrt{3})$R30° and (3×3) supercells.

		E_b(H*) (eV)		E_b(OH*) (eV)	
cell	site	hcp(001)	fcc(111)	hcp(001)	fcc(111)
$(\sqrt{3}\times\sqrt{3})$R30°	top	−2.53	−2.42	−3.12[a]	−3.03[a]
	bridge	−2.79[a]	−2.80[a]	−3.39	−3.39
	fcc	−2.95	−2.95	−3.41	−3.41
	hcp	−2.85	−2.88	−3.43	−3.32
(3×3)	top	−2.53	−2.44	−3.13[a]	−3.04[a]
	bridge	−2.80[a]	−2.81[a]	−3.42	−3.36[a]
	fcc	−2.96	−2.96	−3.46	−3.49
	hcp	−2.86	−2.90	−3.51	−3.47

[a] Obtained by laterally constraining the bottommost adsorbate atom.

Ru-hcp(001) and Ru-fcc(111) surfaces [66], [67]. When comparing adsorption strengths, these studies report that Ru-fcc(111) binds H more strongly compared to Ru-hcp(001), which is not observed from our results.

The most favorable adsorption sites for the OH* fragment are the hcp site on Ru-hcp(001) and the fcc site on Ru-fcc(111) with slightly stronger adsorption observed on the Ru-hcp(001) surface. In contrast to H*, the binding energies of OH* on hollow sites differ between the larger and smaller supercells. As the coverage increases, OH adsorption becomes less stable, especially on the hcp sites. For top and bridge positions, however, only minor differences in binding energy are observed between the two supercell sizes. As with H adsorption, the top site is also the least favorable for OH adsorption, with Ru-hcp(001) binding OH approximately 0.1 eV more strongly compared to Ru-fcc(111). Reported values for OH* adsorption strength in the literature vary: Zhao et al. [67] reported the fcc site as the preferred one on both surfaces, with Ru-fcc(111) exhibiting stronger OH* binding than Ru-hcp(001). Nandi et al. [66] identified the hcp site as the most favorable, with comparable binding energies on both surfaces.

From these results, we conclude that both H* and OH* preferentially adsorb at hollow

sites, with similar binding energies on both Ru-hcp(001) and Ru-fcc(111) surfaces. Adsorption at the top site results in the largest energy difference between the two surfaces—approximately 0.1 eV for both adsorbates. To investigate the origin of the observed differences in adsorption behavior, we analyzed the projected density of states (PDOS) for H and OH adsorbed at the top and fcc sites. Results are shown in Figure 5.17 for both sites. They reveal a clear difference between the two adsorption sites. Upon adsorption of H at the fcc site, the 1s orbital of hydrogen exhibits a distinct peak in the energy range of -7 to -6 eV relative to the Fermi level. On the bare Ru surfaces, no significant density of states is present in this range. However, upon H adsorption, a portion of the states originating from the Ru 5s and 4d orbitals shifts into this region, indicating the formation of a binding interaction. The geometry of these electronic states, visualized with the integrated local density of states (ILDOS) plots in the range between -7 and -6 eV (shown in Figure 5.17a), is similar for both surfaces and resembles tilted d_{z^2}-like orbitals.

On the top site (see Figure 5.17b), the PDOS has different characteristics. The 1s orbital of hydrogen is not localized but instead spread over a broader energy range. The PDOS of the H atom differs between the Ru-fcc(111) and Ru-hcp(001) surfaces, indicating different interactions with the Ru atoms. Among the calculated PDOS of individual orbitals for Ru surface atoms, the $4d_{z^2}$ and 5s orbitals exhibit the largest differences between the bare Ru surface and the surface with H adsorbed at the top site. This is consistent with the geometry of the adsorption bond. The 5s orbital shows a similar PDOS change

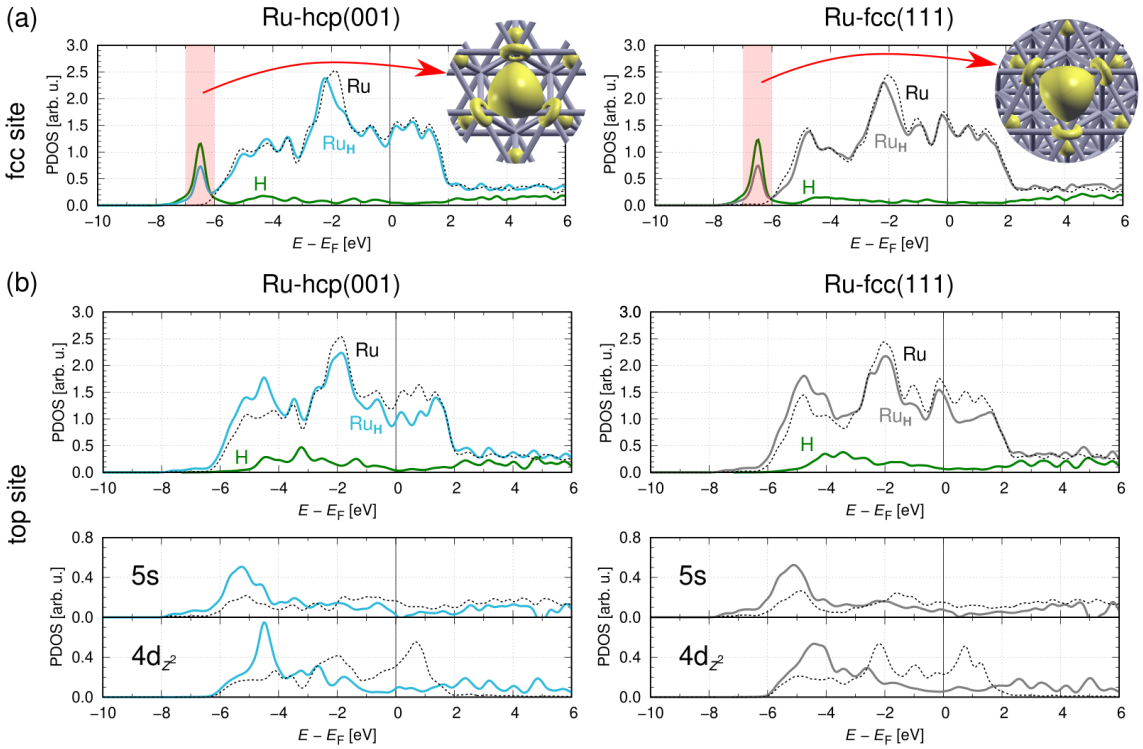


Figure 5.17: PDOS for Ru surface atoms and an adsorbed H atom on the (a) fcc site and (b) top site, calculated using the $(\sqrt{3} \times \sqrt{3})$R30° supercell. For the fcc site, the ILDOS plots in the energy range from -7 to -6 eV relative to the Fermi level are also shown. For the top site, the DOS projected to the 5s and $4d_{z^2}$ orbitals is shown beneath the atom projected DOS. Blue represents the Ru-hcp(001) surface, gray corresponds to the Ru-fcc(111) surface, and green indicates the H atoms. Dotted black lines show the PDOS of a bare surface Ru atom for comparison.

for both Ru-hcp(001) and Ru-fcc(111); however, the $4d_{z^2}$ orbital of Ru-hcp(001) exhibit a more intense peak at lower energies compared to that of Ru-fcc(111). This may explain the stronger interaction between the Ru-hcp(001) surface and H at the top position. The importance of the Ru $4d_{z^2}$ – H 1s orbital interaction in determining adsorption strength has already been reported by Cai et al. [136].

5.2.2.2 Activity of Ru-hcp(001) and Ru-fcc(111)

Based on adsorption energies, no apparent difference is observed between the two investigated surfaces, apart from the 0.1 eV difference in the binding energy of H and OH at the top site. To get more insight into the activity of Ru-hcp(001) and Ru-fcc(111) surfaces, the analysis of water dissociation reaction was conducted. In alkaline media, the source of hydrogen for the Volmer step of HER is water, which dissociates to an adsorbed hydrogen atom (H*) and a hydroxide ion (OH^-). As an approximation of the Volmer step, we modeled the dissociation of adsorbed water:

$$H_2O^* \rightleftharpoons H^* + OH^* \tag{5.7}$$

While the initial state is the same for both reactions, the final state of the modeled reaction (Eq. (5.7)) includes an adsorbed OH* rather than a hydrated hydroxide ion (OH^-), making the reaction easier to model with DFT.

Calculations were performed using both the $(\sqrt{3} \times \sqrt{3})R30°$ and (3×3) supercells with ice-like water bilayer model, to explicitly include water molecules in the calculation. In the smaller, $(\sqrt{3} \times \sqrt{3})R30°$ supercell, only two water molecules are present, resulting in a highly symmetric and constrained bilayer. In contrast, the larger (3×3) supercell contains six water molecules, allowing for a more flexible ice-like structure. In both supercells, dissociation of a water molecule results in OH* occupying the same top site as the dissociating water molecule. However, the dissociating hydrogen atom adsorbs at an adjacent empty top site in the smaller supercell, whereas in the larger supercell, it adsorbs at a more coordinated bridge-like site, as the surrounding water network can reorganize to accommodate it.

For the two supercells employed, we tested different directions for H* dissociation, as illustrated in Figure 5.18. In the $(\sqrt{3} \times \sqrt{3})R30°$ supercell, the dissociation of H* can proceed along three distinct directions, denoted as 180°, 60°, and −60°, where the angles are defined relative to the xy projection of the non-dissociating O–H bond (marked with

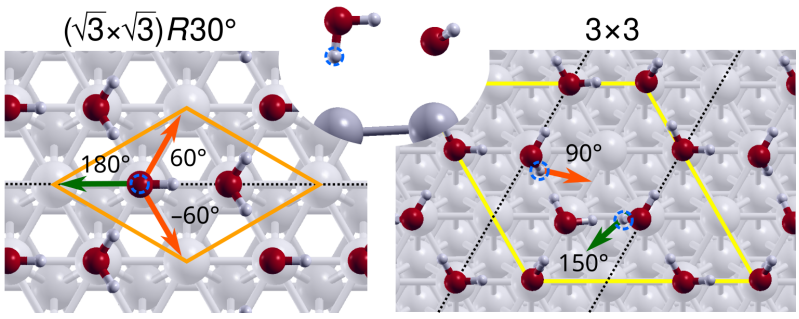


Figure 5.18: Different dissociation pathways of a water molecule above Ru-hcp(001) and Ru-fcc(111) surfaces within the ice-like water bilayer model. Both surfaces have the same possible pathways, therefore only one surface per supercell is shown in the background. The directions of the dissociating H atom are indicated by arrows and the black dotted line represents the reference plane used to define the pathway angles.

a black dotted line in Figure 5.18). The 60° and −60° paths are very similar although not geometrically equivalent and they exhibit nearly identical activation energies, with differences of less than 0.01 eV. Therefore, the −60° path was omitted from further analysis, and only the 180° and 60° directions were considered. In the (3×3) supercell, the dissociating hydrogen atom is more stable at a bridge-like adsorption site. Two geometrically favorable dissociation directions were identified, denoted as 90° and 150°, which are analogous to the 60° and 180° directions in the smaller supercell, respectively. For the 90° pathway, we also observe a proton transfer from a neighboring water molecule to the dissociating one.

The results for the reaction and activation energies of water dissociation are given in Tables 5.5 and 5.6 for the $(\sqrt{3} \times \sqrt{3})$R30° and (3×3) supercells, respectively. Snapshots of the IS, TS, and FS for representative pathways in both supercells are shown in Figure 5.19, while snapshots for each distinct pathway are provided in Figure C.1 and Figure C.2 in the Appendix. If we first look at the results for the smaller $(\sqrt{3} \times \sqrt{3})$R30° supercell, both investigated reaction pathways have identical initial and final states, and thus the reaction energies are the same. The results for Ru-hcp(001) are largely insensitive to slab thickness, whereas those for Ru-fcc(111) converge more slowly and require slabs at least five layers thick. This trend is in agreement with the convergence behavior observed for the adsorption energies. The difference in reaction energies for Ru-hcp(001) and Ru-fcc(111) is around 0.2 to 0.3 eV, with Ru-hcp(001) exhibiting more exothermic values. Since the two surfaces differ only in the stacking of layers, this difference appears large, but it can largely be attributed to the differences in adsorption energies. Due to the constrained structure of ice-like water bilayer in the smaller supercell, both H* and OH* are adsorbed on the top site in the final state. From the adsorption energies (see Table 5.4), it can bee seen that the Ru-hcp(001) surface exhibits by about 0.1 eV stronger adsorption of both H* and OH* on top site compared to Ru-fcc(111).

Table 5.5: Reaction and activation energies for the water dissociation reaction in the $(\sqrt{3} \times \sqrt{3})$R30° supercell on Ru-hcp(001) and Ru-fcc(111) surfaces, evaluated along the 60° and 180° pathways.

	ΔE (eV)		$E_{60°}^{\text{act}}$ (eV)		$E_{180°}^{\text{act}}$ (eV)	
layers	hcp(001)	fcc(111)	hcp(001)	fcc(111)	hcp(001)	fcc(111)
3	−0.60	−0.13	0.43	0.51	0.58	0.63
4	−0.61	−0.48	0.40	0.43	0.54	0.57
5	−0.60	−0.31	0.44	0.49	0.57	0.61
6	−0.59	−0.35	0.46	0.47	0.59	0.58
7	−0.59	−0.36	0.43	0.47	0.56	0.58

Table 5.6: Reaction and activation energies for the water dissociation reaction in the (3×3) supercell on Ru-hcp(001) and Ru-fcc(111) surfaces, evaluated along the 90° and 150° pathways.

	$\Delta E_{90°}$ (eV)		$E_{90°}^{\text{act}}$ (eV)		$\Delta E_{150°}$ (eV)		$E_{150°}^{\text{act}}$ (eV)	
layers	hcp(001)	fcc(111)	hcp(001)	fcc(111)	hcp(001)	fcc(111)	hcp(001)	fcc(111)
5	−0.73	−0.55	0.53	0.57	−0.36	−0.23	0.52	0.60
6	−0.70	−0.60	0.52	0.54	−0.33	−0.25	0.55	0.57
7	−0.73	−0.59	0.51	0.55	−0.35	−0.25	0.52	0.57

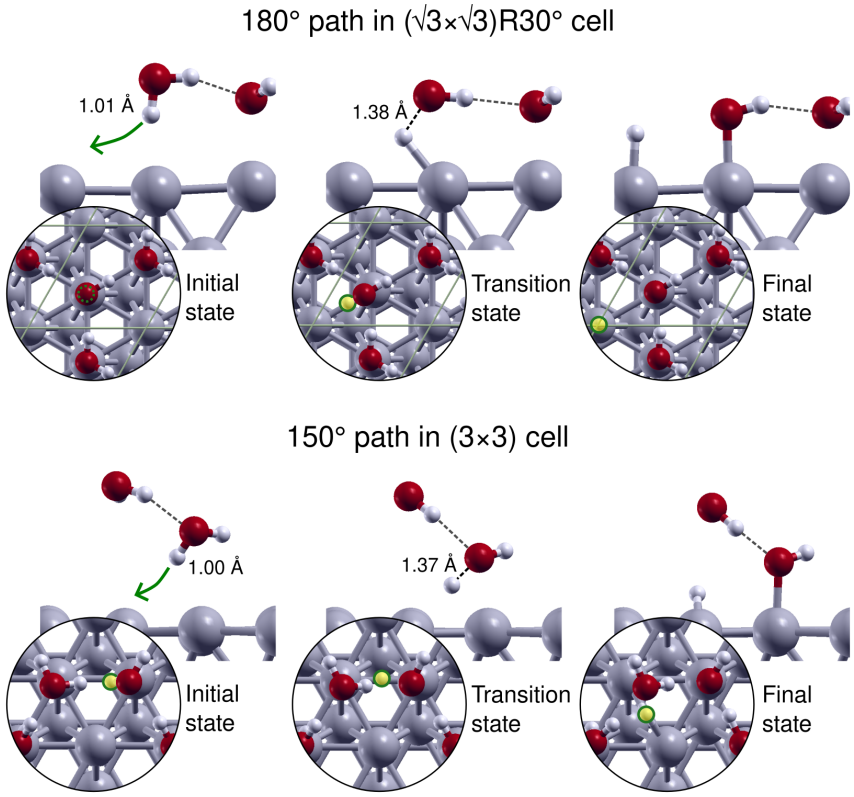


Figure 5.19: Top- and side-view snapshots of the IS, TS, and FS structures for H_2O dissociation within a water bilayer on Ru-hcp(001), shown for the 180° path in the $(\sqrt{3} \times \sqrt{3})$R30° supercell (top) and for the 150° path in the (3×3) supercell (bottom). In the side-view IS, the direction of the dissociating H atom is marked with a green arrow, whereas in the top-view snapshots it is highlighted in green–yellow.

Despite this substantial difference in reaction energies, the activation energies are similar for the two surfaces, with the 60° trajectory showing about 0.1 eV lower values. For this preferred trajectory, Ru-hcp(001) has a slightly lower activation energy than Ru-fcc(111), by an average of 0.03 eV for slabs at least five layers thick.

For the (3×3) supercell (Table 5.6), only the initial state is the same for both considered pathways, but the final states differ. As seen from the table, the reaction energies vary significantly between the two pathways with the 90° path being considerably more exothermic than the 150° path on both Ru surfaces. In the 90° case, a spontaneous proton transfer from a neighboring water molecule to the dissociating one is observed during the reaction, as seen in Figures C.2 in the Appendix. This proton transfer increases the distance between OH* and H* and stabilizes the final state. The difference in reaction energies between the two Ru surfaces is similar for both paths, around 0.1 eV, with Ru-hcp(001) exhibiting more exothermic values. This difference is smaller than the one observed in the $(\sqrt{3} \times \sqrt{3})$R30° supercell, which can be attributed to the fact that in the final state, only OH* is adsorbed on the top site — a site that exhibits significant differences in adsorption energy between the two surfaces. The H* atom occupies a bridge-like site, which exhibits a similar adsorption energy on both surfaces.

In contrast to the reaction energies, no large differences are observed between the activation energies on Ru-hcp(001) and Ru-fcc(111) for the (3×3) supercell. The two reaction paths also yield similar activation energies, with the 90° path displaying marginally smaller values. For this slightly preferred path, Ru-hcp(001) has a slightly lower activation

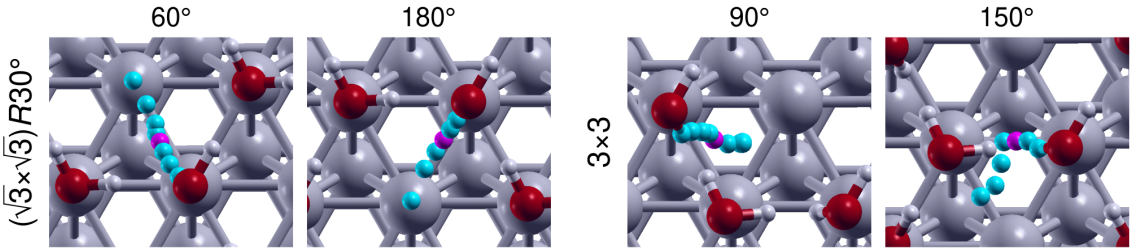


Figure 5.20: Movement of the dissociating hydrogen atom during the reaction in the $(\sqrt{3}\times\sqrt{3})$R30° and (3×3) supercells for all investigated paths. The moving hydrogen atom is shown in blue, and its position in the transition state is highlighted in purple. The depicted structures correspond to the initial states of the pathways.

energy than Ru-fcc(111), by an average of 0.02 eV for slabs at least five layers thick.

A detailed visualization of hydrogen movement for all pathways is shown in Figure 5.20. Since the motion is similar on both investigated surfaces, only the paths on Ru-hcp(001) are illustrated. In all cases, the hydrogen atom passes through a bridge-like transition state. For the 150° path, a pronounced curvature of the trajectory is observed, with H moving toward a more angular, 120°-like transition state. Based on the investigated paths and their respective activation energies, we can conclude that the water molecule prefers to dissociate along a more angular trajectory. This was already shown by Zheng et al. [68], although the angular path was rejected due to the absence of an imaginary frequency for the proposed transition state. For our calculations, vibrational analysis reveals one imaginary frequency for the identified transition states, confirming them as viable options.

5.2.2.3 Activation and reaction Gibbs energies

The results and analysis presented above are based on activation and reaction energies calculated at 0 K without ZPE. However, for evaluating reaction kinetics and thermodynamics, the relevant quantities are the activation and reaction Gibbs energies calculated under experimental conditions. We therefore calculated the vibrational contributions to IS, TS, and FS for each path and determined contributions to their Gibbs energy according to Section 3.2.2. Because vibrational calculations are computationally demanding, they were evaluated for the $(\sqrt{3}\times\sqrt{3})$R30° supercell with slab thicknesses of 3, 4, and 5 atomic layers by diagonalizing the full interatomic force-constants matrix. For the (3×3) supercell, only the 90° pathway was analyzed for the five layered slab by calculating and diagonalizing only the water bilayer part of the interatomic force-constants matrix. For thicker slabs, we used the vibrational contributions to the Gibbs energy derived from the five-layer slabs.

All transition states display a single imaginary frequency of approximately 1000i cm^{-1}, confirming all investigated pathways as valid options. The resulting activation and reaction Gibbs energies calculated at 25 °C, along with the vibrational contributions, are listed in Table 5.7 for the $(\sqrt{3}\times\sqrt{3})$R30° supercell and in Table 5.8 for the (3×3) supercell. Both energies and Gibbs energies are also graphically presented in Figure 5.21 for easier comparison. Note that for $(\sqrt{3}\times\sqrt{3})$R30° both the 60° and 180° reaction paths start from the same initial state and end in the same final state, differing only in the H trajectory during the O–H bond cleavage. Consequently, the two trajectories have identical reaction Gibbs energies but different activation Gibbs energies.

For the $(\sqrt{3}\times\sqrt{3})$R30° supercell, the vibrational contributions (ΔG_{corr}) to the reaction Gibbs energies are small in magnitude, ranging from −0.04 to +0.03 eV, which indicates that they largely cancel between the final and initial states. In contrast, for the (3×3)

Table 5.7: Reaction and activation Gibbs energies calculated at 25 °C for the $(\sqrt{3} \times \sqrt{3})$R30° supercell with the ice-like water bilayer model. The G^{act} values are reported for the 60° and 180° pathways, while the ΔG values are identical for both pathways. The G_{corr} corrections for vibrational degrees of freedom are also given.

	ΔG (eV)		ΔG_{corr} (eV)		G^{act} (eV)		G^{act}_{corr} (eV)	
layers	hcp(001)	fcc(111)	hcp(001)	fcc(111)	hcp(001)	fcc(111)	hcp(001)	fcc(111)
					60° pathway			
3	−0.59	−0.17	0.004	−0.040	0.32	0.40	−0.112	−0.116
4	−0.59	−0.47	0.017	+0.007	0.30	0.32	−0.100	−0.109
5	−0.58	−0.32	0.025	−0.017	0.33	0.37	−0.106	−0.112
6[a]	−0.56	−0.36	/	/	0.35	0.36	/	/
7[a]	−0.56	−0.38	/	/	0.32	0.35	/	/
					180° pathway			
3					0.44	0.50	−0.135	−0.131
4					0.42	0.44	−0.119	−0.125
5					0.44	0.49	−0.123	−0.122
6[a]					0.46	0.46	/	/
7[a]					0.44	0.46	/	/

[a]The ΔG and G^{act} values were obtained by combining the corresponding ΔE and E^{act} values with the G_{corr} corrections from the five-layer slab.

Table 5.8: Reaction and activation Gibbs energies calculated at 25 °C for the (3×3) supercell with the ice-like water bilayer model. The ΔG_{corr} and G^{act}_{corr} corrections were approximated by calculating and diagonalizing only the water-bilayer part of the interatomic force-constants matrix.

	90° pathway							
	ΔG (eV)		ΔG_{corr} (eV)		G^{act} (eV)		G^{act}_{corr} (eV)	
N	hcp(001)	fcc(111)	hcp(001)	fcc(111)	hcp(001)	fcc(111)	hcp(001)	fcc(111)
5	−0.83	−0.65	−0.096	−0.099	0.35	0.39	−0.181	−0.185
6[a]	−0.80	−0.70	/	/	0.34	0.35	/	/
7[a]	−0.83	−0.69	/	/	0.33	0.36	/	/

[a] The ΔG and G^{act} values were obtained by combining the ΔE and E^{act} values with the corresponding G_{corr} corrections from the five-layer slab.

supercell, the ΔG_{corr} values are about −0.1 eV for both Ru-fcc(111) and Ru-hcp(001). Comparing these corrections between Ru-fcc(111) and Ru-hcp(001), we realize that their differences are small compared with the reaction energy differences. Thus, the reaction Gibbs energies follow the same trend as the reaction energies.

For the activation energies, a different pattern is observed. Contributions from vibrations to the Gibbs energy are always negative, and their values are around −0.1 eV for the $(\sqrt{3} \times \sqrt{3})$R30° on both surfaces and about −0.2 eV for (3×3) on both surfaces. These contributions lower all energy barriers for water dissociation but do not alter the overall energy trends. Consequently, Ru-hcp(001) exhibits slightly lower activation Gibbs energies compared to Ru-fcc(111). This trend is not affected by the slab thickness, as all thicknesses consistently reveal it. More specifically, for the $(\sqrt{3} \times \sqrt{3})$R30° supercell, the activation Gibbs energies for the preferred 60° path are 0.33 and 0.36 eV for Ru-hcp(001) and Ru-fcc(111), respectively, calculated as the average over the five- to seven-layer slabs. The corresponding values for the 180° path are 0.44 and 0.47 eV. For the (3×3) super-

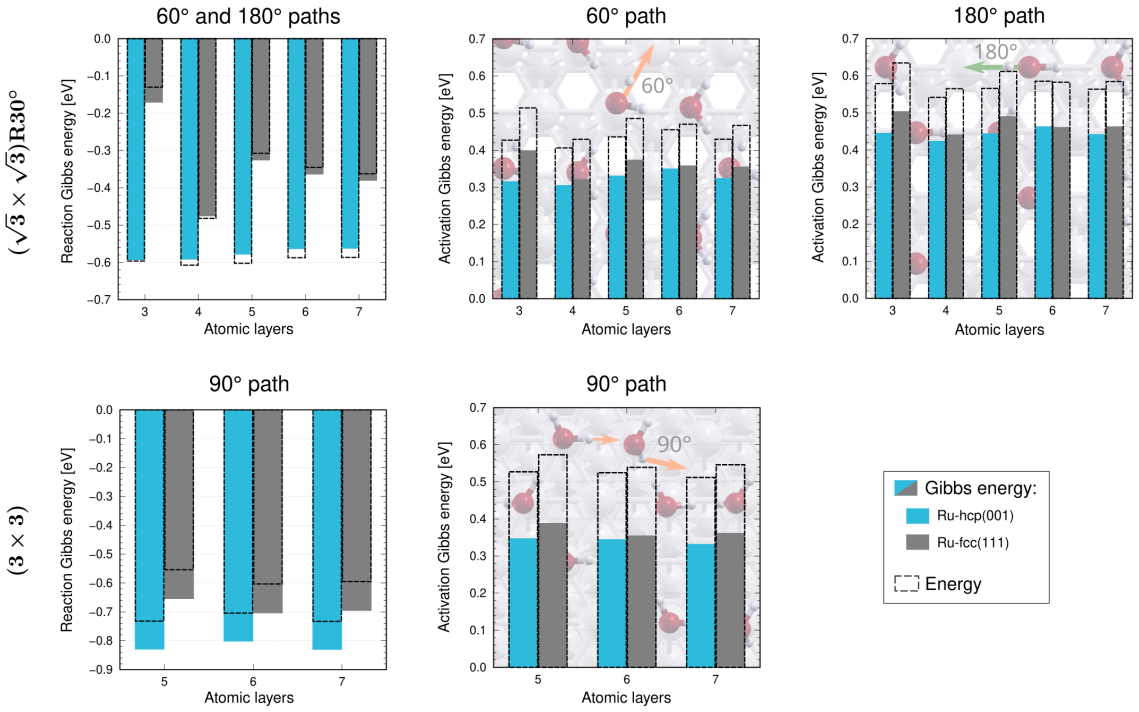


Figure 5.21: The $(\sqrt{3}\times\sqrt{3})$R30° (first row) and (3×3) (second row) reaction and activation Gibbs energies for H_2O dissociation, calculated at 25 °C using the water bilayer model. Results for Ru-hcp(001) are shown in blue and for Ru-fcc(111) in gray. Gibbs energies are represented by solid colored bars, while the corresponding energies are indicated by black dashed bars. Note that for the $(\sqrt{3}\times\sqrt{3})$R30° supercell, the reaction Gibbs energies are identical for the 60° and 180° paths.

cell, the values for the 90° path are 0.34 and 0.37 eV for Ru-hcp(001) and Ru-fcc(111), respectively.

The presented results contrast with the high-impact study of Zheng et al. [68], who attributed the experimentally observed higher activity of the Ru-fcc phase to a DFT-calculated higher intrinsic activity of Ru-fcc(111) compared to Ru-hcp(001). They used three-layer Ru slabs along with the bilayer model of water and the $(\sqrt{3}\times\sqrt{3})$R30° supercell. Their reaction Gibbs energies of −0.59 and −0.24 eV for Ru-hcp(001) and Ru-fcc(111), respectively,[5] follow a similar trend to ours — namely, that the water dissociation reaction is significantly more exergonic on Ru-hcp(001). However, their reported activation Gibbs energies of 0.51 and 0.41 eV for the 180° path on Ru-hcp(001) and Ru-fcc(111), respectively, are in stark contrast to our results. While their calculations suggest that Ru-fcc(111) is considerably more active than Ru-hcp(001), our results indicate that Ru-hcp(001) is in fact slightly more active.

The difference mainly originates from the treatment of the vibrational contribution to the Gibbs energy. Zheng et al. [68] reported vibrational contributions to the activation Gibbs energy of +0.03 eV for Ru-hcp(001) and −0.10 eV for Ru-fcc(111), whereas our $(\sqrt{3}\times\sqrt{3})$R30° value is approximately −0.10 eV for both surfaces. This discrepancy arises from two sources: (a) the incomplete treatment of vibrational contributions in their work, and

[5]Zheng et al. [68] reported only the Gibbs energies for the Volmer step, $\Delta G_{\text{Volmer}} = -0.84$ for Ru-hcp(001) and −0.48 eV for Ru-fcc(111). They are calculated form ΔG for water dissociation with added correction obtained from the thermodynamic cycle. Their final equation to obtain Volmer Gibbs energies is: $\Delta G_{\text{Volmer}} = \Delta G - 0.24$ eV for both Ru-hcp(001) and Ru-fcc(111).

(b) their use of too-thin slabs, which lead to unconverged results as demonstrated above. Specifically, their incomplete treatment of vibrational contributions has three shortcomings:

1. Only the zero-point energy (ZPE) was considered, while thermal contributions to the vibrational Gibbs energy were neglected. In particular, Zheng et al. used $E_{\mathrm{vib}}(T) = \frac{1}{2}\sum_i h\nu_i \equiv \mathrm{ZPE}$, whereas the correct harmonic-oscillator expression is:

$$E_{\mathrm{vib}}(T) = \sum_i h\nu_i \left(\frac{1}{2} + \frac{1}{\exp(\frac{h\nu_i}{k_{\mathrm{B}}T}) - 1} \right). \tag{5.8}$$

   It is worth emphasizing that for low-frequency modes the thermal term becomes larger than the ZPE term (for example, for $h\nu = k_{\mathrm{B}}T/2$, the second term is about 1.5, i.e., three times larger than the first term).

2. In the harmonic-oscillator model, vibrational entropy diverges as the frequency approaches zero. Without correcting for this effect, low-frequency modes contribute excessively to the vibrational Gibbs energy, potentially leading to nonphysical results. Zheng et al. applied no correction for the low-frequency modes, whereas we used the Cramer–Truhlar correction [89].

3. Zheng et al. [68] diagonalized only the adsorbate part of the interatomic force-constants matrix, whereas, for the smaller cell, we calculated and diagonalized the full matrix.

For the results reported by Zhang et al., using the full vibrational thermal energy and the Cramer–Truhlar correction for the low-frequency modes would yield activation Gibbs energies of 0.39 and 0.37 eV for Ru-hcp(001) and Ru-fcc(111), respectively, instead of their originally reported values of 0.51 and 0.41 eV. The reported shortcomings of the DFT study by Zheng et al. together with our results indicate that the ideal Ru-fcc(111) surface is not intrinsically more active than Ru-hcp(001). If anything, the presented findings suggest that Ru-hcp(001) may be slightly more active.

5.2.2.4 Activity of low-index surfaces

Since the higher activity of fcc-structured nanoparticles cannot be explained by the activity of close-packed Ru-fcc(111) and Ru-hcp(001), we also investigated other facets that are present on nanoparticles. As nanoparticles expose a variety of facets, their overall catalytic performance may be significantly influenced by the less stable ones. To reveal the activity trends of other facets present on the nanoparticles, we examined the adsorption of H* and OH*, as well as the dissociation of a single water molecule on low-index surface terminations. In addition to the already presented Ru-hcp(001) and Ru-fcc(111) surfaces, we investigated Ru-hcp(100) and Ru-hcp(011) for the hcp phase, and Ru-fcc(100) and Ru-fcc(011) for the fcc phase (structures are shown in Figure 3.8 in Section 3.5). Unlike the close-packed surfaces, the other terminations are not directly comparable between the two phases. For each of these surface terminations, slabs with dimensions similar to the 6-layered (3×3) slabs of Ru-hcp(001) and Ru-fcc(111) were constructed.

The binding energies of H*, OH*, and H_2O* at their most stable adsorption sites are presented in Figure 5.22a. H* preferentially adsorbs at the hollow site on all investigated Ru-hcp surfaces and Ru-fcc(111), while on Ru-fcc(100) and Ru-fcc(011) it favors the bridge site. The OH* fragment also predominantly binds at hollow sites, except on Ru-hcp(100) and Ru-fcc(011), where it prefers the bridge position. Water molecule adsorbs on a top site or close to a top site on all surfaces. All adsorption geometries are shown in Figure C.3 in

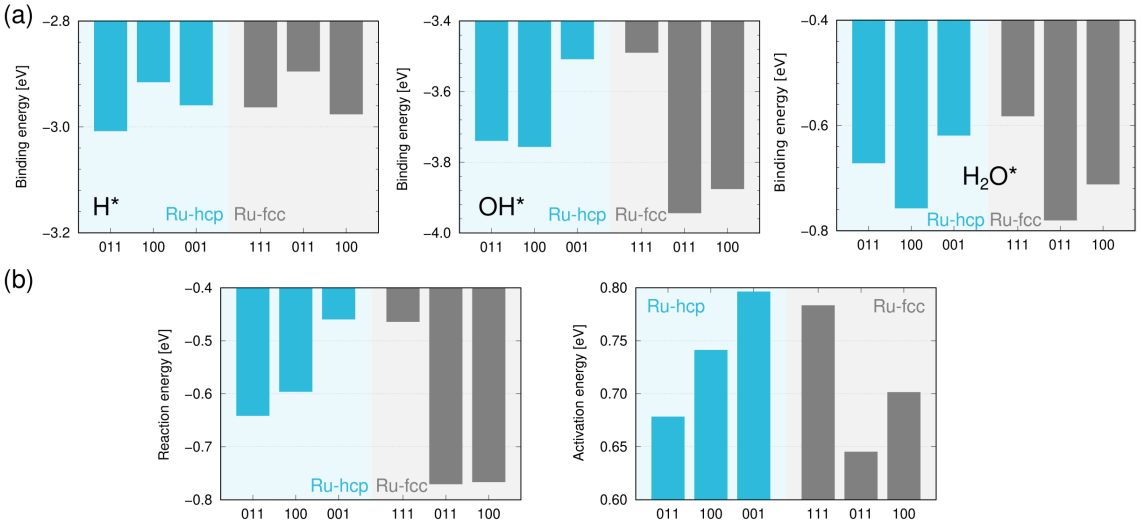


Figure 5.22: (a) Binding energies of H*, OH*, and H_2O*; (b) reaction and activation energies for the dissociation of a single water molecule on low Miller-index Ru-hcp and Ru-fcc surfaces. Blue bars correspond to the hcp crystal phase, while gray bars represent the fcc phase.

the Appendix. The binding energies of H* exhibit minimal variations, with no significant difference between the hcp and fcc crystal phases. A similar behavior is observed for a water molecule. In contrast, OH* exhibits stronger binding on fcc surfaces, except on the close-packed Ru-fcc(111), where the binding energy is comparable to that on the analogous Ru-hcp(001) surface.

The reaction and activation energies are graphically presented in Figure 5.22b, and the corresponding reaction pathways are provided in Figure C.4 the Appendix. In contrast to the ice-like water bilayer model, the reaction energies on the Ru-hcp(001) and Ru-fcc(111) surfaces are similar. This can be attributed to the structure of the final state, in which both H* and OH* are adsorbed at hollow sites. As seen from Table 5.4, the hollow sites give comparable binding energies between the surfaces. The activation energies are also similar between the two surfaces. For other low-index surfaces, the reaction and activation energies vary. In general, Ru-fcc surfaces exhibit more exothermic reaction energies and lower activation barriers compared to the investigated Ru-hcp terminations. The lowest activation energies within each crystal phase are observed on the Ru-hcp(011) and Ru-fcc(011) surfaces, with values of 0.68 eV and 0.64 eV, respectively.

The values of reaction energy for water dissociation is governed by three primary factors: (i) the binding energy of the water molecule, (ii) the binding energy of H*, and (iii) the binding energy of OH*. For the Ru surfaces studied here, the largest discrepancies in the binding energies are observed for the OH* and as a result, its binding energies are the dominant contributors to the observed differences in reaction energies. Given that OH* is the product of water dissociation, its stronger adsorption to the surface leads to a more exothermic reaction energy. Additionally, lower reaction energies for water dissociation on Ru surfaces tend to result in lower activation energies. However, this relation is less pronounced, as the variations in activation energies are smaller than that in reaction energies. This observation aligns with the well-established BEP relation. However, the correlation is weaker due to structural differences among the surface terminations and their active sites.

5.2.2.5 Wulff construction

To extend the findings obtained for ideal surfaces to catalysts composed of nanoparticles, we performed a thermodynamic Wulff construction using the investigated low-index facets. Based on Wulff constructions employing surface energies for a broader range of surface terminations, as reported by Li et al. [63] and Zhao et al. [64], the three facets considered in this study account for more than 60% of the total surface area of the Wulff-constructed polyhedron for both crystal phases. Moreover, for nanoparticles up to 6 nm in diameter, these facets cover the majority of the surface.

A comparison of our calculated surface energies with those reported by Zhao et al. [64] and Li et al. [63] is presented in Table 5.2 in Section 5.2.2 on p. 59. Our surface energies for the hcp crystal phase agree well with both literature sources, whereas our values for the fcc phase show the largest difference with those reported by Zhao et al. Based on this comparison, we constructed Wulff polyhedra and five representative atomistic nanoparticle models with diameters between 2 and 6 nm, using both our calculated surface energies (named as this work) and those from Zhao et al. The constructed structures are shown in Figure 5.23. The surface fractions of each facet obtained from the Wulff polyhedra, which presents a thermodynamic limit, along with the corresponding activation energies for water dissociation calculated on ideal surfaces (discussed in the previous section), are given in Table 5.9. For the fcc phase, the Wulff-constructed structures differ between the two datasets; the surface energies from this work result in nanoparticles dominated by the (111) facet, whereas the surface energies by Zhao favor greater exposure of (100) and (011) facets. In contrast, the hcp crystal phase gives very similar results between the two datasets, with the (011) facet covering the largest portion of the surface. This facet is also the most catalytically active. However, for the fcc particles, the dominant (111) facet is the least active among the considered surfaces.

To compare the catalytic activity of the constructed nanoparticles, an effective activa-

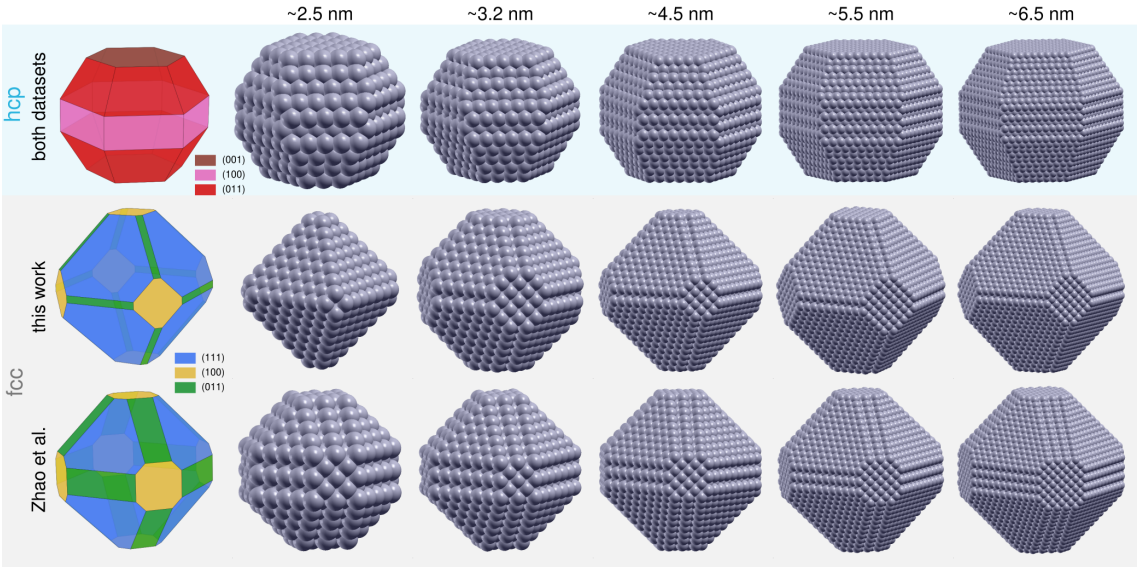


Figure 5.23: Wulff polyhedrons and the corresponding atomistic structures for the hcp and fcc crystal phases, constructed using our calculated surface energies (named this work) and those reported by Zhao et al. [64] (see Table 5.2). For the hcp crystal phase, only one set of structures is shown as both sets of surface energies yield identical particles within the investigated size range. For the atomistic particles, an approximate diameter is also given.

Table 5.9: Thermodynamic surface fractions of different facets obtained from Wulff-constructed polyhedron. The corresponding activation barriers for water dissociation, as presented in Figure 5.22 are also included.

fcc	x_i – this work	x_i – Zhao	E_i^{act} (eV)	hcp	x_i – this work	x_i – Zhao	E_i^{act} (eV)
(111)	0.77	0.49	0.78	(001)	0.20	0.19	0.80
(100)	0.13	0.16	0.70	(100)	0.24	0.23	0.74
(011)	0.10	0.34	0.64	(011)	0.56	0.58	0.68

tion energy was calculated for each structure. The overall reaction rate on a nanoparticle can be expressed as the sum of the individual rates over all facets:

$$r = \sum_{i}^{\text{facets}} r_i = \sum_{i}^{\text{facets}} \left[C_i A_i y_i \exp\left(-\frac{E_i^{\mathrm{act}}}{k_{\mathrm{B}} T} \right) \right] \tag{5.9}$$

where r_i is the reaction rate on facet i, which can be expressed in terms of activation energy E_i^{act} and the number of active sites $A_i y_i$, with A_i representing the surface area of the facet and y_i the number of active sites per area. C_i is the pre-exponetial factor in Arrhenius equation, k_{B} is the Boltzmann constant, and T is the temperature. The overall reaction rate on the nanoparticle can also be described using an effective activation barrier:

$$r = C_{\mathrm{eff}} A \overline{y} \exp\left(-\frac{E_{\mathrm{eff}}^{\mathrm{act}}}{k_{\mathrm{B}} T} \right) \tag{5.10}$$

where A is the total surface area of the nanoparticle and $\overline{y}$ is the average number of active sites per unit area. Assuming that the pre-exponential factors and the number of active sites per area are similar across different facets, the effective activation energy can be written as:

$$E_{\mathrm{eff}}^{\mathrm{act}} = -k_{\mathrm{B}} T \ln \sum_{i}^{\text{facets}} x_i \exp(-\frac{E_i^{\mathrm{act}}}{k_{\mathrm{B}} T}) \tag{5.11}$$

To calculate the fraction of the surface area of each facet ($x_i = A_i/A$), we tested two approaches. The first approach is geometric, in which edges and kinks are used to define the boundaries between surface facets. The surface area of each facet is then determined by calculating the area of the resulting polygonal regions. The second approach is based on the coordination numbers of surface atoms: for each surface atom, its coordination number is compared with the values corresponding to the low-index facets (see Table 5.2). The atom is then assigned to the facet whose coordination number most closely matches its own. The fraction of the surface area is then calculated with respect to the number of surface atoms ($x_i = N_i/N$). This method is only applicable when all investigated facets have distinct coordination numbers. In our case, this is true for the fcc facets; therefore, we compared the two methods on fcc nanoparticles. With the coordination number approach, the fraction of the (011) facet, which has the lowest coordination number (7), is considerably higher than with the geometric approach, because all kink and edge atoms are attributed to this facet. As a consequence, the calculated effective activation barriers are lower by approximately 0.01 eV. Since the coordination number based method cannot be applied to hcp nanoparticles, all subsequent analyses were performed with geometrically determined surface areas. The resulting fractions of surface areas for all considered atomistic nanoparticles are given in Table 5.10. The surface fractions of all hcp particles

Table 5.10: Characteristics of Wulff-constructed nanoparticles for the fcc and hcp phases, based on the currently calculated surface energies and those reported by Zhao et al. For each particle, the surface fractions (x_i) and the corresponding effective barriers (see Eq. (5.11)) are provided. For the hcp phase, only one set of values is shown, as the particles constructed from both sets of surface energies are identical. The TD limit denotes the ideal Wulff-constructed polyhedrons.

N	d (nm)	$x_{(111)}$	$x_{(100)}$	$x_{(011)}$	$E_{\text{eff}}^{\text{act}}$ (eV)
hcp – based on surface energies of this work and of Zhao et al.					
588	2.5	0.19	0.18	0.62	0.69
978	3.1	0.19	0.15	0.66	0.69
2430	4.2	0.20	0.22	0.58	0.69
4872	5.4	0.21	0.25	0.54	0.69
8076	6.4	0.18	0.22	0.60	0.69
TD limit		0.19	0.23	0.58	0.69
fcc – this work					
483	2.7	0.97	0.03	0.00	0.77
1229	3.3	0.63	0.22	0.15	0.69
2993	4.7	0.75	0.12	0.14	0.69
5527	5.7	0.73	0.18	0.09	0.70
7441	6.4	0.77	0.14	0.09	0.70
TD limit		0.77	0.13	0.10	0.70
fcc – based on surface energies of Zhao et al.					
579	2.5	0.29	0.25	0.47	0.66
1085	3.2	0.40	0.16	0.44	0.66
2675	4.4	0.54	0.16	0.29	0.67
5287	5.6	0.59	0.17	0.23	0.68
8457	6.5	0.51	0.21	0.28	0.68
TD limit		0.49	0.16	0.34	0.67

are similar to the ideal values, whereas fcc particles with diameters below 4 nm exhibit deviations from the ideal distributions.

Effective activation energies were calculated for all atomistically constructed nanoparticles as well as for the the ideal Wulff polyhedra. The results are also given in Table 5.10. The hcp particles yield a consistent effective activation energy of 0.69 eV, independent of nanoparticle size. In contrast, the values for fcc particles vary, with smaller particles exhibiting different barriers compared to larger ones. This variation arises because, in smaller particles, the total number of atoms significantly affects the obtained geometry of the particle and consequently the surface fraction of each facet. Comparing the effective barriers of larger fcc nanoparticles, the results based on the surface energies from this work give a higher effective activation energy (0.70 eV) compared to the results based on the surface energies by Zhao (0.67 eV). This difference is due to the larger surface fraction of the (011) facet predicted by the surface energies by Zhao, which is the most active and has the greatest influence on the effective barrier. Specifically, increasing the (011) facet area fraction from 0.10 (as obtained with the surface energies from this work) to 0.34 (as obtained from the surface energies by Zhao) reduces the effective activation barrier from 0.70 eV to 0.67 eV. This corresponds to an increase in reaction rate by a factor of three at room temperature.

As observed from the results, the activity of hcp nanoparticles is relatively insensitive to

details. For all hcp particles, the most active (011) facet covers the largest surface area, and the effective activation energies of the constructed particles are only 0.01 eV higher than the barrier on the ideal (011) surface. This suggests limited potential for enhancing catalytic activity by tuning the shape of hcp nanoparticles. The fcc particles constructed from the surface energies based on this work exhibit slightly higher effective activation barriers compered to the hcp ones. However, increasing the surface fraction of the most active (011) facet can improve their overall activity, as demonstrated by comparing the results based on our surface energies with those obtained using the surface energies by Zhao. The limit of the effective barrier for the fcc particles is 0.64 eV, which is the barrier on the Ru-fcc(011) ideal surface. These findings imply that synthesizing Ru-fcc nanoparticles with a higher proportion of the (011) facet could enhance catalytic performance toward HER in alkaline conditions, where water dissociation is relevant.

An important consideration is also how the morphology of Ru nanoparticles is affected under experimental conditions. According to the surface Pourbaix diagram for Ru (see Figure 5.14), during HER, the surface is covered with hydrogen atoms, which may affect the morphology of the nanoparticle. For the fcc nanoparticles, it was observed that with increasing coverage, the fraction of the fcc(011) facet increases [137]. According to our results, this enhances the activity of nanoparticles toward water dissociation. We did not find a similar study of morphology changes for hcp Ru nanoparticles. However, based on CO adsorption studies on nanoparticles of both crystal phases by Zhao et al. [64], it is likely that hcp particles are also affected by the increased H coverage. As previously noted, the shape of Ru-hcp particles is already dominated by the most active (011) facet, so any morphological change would either decrease or marginally increase the activity. On the other hand, if the shape of the fcc particles evolves in favor of the (011) facet, their activity is expected to surpass that of the hcp particles.

According to the presented results, the experimentally observed higher activity of Ru-fcc catalysts compared to their Ru-hcp counterparts [68]–[71] may originate from the nanoparticle morphology. For the fcc crystal phase, lower barriers were observed on the less stable low-index facets. Therefore, with the right morphology, the fcc particles could be more active than the hcp ones, which are less tunable due to the already dominant surface fraction of the most active hcp(011) facet.

Within the present approach to evaluating nanoparticle activity, the contributions of edge and kink sites to the overall catalytic activity are not explicitly considered. While edge sites have been identified as the primary active sites for the HER on platinum nanoparticles in acidic environments [138], [139], their role under alkaline conditions is less straightforward. In alkaline media, the water dissociation reaction presents an additional step, and edge sites are hypothesized to be occupied by competing adsorbates [138] or to exhibit a lower coverage of active H atoms [139]. Additionally, studies on ruthenium catalysts in alkaline media have shown that highly crystalline nanoparticles with preferential exposure of the (001) facet exhibit higher activity than small, polycrystalline aggregates with low crystallinity [140]. These observations highlight the non-negligible contribution of facet sites to HER activity under alkaline conditions. A more comprehensive assessment of nanoparticle activity would require explicitly accounting for edge and kink sites and evaluating the contribution of higher-index facets that become increasingly prevalent in larger particles.

5.3 Models of Supported Nanoparticles

Studies of supported metal nanoparticles were conducted in collaboration with the Laboratory of Electrocatalysis at the National Institute of Chemistry. Our research led to two publications: Smiljanić et al. [40] for Pt catalysts and Smiljanić et al. [41] for Ru catalysts.

Both are published under a Creative Commons license. The content of this subsection is based on the DFT analysis presented in the two articles.

In practical applications, platinum and ruthenium metal catalysts are commonly used in the form of supported nanoparticles. To enable a more direct comparison between experimental results and DFT calculations, we employed idealized models of supported nanoparticles for both platinum and ruthenium on graphene and $Ti_{1.5}ON$ supports. Graphene was chosen to represent a conventional carbon-based support, while $Ti_{1.5}ON$ served as a model of titanium oxynitride (TiON), which has been observed to be a promising support material for various metal catalysts [40], [41], [58].

5.3.1 Platinum

In order to achieve a reasonable compromise between accuracy and computational efficiency, we performed calculations with two Pt nanoparticles: Pt_{38} and Pt_{55}. They have a diameter of 1.1 and 1.3 nm, respectively. The symmetry of the nanoparticles was chosen to reflect experimental observations [40], and their placement on the TiON support was determined to preserve the fcc stacking sequence of the Ti layers. On graphene, different lateral positions of nanoparticles were tested, and the most stable identified configuration was used for further analysis. Snapshots of the nanoparticle models and their placement on supports are shown in Figure 5.24. On these models, varying numbers of H atoms were adsorbed, ranging from a single H atom to coverages exceeding two H atoms per surface Pt atom.

We calculated the average hydrogen chemisorption energy using Eq. (3.5) and included thermal corrections to energy and entropy via Eq. (3.16) to obtain the average chemisorption Gibbs energy. The vibrational contributions were approximated from analysis on ideal surfaces. The results for both considered nanoparticles on TiON and C supports at 298 K and 1 atm are presented in Figure 5.25. For each H* coverage, multiple adsorption patterns were tested; however, only the energies of the most stable identified structures are shown in the figure. The corresponding adsorption structures are shown in Figures D.1 and D.2 in the Appendix. In general, hydrogen chemisorption Gibbs energy becomes less exergonic with increasing coverage, as hydrogen atoms are forced to occupy less favorable adsorption sites. When comparing the two supports, we observe that Pt/C systems consistently exhibit slightly more exergonic adsorption Gibbs energies across the entire coverage range.

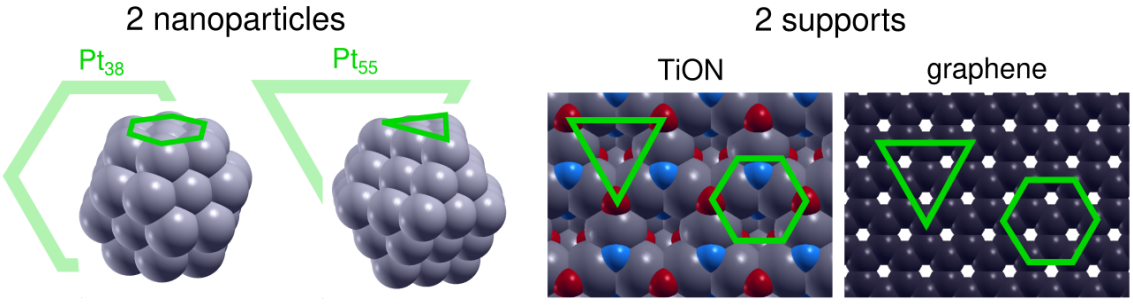


Figure 5.24: Structures of the Pt nanoparticles and supports used for calculations. On the supports, the positions of adhesion are labeled with green triangle (corresponding to Pt_{55} particle) and green hexagon (corresponding to Pt_{38} nanoparticle). On the TiON support, the O atoms at the vertices of the green triangle and hexagon were displaced to accommodate the nanoparticles.

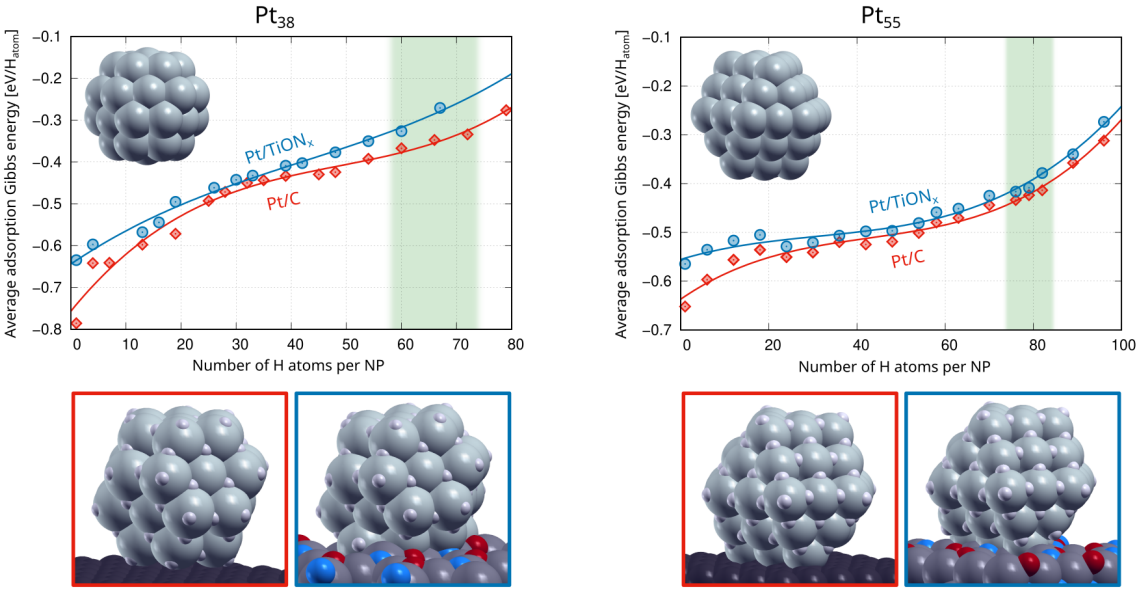


Figure 5.25: Average H adsorption Gibbs energy as a function of the number of H atoms on two Pt nanoparticles supported on TiON and graphene. Vertical green bands indicate H coverages relevant under HER conditions. For each number of adsorbed H atoms, only the adsorption Gibbs energy of the most stable identified structure is reported. Below the graphs, snapshots of the most stable structures at 0 V are shown.

This suggests that H atoms bind slightly more strongly to Pt/C than to Pt/TiON at the equivalent number of H atoms.

To determine which H* coverages are relevant under experimental conditions, we performed a thermodynamic analysis based on the surface adsorption Gibbs energy as a function of electrode potential. The surface adsorption Gibbs energy was calculated per surface Pt atom according to the following equation:

$$\gamma_{\text{ads}} = \frac{n}{N_{\text{Pt}}} \Delta G_{\text{ads}} = \frac{n}{N_{\text{Pt}}} \left(\Delta \overline{G}^{\ominus}_{\text{ads}} + e(U - U_{\text{RHE}}) \right) \tag{5.12}$$

Here, n is the number of adsorbed H atoms and N_{Pt} is the number of surface Pt atoms (32 for the Pt_{38} particle and 42 for Pt_{55}). $\Delta \overline{G}^{\ominus}_{\text{ads}}$ represents the average H adsorption Gibbs energy, shown in Figure 5.25. The eU term accounts for the electode potential (see Eq. (3.24)). Since we are interested in potentials relative to the reversible hydrogen electrode (RHE), the pH-dependent term cancels out.

The resulting lines from Eq. (5.12) for each investigated system are shown in Figure 5.26. Each line represents the most stable identified structure for a specific number of adsorbed hydrogen atoms. The slope of each line differs, as it is determined by the ratio n/N_{Pt}, which depends on the number of adsorbed hydrogen atoms and the size of the nanoparticle. As the number of adsorbed hydrogen atoms increases, the slope becomes steeper, which is evident from the graph. At a given electrode potential, the thermodynamically preferred structure is the one corresponding to the line with the lowest surface adsorption Gibbs energy. If all lines lie above $y = 0$, this indicates that the bare nanoparticle is more stable than any structure with adsorbed hydrogen.

If we examine the results presented in Figure 5.26, we observe a general trend: the number of adsorbed hydrogen atoms increases as the electrode potential decreases. In contrast, at sufficiently positive potentials, the bare surface is more stable than the H-

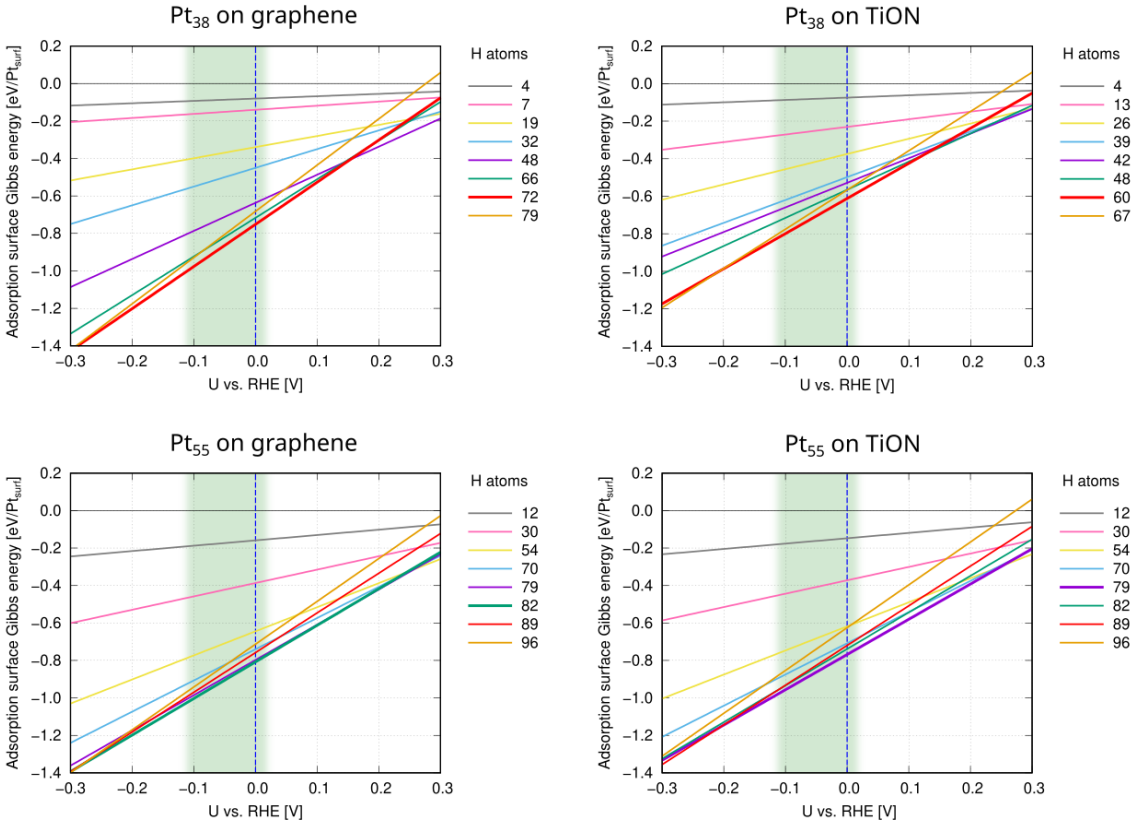


Figure 5.26: Surface adsorption Gibbs energy, as defined by Eq. (5.12), plotted as a function of electrode potential. Green background bands represent the region of electrode potentials experimentally relevant for HER [40]. Each line represents the most stable identified structure with a certain number of H atoms. Only selected coverages are shown due to clarity. Each line corresponds to the most stable identified structure for a given number of hydrogen atoms. To maintain visual clarity, only a selection of lines is shown.

covered ones, as all adsorption lines eventually lie above $y = 0$. In the range of electrode potentials relevant to HER (between -0.1 and 0 V versus RHE [40]), the most stable structures for the Pt_{38} nanoparticle contain 72 and 60 H atoms per nanoparticle for the C and TiON supports, respectively. This difference in coverage arises form the weaker binding of the nanoparticle on graphene, which allows hydrogen atoms to adsorb at the perimeter Pt atoms of the bottomost Pt layer bonded to the graphene support — sites that are energetically unfavorable on the TiON support. Hydrogen chemisorption on the supported Pt_{55} nanoparticle follows a similar adsorption pattern on both supports, yielding similar coverages at experimental conditions: 82 and 79 H atoms per nanoparticle for graphene and TiON, respectively. From Figure 5.26, we can also observe that some lines lie very close to the lowest-lying line at experimental conditions. These correspond to structures with coverages similar to the most stable structure, suggesting that the experimentally relevant coverage may fluctuate, but is generally expected to be around 2 hydrogen atoms per surface Pt atom.

Returning to Figure 5.25, the green bands denote the most stable hydrogen coverages at experimental conditions. Since slightly weaker adsorption is observed on Pt/TiON across the entire range of H coverages, this trend also holds in the experimentally relevant region. In the HER volcano plot [42], platinum lies near the peak, although it slightly overbinds the H atom. According to our results, the Pt/TiON system binds H somewhat

more weakly than Pt/C. Based on the volcano plot argument, this suggests that Pt/TiON should be slightly more active for HER than Pt/C. The small but consistent difference in hydrogen adsorption energies suggests that the support can influence the energetics of reaction intermediates — at least for the structures examined in this study.

In addition to investigating the effect of the support on H adsorption, we also examined the adhesion strength of the two supports. The adhesion energy of the Pt_{55} nanoparticle was calculated according to Eq. (3.10), with respect to the undeformed TiON structure. DFT calculations reveal that Pt nanoparticles adhere significantly more strongly to TiON than to graphene. For Pt_{55}, the adhesion energies are -15.9 eV on TiON and -3.6 eV on graphene; for Pt_{38}, the corresponding values are -14.7 and -2.4 eV, respectively. Additionally, electron charge density differences and the planar integrated electron charge density differences were calculated according to Eq. (3.11) and (3.12), respectively. The results are presented in Figure 5.27. A much more pronounced electron redistribution is observed at the Pt_{55}/TiON interface compared to that with C. There is a strong electron flow from the surface Ti atoms and the bottom region of the Pt nanoparticle toward the interface region. The greater electron charge transfer observed for TiON is consistent with its significantly stronger adhesion energy compared to graphene. Strong adhesion provides two benefits for the catalysts. First, it reduces the likelihood of Pt nanoparticle detachment and coalescence, thereby keeping the particle dispersed and maximizing the platinum surface area during HER. Second, it is known that stronger binding to a support can influence nanoparticle reactivity by weakening the adsorption of small molecules — provided the adsorbates bind primarily through covalent interactions [141].

The presented electron density difference results and adhesion energies correspond to the bare catalyst systems. However, under experimental HER conditions, Pt nanoparticles are covered with hydrogen atoms. Therefore, we also calculated the adhesion energies of the Pt_{55} nanoparticle covered with different numbers of adsorbed H atoms. They were calculated according to Eq. (3.10), using the energy of the relaxed Pt_{55} nanoparticle with the adsorbed H atoms as the energy for the standalone nanoparticle (E_{NP} in the equation). The results are shown in Figure 5.28, alongside the calculated overlap volume between

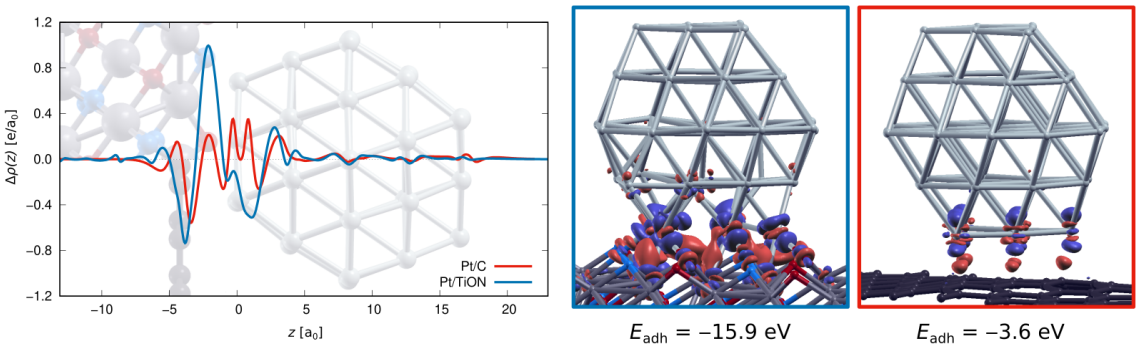


Figure 5.27: Left: planar integrated electron charge density difference, calculated with Eq. (3.12), for Pt/TiON (blue curve) and Pt/C (red curve). Positive $\Delta\rho(z)$ corresponds to an excess in electron density. The x-axis origin ($z = 0$) is arbitrarily set to the position of the bottom layer of Pt_{55}, as shown in the background images where the nanoparticle and support structures are visualized to aid interpretation. Right: Corresponding 3D electron charge density difference plots, calculated with Eq. (3.11). Isosurfaces are drawn at ± 0.01 e/a_0^3, with blue and red regions representing electron depletion and accumulation, respectively. Adhesion energies are reported below the structures.

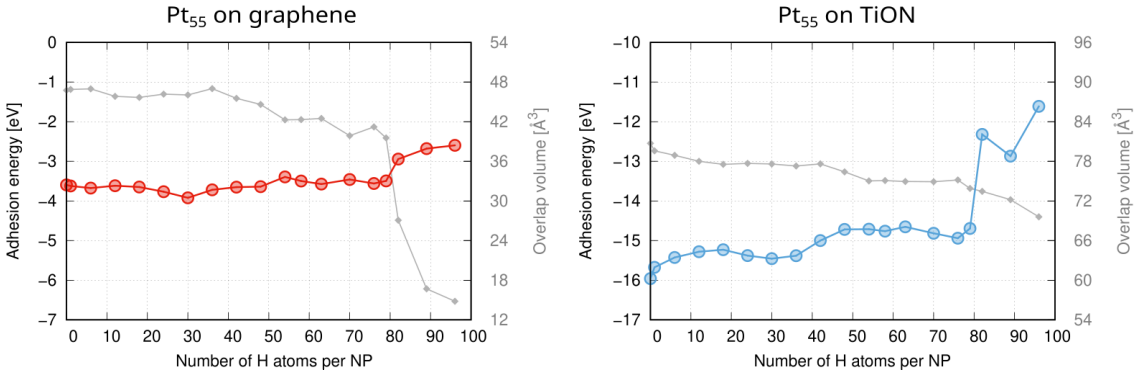


Figure 5.28: Dependence of adhesion energy on the number of adsorbed H atoms on the supported Pt_{55} nanoparticle. Red and blue data points correspond to the graphene and TiON supports, respectively. Gray data on both graphs represent the overlap volume at the nanoparticle–support interface, which is displayed on the secondary axis.

the atoms of the adhered nanoparticle and the atoms comprising the support structure.[6] For the graphene-supported system, we observe minimal changes in adhesion energy for coverages up to 80 adsorbed H atoms. Beyond this point, a sharp increase of approximately 0.5 eV is observed. A similar trend is seen for the overlap volume: it decreases gradually up to 80 atoms, followed by a distinct drop, indicating that the nanoparticle and the graphene support drift further apart. In the case of TiON, the adhesion energy increases slowly up to 80 adsorbed H atoms, after which a sharp rise of about 2 eV occurs. Unlike the graphene system, no sharp decrease in overlap volume is observed at this point. Both supports exhibit an inflection point in adhesion energy behavior at 80 adsorbed hydrogen atoms. At this coverage, both catalysts begin to adsorb additional H atoms in close proximity to the Pt–support interface, which destabilizes the nanoparticle's adhesion. Even at the highest coverage considered, the Pt_{55}/TiON catalyst maintains significantly stronger adhesion compared to the Pt_{55}/C system, where the nanoparticle is primarily bound to the support through van der Waals interactions.

From the presented results, two effects of the support are observed: (i) its influence on the adsorption of intermediates and (ii) its impact on the nanoparticle adhesion strength. The influence on intermediate binding is relatively small but persistent, and may contribute to tuning reaction energetics and enhancing catalytic activity. In contrast, the effect of the support on nanoparticle adhesion is more pronounced. The graphene support binds Pt nanoparticles considerably more weakly than TiON even at higher H coverages. As a result, the Pt/TiON catalyst is expected to exhibit enhanced stability and durability owing to its stronger adhesion, as well as higher activity than Pt/C resulting from altered hydrogen adsorption.

5.3.2 Ruthenium

Similar as for Pt nanoparticles, analysis of Ru nanoparticles supported on graphene and TiON supports was also preformed. While Ru crystallizes in the hcp phase, supported fcc-structured Ru nanoparticles have also been observed experimentally [62], [68]–[71]. In

[6] The overlap volume was estimated using a Monte Carlo method. Atoms were modeled as van der Waals spheres with the following radii: $r_C = 1.70$ Å, $r_N = 1.60$ Å, $r_O = 1.55$ Å, $r_{Ti} = 2.15$ Å, $r_{Pt} = 2.05$ Å, in accordance with the crystallographic radii recommended by Batasanov [142]. For H atom, a value of 1.20 Å was used as proposed by Bondi [143]. The estimated uncertainty in the calculated overlap volumes is ± 0.5 Å^3, which is sufficiently small to ensure reliable trends.

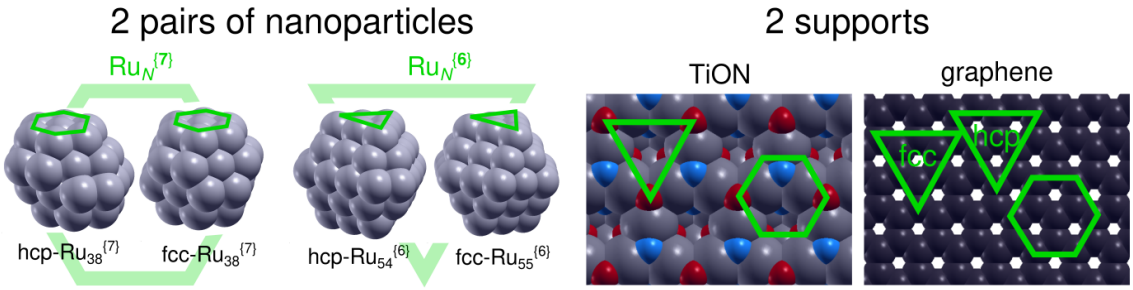


Figure 5.29: Structures of the Ru nanoparticles and supports used for calculations. On the supports, the positions of adhesion are labeled with green triangle (corresponding to $Ru_N^{\{6\}}$ nanoparticles) and green hexagon (corresponding to $Ru_N^{\{7\}}$ nanoparticles). On the TiON support, the O atoms at the vertices of the green triangle and hexagon were displaced to accommodate the nanoparticles.

addition, there are also experimental indications that fcc Ru particles could be present in the catalyst with TiON support [41]. As already presented in Section 5.2.2, the stability of Ru-hcp and Ru-fcc nanoparticles is very similar at least up to particle sizes of about 2 nm. To analyze a potential preference of either graphene or TiON supports for a specific crystal phase, the adhesion energies of similar nanoparticles of both phases were calculated according to Eq. (3.10). Nanoparticles were chosen in pairs, and within each pair, the hcp and fcc nanoparticles are mutually comparable because they have the same two bottom layers, where the bottommost layer adheres to the support. In particular, hcp-$Ru_{38}^{\{7\}}$ vs fcc-$Ru_{38}^{\{7\}}$ and hcp-$Ru_{54}^{\{6\}}$ vs fcc-$Ru_{55}^{\{6\}}$ pairs are considered, where the super-scripted number ($Ru^{\{N\}}$) indicates the number of Ru atoms in the bottommost layer that faces the support. The fcc nanoparticles were adsorbed on TiON in a similar way as the Pt nanoparticles to continue the fcc stacking of layers. The hcp particles were adsorbed with the same orientation of the bottom two layers as the corresponding fcc particles. On graphene, different lateral positions were tested for all four particles and the most stable identified one was used for analysis. The adhesion positions of the selected nanoparticles are shown in Figure 5.29.

The calculated cohesion and adhesion energies of the selected pairs of particles are given in Table 5.11. The adhesion energies were calculated with respect to the undeformed TiON slab.[7] Both pairs of nanoparticles have similar cohesion energies and therefore similar stability. For different supports, we can observe that TiON binds these nanoparticles about four times stronger than graphene, thus immobilizing and stabilizing them. As for the hcp vs fcc adhesion preference, the hcp nanoparticles adhere to graphene by 0.3 eV stronger than the fcc nanoparticles. In contrast, on the TiON support, fcc-$Ru_{38}^{\{7\}}$ binds by 0.6 eV stronger than hcp-$Ru_{38}^{\{7\}}$, but vice-versa is true for the $Ru_n^{\{6\}}$ nanoparticles, where hcp-$Ru_{54}^{\{6\}}$ adheres by 0.3 eV stronger than fcc-$Ru_{55}^{\{6\}}$. The results show a small preference of graphene to bind hcp structure compared to fcc, but adhesion on TiON gives no consistent trend and depends on the nanoparticle's shape. However, the number of cases considered is far insufficient to reach any statistically valid conclusion.

[7] In the article, where the results are published [41], the reported adhesion energies are with respect to a more stable identified TiON structure (∼0.4 eV more stable compared to the undeformed one). It was identified with re-optimization of TiON slab after adsorption of $Ru_N^{\{6\}}$ nanoparticle. In this work, adhesion energies are reported with respect to the undeformed TiON slab to maintain consistency with the Pt analysis. Consequently, the obtained values are about 0.4 eV lower than those reported in the original article.

Table 5.11: The cohesion energies (Eq. (3.9)) and adhesion energies (Eq. (3.10)) of the selected comparable Ru nanoparticles on TiON and graphene supports. The adhesion energies were calculated with respect to the undeformed TiON structure.[7]

nanoparticle	E_{coh} (eV)	E_{adh}@C (eV)	E_{adh}@TiON (eV)
hcp-$\text{Ru}_{38}^{\{7\}}$	−5.03	−4.3	−17.4
fcc-$\text{Ru}_{38}^{\{7\}}$	−5.04	−4.0	−18.0
hcp-$\text{Ru}_{54}^{\{6\}}$	−5.21	−4.1	−16.6
fcc-$\text{Ru}_{55}^{\{6\}}$	−5.18	−3.8	−16.3

Adhesion was further analyzed with electron density difference for $\text{Ru}_N^{\{6\}}$ nanoparticles on both supports. Planar integrated electron density difference along the surface normal direction ($\Delta\rho(z)$; see Eq. (3.12)) and structures with isosurfaces of electron density difference ($\Delta\rho(\mathbf{r})$; see Eq. (3.11)) are shown in Figure 5.30. For both supports, electron deficit is observed in the support and electron surplus in the bonding region between the nanoparticle and the support. However, for TiON support, a much larger electron flow is observed. The bottom layer of Ru and the upper layer of Ti ions donate electrons to the binding region, resulting in notable electron accumulation. A similar pattern was observed for Pt metal, which indicates that TiON support strongly binds different metal nanoparticles and can enhance their durability and catalytic activity [40], [41], [58]. On TiON support, the $\Delta\rho(z)$ curves for fcc-$\text{Ru}_{55}^{\{6\}}$ and hcp-$\text{Ru}_{54}^{\{6\}}$ are almost superimposed and no relevant difference can be observed for the two phases. For the graphene support, the curves are more different, which can be attributed to the different binding site (see

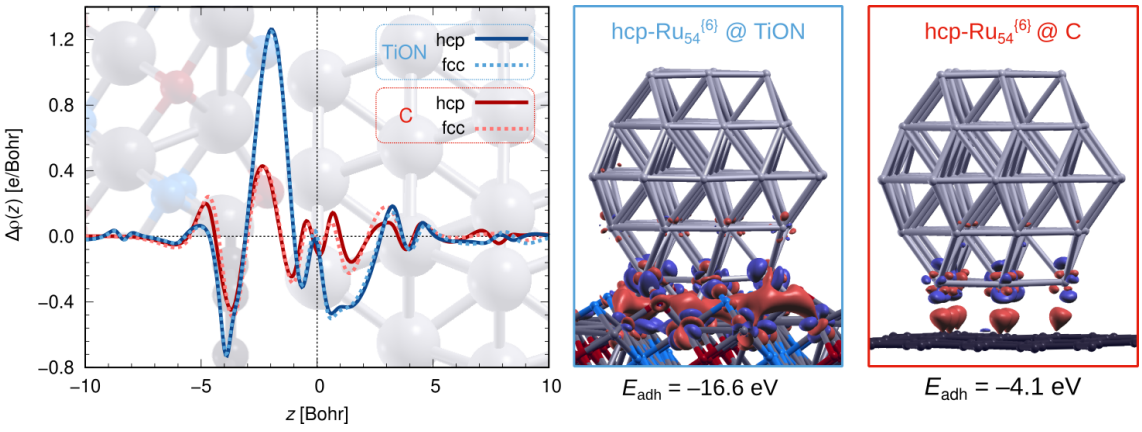


Figure 5.30: Left: planar integrated electron density difference along the z direction for $\text{Ru}_N^{\{6\}}$ pair of nanoparticles on both graphene and TiON supports. $z = 0$ corresponds to the positions of the bottommost Ru layer, as indicated by the atomic structure shown as a watermark behind the $\Delta\rho(z)$ curves. Red and blue colors represents structures with the graphene and the TiON support, respectively. For the hcp structure, a darker shade is used, whereas a lighter shade of color and dotted lines are used for the fcc phase. Right: snapshots of hcp-$\text{Ru}_{54}^{\{6\}}$ nanoparticle on TiON and graphene with electron density difference isosurfaces of ± 0.01 e/a_0^3. Red color represents electron excess and blue is used for electron deficit.

Figure 5.29). This analysis further confirms the observed small difference of adhesion for fcc and hcp nanoparticles. The presented results indicate that the fcc phase can be present on the TiON support, but gives no evidence for its formation.

Since no clear preference for the formation of fcc and hcp structures on C or TiON supports was observed, we analyzed H adsorption only for the thermodynamically stable hcp phase. Similar to the supported Pt nanoparticles, we adsorbed H atoms on the supported Ru nanoparticle, but the analysis was simplified. Only the hcp-$Ru_{54}^{\{6\}}$ particle was analysed and two cases were investigated: (i) low coverage with a single H atom on various adsorption sites, and (ii) high coverage with 76 H atoms adsorbed on the supported nanoparticle.

For the investigation of a single chemisorbed H atom, we constructed 44 and 41 initial adsorption structures for TiON and graphene, respectively. After structural optimization, we obtained 27 distinct relaxed structures on each support, as some converged to the same configuration — snapshots of the optimized structures for both supports are provided in Figures D.3 and D.4 in the Appendix. Chemisorption energies were calculated according to Eq. (3.4) and the results are shown in Figure 5.31. The range of chemisorption values is quite wide for both supports (they span from −0.2 eV to −0.8 eV) without any clear or consistent trend. The only apparent difference is in the adsorption at the bottom layer, where the hcp-$Ru_{54}^{\{6\}}$/TiON system gives only one super stable site for chemisorption of H. In contrast, graphene support do not influence the binding of H in the bottom layer significantly, because more sites are stable and the corresponding binding energies are more similar to other sites.

Since the results for low coverage case give limited insight, we also performed calculations with high coverage structures. This setup is a better representation of experimental conditions, where high coverage of H is expected (see Figure 5.14). The adsorbed hcp-$Ru_{54}^{\{6\}}$ particle was covered with 76 H atoms with the same adsorption sites occupied on both supports. The optimized structures and the corresponding average chemisorp-

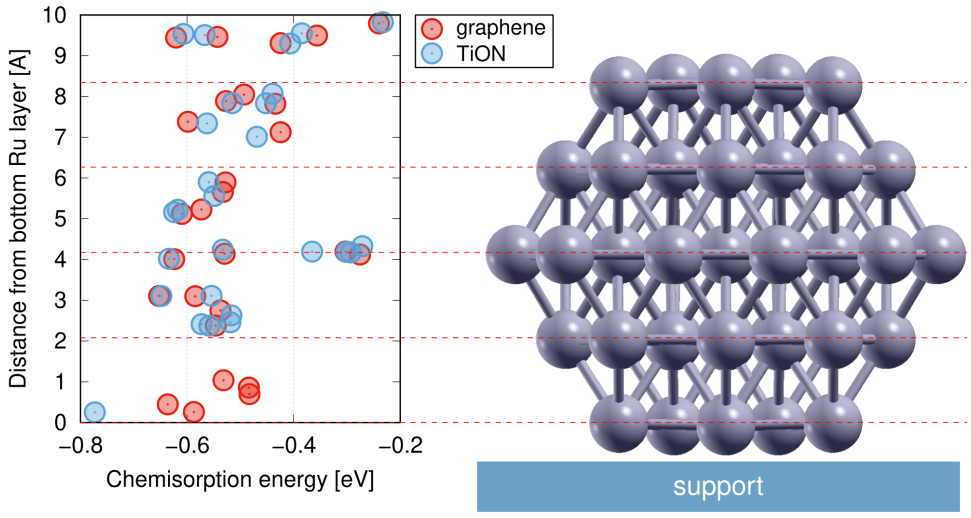


Figure 5.31: Chemisorption energy of a single H atom on various sites of the hcp-$Ru_{54}^{\{6\}}$ nanoparticle, supported on TiON and graphene. Next to the graph a picture of nanoparticle is shown to facilitate interpretation; y=0 is arbitrarily set to the bottommost Ru layer and red dashed lines indicate the positions of the Ru layers in the supported nanoparticle. Snapshots of the corresponding optimized structures are provided in Figures D.3 and D.4 in the Appendix for graphene and TiON, respectively.

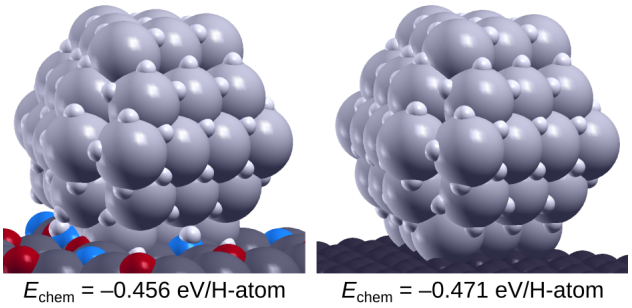


Figure 5.32: Snapshots of the hcp-$Ru_{54}^{\{6\}}$ nanoparticle covered with 76 chemisorbed H atoms supported on TiON support (left) and graphene (right). The average H chemisorption energies are also stated.

tion energies calculated according to Eq. (3.5) are shown in Figure 5.32. The average H chemisorption energies are -0.456 and -0.471 eV per H atom for hcp-$Ru_{54}^{\{6\}}$ on TiON and graphene, respectively. These values indicate that the binding on hcp-$Ru_{54}^{\{6\}}$/TiON system is slightly weaker compared to that on hcp-$Ru_{54}^{\{6\}}$/C. A similar trend was already observed for Pt/TiON catalyst in Figure 5.25 in the whole investigated range of coverages. In the Volcano plot for HER, Ru binds H too strongly [144], [145] and the observed lowering of the strength of H binding could facilitate HER and potentially make the catalyst more active.

When studying the TiON support, we observed similar trends with both Ru and Pt metals. The adhesion of the investigated metal nanoparticles is significantly stronger compared to graphene support, which stabilizes the catalyst and makes it more durable. In addition, slightly weaker chemisorption energy was observed on metal particles supported on TiON, which could make the catalyst more active. This is also consistent with the findings that supports which bind metal nanoparticles strongly tend to weaken their interaction with small adsorbates that bind predominantly covalently [141]. The combination of strong adhesion and favorable effect on hydrogen adsorption energy makes the TiON support highly promising for nanoparticle-based catalysts for HER and other similar reactions [40], [41], [58].

Chapter 6

Conclusions

This thesis investigated the structure–activity relationships of selected DRM and HER catalysts. In the first part, we examined Ni/CeO_2 and Ni/Mn_xCeO_2 catalysts for the dry reforming of methane. The analysis showed that the experimentally observed 2020 cm^{-1} vibrational frequency, present for the Ni/CeO_2 catalyst and absent for the Ni/Mn_xCeO_2 catalyst, corresponds to CO species adsorbed on the Ni surface. Our results suggest that partial oxidation of Ni upon MnO_x doping could explain this observation. Vibrational analysis confirmed that oxidation of the Ni surface shifts the CO stretching frequency to higher values. Reaction pathway analysis further revealed that Ni(111) is active but prone to carbon deposition, whereas NiO(100) is inactive but resistant to carbon deposition. A partially oxidized Ni surface could thus remain active, due to metallic Ni centers, while being less susceptible to deactivation owing to oxidized regions that suppress carbon buildup. The corresponding pathways on both Ni and NiO do not support the first hypothesis ("*Doping the Ni/CeO_2 catalyst with MnO_x alters the reaction mechanism, as proposed by Sagar et al.*"), since in both cases the reaction proceeds via CH_xO intermediates. Instead, our analysis indicates that the key factor differentiating the activity of the two catalysts is the oxidation state of Ni.

The second part of this thesis addresses HER, focusing on platinum- and ruthenium-based catalysts. For platinum, we compared ideal surface models with the Pt_{55} nanoparticle. The nanoparticle exhibits higher adsorbate coverages and stronger adsorption of H*, O*, and OH* than the ideal surfaces, demonstrating that the second hypothesis ("*Models of ideal surfaces capture the same activity trends as nanoparticle models*") is overly optimistic. The main difference between the models lies in the presence of edge and kink sites on the nanoparticle, which bind adsorbates more strongly. Pourbaix diagram predicts high overall nanoparticle coverage, suggesting that adsorbates on facet centers contribute to the activity as well. This is particularly relevant for larger nanoparticles, where the fraction of atoms located on the facets is high compared to that at edge and kink sites. For such nanoparticles, the hypothesis becomes more credible. Among the models of ideal surfaces, Pt(100) was found to be more reactive than Pt(111), exhibiting stronger adsorption energies and higher coverages. Kinetic analysis revealed a clear coverage dependence: the barrier for the Volmer step increased with H* coverage, whereas those for the Tafel and Heyrovsky steps decreased. A detailed examination of the Tafel step further showed higher activity on Pt(111) compared to Pt(100) for this elementary reaction.

For ruthenium, we compared the fcc and hcp crystal phases. Calculations on close-packed Ru-fcc(111) and Ru-hcp(001) suggested slightly higher activity for Ru-hcp(001). This trend was observed from both activation Gibbs energies and activation energies, as the vibrational contributions did not change the trends. However, analysis of additional low-index surfaces together with Wulff constructions indicated that fcc nanoparticles may

achieve higher overall activity by tuning morphology toward a greater share of the active fcc(011) facet. These findings therefore partially support the third hypothesis ("*The fcc phase of Ru is more active toward HER than the thermodynamically stable hcp phase*"), though the enhancement originates from the morphology and facet distribution of the nanoparticles rather than the activity of the close-packed surfaces, as claimed in the literature [68].

Finally, we examined platinum and ruthenium nanoparticles supported on TiON and graphene. For both metals, TiON provided substantially stronger adhesion than graphene, which reduces detachment and agglomeration of the nanoparticles. While adsorption of a single H atom on Ru nanoparticles showed no clear support-dependent trends, high H coverage revealed slightly weaker binding on both Pt and Ru when supported on TiON. This finding suggests that the support can also tune interactions between active sites and intermediates, thereby influencing the activity. These results partially agree with the fourth hypothesis ("*The TiON support forms stronger covalent bonds with metal nanoparticles but does not significantly affect the interaction between adsorbed H and the metal compared to a conventional carbon support*"). The TiON support indeed binds metal nanoparticles strongly, but it also subtly alters intermediate–metal interactions. It is worth noting that even small energy changes can noticeably affect reaction rates.

Overall, this thesis demonstrates that subtle structural modifications — such as the oxidation state of Ni in DRM, the morphology and phase of Ru nanoparticles in HER, and the influence of the TiON support — can affect catalytic activity. These results provide atomic-level insights into how catalytic performance can be tuned by nanoparticle morphology and metal–support interactions. In turn, such understanding provides a basis for the rational design of more efficient HER and DRM catalysts, contributing to more sustainable hydrogen production technologies.

Appendix A

Dry Reforming of Methane on Nickel-Based Catalysts

In this appendix, figures detailing reaction pathways corresponding to the elementary steps considered in the analysis of the DRM reaction for both the Ni(111) and NiO(100) surface models are shown.

Ni(111)

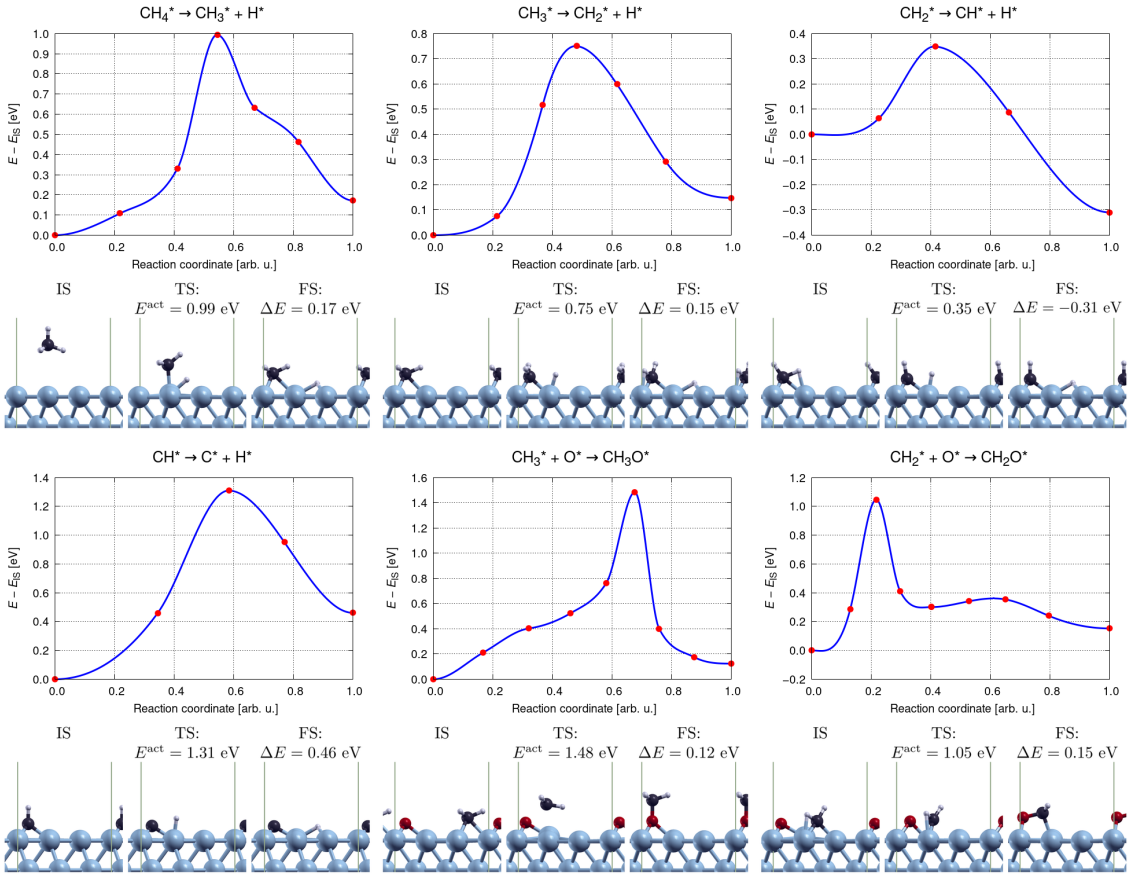


Figure A.1: Reaction pathways for the analyzed elementary steps on Ni(111). Each panel shows the reaction path obtained from the NEB calculations, along with snapshots of the initial (IS), transition (TS), and final (FS) states, as well as the corresponding activation and reaction energies.

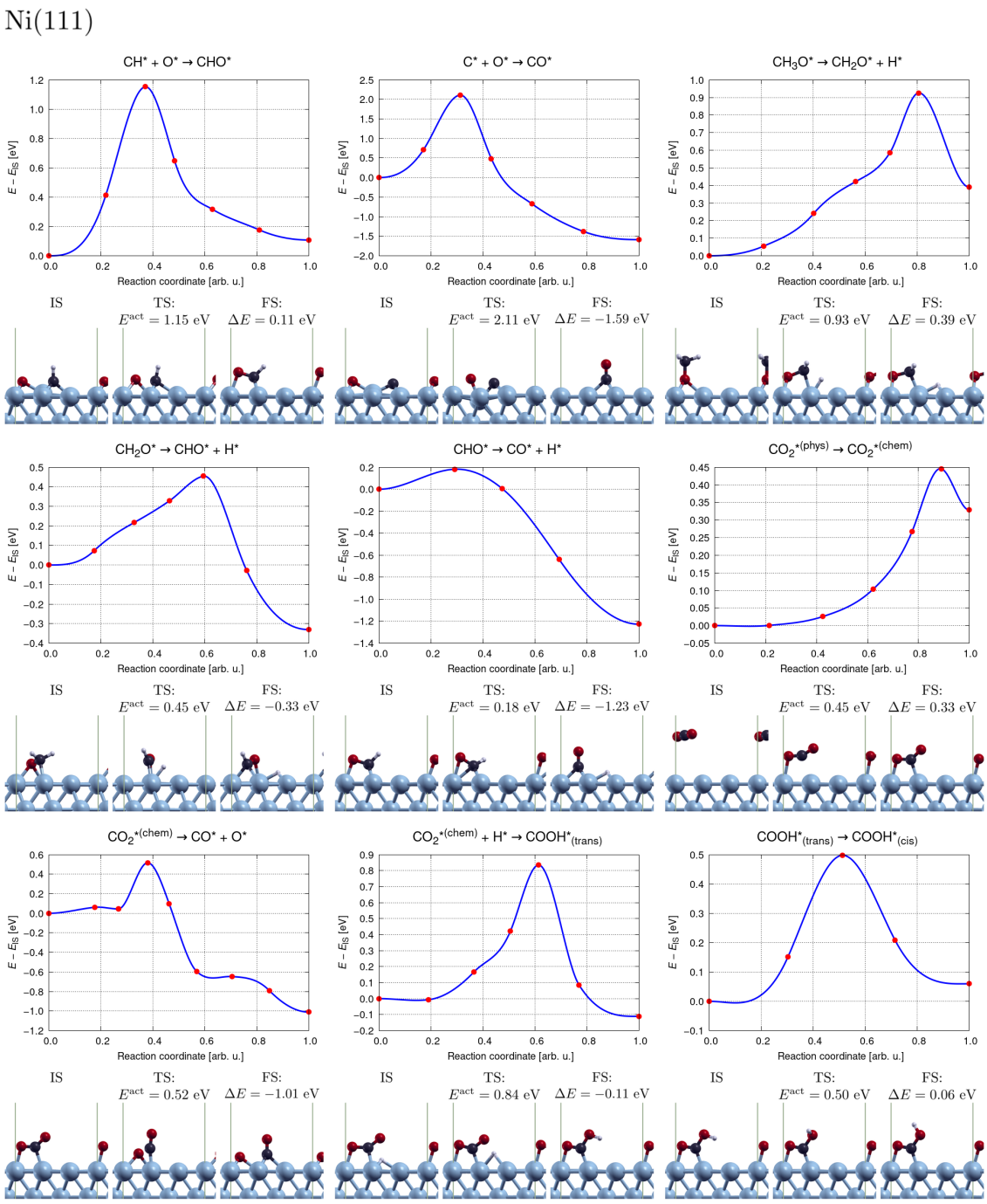


Figure A.1 (continued): Reaction pathways for the analyzed elementary steps on Ni(111). Each panel shows the reaction path obtained from the NEB calculations, along with snapshots of the initial (IS), transition (TS), and final (FS) states, as well as the corresponding activation and reaction energies.

Ni(111)

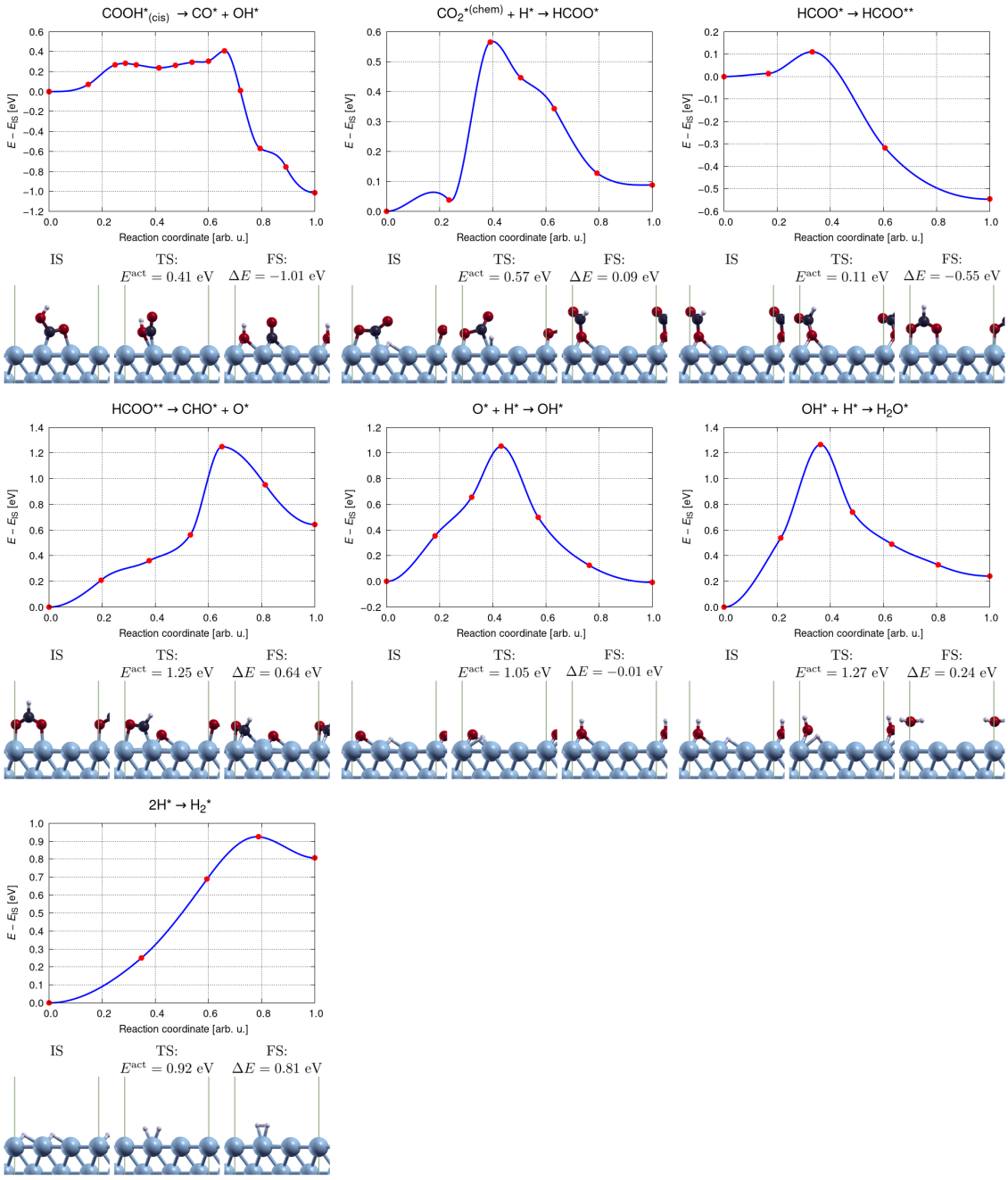


Figure A.1 (continued): Reaction pathways for the analyzed elementary steps on Ni(111). Each panel shows the reaction path obtained from the NEB calculations, along with snapshots of the initial (IS), transition (TS), and final (FS) states, as well as the corresponding activation and reaction energies.

NiO(100)

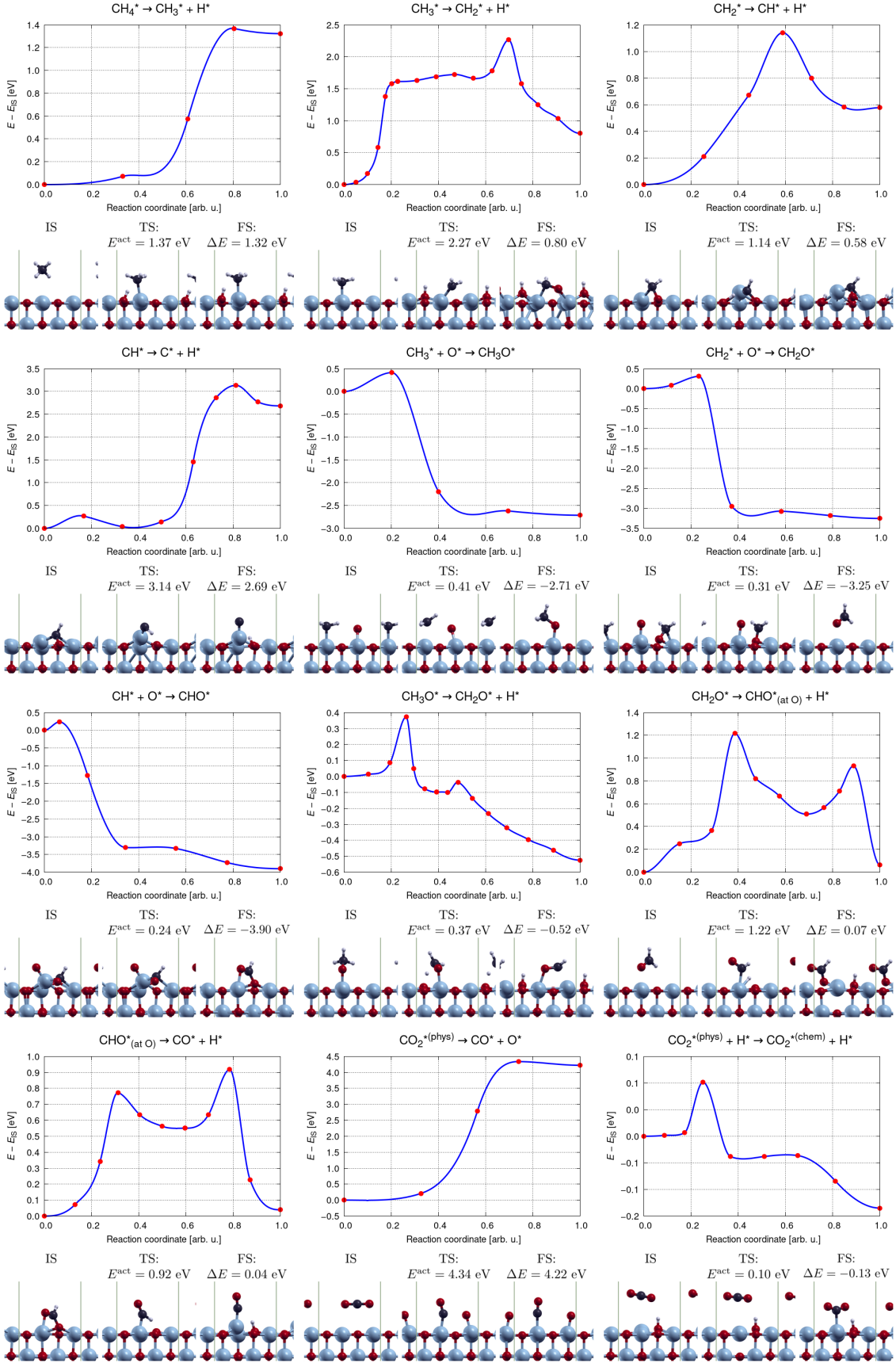


Figure A.2: Similar to Figure A.1 but for the analyzed elementary steps on NiO(100) model.

NiO(100)

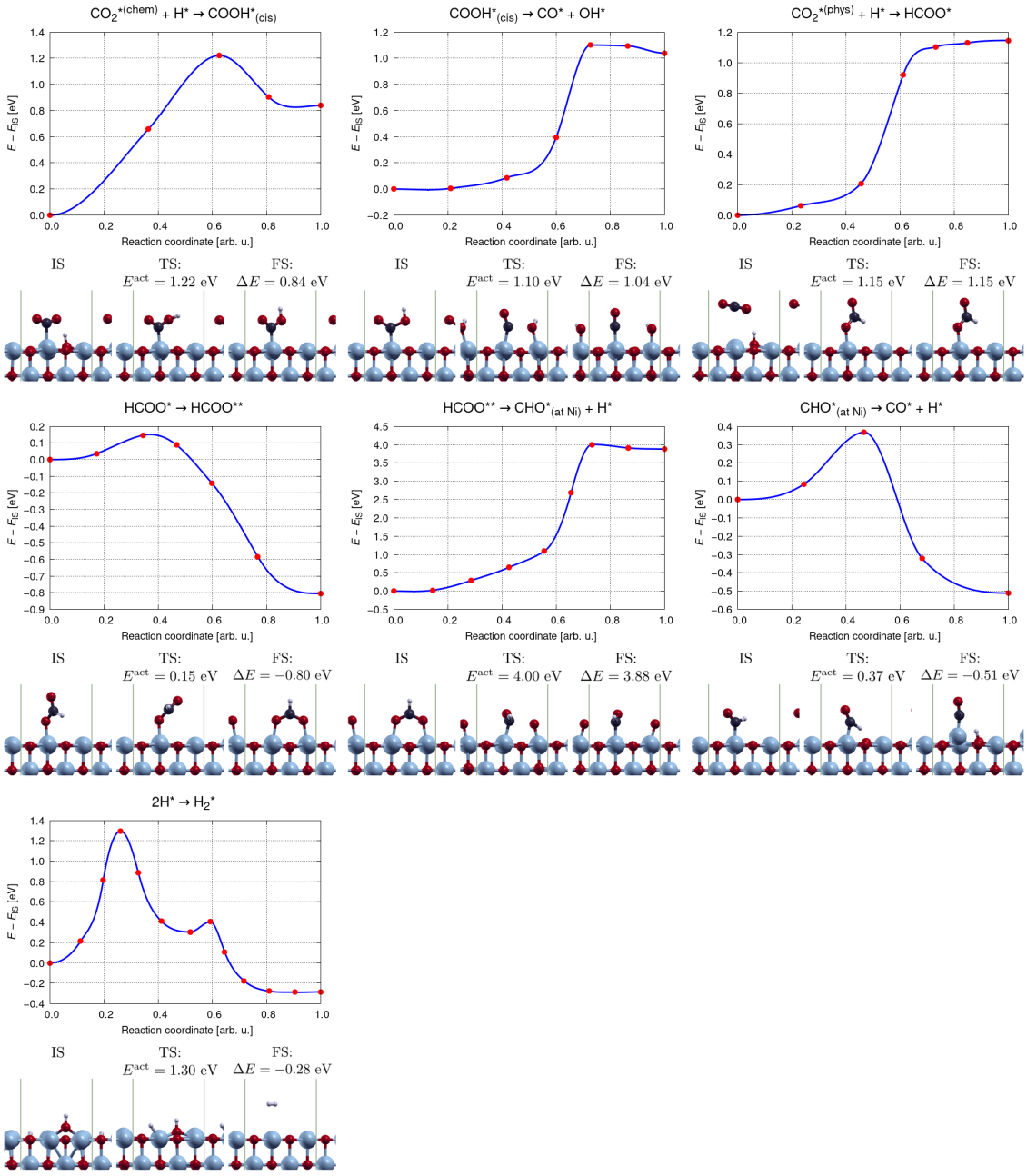


Figure A.2 (continued): Similar to Figure A.1 but for the analyzed elementary steps on NiO(100) model.

Appendix B

Platinum Catalysts for HER

This appendix presents figures of the optimized H*, OH*, and O*-covered Pt surface models used in the analysis, along with the reaction pathways of the considered HER steps.

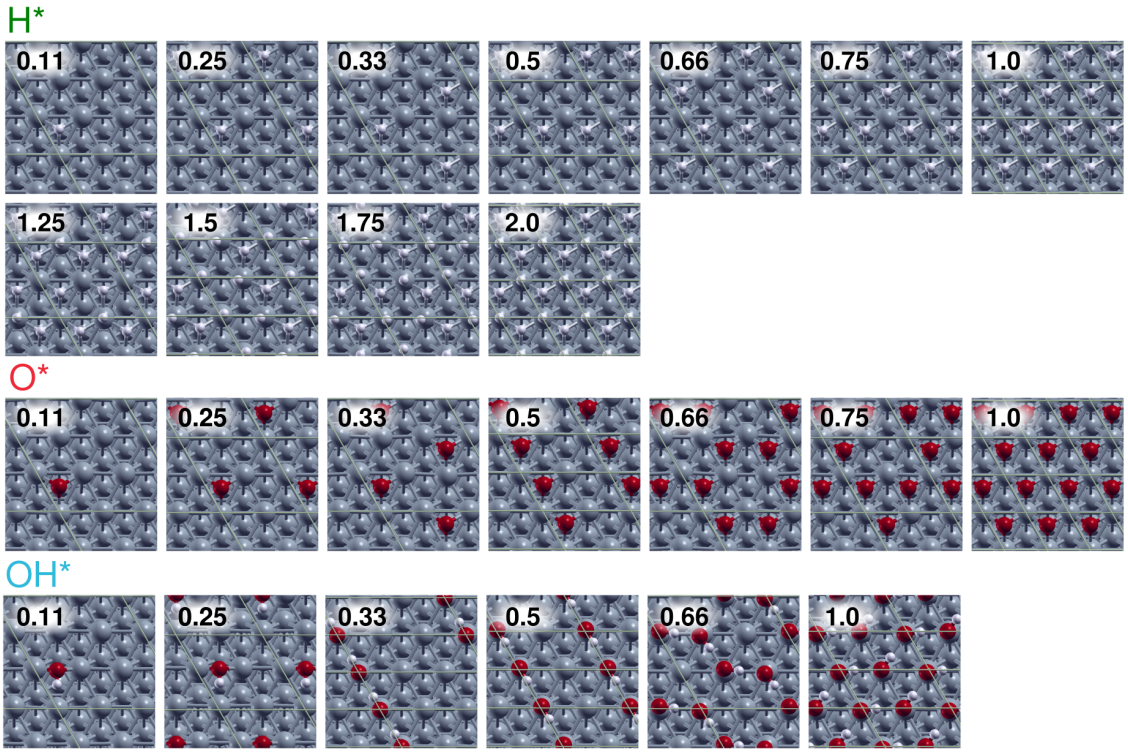


Figure B.1: Top-view snapshots of adsorption structures on Pt(111) for H*, O* and OH*. On each snapshot, adsorbate coverage is stated in ML units.

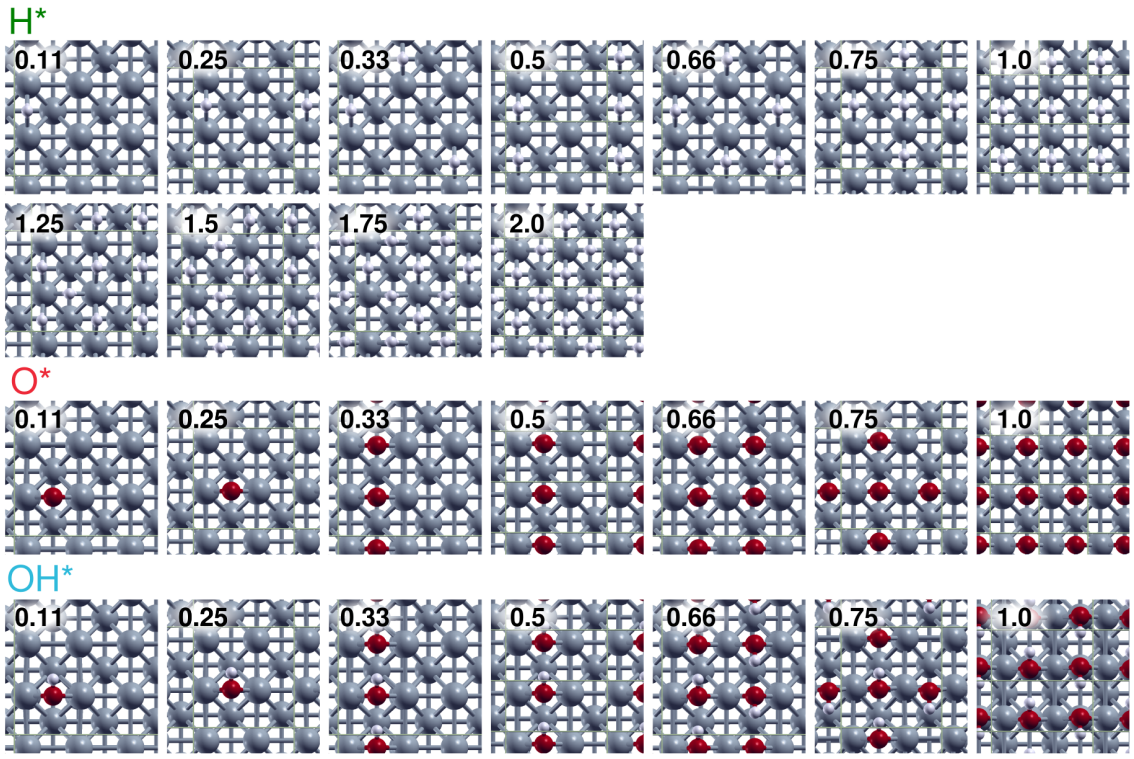


Figure B.2: Top-view snapshots of adsorption structures on Pt(100) for H*, O* and OH*. On each snapshot, adsorbate coverage is stated in ML units.

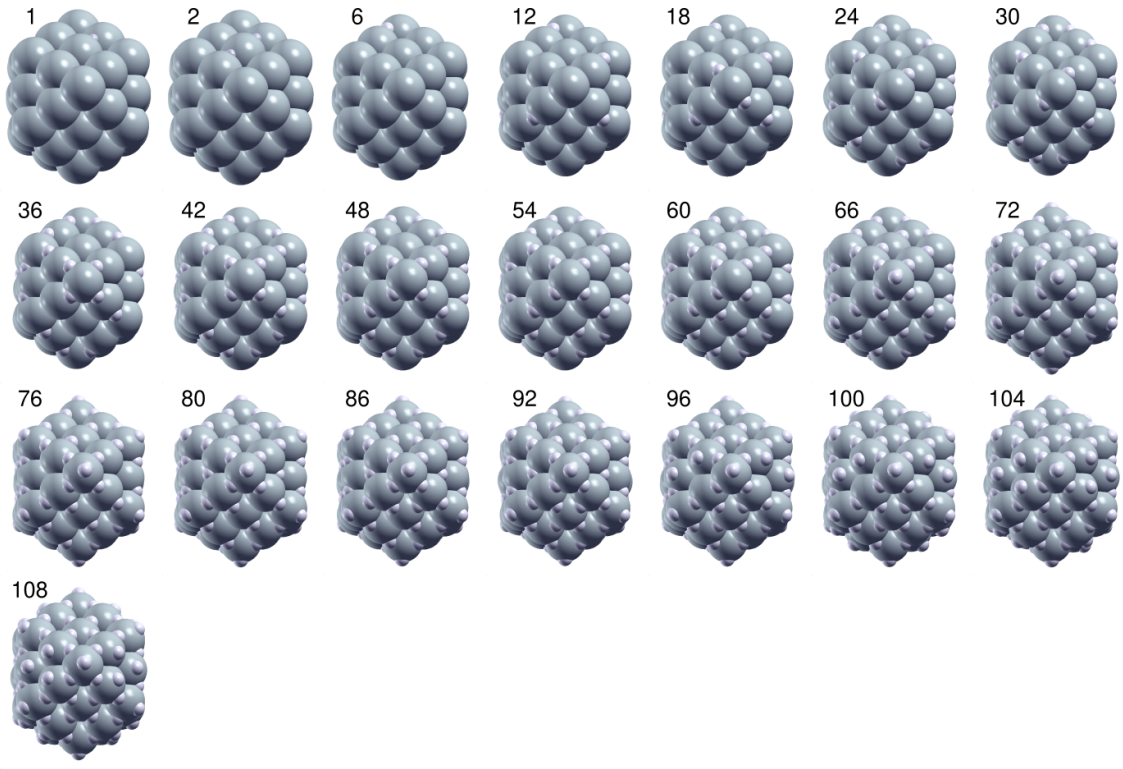


Figure B.3: Adsorption structures of H* on the Pt_{55} particle. Next to each structure the number of adsorbed H atoms is written.

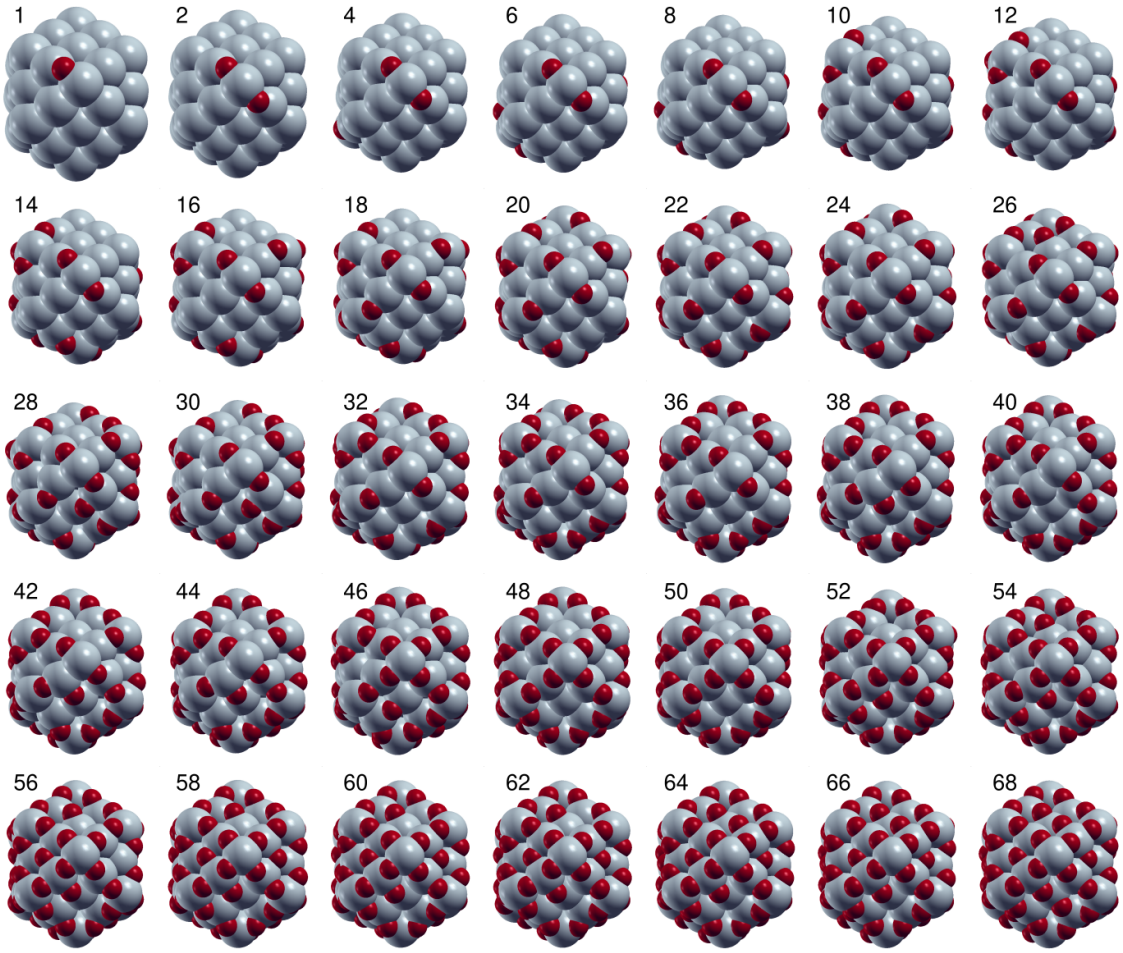


Figure B.4: Adsorption structures of O* on the Pt_{55} particle. Next to each structure the number of adsorbed O atoms is written.

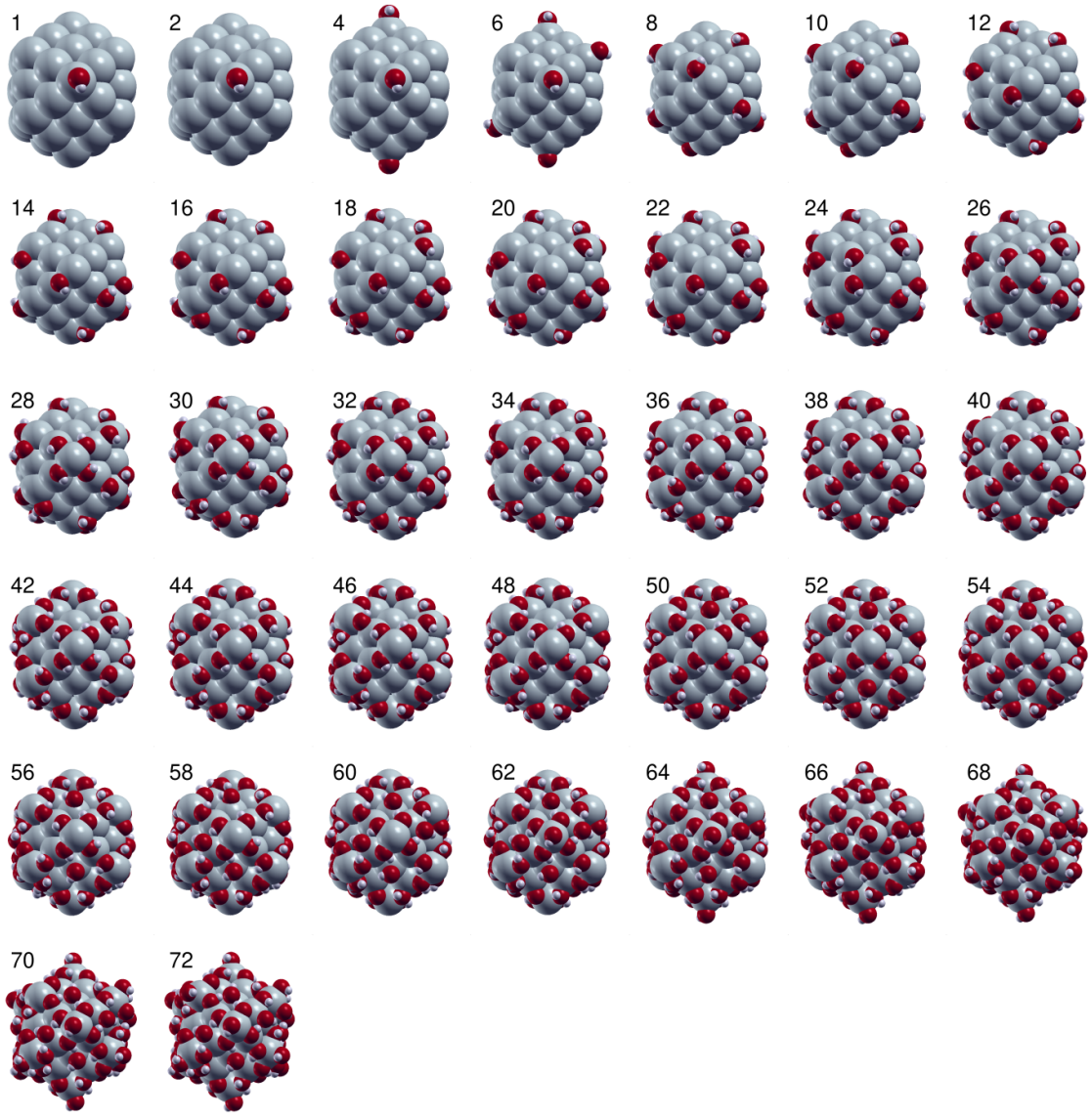


Figure B.5: Adsorption structures of OH* on the Pt_{55} particle. Next to each structure the number of adsorbed OH fragments is written.

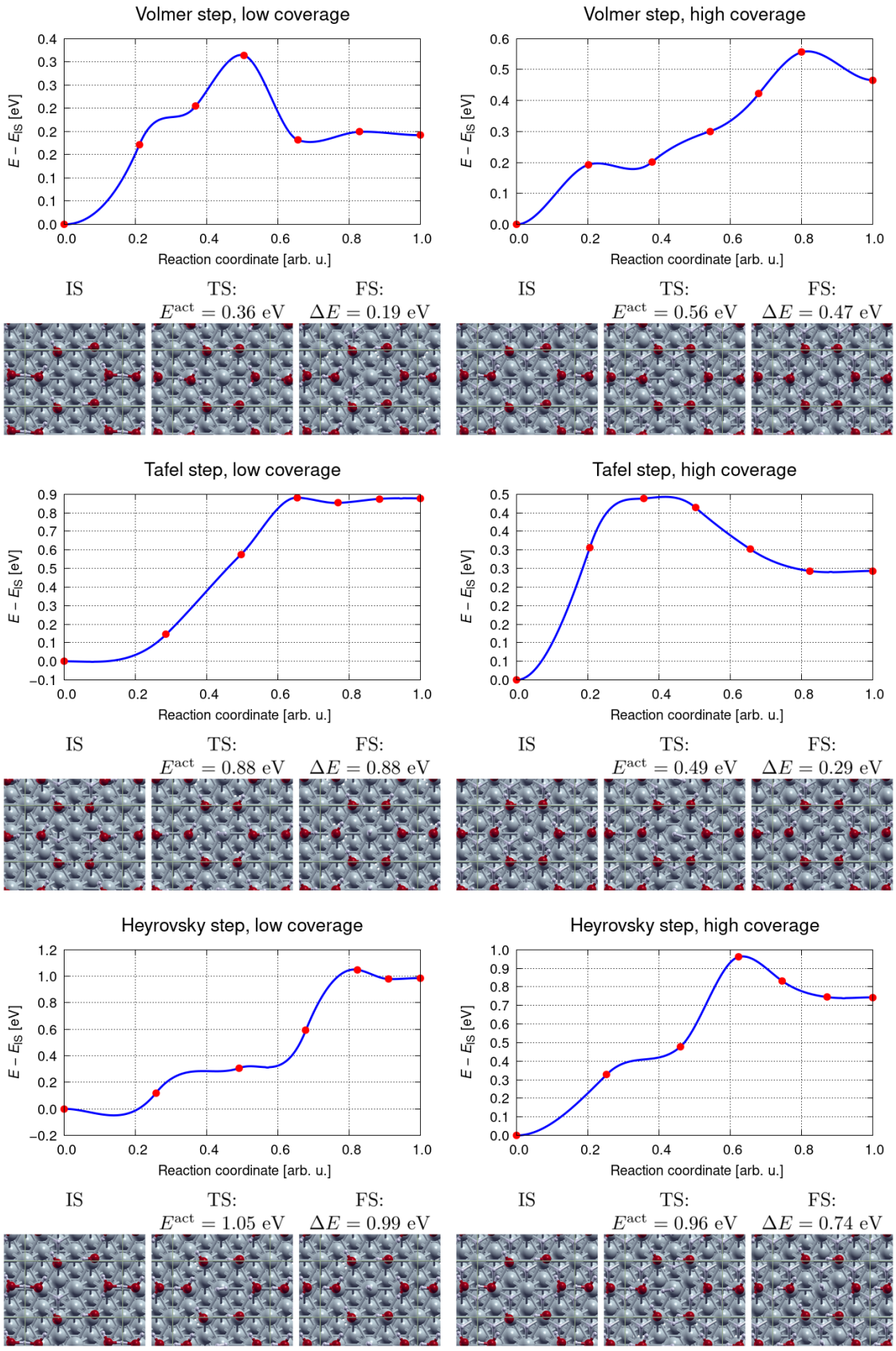


Figure B.6: Reaction pathways for HER on Pt(111) modeled with an ice-like water bilayer model. Each panel shows the minimum-energy path from NEB calculations, with snapshots of IS, TS, and FS, together with the corresponding activation and reaction energy.

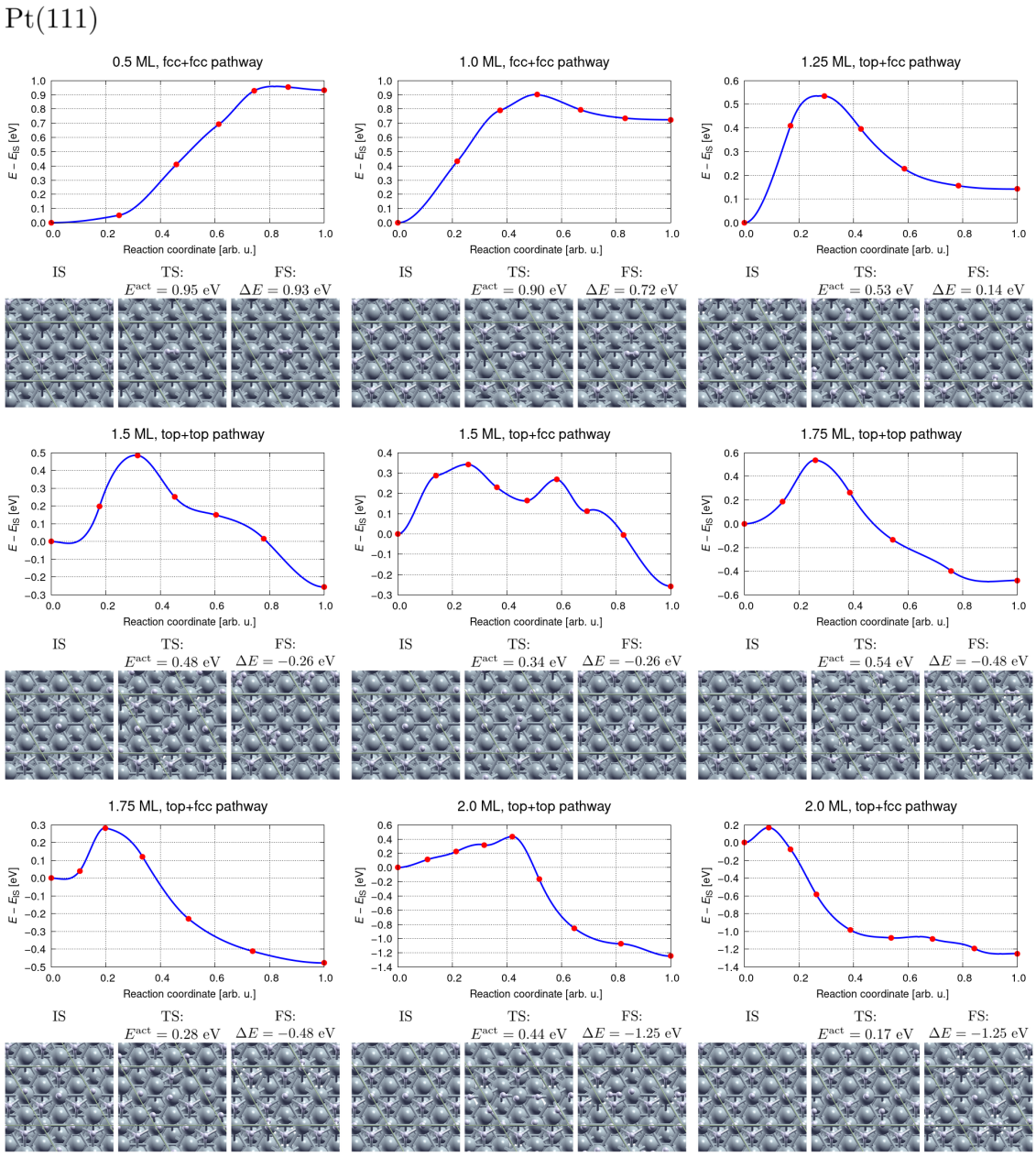


Figure B.7: Reaction pathways for the Tafel step on Pt(111) at different coverage of H*. Each panel shows the minimum-energy path from NEB calculations, with snapshots of IS, TS, and FS, together with the corresponding activation and reaction energy.

Pt(100)

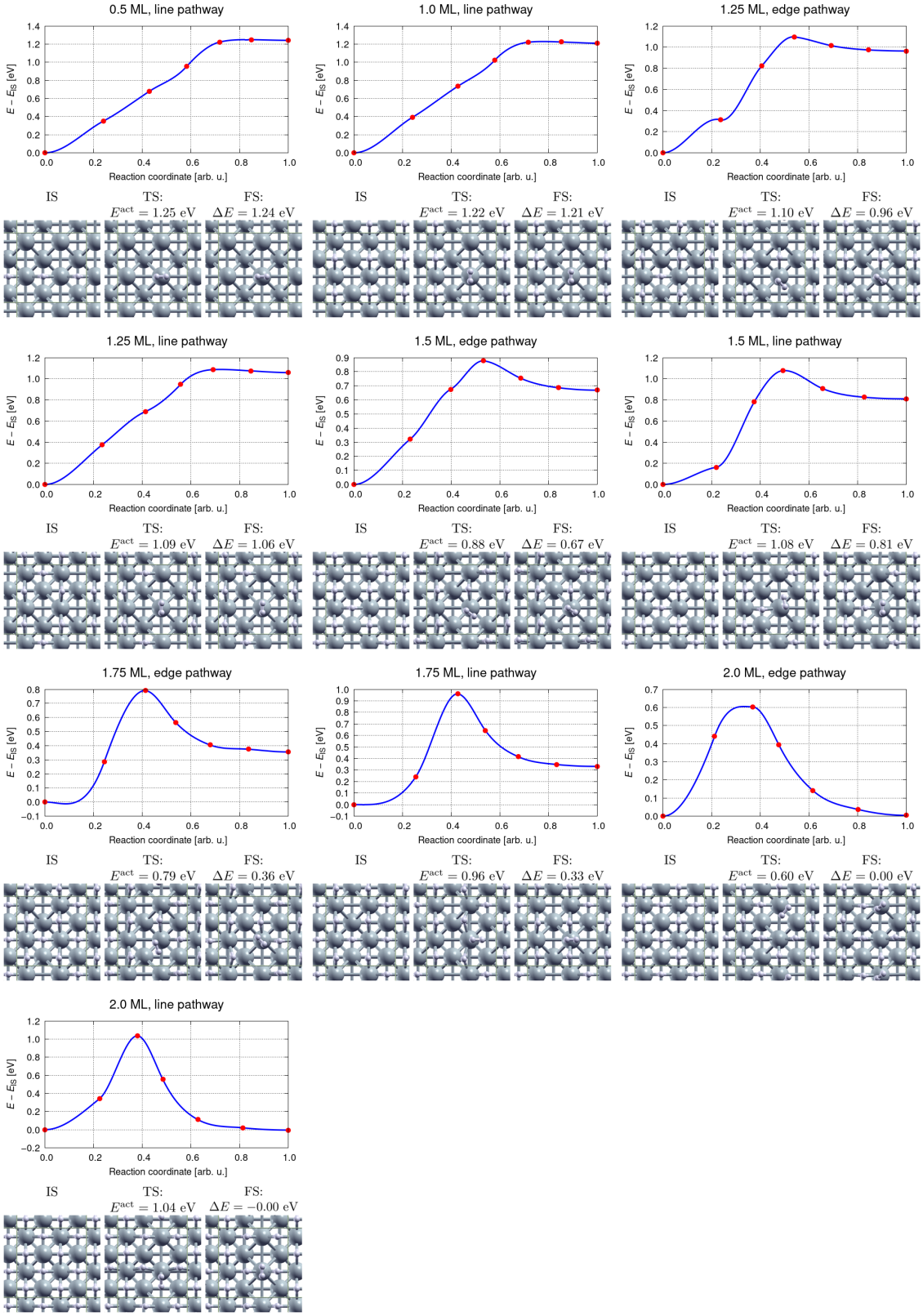


Figure B.8: Reaction pathways for the Tafel step on Pt(100) at different coverage of H*. Each panel shows the minimum-energy path from NEB calculations, with snapshots of IS, TS, and FS, together with the corresponding activation and reaction energy.

Appendix C

Ruthenium Catalysts for HER

This appendix presents figures of the reaction pathways of water dissociation on the analyzed surfaces and supercells, with the corresponding initial (IS), transition (TS), and final (FS) states.

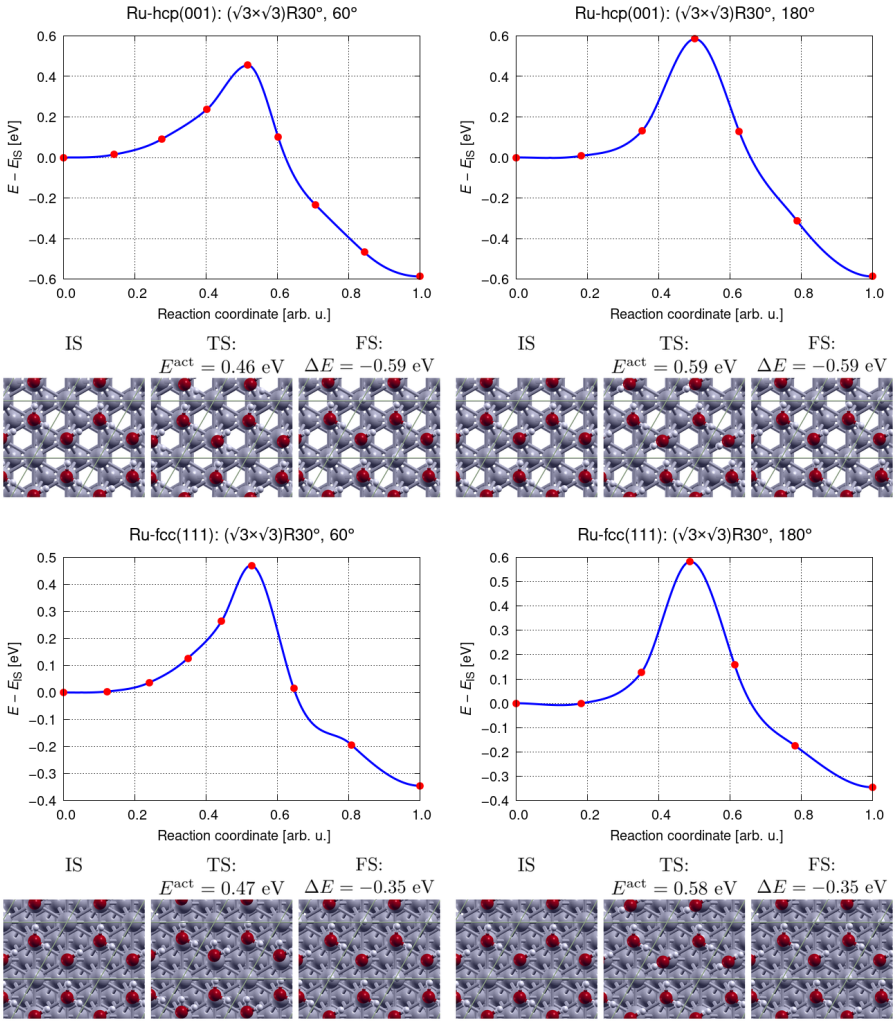


Figure C.1: Water dissociation on Ru-hcp(001) (top row) and Ru-fcc(111) (bottom row) modeled with the $(\sqrt{3} \times \sqrt{3})$R30° supercell and an ice-like water bilayer.

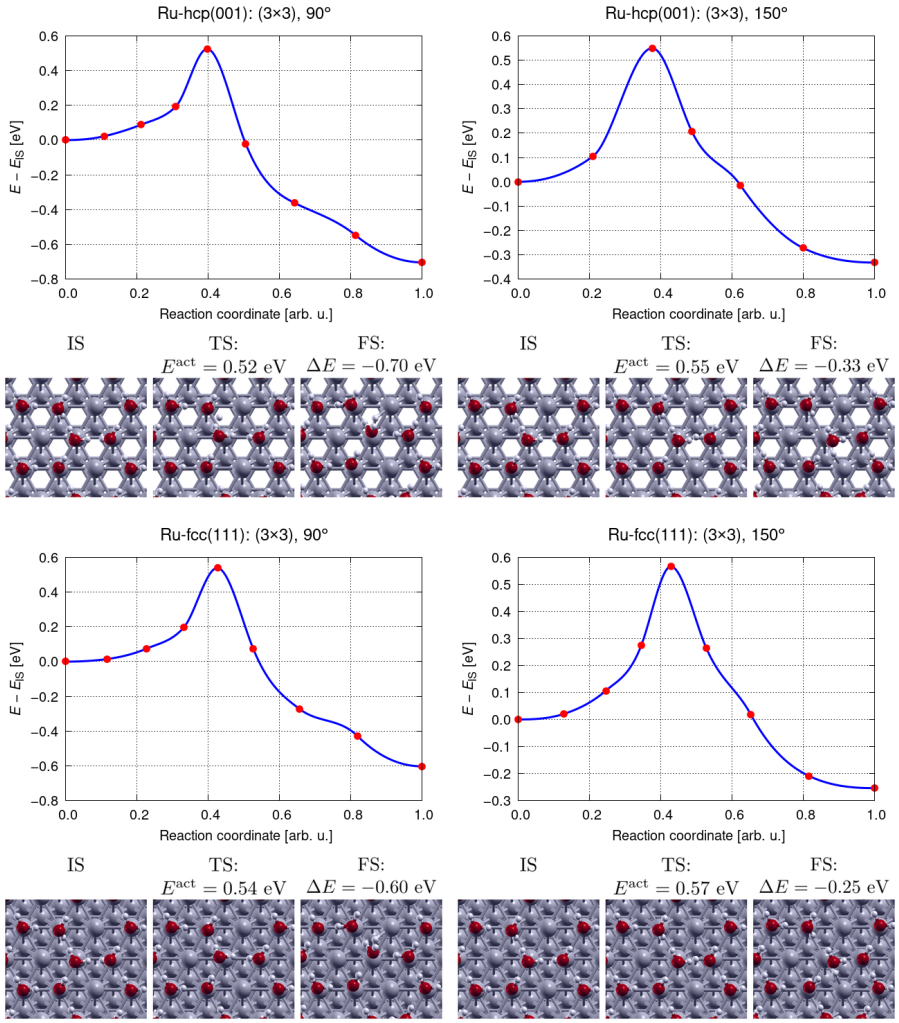


Figure C.2: Water dissociation on Ru-hcp(001) (top row) and Ru-fcc(111) (bottom row) modeled with the (3×3) supercell and an ice-like water bilayer.

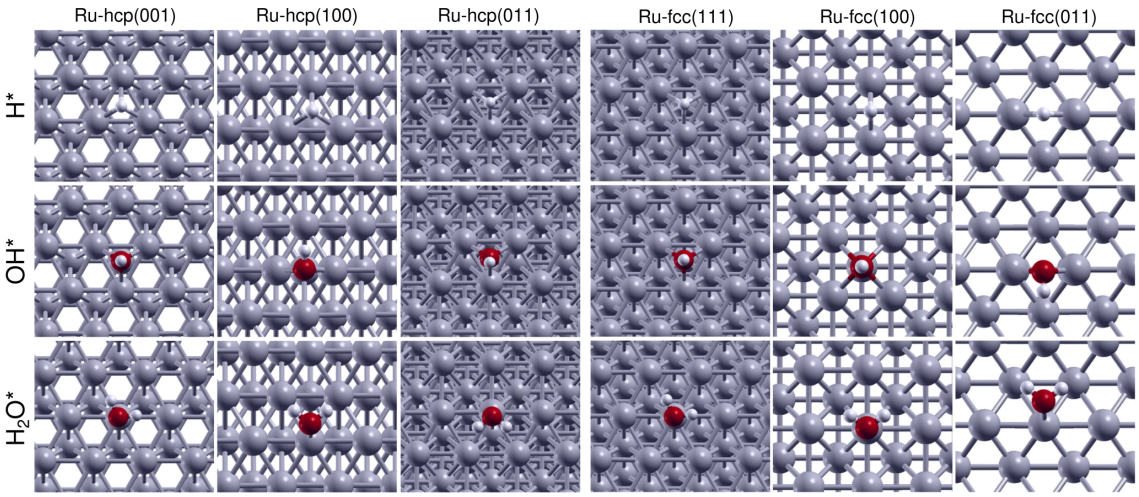


Figure C.3: The most stable adsorption sites for H*, OH*, and H_2O* on all investigated Ru-hcp and Ru-fcc surfaces.

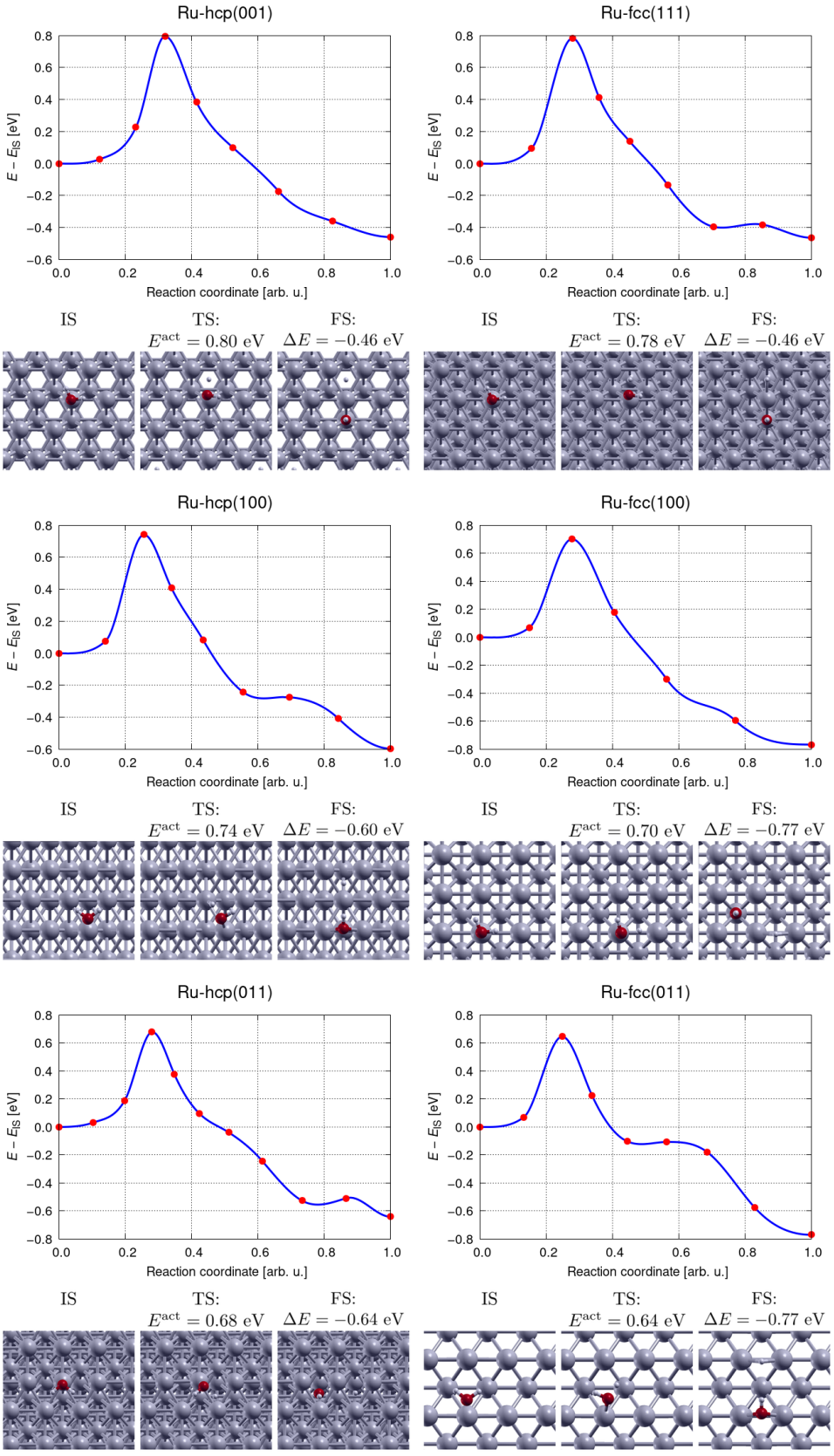


Figure C.4: Reaction pathways for water dissociation on low-index surfaces of hcp (left) and fcc Ru (right). Each panel shows the minimum-energy path from NEB calculations, with snapshots of IS, TS, and FS, together with the corresponding activation and reaction energy.

Appendix D

Structures of Supported Nanoparticles

In this appendix, the snapshots of structures used in the analysis of supported nanoparticles are provided.

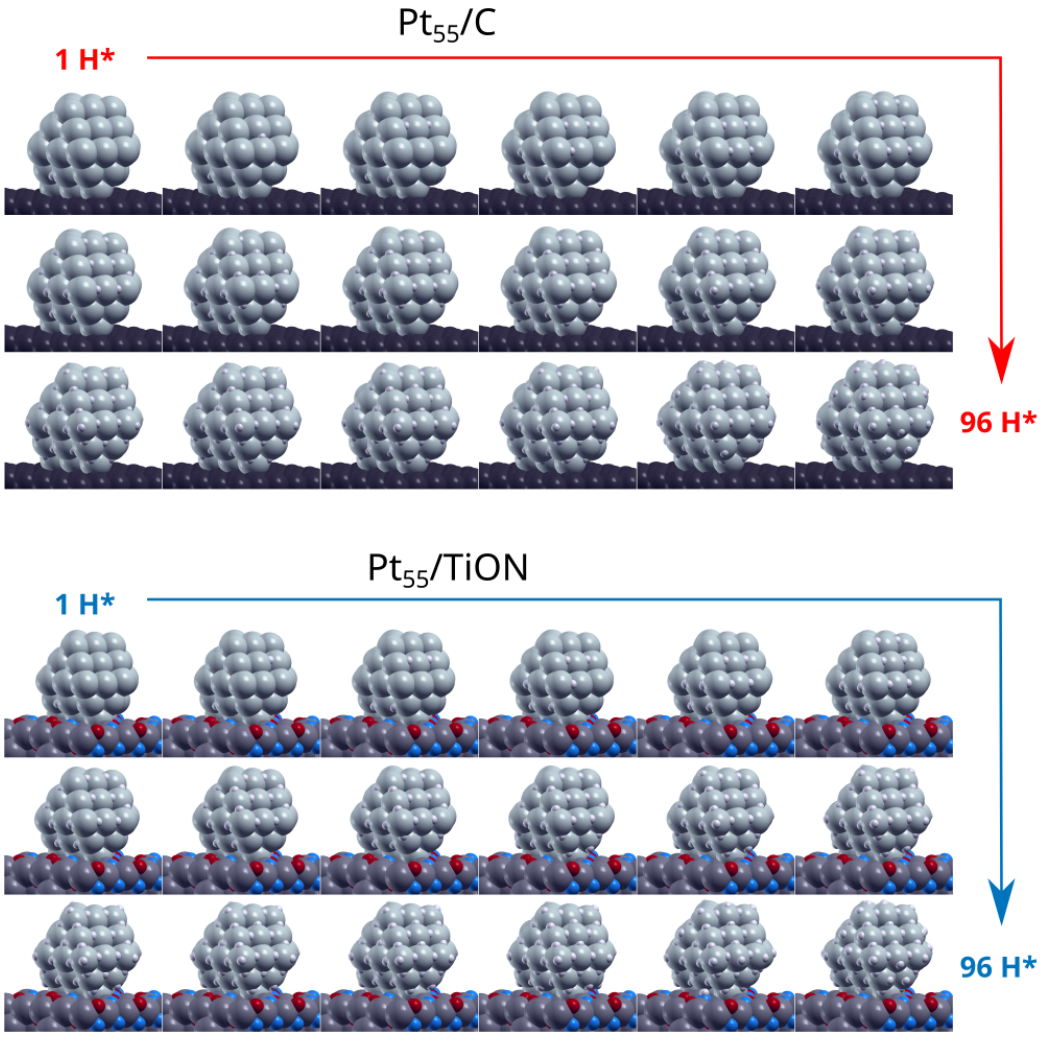


Figure D.1: Snapshots of the most stable identified structures of the Pt_{55} nanoparticle supported on graphene and TiON with different number of adsorbed H atoms.

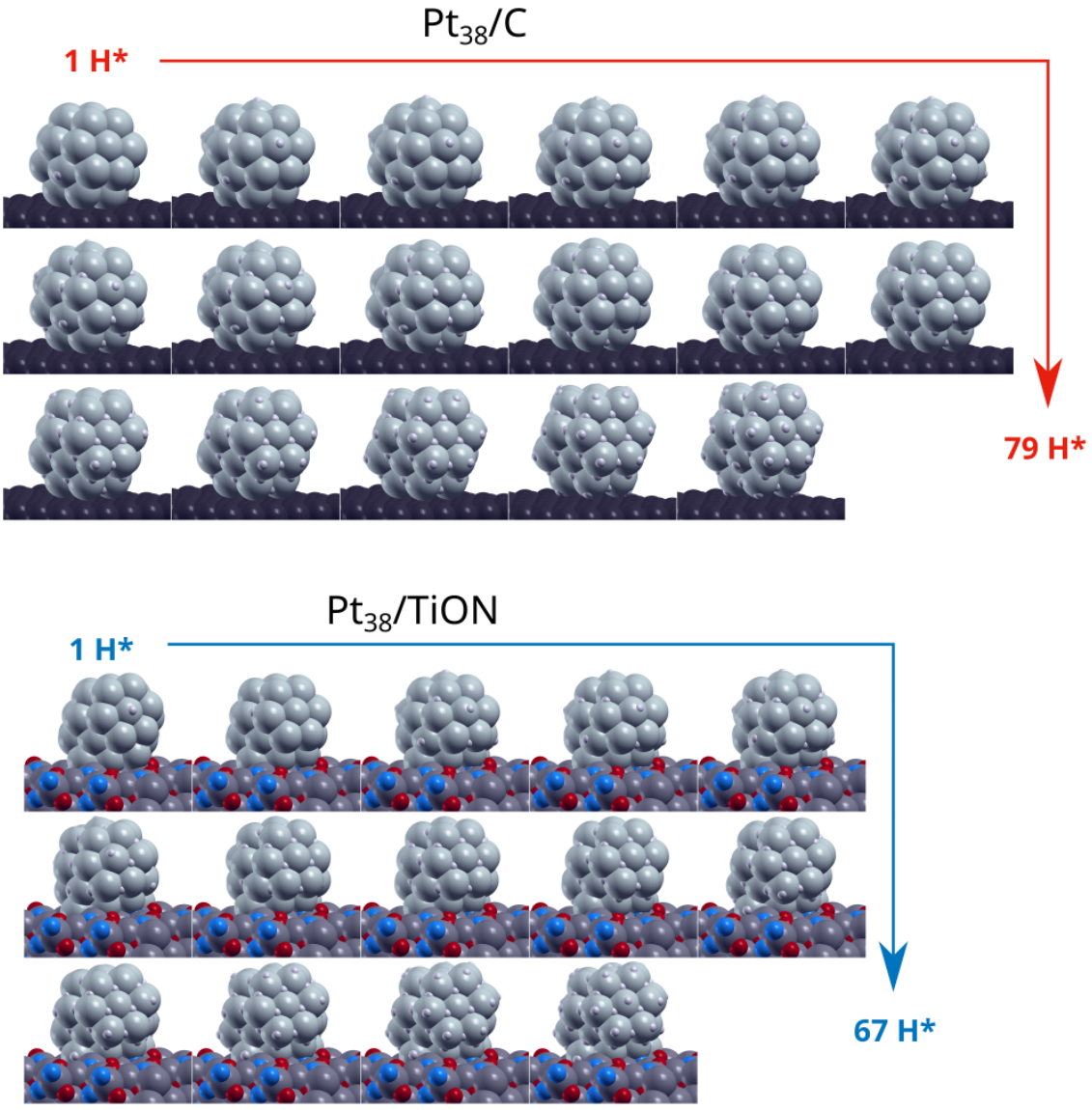


Figure D.2: Snapshots of the most stable identified structures of the Pt_{38} nanoparticle supported on graphene and TiON with different number of adsorbed H atoms.

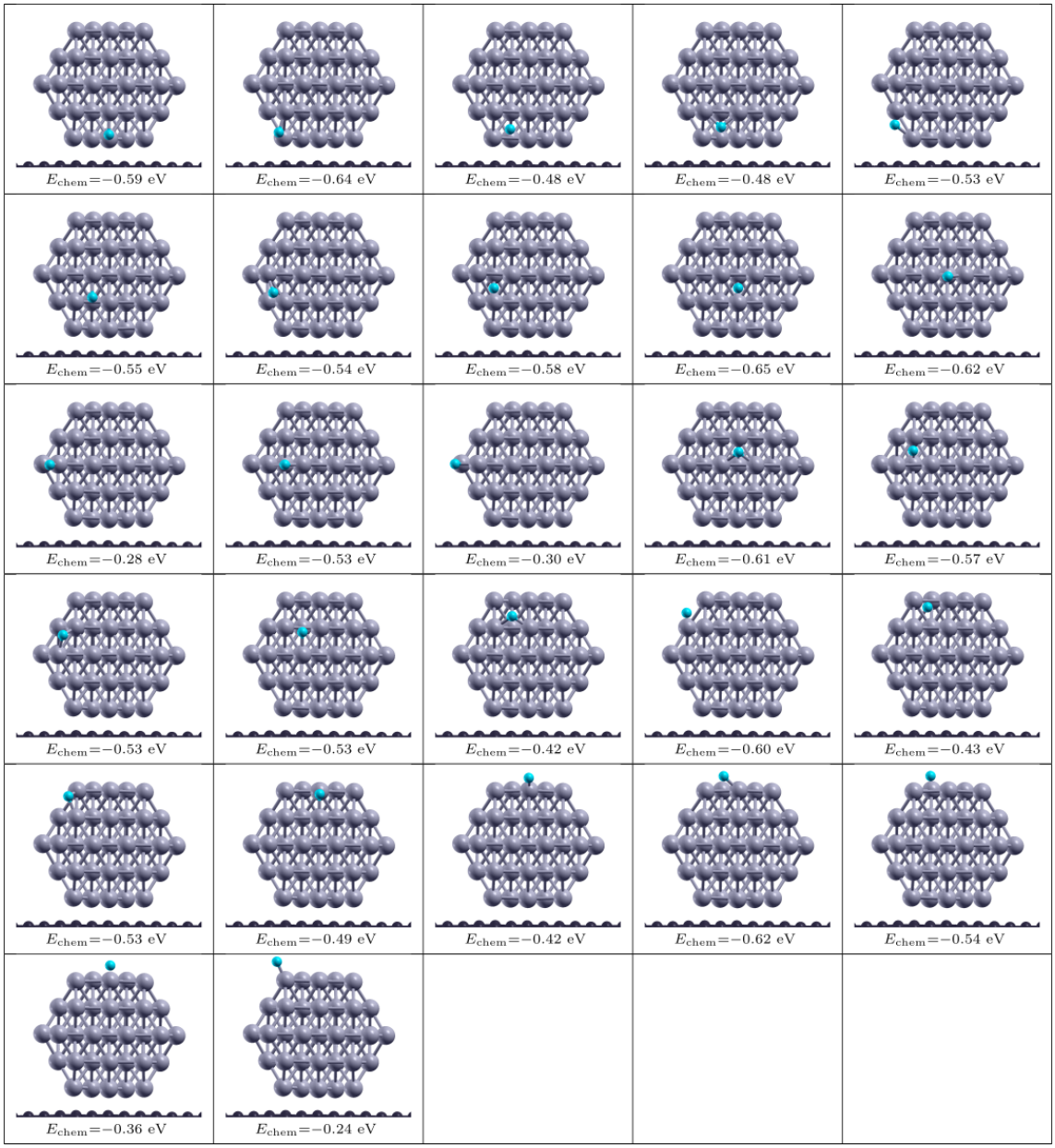


Figure D.3: Snapshots of optimized structures and chemisorption energies of a single H atom adsorbed on various sites of hcp-$Ru_{54}^{\{6\}}$ supported on graphene. Snapshots are ordered according to the increasing height of the adsorbed H atom above the support.

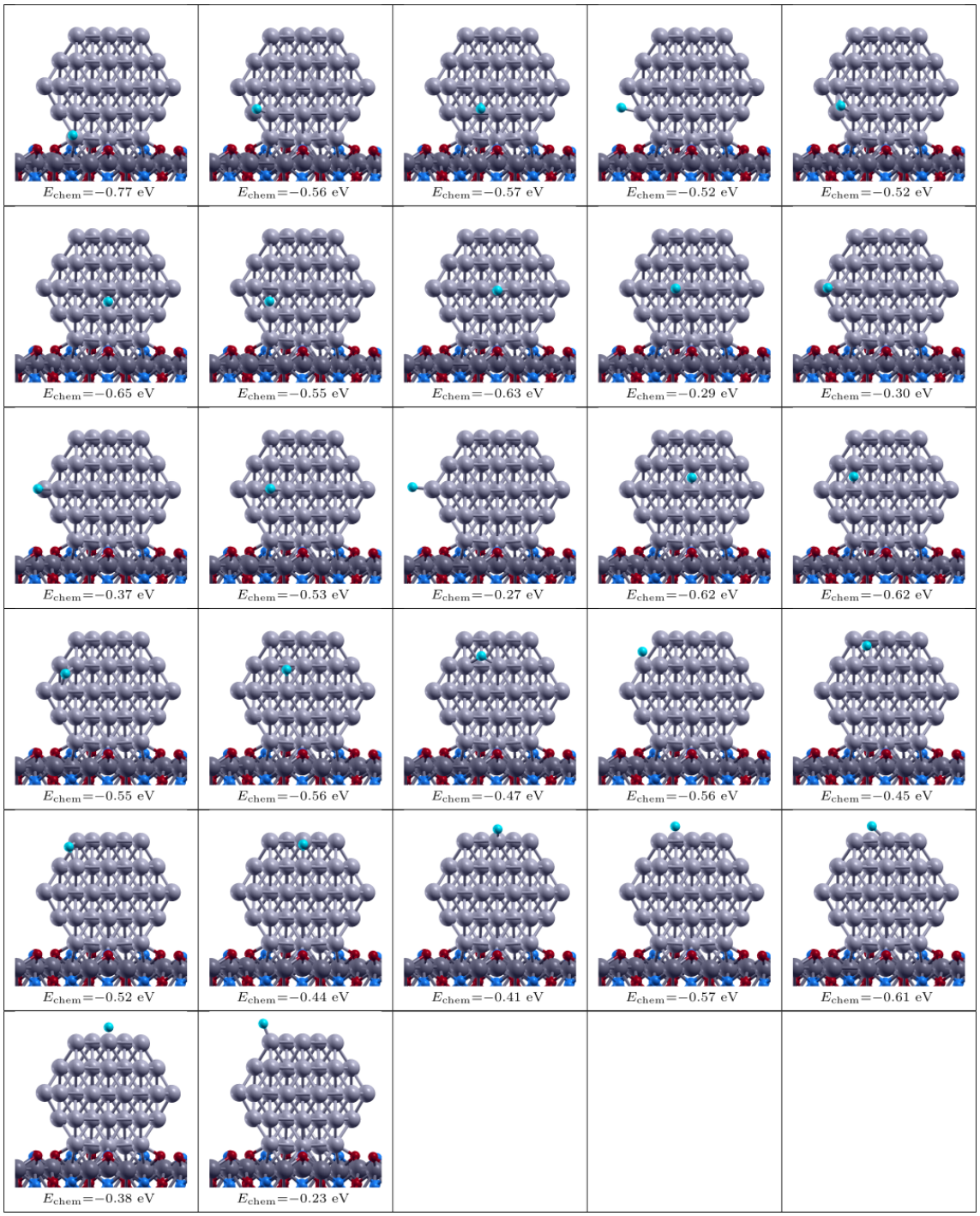


Figure D.4: Snapshots of optimized structures and chemisorption energies of a single H atom adsorbed on various sites of hcp-$Ru_{54}^{\{6\}}$ supported on TiON. Snapshots are ordered according to the increasing height of the adsorbed H atom above the support.

References

[1] A. Ajanovic, M. Sayer, and R. Haas, "The economics and the environmental benignity of different colors of hydrogen," *Int. J. Hydrogen Energy*, vol. 47, no. 57, pp. 24 136–24 154, 2022. DOI: 10.1016/j.ijhydene.2022.02.094.

[2] O. Massarweh, M. Al-khuzaei, M. Al-Shafi, Y. Bicer, and A. S. Abushaikha, "Blue hydrogen production from natural gas reservoirs: A review of application and feasibility," *J. CO2 Util.*, vol. 70, p. 102 438, 2023. DOI: 10.1016/j.jcou.2023.102438.

[3] R. Yukesh Kannah, S. Kavitha, Preethi, *et al.*, "Techno-economic assessment of various hydrogen production methods – A review," *Bioresour. Technol.*, vol. 319, p. 124 175, 2021. DOI: 10.1016/j.biortech.2020.124175.

[4] K. T. Møller, T. R. Jensen, E. Akiba, and H.-w. Li, "Hydrogen - A sustainable energy carrier," *Prog. Nat. Sci.: Mater. Int.*, vol. 27, no. 1, pp. 34–40, 2017. DOI: 10.1016/j.pnsc.2016.12.014.

[5] J. Zhu, L. Hu, P. Zhao, L. Y. S. Lee, and K.-Y. Wong, "Recent advances in electrocatalytic hydrogen evolution using nanoparticles," *Chem. Rev.*, vol. 120, no. 2, pp. 851–918, 2020. DOI: 10.1021/acs.chemrev.9b00248.

[6] R. W. Howarth and M. Z. Jacobson, "How green is blue hydrogen?" *Energy Sci. Eng.*, vol. 9, no. 10, pp. 1676–1687, 2021. DOI: 10.1002/ese3.956.

[7] A. Al-Qahtani, B. Parkinson, K. Hellgardt, N. Shah, and G. Guillen-Gosalbez, "Uncovering the true cost of hydrogen production routes using life cycle monetisation," *Appl. Energy*, vol. 281, p. 115 958, 2021. DOI: 10.1016/j.apenergy.2020.115958.

[8] Nature, "Overhyping hydrogen as a fuel risks endangering net-zero goals," *Nature*, vol. 611, p. 426, 2022. DOI: 10.1038/d41586-022-03693-6.

[9] S. Vitta, "Sustainability of hydrogen manufacturing: A review," *RSC Sustain.*, vol. 2, no. 11, pp. 3202–3221, 2024. DOI: 10.1039/D4SU00420E.

[10] L. Gašparič, A. Pintar, and A. Kokalj, "A DFT study of elementary reaction steps of dry reforming of methane catalyzed by Ni: Explaining the difference between Ni particles supported on CeO_2 and MnO_x-doped CeO_2," *Appl. Surf. Sci.*, vol. 648, p. 159 029, 2024. DOI: 10.1016/j.apsusc.2023.159029.

[11] M. Rezaei, S. M. Alavi, S. Sahebdelfar, P. Bai, X. Liu, and Z.-F. Yan, "CO_2 reforming of CH_4 over nanocrystalline zirconia-supported nickel catalysts," *Appl. Catal., B*, vol. 77, no. 3, pp. 346–354, 2008. DOI: 10.1016/j.apcatb.2007.08.004.

[12] M. Jafarbegloo, A. Tarlani, A. W. Mesbah, and S. Sahebdelfar, "Thermodynamic analysis of carbon dioxide reforming of methane and its practical relevance," *Int. J. Hydrogen Energy*, vol. 40, no. 6, pp. 2445–2451, 2015. DOI: 10.1016/j.ijhydene.2014.12.103.

[13] I. V. Yentekakis, P. Panagiotopoulou, and G. Artemakis, "A review of recent efforts to promote dry reforming of methane (DRM) to syngas production via bimetallic catalyst formulations," *Appl. Catal., B*, vol. 296, p. 120 210, 2021. DOI: 10.1016/j.apcatb.2021.120210.

[14] J. J. Torrez-Herrera, S. A. Korili, and A. Gil, "Recent progress in the application of Ni-based catalysts for the dry reforming of methane," *Catal. Rev.*, vol. 65, no. 4, pp. 1300–1357, 2023. DOI: 10.1080/01614940.2021.2006891.

[15] F. d. A. R. da Silva, R. C. R. dos Santos, R. S. Nunes, and A. Valentini, "Role of tin on the electronic properties of Ni/Al_2O_3 catalyst and its effect over the methane dry reforming reaction," *Appl. Catal., A*, vol. 618, p. 118 129, 2021. DOI: 10.1016/j.apcata.2021.118129.

[16] W. Liu, L. Li, S. Lin, *et al.*, "Confined Ni-In intermetallic alloy nanocatalyst with excellent coking resistance for methane dry reforming," *J. Energy Chem.*, vol. 65, pp. 34–47, 2022. DOI: 10.1016/j.jechem.2021.05.017.

[17] C. Pizzolitto, E. Pupulin, F. Menegazzo, *et al.*, "Nickel based catalysts for methane dry reforming: Effect of supports on catalytic activity and stability," *Int. J. Hydrogen Energy*, vol. 44, no. 52, pp. 28 065–28 076, 2019. DOI: 10.1016/j.ijhydene.2019.09.050.

[18] L. P. Teh, H. D. Setiabudi, S. N. Timmiati, M. A. A. Aziz, N. H. R. Annuar, and N. N. Ruslan, "Recent progress in ceria-based catalysts for the dry reforming of methane: A review," *Chem. Eng. Sci.*, vol. 242, p. 116 606, 2021. DOI: 10.1016/j.ces.2021.116606.

[19] O. Mohan, Shambhawi, A. A. Lapkin, and S. H. Mushrif, "Investigating methane dry reforming on Ni and B promoted Ni surfaces: DFT assisted microkinetic analysis and addressing the coking problem," *Catal. Sci. Technol.*, vol. 10, no. 19, pp. 6628–6643, 2020. DOI: 10.1039/D0CY00939C.

[20] C. Fan, Y.-A. Zhu, M.-L. Yang, Z.-J. Sui, X.-G. Zhou, and D. Chen, "Density functional theory-assisted microkinetic analysis of methane dry reforming on Ni catalyst," *Ind. Eng. Chem. Res.*, vol. 54, no. 22, pp. 5901–5913, 2015. DOI: 10.1021/acs.iecr.5b00563.

[21] S.-G. Wang, D.-B. Cao, Y.-W. Li, J. Wang, and H. Jiao, "CO_2 reforming of CH_4 on Ni(111): A density functional theory calculation," *J. Phys. Chem. B*, vol. 110, no. 20, pp. 9976–9983, 2006. DOI: 10.1021/jp060992g.

[22] M. Zhang, K. Yang, X. Zhang, and Y. Yu, "Effect of Ni(111) surface alloying by Pt on partial oxidation of methane to syngas: A DFT study," *Surf. Sci.*, vol. 630, pp. 236–243, 2014. DOI: 10.1016/j.susc.2014.08.023.

[23] Z. Han, Z. Yang, and M. Han, "Comprehensive investigation of methane conversion over Ni(111) surface under a consistent DFT framework: Implications for anti-coking of SOFC anodes," *Appl. Surf. Sci.*, vol. 480, pp. 243–255, 2019. DOI: 10.1016/j.apsusc.2019.02.084.

[24] S. Kawi, Y. Kathiraser, J. Ni, U. Oemar, Z. Li, and E. T. Saw, "Progress in synthesis of highly active and stable nickel-based catalysts for carbon dioxide reforming of methane," *ChemSusChem*, vol. 8, no. 21, pp. 3556–3575, 2015. DOI: 10.1002/cssc.201500390.

[25] P. M. Mortensen and I. Dybkjær, "Industrial scale experience on steam reforming of CO_2-rich gas," *Appl. Catal., A*, vol. 495, pp. 141–151, 2015. DOI: 10.1016/j.apcata.2015.02.022.

[26] P. A. U. Aldana, F. Ocampo, K. Kobl, *et al.*, "Catalytic CO_2 valorization into CH_4 on Ni-based ceria-zirconia. Reaction mechanism by operando IR spectroscopy," *Catal. Today*, vol. 215, pp. 201–207, 2013. DOI: 10.1016/j.cattod.2013.02.019.

[27] X. Li, D. Li, H. Tian, L. Zeng, Z.-J. Zhao, and J. Gong, "Dry reforming of methane over Ni/La_2O_3 nanorod catalysts with stabilized Ni nanoparticles," *Appl. Catal., B*, vol. 202, pp. 683–694, 2017. DOI: 10.1016/j.apcatb.2016.09.071.

[28] J. Carrasco, L. Barrio, P. Liu, J. A. Rodriguez, and M. V. Ganduglia-Pirovano, "Theoretical studies of the adsorption of CO and C on Ni(111) and $Ni/CeO_2(111)$: Evidence of a strong metal−support interaction," *J. Phys. Chem. C*, vol. 117, no. 16, pp. 8241–8250, 2013. DOI: 10.1021/jp400430r.

[29] Z. Mao, P. G. Lustemberg, J. R. Rumptz, M. V. Ganduglia-Pirovano, and C. T. Campbell, "Ni nanoparticles on $CeO_2(111)$: Energetics, electron transfer, and structure by Ni adsorption calorimetry, spectroscopies, and density functional theory," *ACS Catal.*, vol. 10, no. 9, pp. 5101–5114, 2020. DOI: 10.1021/acscatal.0c00333.

[30] K. Yuan, J.-Q. Zhong, X. Zhou, *et al.*, "Dynamic oxygen on surface: Catalytic intermediate and coking barrier in the modeled CO_2 reforming of CH_4 on Ni(111)," *ACS Catal.*, vol. 6, no. 7, pp. 4330–4339, 2016. DOI: 10.1021/acscatal.6b00357.

[31] Z. Wang, X.-M. Cao, J. Zhu, and P. Hu, "Activity and coke formation of nickel and nickel carbide in dry reforming: A deactivation scheme from density functional theory," *J. Catal.*, vol. 311, pp. 469–480, 2014. DOI: 10.1016/j.jcat.2013.12.015.

[32] S. Praserthdam, S. Somdee, M. Rittiruam, and P. B. Balbuena, "Computational study of the evolution of Ni-based catalysts during the dry reforming of methane," *Energy Fuels*, vol. 34, no. 4, pp. 4855–4864, 2020. DOI: 10.1021/acs.energyfuels.9b04350.

[33] Y. J. O. Asencios and E. M. Assaf, "Combination of dry reforming and partial oxidation of methane on $NiO–MgO–ZrO_2$ catalyst: Effect of nickel content," *Fuel Process. Technol.*, vol. 106, pp. 247–252, 2013. DOI: 10.1016/j.fuproc.2012.08.004.

[34] U. Oemar, K. Hidajat, and S. Kawi, "Role of catalyst support over PdO–NiO catalysts on catalyst activity and stability for oxy-CO_2 reforming of methane," *Appl. Catal., A*, vol. 402, no. 1, pp. 176–187, 2011. DOI: 10.1016/j.apcata.2011.06.002.

[35] S. P. Padi, L. Shelly, E. P. Komarala, D. Schweke, S. Hayun, and B. A. Rosen, "Coke-free methane dry reforming over nano-sized $NiO\text{-}CeO_2$ solid solution after exsolution," *Catal. Commun.*, vol. 138, p. 105 951, 2020. DOI: 10.1016/j.catcom.2020.105951.

[36] J. Titus, T. Roussière, G. Wasserschaff, *et al.*, "Dry reforming of methane with carbon dioxide over $NiO–MgO–ZrO_2$," *Catal. Today*, vol. 270, pp. 68–75, 2016. DOI: 10.1016/j.cattod.2015.09.027.

[37] Y. J. O. Asencios, J. D. A. Bellido, and E. M. Assaf, "Synthesis of $NiO–MgO–ZrO_2$ catalysts and their performance in reforming of model biogas," *Appl. Catal., A*, vol. 397, no. 1, pp. 138–144, 2011. DOI: 10.1016/j.apcata.2011.02.023.

[38] V. T. Sagar and A. Pintar, "Enhanced surface properties of CeO_2 by MnO_x doping and their role in mechanism of methane dry reforming deduced by means of in-situ DRIFTS," *Appl. Catal., A*, vol. 599, p. 117 603, 2020. DOI: 10.1016/j.apcata.2020.117603.

[39] L. Gašparič and A. Kokalj, "Revisiting the activity of Ru-hcp(001) and Ru-fcc(111) for alkaline HER: a DFT study," *J. Catal.*, vol. 454, p. 116 641, 2026. DOI: 10.1016/j.jcat.2025.116641.

[40] M. Smiljanić, S. Panić, M. Bele, *et al.*, "Improving the HER activity and stability of Pt nanoparticles by titanium oxynitride support," *ACS Catal.*, vol. 12, no. 20, pp. 13 021–13 033, 2022. DOI: 10.1021/acscatal.2c03214.

[41] M. Smiljanić, M. Bele, L. Pavko, *et al.*, "Titanium oxynitride-supported Ru nanoparticles as exceptional electrocatalysts for alkaline hydrogen evolution reaction," *Chem. Eng. J.*, vol. 517, p. 164 204, 2025. DOI: 10.1016/j.cej.2025.164204.

[42] J. K. Nørskov, T. Bligaard, A. Logadottir, *et al.*, "Trends in the exchange current for hydrogen evolution," *J. Electrochem. Soc.*, vol. 152, no. 3, J23, 2005. DOI: 10.1149/1.1856988.

[43] W.-G. Cui, F. Gao, G. Na, *et al.*, "Insights into the pH effect on hydrogen electrocatalysis," *Chem. Soc. Rev.*, vol. 53, no. 20, pp. 10 253–10 311, 2024. DOI: 10.1039/D4CS00370E.

[44] L. Rebollar, S. Intikhab, N. J. Oliveira, *et al.*, ""Beyond adsorption" descriptors in hydrogen electrocatalysis," *ACS Catal.*, vol. 10, no. 24, pp. 14 747–14 762, 2020. DOI: 10.1021/acscatal.0c03801.

[45] N. Govindarajan, A. Xu, and K. Chan, "How pH affects electrochemical processes," *Science*, vol. 375, no. 6579, pp. 379–380, 2022. DOI: 10.1126/science.abj2421.

[46] P. Lamoureux, A. R. Singh, and K. Chan, "pH effects on hydrogen evolution and oxidation over Pt(111): Insights from first-principles," *ACS Catal.*, vol. 9, no. 7, pp. 6194–6201, 2019. DOI: 10.1021/acscatal.9b00268.

[47] R. Subbaraman, D. Tripkovic, K.-C. Chang, *et al.*, "Trends in activity for the water electrolyser reactions on 3d M(Ni,Co,Fe,Mn) hydr(oxy)oxide catalysts," *Nat. Mater.*, vol. 11, no. 6, pp. 550–557, 2012. DOI: 10.1038/nmat3313.

[48] I. T. McCrum and M. T. M. Koper, "The role of adsorbed hydroxide in hydrogen evolution reaction kinetics on modified platinum," *Nat. Energy*, vol. 5, no. 11, pp. 891–899, 2020. DOI: 10.1038/s41560-020-00710-8.

[49] P. Lindgren, G. Kastlunger, and A. A. Peterson, "A challenge to the $G \sim 0$ interpretation of hydrogen evolution," *ACS Catal.*, vol. 10, no. 1, pp. 121–128, 2020. DOI: 10.1021/acscatal.9b02799.

[50] R. Kronberg and K. Laasonen, "Reconciling the experimental and computational hydrogen evolution activities of Pt(111) through DFT-based constrained MD simulations," *ACS Catal.*, vol. 11, no. 13, pp. 8062–8078, 2021. DOI: 10.1021/acscatal.1c00538.

[51] M. T. Tang, X. Liu, Y. Ji, J. K. Norskov, and K. Chan, "Modeling hydrogen evolution reaction kinetics through explicit water–metal interfaces," *J. Phys. Chem. C*, vol. 124, no. 51, pp. 28 083–28 092, 2020. DOI: 10.1021/acs.jpcc.0c08310.

[52] S. Wang, A. Lu, and C.-J. Zhong, "Hydrogen production from water electrolysis: Role of catalysts," *Nano Converg.*, vol. 8, no. 1, pp. 4–23, 2021. DOI: 10.1186/s40580-021-00254-x.

[53] M. Ďurovič, J. Hnát, and K. Bouzek, "Electrocatalysts for the hydrogen evolution reaction in alkaline and neutral media. A comparative review," *J. Power Sources*, vol. 493, p. 229 708, 2021. DOI: 10.1016/j.jpowsour.2021.229708.

[54] L. G. Verga, J. Aarons, M. Sarwar, D. Thompsett, A. E. Russell, and C.-K. Skylaris, "DFT calculation of oxygen adsorption on platinum nanoparticles: Coverage and size effects," *Faraday Discuss.*, vol. 208, no. 0, pp. 497–522, 2018. DOI: 10.1039/C7FD00218A.

[55] R. Jinnouchi, K. K. T. Suzuki, and Y. Morimoto, "DFT calculations on electro-oxidations and dissolutions of Pt and Pt–Au nanoparticles," *Catal. Today*, vol. 262, pp. 100–109, 2016. DOI: 10.1016/j.cattod.2015.08.020.

[56] G.-F. Wei and Z.-P. Liu, "Optimum nanoparticles for electrocatalytic oxygen reduction: The size, shape and new design," *Phys. Chem. Chem. Phys.*, vol. 15, no. 42, pp. 18 555–18 561, 2013. DOI: 10.1039/C3CP53758G.

[57] Y. Liu, Q. Wang, J. Zhang, *et al.*, "Recent advances in carbon-supported noble-metal electrocatalysts for hydrogen evolution reaction: Syntheses, structures, and properties," *Adv. Energy Mater.*, vol. 12, no. 28, p. 2 200 928, 2022. DOI: 10.1002/aenm.202200928.

[58] M. Bele, P. Jovanovič, Ž. Marinko, *et al.*, "Increasing the oxygen-evolution reaction performance of nanotubular titanium oxynitride-supported Ir nanoparticles by a strong metal–support interaction," *ACS Catal.*, vol. 10, no. 22, pp. 13 688–13 700, 2020. DOI: 10.1021/acscatal.0c03688.

[59] G. Koderman Podboršek, L. Suhadolnik, A. Lončar, *et al.*, "Iridium stabilizes ceramic titanium oxynitride support for oxygen evolution reaction," *ACS Catal.*, vol. 12, no. 24, pp. 15 135–15 145, 2022. DOI: 10.1021/acscatal.2c04160.

[60] W. Luo, Y. Wang, and C. Cheng, "Ru-based electrocatalysts for hydrogen evolution reaction: Recent research advances and perspectives," *Mater. Today Phys.*, vol. 15, p. 100 274, 2020. DOI: 10.1016/j.mtphys.2020.100274.

[61] L. Hou, H. Jang, X. Gu, *et al.*, "Design strategies of ruthenium-based materials toward alkaline hydrogen evolution reaction," *EcoEnergy*, vol. 1, no. 1, pp. 16–44, 2023. DOI: 10.1002/ece2.4.

[62] K. Kusada, H. Kobayashi, T. Yamamoto, *et al.*, "Discovery of face-centered-cubic ruthenium nanoparticles: Facile size-controlled synthesis using the chemical reduction method," *J. Am. Chem. Soc.*, vol. 135, no. 15, pp. 5493–5496, 2013. DOI: 10.1021/ja311261s.

[63] W.-Z. Li, J.-X. Liu, J. Gu, *et al.*, "Chemical insights into the design and development of face-centered cubic ruthenium catalysts for Fischer–Tropsch synthesis," *J. Am. Chem. Soc.*, vol. 139, no. 6, pp. 2267–2276, 2017. DOI: 10.1021/jacs.6b10375.

[64] P. Zhao, Z. Cao, X. Liu, *et al.*, "Morphology and reactivity evolution of HCP and FCC Ru nanoparticles under CO atmosphere," *ACS Catal.*, vol. 9, no. 4, pp. 2768–2776, 2019. DOI: 10.1021/acscatal.8b05074.

[65] Y. Nanba, T. Ishimoto, and M. Koyama, "Structural stability of ruthenium nanoparticles: A density functional theory study," *J. Phys. Chem. C*, vol. 121, no. 49, pp. 27 445–27 452, 2017. DOI: 10.1021/acs.jpcc.7b08672.

[66] S. Nandi, A. S. Nair, and B. Pathak, "First principles investigation on the applicability of ruthenium as a potential ORR catalyst," *J. Chem. Sci.*, vol. 132, no. 1, pp. 2–9, 2019. DOI: 10.1007/s12039-019-1691-9.

[67] T. Zhao, D. Xiao, Y. Chen, *et al.*, "Boosting alkaline hydrogen electrooxidation on an unconventional fcc-Ru polycrystal," *J. Energy Chem.*, vol. 61, pp. 15–22, 2021. DOI: 10.1016/j.jechem.2020.12.008.

[68] Y. Zheng, Y. Jiao, Y. Zhu, *et al.*, "High electrocatalytic hydrogen evolution activity of an anomalous ruthenium catalyst," *J. Am. Chem. Soc.*, vol. 138, no. 49, pp. 16 174–16 181, 2016. DOI: 10.1021/jacs.6b11291.

[69] K. Chen, Z. Liu, S. Zhu, *et al.*, "Ruthenium–nickel nanoparticles with unconventional face-centered cubic crystal phase for highly active electrocatalytic hydrogen evolution," *Adv. Funct. Mater.*, vol. 34, no. 44, p. 2 406 259, 2024. DOI: 10.1002/adfm.202406259.

[70] L. Li, C. Liu, S. Liu, *et al.*, "Phase engineering of a ruthenium nanostructure toward high-performance bifunctional hydrogen catalysis," *ACS Nano*, vol. 16, no. 9, pp. 14 885–14 894, 2022. DOI: 10.1021/acsnano.2c05776.

[71] K. Gao, Y. Wang, Z. Wang, *et al.*, "Ru nanodendrites composed of ultrathin fcc/hcp nanoblades for the hydrogen evolution reaction in alkaline solutions," *Chem. Commun.*, vol. 54, no. 36, pp. 4613–4616, 2018. DOI: 10.1039/C8CC01343H.

[72] Y. Li, L. A. Zhang, Y. Qin, *et al.*, "Crystallinity dependence of ruthenium nanocatalyst toward hydrogen evolution reaction," *ACS Catal.*, vol. 8, no. 7, pp. 5714–5720, 2018. DOI: 10.1021/acscatal.8b01609.

[73] P. Hohenberg and W. Kohn, "Inhomogeneous electron gas," *Phys. rev.*, vol. 136, no. 3B, B864, 1964. DOI: 10.1103/PhysRev.136.B864.

[74] R. M. Martin, *Electronic structure: basic theory and practical methods*. Cambridge, UK: Cambridge university press, 2020.

[75] W. Kohn and L. J. Sham, "Self-consistent equations including exchange and correlation effects," *Phys. Rev.*, vol. 140, no. 4A, A1133, 1965. DOI: 10.1103/PhysRev.140.A1133.

[76] P. Giannozzi, S. Baroni, N. Bonini, *et al.*, "QUANTUM ESPRESSO: A modular and open-source software project for quantum simulations of materials," *J. Phys.: Condens. Matter*, vol. 21, no. 39, p. 395 502, 2009, Code available from http://www.quantum-espresso.org/. DOI: 10.1088/0953-8984/21/39/395502.

[77] P. Giannozzi, O. Andreussi, T. Brumme, *et al.*, "Advanced capabilities for materials modelling with QUANTUM ESPRESSO," *J. Phys.: Condens. Matter*, vol. 29, p. 465 901, 2017. DOI: 10.1088/1361-648X/aa8f79.

[78] J. P. Perdew, K. Burke, and M. Ernzerhof, "Generalized gradient approximation made simple," *Phys. Rev. Lett.*, vol. 77, no. 18, pp. 3865–3868, 1996. DOI: 10.1103/PhysRevLett.77.3865.

[79] J. M. Rahm and P. Erhart, "WulffPack – a package for wulff constructions," *J. Open Source Softw.*, vol. 5, p. 1944, 2025. DOI: 10.5281/zenodo.16616842.

[80] G. Henkelman and H. Jónsson, "Improved tangent estimate in the nudged elastic band method for finding minimum energy paths and saddle points," *J. Chem. Phys.*, vol. 113, no. 22, pp. 9978–9985, 2000. DOI: 10.1063/1.1323224.

[81] G. Henkelman, B. P. Uberuaga, and H. Jónsson, "A climbing image nudged elastic band method for finding saddle points and minimum energy paths," *J. Chem. Phys.*, vol. 113, no. 22, pp. 9901–9904, 2000. DOI: 10.1063/1.1329672.

[82] G. T. Barkema and N. Mousseau, "Event-based relaxation of continuous disordered systems," *Phys. Rev. Lett.*, vol. 77, no. 21, pp. 4358–4361, 1996. DOI: 10.1103/PhysRevLett.77.4358.

[83] M. Poberžnik, M. Gunde, N. Salles, *et al.*, "pARTn: A plugin implementation of the activation relaxation technique nouveau that takes over the FIRE minimisation algorithm," *Comput. Phys. Commun.*, vol. 295, p. 108 961, 2024. DOI: 10.1016/j.cpc.2023.108961.

[84] A. Michaelides, Z.-P. Liu, C. J. Zhang, A. Alavi, D. A. King, and P. Hu, "Identification of general linear relationships between activation energies and enthalpy changes for dissociation reactions at surfaces," *J. Am. Chem. Soc.*, vol. 125, no. 13, pp. 3704–3705, 2003. DOI: 10.1021/ja027366r.

[85] T. Bligaard, J. K. Nørskov, S. Dahl, J. Matthiesen, C. H. Christensen, and J. Sehested, "The Brønsted–Evans–Polanyi relation and the volcano curve in heterogeneous catalysis," *J. Catal.*, vol. 224, no. 1, pp. 206–217, 2004. DOI: 10.1016/j.jcat.2004.02.034.

[86] S. Baroni, S. de Gironcoli, A. Dal Corso, and P. Giannozzi, "Phonons and related crystal properties from density-functional perturbation theory," *Rev. Mod. Phys.*, vol. 73, pp. 515–562, 2 2001. DOI: 10.1103/RevModPhys.73.515.

[87] C. J. Cramer, *Essentials of Computational Chemistry: Theories and Models*. Chichester, UK: John Wiley & Sons, Ltd, 2004.

[88] M. Poberžnik, D. Costa, A. Hemeryck, and A. Kokalj, "Insight into the bonding of silanols to oxidized aluminum surfaces," *J. Phys. Chem. C*, vol. 122, no. 17, pp. 9417–9431, 2018. DOI: 10.1021/acs.jpcc.7b12552.

[89] R. F. Ribeiro, A. V. Marenich, C. J. Cramer, and D. G. Truhlar, "Use of solution-phase vibrational frequencies in continuum models for the free energy of solvation," *J. Phys. Chem. B*, vol. 115, no. 49, pp. 14 556–14 562, 2011. DOI: 10.1021/jp205508z.

[90] J. O. Bockris, A. K. N. Reddy, and M. Gamboa-Aldeco, *Modern Electrochemistry 2A*. New York, USA: Kluwer Academic/Plenum Publishers, 2000.

[91] S. Trasatti, "The absolute electrode potential: An explanatory note (recommendations 1986)," *Pure Appl. Chem.*, vol. 58, no. 7, pp. 955–966, 1986. DOI: 10.1016/0022-0728(86)80570-8.

[92] B. W. J. Chen, L. Xu, and M. Mavrikakis, "Computational methods in heterogeneous catalysis," *Chem. Rev.*, vol. 121, no. 2, pp. 1007–1048, 2021. DOI: 10.1021/acs.chemrev.0c01060.

[93] R. Sundararaman and K. Schwarz, "Evaluating continuum solvation models for the electrode-electrolyte interface: Challenges and strategies for improvement," *J. Chem. Phys.*, vol. 146, no. 8, 2017. DOI: 10.1063/1.4976971.

[94] "Environ documentation." (2019), [Online]. Available: https://environ.readthedocs.io/en/latest/index.html (visited on 01/17/2025).

[95] O. Andreussi, I. Dabo, and N. Marzari, "Revised self-consistent continuum solvation in electronic-structure calculations," *J. Chem. Phys.*, vol. 136, no. 6, 2012. DOI: 10.1063/1.3676407.

[96] G. Fisicaro, L. Genovese, O. Andreussi, *et al.*, "Soft-sphere continuum solvation in electronic-structure calculations," *J. Chem. Theory Comput.*, vol. 13, no. 8, pp. 3829–3845, 2017. DOI: 10.1021/acs.jctc.7b00375.

[97] H. Ogasawara, B. Brena, D. Nordlund, *et al.*, "Structure and bonding of water on Pt(111)," *Phys. Rev. Lett.*, vol. 89, no. 27, p. 276 102, 2002. DOI: 10.1103/PhysRevLett.89.276102.

[98] V. Tripkovic, M. E. Björketun, E. Skúlason, and J. Rossmeisl, "Standard hydrogen electrode and potential of zero charge in density functional calculations," *Phys. Rev. B*, vol. 84, no. 11, p. 115 452, 2011. DOI: 10.1103/PhysRevB.84.115452.

[99] S. Schnur and A. Groß, "Properties of metal–water interfaces studied from first principles," *New J. Phys.*, vol. 11, no. 12, p. 125 003, 2009. DOI: 10.1088/1367-2630/11/12/125003.

[100] P. Xu, A. D. von Rueden, R. Schimmenti, M. Mavrikakis, and J. Suntivich, "Optical method for quantifying the potential of zero charge at the platinum–water electrochemical interface," *Nat. Mater.*, vol. 22, no. 4, pp. 503–510, 2023. DOI: 10.1038/s41563-023-01474-8.

[101] E. Skúlason, V. Tripkovic, M. E. Björketun, *et al.*, "Modeling the electrochemical hydrogen oxidation and evolution reactions on the basis of density functional theory calculations," *J. Phys. Chem. C*, vol. 114, no. 42, pp. 18 182–18 197, 2010. DOI: 10.1021/jp1048887.

[102] J. K. Nørskov, J. Rossmeisl, A. Logadottir, *et al.*, "Origin of the overpotential for oxygen reduction at a fuel-cell cathode," *J. Phys. Chem. B*, vol. 108, no. 46, pp. 17 886–17 892, 2004. DOI: 10.1021/jp047349j.

[103] J. Rossmeisl, E. Skúlason, M. E. Björketun, V. Tripkovic, and J. K. Nørskov, "Modeling the electrified solid–liquid interface," *Chem. Phys. Lett.*, vol. 466, no. 1, pp. 68–71, 2008. DOI: 10.1016/j.cplett.2008.10.024.

[104] R. Sundararaman, W. A. Goddard, and T. A. Arias, "Grand canonical electronic density-functional theory: Algorithms and applications to electrochemistry," *J. Chem. Phys.*, vol. 146, no. 11, 2017. DOI: 10.1063/1.4978411.

[105] N. Bonnet, T. Morishita, O. Sugino, and M. Otani, "First-principles molecular dynamics at a constant electrode potential," *Phys. Rev. Lett.*, vol. 109, no. 26, p. 266 101, 2012. DOI: 10.1103/PhysRevLett.109.266101.

[106] D. Vanderbilt, "Soft self-consistent pseudopotentials in a generalized eigenvalue formalism," *Phys. Rev. B*, vol. 41, pp. 7892–7895, 1990. DOI: 10.1103/PhysRevB.41.7892.

[107] Ultrasoft pseudopotentials for the H, C, O, Mn, and Ni atoms were taken from the Quantum ESPRESSO Pseudopotential Download Page at http://www.quantum-espresso.org/pseudopotentials (files: H.pbe-rrkjus.UPF, C.pbe-rrkjus.UPF, O.pbe-rrkjus.UPF, Ni.pbe-nd-rrkjus.UPF, and Mn.pbe-sp-van.UPF)., 2021.

[108] V. I. Anisimov, J. Zaanen, and O. K. Andersen, "Band theory and Mott insulators: Hubbard U instead of Stoner I," *Phys. Rev. B*, vol. 44, no. 3, pp. 943–954, 1991. DOI: 10.1103/PhysRevB.44.943.

[109] M. Cococcioni and S. de Gironcoli, "Linear response approach to the calculation of the effective interaction parameters in the LDA+U method," *Phys. Rev. B*, vol. 71, no. 3, p. 035 105, 2005. DOI: 10.1103/PhysRevB.71.035105.

[110] I. Timrov, N. Marzari, and M. Cococcioni, "Hubbard parameters from density-functional perturbation theory," *Phys. Rev. B*, vol. 98, no. 8, p. 085 127, 2018. DOI: 10.1103/PhysRevB.98.085127.

[111] M. Methfessel and A. T. Paxton, "High-precision sampling for brillouin-zone integration in metals," *Phys. Rev. B*, vol. 40, no. 6, pp. 3616–3621, 1989. DOI: 10.1103/PhysRevB.40.3616.

[112] N. Marzari, D. Vanderbilt, A. De Vita, and M. C. Payne, "Thermal contraction and disordering of the Al(110) surface," *Phys. Rev. Lett.*, vol. 82, no. 16, pp. 3296–3299, 1999. DOI: 10.1103/PhysRevLett.82.3296.

[113] P. E. Blöchl, "Projector augmented-wave method," *Phys. Rev. B*, vol. 50, no. 24, pp. 17 953–17 979, 1994. DOI: 10.1103/PhysRevB.50.17953.

[114] A. Dal Corso, "Pseudopotentials periodic table: From H to Pu," *Comput. Mater. Sci.*, vol. 95, pp. 337–350, 2014. DOI: 10.1016/j.commatsci.2014.07.043.

[115] PAW pseudopotentials for the Pt, Ru, Ti, O, N, C and H atoms were taken from the Quantum ESPRESSO Pseudopotential Library at http://pseudopotentials.quantum-espresso.org/legacy_tables (files: Pt.pbe-n-kjpaw_psl.1.0.0.UPF, Ru.pbe-spn-kjpaw_psl.1.0.0.UPF, Ti.pbe-spn-kjpaw_psl.1.0.0.UPF, O.pbe-n-kjpaw_psl.1.0.0.UPF, N.pbe-n-kjpaw_psl.1.0.0.UPF, C.pbe-n-kjpaw_psl.1.0.0.UPF, H.pbe-kjpaw_psl.1.0.0.UPF), 2021.

[116] M. Methfessel and A. T. Paxton, "High-precision sampling for brillouin-zone integration in metals," *Phys. Rev. B*, vol. 40, no. 6, pp. 3616–3621, 1989. DOI: 10.1103/PhysRevB.40.3616.

[117] L. Bengtsson, "Dipole correction for surface supercell calculations," *Phys. Rev. B*, vol. 59, no. 19, pp. 12 301–12 304, 1999. DOI: 10.1103/PhysRevB.59.12301.

[118] S. Grimme, J. Antony, S. Ehrlich, and H. Krieg, "A consistent and accurate ab initio parametrization of density functional dispersion correction (DFT-D) for the 94 elements H–Pu," *J. Chem. Phys.*, vol. 132, no. 15, p. 154 104, 2010. DOI: 10.1063/1.3382344.

[119] G. Makov and M. C. Payne, "Periodic boundary conditions in ab initio calculations," *Phys. Rev. B*, vol. 51, no. 7, pp. 4014–4022, 1995. DOI: 10.1103/PhysRevB.51.4014.

[120] M. Cococcioni and S. de Gironcoli, "Linear response approach to the calculation of the effective interaction parameters in the LDA + U method," *Phys. Rev. B*, vol. 71, no. 3, p. 035 105, 2005. DOI: 10.1103/PhysRevB.71.035105.

[121] A. J. Bradley, J. Thewlis, and W. L. Bragg, "The crystal structure of α-manganese," *P. R. Soc. Lond. A-Conta.*, vol. 115, no. 771, pp. 456–471, 1927. DOI: 10.1098/rspa.1927.0103.

[122] D. R. Lide, Ed., *CRC Handbook of Chemistry and Physics*, 85th. Boca Raton, Florida USA: CRC Press, 2005.

[123] J. C. Campuzano and R. G. Greenler, "The adsorption sites of CO on Ni(111) as determined by infrared reflection-absorption spectroscopy," *Surf. Sci.*, vol. 83, no. 1, pp. 301–312, 1979. DOI: 10.1016/0039-6028(79)90495-3.

[124] A. Politano and G. Chiarello, "Vibrational investigation of catalyst surfaces: Change of the adsorption site of CO molecules upon coadsorption," *J. Phys. Chem. C*, vol. 115, no. 28, pp. 13 541–13 553, 2011. DOI: 10.1021/jp202212a.

[125] B. Voigtländer, D. Bruchmann, S. Lehwald, and H. Ibach, "Structure and adsorbate-adsorbate interactions of the compressed Ni(110)-(2×1)CO structure," *Surf. Sci.*, vol. 225, no. 1, pp. 151–161, 1990. DOI: 10.1016/0039-6028(90)90433-9.

[126] G. Zhou, H. Liu, K. Cui, *et al.*, "Role of surface Ni and Ce species of Ni/CeO_2 catalyst in CO_2 methanation," *Appl. Surf. Sci.*, vol. 383, pp. 248–252, 2016. DOI: 10.1016/j.apsusc.2016.04.180.

[127] P. J. Feibelman, B. Hammer, J. K. Nørskov, *et al.*, "The CO/Pt(111) puzzle," *J. Phys. Chem. B*, vol. 105, no. 18, pp. 4018–4025, 2001. DOI: 10.1021/jp002302t.

[128] P. Janthon, F. Viñes, J. Sirijaraensre, J. Limtrakul, and F. Illas, "Adding pieces to the CO/Pt(111) puzzle: The role of dispersion," *J. Phys. Chem. C*, vol. 121, no. 7, pp. 3970–3977, 2017. DOI: 10.1021/acs.jpcc.7b00365.

[129] V. Sumaria, L. Nguyen, F. F. Tao, and P. Sautet, "Optimal packing of CO at a high coverage on Pt(100) and Pt(111) surfaces," *ACS Catal.*, vol. 10, no. 16, pp. 9533–9544, 2020. DOI: 10.1021/acscatal.0c01971.

[130] M. Dlouhy and A. Kokalj, "How adsorbed H, O, OH, and Cl affect plain adsorption of imidazole on copper," *Corros. Sci.*, vol. 205, p. 110 443, 2022. DOI: 10.1016/j.corsci.2022.110443.

[131] J. Rossmeisl, A. Logadottir, and J. K. Nørskov, "Electrolysis of water on (oxidized) metal surfaces," *Chem. Phys.*, vol. 319, no. 1, pp. 178–184, 2005. DOI: 10.1016/j.chemphys.2005.05.038.

[132] C.-C. Hu and K.-Y. Liu, "Voltammetric investigation of platinum oxides. I. Effects of ageing on their formation/reduction behavior as well as catalytic activities for methanol oxidation," *Electrochim. Acta*, vol. 44, no. 16, pp. 2727–2738, 1999. DOI: 10.1016/S0013-4686(98)00400-9.

[133] M. Wakisaka, Y. Udagawa, H. Suzuki, H. Uchida, and M. Watanabe, "Structural effects on the surface oxidation processes at Pt single-crystal electrodes studied by X-ray photoelectron spectroscopy," *Energy Environ. Sci.*, vol. 4, no. 5, pp. 1662–1666, 2011. DOI: 10.1039/C0EE00756K.

[134] H. Tanaka, S. Sugawara, K. Shinohara, *et al.*, "Infrared reflection absorption spectroscopy of OH adsorption on the low index planes of Pt," *Electrocatalysis*, vol. 6, no. 3, pp. 295–299, 2015. DOI: 10.1007/s12678-014-0245-7.

[135] K. Chan and J. K. Nørskov, "Electrochemical barriers made simple," *J. Phys. Chem. Lett.*, vol. 6, no. 14, pp. 2663–2668, 2015. DOI: 10.1021/acs.jpclett.5b01043.

[136] C. Cai, K. Liu, Y. Zhu, *et al.*, "Optimizing hydrogen binding on Ru sites with RuCo alloy nanosheets for efficient alkaline hydrogen evolution," *Angew. Chem.*, vol. 134, no. 4, e202113664, 2022. DOI: 10.1002/ange.202113664.

[137] L. Liu, M. Yu, B. Hou, *et al.*, "Morphology evolution of fcc Ru nanoparticles under hydrogen atmosphere," *Nanoscale*, vol. 11, no. 16, pp. 8037–8046, 2019. DOI: 10.1039/C9NR01611B.

[138] C. M. Zalitis, A. R. Kucernak, J. Sharman, and E. Wright, "Design principles for platinum nanoparticles catalysing electrochemical hydrogen evolution and oxidation reactions: Edges are much more active than facets," *J. Mater. Chem. A*, vol. 5, no. 44, pp. 23 328–23 338, 2017. DOI: 10.1039/C7TA05543A.

[139] Z. Huang, T. Cheng, A. H. Shah, *et al.*, "Edge sites dominate the hydrogen evolution reaction on platinum nanocatalysts," *Nat. Catal.*, vol. 7, no. 6, pp. 678–688, 2024. DOI: 10.1038/s41929-024-01156-x.

[140] Y. Duan, X. Xin, S. Gao, L. Zhou, H. Tang, and C. Ce, "Facet-defined crystalline ruthenium enables ampere-level alkaline hydrogen evolution via lattice reconstruction," *Appl. Surf. Sci.*, vol. 720, p. 165 130, 2026. DOI: 10.1016/j.apsusc.2025.165130.

[141] C. T. Campbell and J. R. V. Sellers, "Anchored metal nanoparticles: Effects of support and size on their energy, sintering resistance and reactivity," *Faraday Discuss.*, vol. 162, no. 0, pp. 9–30, 2013. DOI: 10.1039/C3FD00094J.

[142] S. S. Batsanov, "Van der Waals radii of elements," *Inorg. Mater.*, vol. 37, no. 9, pp. 871–885, 2001. DOI: 10.1023/A:1011625728803.

[143] A. Bondi, "Van der Waals volumes and radii," *J. Phys. Chem.*, vol. 68, no. 3, pp. 441–451, 1964. DOI: 10.1021/j100785a001.

[144] Y. Yang, Y. Yu, J. Li, *et al.*, "Engineering ruthenium-based electrocatalysts for effective hydrogen evolution reaction," *Nano-Micro Lett.*, vol. 13, no. 1, pp. 160–20, 2021. DOI: 10.1007/s40820-021-00679-3.

[145] U. Joshi, S. Malkhandi, Y. Ren, T. L. Tan, S. Y. Chiam, and B. S. Yeo, "Ruthenium–tungsten composite catalyst for the efficient and contamination-resistant electrochemical evolution of hydrogen," *ACS Appl. Mater. Interfaces*, vol. 10, no. 7, pp. 6354–6360, 2018. DOI: 10.1021/acsami.7b17970.

Bibliography

Publications Related to the Thesis

Journal Articles

L. Gašparič, A. Pintar, and A. Kokalj, "A DFT study of elementary reaction steps of dry reforming of methane catalyzed by Ni: Explaining the difference between Ni particles supported on CeO_2 and MnO_x-doped CeO_2," *Appl. Surf. Sci.*, vol. 648, p. 159 029, 2024. DOI: 10.1016/j.apsusc.2023.159029.

L. Gašparič and A. Kokalj, "Revisiting the activity of Ru-hcp(001) and Ru-fcc(111) for alkaline HER: a DFT study," *J. Catal.*, vol. 454, p. 116 641, 2026. DOI: 10.1016/j.jcat.2025.116641.

M. Smiljanić, S. Panić, M. Bele, *et al.*, "Improving the HER activity and stability of Pt nanoparticles by titanium oxynitride support," *ACS Catal.*, vol. 12, no. 20, pp. 13 021–13 033, 2022. DOI: 10.1021/acscatal.2c03214.

M. Smiljanić, M. Bele, L. Pavko, *et al.*, "Titanium oxynitride-supported Ru nanoparticles as exceptional electrocatalysts for alkaline hydrogen evolution reaction," *Chem. Eng. J.*, vol. 517, p. 164 204, 2025. DOI: 10.1016/j.cej.2025.164204.

Published Scientific Conference Contribution

L. Gašparič, A. Kokalj, and S. Džeroski, "Predicting hydrogen adsorption energies on platinum nanoparticles and surfaces with machine learning," in *Slovenian Conference on Artificial Intelligence. Vol. A: proceedings of the 27th International Multiconference Information Society - IS 2024*, M. Luštrek, M. Gams, and R. Piltaver, Eds., Ljubljana, Slovenia: Jožef Stefan Institute, 2024, pp. 67–70.

Published Scientific Conference Contribution Abstracts

L. Gašparič, M. Smiljanić, M. Bele, N. Hodnik, and A. Kokalj, "Activity of ruthenium catalysts for HER: Influence of support and crystal phase," in *Psi-K 2025: abstracts book*, Lausanne, Switzerland, 2025, p. 205.

L. Gašparič, M. Smiljanić, M. Bele, N. Hodnik, and A. Kokalj, "Exploring the activity of TiON supported ruthenium nanoparticles for the hydrogen evolution reaction," in *17th Jožef Stefan International Postgraduate School Students' Conference: book of abstracts*, S. Mežnar, *et al.*, Ed., Kamnik, Slovenia: Jožef Stefan International Postgraduate School, 2025, p. 49.

L. Gašparič, A. Kokalj, and S. Džeroski, "Predicting hydrogen adsorption energy on platinum catalysts with DFT and machine learning," in *Machine Learning for Material Design*, Espoo, Finland: Aalto University, 2025, p. 53.

L. Gašparič and A. Kokalj, "Structure-activity relationship of ruthenium catalysts for hydrogen evolution reaction," in *16th Jožef Stefan International Postgraduate School Students' Conference: book of abstracts*, A. C. B. Lobato, *et al.*, Ed., Piran, Slovenia: Jožef Stefan International Postgraduate School, 2024, p. 41.

M. Smiljanić, M. Bele, I. Marić, *et al.*, "Optimizing hydrogen evolution reaction on low-loaded Ru nanocatalysts supported on titanium oxynitride," in *Book of abstracts: 9th Regional Symposium on Electrochemistry South-East Europe*, B. Grgur, I. A. Pašti, and A. Dekanski, Eds., Novi Sad, Serbia: Serbian Chemical Society, 2024, p. 36.

L. Gašparič and A. Kokalj, "Hydrogen is supposed to be simple," in *15th Jožef Stefan International Postgraduate School Students' Conference: book of abstracts*, N. Kuzmić, *et al.*, Ed., Kamnik, Slovenia: Jožef Stefan International Postgraduate School, 2023, p. 40.

M. Smiljanić, S. R. Panić, M. Bele, *et al.*, "Strong metal-support interaction: A tool for enhancing the hydrogen evolution reaction performance," in *244th ECS Meeting*, Gothenburg, Sweden: The Electrochemical Society, 2023.

L. Gašparič and A. Kokalj, "Computational insight into hydrogen evolution reaction on pt surfaces," in *CrossNano 2023: Crossborder Workshop in Nanoscience and Nanotechnology*, Trieste, Italy: University of Trieste, 2023.

M. Smiljanić, M. Bele, L. Pavko, *et al.*, "Towards advanced electrocatalytic composites for hydrogen evolution reaction," in *2nd Renewable hydrogen energy convention*, Zagreb, Croatia: University of Zagreb, Faculty of Mechanical Engineering and Naval Architecture, 2023, p. 44.

L. Gašparič and A. Kokalj, "Surface reactivity of Pt and Ru towards hydrogen," in *29th Annual Meeting of the Slovenian Chemical Society: book of abstracts*, A. Pintar, *et al.*, Ed., Portorož, Slovenia: Slovensko kemijsko društvo, 2023, p. 108.

L. Gašparič and A. Kokalj, "DFT study of hydrogen evolution reaction on Pt," in *Young Researchers' School on Theory and Simulation in Electrochemical Conversion Processes*, Paris, France: CECAM, 2023.

L. Gašparič and A. Kokalj, "DFT study of dry reforming of methane at Ni/CeO_2 and Ni/Mn_xCeO_2 catalysts," in *14th Jožef Stefan International Postgraduate School Students' Conference: book of abstracts*, R. Novak, *et al.*, Ed., Kamnik, Slovenia: Jožef Stefan International Postgraduate School, 2022, p. 67.

L. Gašparič and A. Kokalj, "DFT analysis of HER on titanium oxynitride and graphene supported Pt nanoparticles," in *4th International Meeting on Materials Science for Energy related Applications: Book of Abstracts*, I. A. Pašti and A. S. Dobrota, Eds., Belgrade, Serbia: University of Belgrade, Faculty of Physical Chemistry, 2021, p. 52.

L. Gašparič and A. Kokalj, "DFT study of hydrogen adsorption on pt nanoparticles supported on graphene and TiON," in *Book of abstracts: 27th Annual Meeting of the Slovenian Chemical Society*, A. Pintar, *et al.*, Ed., Portorož, Slovenia: Slovensko kemijsko društvo, 2021, p. 107.

Biography

Lea Gašparič was born in Ptuj, Slovenia, where she attended primary and secondary school. She finished secondary school (Gimnazija Ptuj) in 2015, earning the Golden Matura Award for outstanding performance in the national final examination. Then she enrolled at the Faculty of Chemistry and Chemical Technology, University of Ljubljana. Throughout her studies, she was awarded a certificate of commendation for the highest grade average. From the beginning of her studies, her focus was on computational chemistry, and she completed the undergraduate program in chemistry with a thesis titled *"Effect of hydrogen bond on the properties of chemical and biological systems"* in 2018. In 2020, she completed the master's program in chemistry at the same faculty with a thesis entitled *"Study of hydrogen bonds between metal hydroxides and organic molecules with molecular modeling"*.

During her undergraduate studies, she began collaborating with the Department of Physical and Organic Chemistry at the Jožef Stefan Institute, and her master's thesis was carried out under the supervision of Prof. Dr. Anton Kokalj (Jožef Stefan Institute) and Prof. Dr. Andrej Jamnik (University of Ljubljana). After completing her master's degree, she was employed as a research assistant at the Department of Physical and Organic Chemistry of the Jožef Stefan Institute and at the National Institute of Chemistry, working on various projects.

In 2021, she enrolled in the doctoral program at the Jožef Stefan International Postgraduate School under the supervision of Prof. Dr. Anton Kokalj. Her research focused on different catalysts and the investigation of their activity, with an emphasis on electrocatalysis. Throughout her doctoral work, she collaborated on different projects, working with experimental research groups and with the artificial intelligence department. She also held a short Erasmus+ fellowship in Trieste, Italy, where she worked on interfacing a transition-state algorithm with existing engines for electronic structure calculations.

During her doctoral studies, she attended numerous conferences and summer schools, including Psi-K, the European Summer School in Quantum Chemistry, and the CAMD Summer School, and received two awards for outstanding contributions. She published three articles as first author and co-authored three joint experimental–computational articles. She also serves as a reviewer for the Journal of The Electrochemical Society and Electrochimica Acta. In addition to her scientific work, she co-organized two student conferences (16th and 17th Jožef Stefan International Postgraduate School Students' Conference) and a PWTK workshop in 2024.